University of Southampton

Faculty of Environmental and Life Sciences
School of Ocean and Earth Science

High-resolution spectrographic studies of strange aurora over Svalbard

DOI: . . .

by

Rowan Dayton-Oxland
MSci
ORCiD: 0000-0001-9642-7647

A thesis for the degree of
Doctor of Philosophy

March 2026

"There is nothing like looking, if you want to find something. You certainly usually find something, if you look, but it is not always quite the something you were after."

J.R.R. Tolkien in *The Hobbit*

Abstract

University of Southampton
Faculty of Environmental and Life Sciences
School of Ocean and Earth Science

Doctor of Philosophy

High-resolution spectrographic studies of strange aurora over Svalbard
by Rowan Dayton-Oxland

The Arctic archipelago of Svalbard experiences unique auroral conditions, due to its ability to observe aurora on the dayside of Earth during the polar night. Here, many auroral forms deviate from the traditional bright green and red emissions of electron precipitation. These strange aurora include dayside proton aurora, pseudo-continuum emissions, and green fragments.

High-resolution spectrography is an extremely powerful analytical tool in auroral studies. Spectra can be used to determine the intensity, emitting species, temperature, energy partition, and many more physical characteristics by examination of the rotational spectrum, or by well-resolving profiles such as the proton blueshift velocity profile. The High-Throughput Imaging Echelle Spectrograph (HiTIES), located on Svalbard, is capable of reaching sub-Ångström resolution, and is the only such instrument in Svalbard. This thesis presents the results of using high-resolution spectrograph data to provide evidence for new and unanswered topics in aurora science.

While low latitude and nightside proton aurora is strongly linked to electromagnetic ion-cyclotron (EMIC) wave activity, we present the first observational study directly comparing Pc1 pulsations and proton aurora on the dayside. Using statistical methods to analyse HiTIES data and magnetometer measurements of Pc1 pulsations, either no - or only a very weak - link is found between EMIC waves and the acceleration and precipitation of auroral protons. This is contrary to initial expectations, and indicates that the mechanisms driving dayside proton aurora are more separate from the nightside regime than first assumed.

The study of pseudo-continuum aurora is a recent development in the field. We present the discovery of pseudo-continuum in the dayside region, poleward of the auroral oval, naming our new strange aurora GHOST. In this thesis I present my contributions to the discovery and characterisation of GHOST using high-resolution spectrography. The use of this method has allowed me to present the first spectra of the pseudo-continuum at high-resolution, with the ability to discern the rotational spectrum. Using HiTIES we also identify patchy proton events concurrent with the GHOST sightings, which we identify as reconnection signatures, locating most of our events in the cusp.

By spectral fitting of the pseudo-continuum, I made the discovery that the spectrum was consistent with N_2 at extreme temperatures. We present the first discussion of N_2 as a possible emitting mechanism for GHOST and for atmospheric pseudo-continuum in general. The magnetospheric origin of the drivers for this excited hot N_2 are also investigated for the first time, and we postulate that strong By dominance in the Interplanetary Magnetic Field (IMF) combined with negative Bz, induces both active reconnection and strong shear flow in the polar cap. GHOST is also brightest and most often found in the cusp, where it is additionally heated by soft precipitation, and excited by sunlight. This combination could produce an ionosphere primed with the high-energy N_2, which is then enhanced by precipitation, resulting in the pseudo-continuum characteristic of GHOST.

Weird aurora such as GHOST, STEVE, and fragments, are also some of the core topics of interest of the ISSI working group Auroral Research Coordination: Towards Internationalised Citizen Science (ARCTICS), of which I am a core member. As an ARCTICS member I have been involved in a variety of citizen science projects, using citizen science observations to understand some of these particularly strange and rare features. Within the ARCTICS group I have also been a core contributor to the creation of the Aurora Field Guide and Handbook for Citizen Science, an open-access pair of documents laying out the basic principles of collaboration in aurora science for both scientists and the public.

Finally, we present preliminary findings on quantifying the effects of proton precipitation on the Arctic mesopause region using HiTIES data. This work outlines possible mechanisms by which the $\mathrm{OH}*$ airglow spectrum, visible in HiTIES, could be disturbed by energetic proton precipitation, and how that impact might appear in optical measurements, and presents initial results.

Contents

List of Figures

List of Tables

List of Additional Material

Event1-03012020.mp4
Event2-28022020_0213.avi
Event2-2802020_0314.avi
Event3-03122021.avi

Declaration of Authorship

I declare that this thesis and the work presented in it is my own and has been generated by me as the result of my own original research.

I confirm that:

1. This work was done wholly or mainly while in candidature for a research degree at this University;
2. Where any part of this thesis has previously been submitted for a degree or any other qualification at this University or any other institution, this has been clearly stated;
3. Where I have consulted the published work of others, this is always clearly attributed;
4. Where I have quoted from the work of others, the source is always given. With the exception of such quotations, this thesis is entirely my own work;
5. I have acknowledged all main sources of help;
6. Where the thesis is based on work done by myself jointly with others, I have made clear exactly what was done by others and what I have contributed myself;
7. Parts of this work have been published as:

Dayton-Oxland, R., Ball, F., Whiter, D., Samaddar, S., Partamies, N., Barthelemy, M., Herlingshaw, K., Karvinen, E., GHOST aurora - continuum emission produced by hot N_2, EGUsphere Preprint, https://doi.org/10.5194/egusphere-2025-5317 2026.

Partamies, N., **Dayton-Oxland, R.**, Herlingshaw, K., Virtanen, I., Gallardo-Lacourt, B., Syrjäsuo, M., Sigernes, F., Nishiyama, T., Nishimura, T., Barthelemy, M., Aruliah, A., Whiter, D., Mielke, L., Grandin, M., Karvinen, E., Spijkers, M., and Ledvina, V. E.: First observations of continuum emission in dayside aurora, Ann. Geophys., 43, 349–367, https://doi.org/10.5194/angeo-43-349-2025, 2025

Grandin, M., Bruus, E., Ledvina, V. E., Partamies, N., Barthelemy, M., Martinis, C., **Dayton-Oxland, R.**, Gallardo-Lacourt, B., Nishimura, Y., Herlingshaw, K., Thomas, N., Karvinen, E., Lach, D., Spijkers, M., and Bergstrand, C.: The Gannon Storm: citizen science observations during the geomagnetic superstorm of 10 May 2024, Geoscience Communication, 7, 297–316, https://doi.org/10.5194/gc-7-297-2024, 2024

Herlingshaw, K., Lach, D., **Dayton-Oxland, R.**, Bruus, E., Karvinen, E., Ledvina, V., Partamies, N., Grandin, M., Spijkers, M., and Nishimura, Y.: ARCTICS Aurora Field Guide and Handbook for Citizen Science, ARCTICS Working Group, https://doi.org/10.5281/zenodo.13932081 2024a

Dayton-Oxland, R., Whiter, D., Kim, H., and Lanchester, B.: No statistical link between proton aurora and Pc1 pulsations in the high-latitude dayside, ESS Open Archive, https://doi.org/10.22541/essoar.169945307.73073056/v2, 2024

Signed:..... Date:.....

Acknowledgements

There are so many people without which this thesis would have been a lot harder, a lot worse, and probably never completed at all, my gratitude knows no bounds.

Dan, you've been the best supervisor anyone could ask for. I've had a fabulous time doing science with you for the last four years, from the roughest patches to the most exciting graphs, you've been an ever-present source of support and a near-infinite source of knowledge. Thank you also for the best field-work experiences, teaching me to figure-skate, introducing me to Svalbard, Safari biscuits, and the inside of a desktop, and for all the delirious campaign memories and Google maps explorations. #1 PhD supervisor.

James, thank you so much, best partner ever. Thanks for letting me distract you for your entire PhD with 2 hour lunches, Pret trips, and random outdoor adventures, and thank you for supporting me through mine. Thank you for your love and support, help, encouragement, ideas, and being a fantastic rubber duck. Man door hand hook car door.

Next, thank you so much to all my collaborators without whom most of my work would be impossible. Noora in particular, thank you for all your guidance, all the fun science we've done, morning dooks, excellent hiking, and many Freune cakes eaten. Couldn't have done it without you. Thank you Maxime for being a great running and dooking partner, but most of all for inviting me to join the ARCTICS group which has been a core experience of my PhD. With that, thank you to all the rest of the ARCTICS members, Katie, Mathieu, Lena, Bea, Vincent, Emma, David, Donna, Neethal, Eero, Toshi, Eric and everyone else! It's been an honour doing great science with you all. Thank you also to Betty and Fiona, you've both been a source of excellent discussions, information, and help.

All the SEP gang have made my PhD such an excellent time, you are all a supremely weird and lunatic group of people to play geography games with (complimentary). Patrik, it was a joy bouldering, field-working, and aurora hunting with you, getting in car crashes, and attending your wedding. Kamalam, you've managed to make me laugh through the direst of conference experiences, you've dooked in the ice with me, one time I saved you from drowning in Kilpisjärvi, you make the best food, and you're so funny and brilliant. Fiona and Kate, I love yapping with you, we're natural besties and I only wish our bestie era could have been longer. Thanks to all the other SEP legends, Nick, Srimoyee, Hannah, Siyuan, Nawapat, Konrad, James W, Laura, Imogen, and Rob. I've learned a lot from you all.

Eloïse, I have loved every camping trip, every pagan ritual, every muddy horrible run, every meal shared, every tea spilled, you're a gem and I hope we can mermaid together for all time. Farin, it's been a joy having someone to share all my fascinations with, you're like if a molotov cocktail and some traditional handcrafts had a baby. Mwah, mwah, mwah. Shrimps is bugs. Also thank you to Beth, and Seb, it's been an honour adventuring with you for the last four years. Thank you all.

Thank you, Carys, you've been keeping me sane for 15 years on a daily basis, what a feat. Also Ruby, Lizzie, Rowanne, and Daisy, though distance conspires against us, I'll see you soon or die trying.

Last but not least, thank you to my family for your love and support. Beithean, you've been an excellent flatmate. Thanks to my other sisters, Haesel, Polly, and Maya. My mum, my dad, Cara, Evie, Jim and Mave, my granny Hannah, you all made me the person I am and even if I'm away down south and bad at ringing, I love you all. Thank you also to my newly acquired family-in-committent, Matt, Ellie, Charlie, Alison, Steve, Jo, Simon, and Grandma, for your support, and for welcoming me into your excellent barbecues and Minecraft realms.

Chapter 1

Introduction

The aurora is a natural light in the upper atmosphere, driven by magnetospheric processes. The Earth's aurora is the visible part of an enormous, invisible system transferring energy from the Sun and Earth's core, all the way down into the upper and middle atmospheres. Studying the aurora can allow us to observe the quite poorly understood physics and chemistry in the Earth system's largest interface; air-space. The aurora allows us to observe fairly directly plasma physics, magnetospheric dynamics, atmospheric chemistry, and the flow of energy in and out of the upper atmosphere. Some important applications of this are improving understanding of Earth's atmosphere, necessary to accurately model weather and climate change, to understand and hopefully one day to forecast space weather, which can damage satellites and communications, and to study plasma physics in an accessible, natural laboratory, with applications such as nuclear fusion and space travel.

This thesis uses high-resolution spectroscopy of both proton aurora and molecular emissions, to explore strange aurora in the high Arctic, over Svalbard, which are poorly understood, and their physical mechanisms largely unknown. The following chapter provides a brief overview of the solar wind, magnetosphere and ionosphere, and the resulting strange aurora, specifically all the different forms of proton aurora, continuum emissions, and green blobby things that we don't yet understand. Chapter 2 will go through the more specific details of the physics and chemistry foundational for this work, mostly molecular spectroscopy details and certain plasma physics concepts. Chapter 3 will describe the main instrumentation used in this thesis, HiTIES, magnetometer, and EISCAT Svalbard radar. Chapter 4 presents my work comparing Pc1 pulsations and proton aurora in the Svalbard dayside. Chapter 5 presents the first observations of GHOST aurora including my high-resolution data, followed by my proposed mechanism for GHOST in Chapter 6. Next, my citizen science contributions are listed in Chapter 7, and my parts of the Aurora Handbook for Citizen Science. Finally, I present some preliminary work on $\mathrm{OH}*$ airglow and proton aurora in Chapter 8, and conclude my thesis in Chapter 9.

1.1 The Sun and Earth

The origin for all this energy lies in the sun and in the Earth's core. The solar dynamo produces a massive and complex magnetic field, which creates a 'bubble' of space dominated by the Sun called the heliosphere, and filled by the interplanetary magnetic field (IMF). The leading edge sits at approximately 100 AU behind a bow shock produced as the heliosphere travels through the interstellar medium, see Figure 1.1. The tail extends for many thousands of AU as it trails behind the sun's path. Embedded within the IMF is the Earth's geomagnetic field - generated by the motion of molten iron and nickel in the core - this produces an area of space dominated by the geomagnetic field, the Earth's magnetosphere (and henceforth just, the magnetosphere).

The Sun is constantly emitting highly ionised plasma, called the solar wind, originating in the solar corona - the outermost region of the solar atmosphere, which is superheated by some still unknown process, resulting in fast ions and electrons escaping the sun's gravity. There are two regimes of solar wind, fast and slow, which outflow at about $700\mathrm{kms}^{-1}$ and $400\mathrm{kms}^{-1}$ respectively. Due to its high conductivity, the IMF is 'frozen in' (see section 2.4.4) to the solar wind plasma, and as the sun rotates the solar wind drags behind the rotation, resulting in the Parker spiral.

The electromagnetic interaction between the plasma flowing from the sun in the solar wind and the magnetosphere produces a complex system of electric and magnetic fields and currents which in turn drive many plasma processes, and eventually deposit energised plasma in the atmosphere, producing the aurora. The origin of the plasma population is a combination of the solar wind and atmospheric loss from the Earth.

Figure 1.1: Hubble image of the star LL Ori's bow shock in the interstellar medium, which probably looks quite similar to our own. Credit: NASA/ESA and The Hubble Heritage Team STScI/AURA

1.2 Magnetosphere

Let's have a closer look at the magnetosphere, Figure 1.2. First on the largest scale, we can see a bow shock and 'bubble' of space dominated by the geomagnetic field. The geomagnetic field lines show an approximate dipole field, with field lines close to the poles connecting directly to the IMF. About 14 R_{Earth} in the sunward direction we can find the bow shock, the shock wave produced by the super-Alfvénic solar wind hitting the Earth - closer in at 11 R_{Earth} is the boundary between the geomagnetic field and the IMF, the magnetopause (Fairfield, 1971), and between them is a region of turbulent post-bow shock solar wind, the magnetosheath. The figure shows the convection of the geomagnetic field - the Dungey Cycle. Proposed originally in Dungey (1961), it describes how the geomagnetic field flows around the Earth in response to the IMF, illustrated in Figure 1.3.

At the subsolar point of the magnetopause, the geomagnetic field and IMF field undergo magnetic reconnection, see Section 2.4.4, resulting in an 'open' field line and allowing solar wind plasma to enter the magnetosphere. The open field line is then convected over the polar cap toward the magnetotail, dragged along by the flow of the solar wind, where it undergoes reconnection again and closes. The closed field line then convects back from the tail towards the Earth, finally travelling toward the dayside where it is opened again by reconnection with the IMF. This results in a region of open field around the geomagnetic poles, called the polar cap, where convection of field lines causes plasma to be dragged around in two convection cells, see the right panel in Figure 1.3. Within the polar cap close to the dayside open/closed boundary lies the cusp, a region of open field where shocked magnetosheath solar wind plasma can flow directly into the ionosphere.

Within the magnetosphere are many trapped plasma populations originating from particles lost from the atmosphere and solar wind plasma which enters through reconnection. These include the ring current, Van Allen belts, plasma sheet, and plasmasphere. Magnetospheric dynamics can cause plasma to be lost from these populations and propagate down the magnetic field lines to the ionosphere; this and the direct polar cap entry provide the charged particles which flow down to produce the aurora.

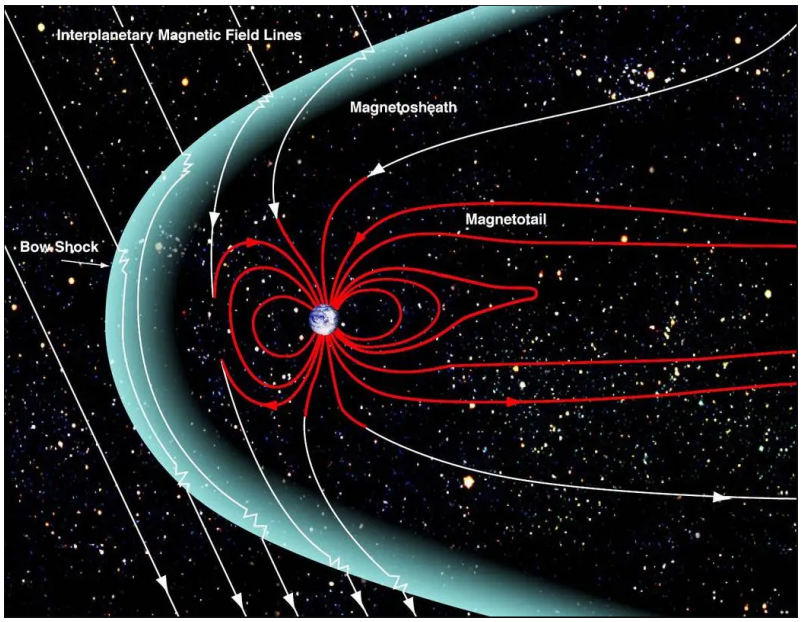

Figure 1.2: Classic diagram of the magnetosphere, sun to the left, showing the bow shock, magnetopause, selected field lines, and open field lines connecting to the IMF, Credit: NASA.

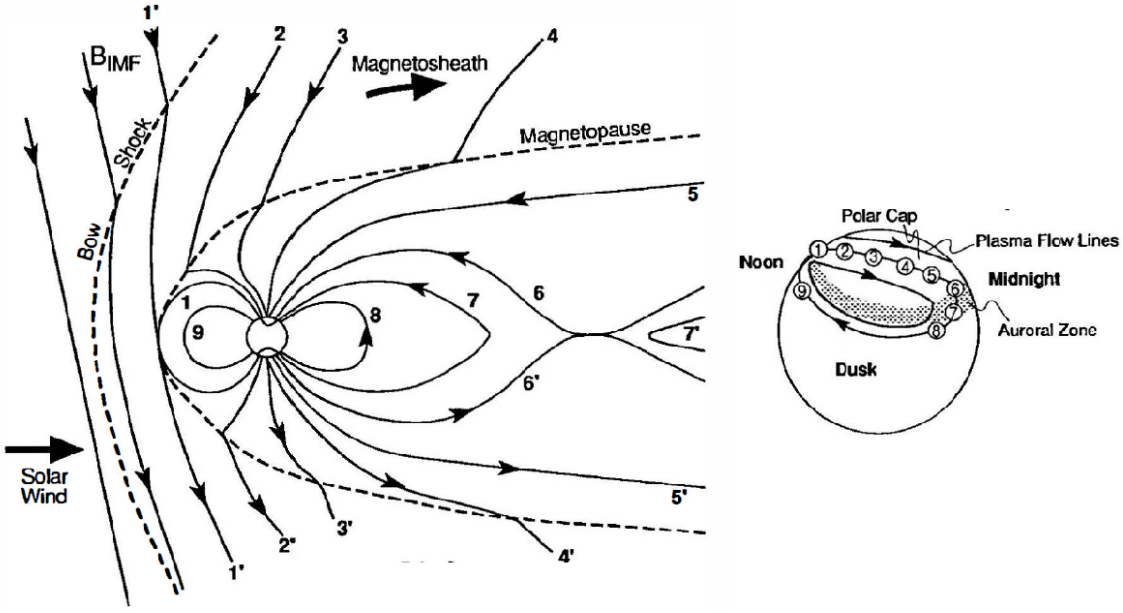

Figure 1.3: Dungey cycle schematic and polar cap view, from Kivelson and Russel (1995)

1.3 Ionosphere and atmosphere

The atmosphere is the neutral gas layer stretching from the Earth's surface up into space. This thesis is concerned with the thermosphere, which extends from ~ 100 km up to about 350 km. The thermosphere and ionosphere overlap significantly, and this is the location of the aurora. The most abundant species in the upper atmosphere and ionosphere are molecular nitrogen N_2, molecular oxygen O_2, and atomic oxygen O.

The ionisation of the upper atmosphere is primarily driven by solar UV and X-ray radiation during the day, and to a much smaller extent by cosmic rays. Above 80-100 km, the rate of collisions between ionised and neutral molecules is low enough for a permanent plasma population to exist; this is the ionosphere, shown in Figure 1.4 compared to the atmosphere. Most of the ionosphere is not fully ionised, but lies alongside fairly high density neutral atmosphere, though it is conductive enough for magnetospheric current systems to flow through it. The level of ionisation is also dependent on the density and species of the atmospheric constituents, and so varies strongly with altitude - leading to multiple layers of ionised plasma. The upper layer is the F-region, which splits into two under daylight conditions, followed by the E and D-regions. Most aurora takes place within the F and E regions between 90 and 300 km altitude.

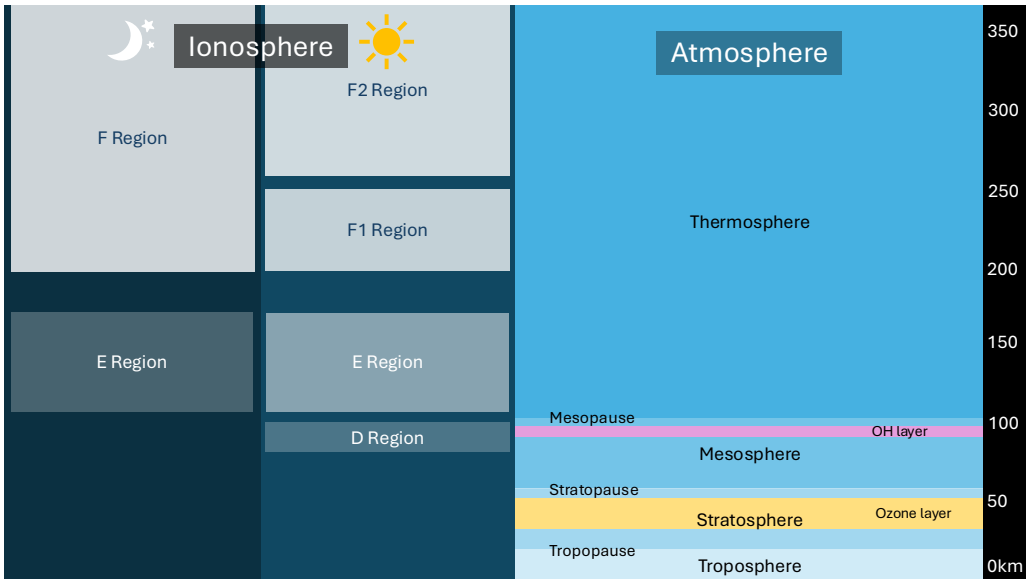

Figure 1.4: Important layers of the Earth's daytime and nighttime ionosphere and atmosphere.

1.4 The aurora

Since there is no universally agreed on definition of aurora, I am choosing my own. In this thesis I am defining aurora as natural light emissions caused by particles energised by magnetospheric processes interacting with the atmosphere.

I've selected four key magnetosphere-ionosphere processes here to show how most of the main types of aurora are produced. The first three are particle precipitation - this is often considered to be what defines aurora, and includes proton and electron aurora. Probably controversially, I am including aurora-like emissions in my definition, firstly because they look like aurora, and secondly because they come ultimately from magnetospheric processes. This broader definition includes things like Strong Thermal Emission Velocity Enhancement (STEVE) and fragments. I have certainly left some things out, for example Auroral Kilometric Radiation (which fits the definition and I think is aurora), but I think this a good overview.

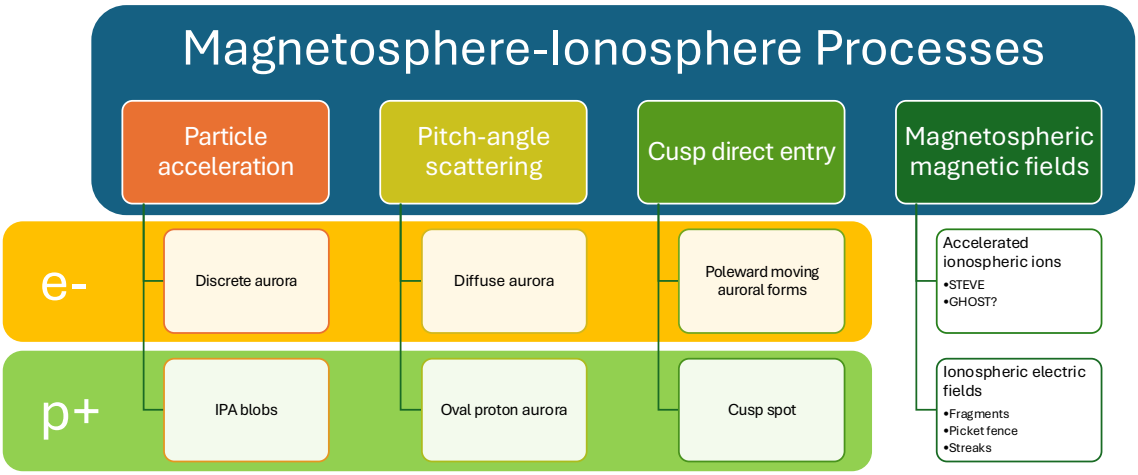

Figure 1.5: All aurora are unified by their origin in magnetosphere-ionosphere coupling processes.

1.4.1 Proton aurora

The Earth's proton aurora occurs as a result of energetic protons from space interacting with the upper atmosphere. This light was first detected as 'hydrogen showers' in the atmosphere nearly a century ago (Vegard, 1939), and was identified as aurora caused by 1-100keV proton precipitation a decade later by observing the Doppler shift of the hydrogen lines (Eather, 1967) which indicated that the emitting hydrogen atoms were travelling towards the ground with velocities $\sim 1000\mathrm{km\,s^{-1}}$ (Egeland and Burke, 2019).

Unlike the bright, structured, electron aurora, it is impossible to discern proton aurora with the naked eye. However, it is easily detectable in the hydrogen Lyman and Balmer series spectral lines by ground instruments. The proton auroral spectrum is measured by tens of high-latitude spectrographs and cameras, and global measurements are taken by space-based observatories. Precipitation enhanced ion and electron populations in the atmosphere can also be directly measured by rocket campaigns (Jones, 2010), or by radar such as the European Incoherent SCATter radar (EISCAT), mapping the ionospheric response to proton aurora.

When one says, 'proton aurora,' most people will think only of one form. This proton aurora is concentrated in the proton auroral oval - a broad ($3-7^{\circ}$ of latitude) elliptical region encircling the magnetic pole which experiences a high proportion of energetic proton precipitation (Eather, 1967; Feldstein, 1986). The proton auroral oval is bright equatorward of the (electron) auroral oval in the dusk sector of the ionosphere and poleward in the dawn sector, see Figure 1.6. In these regions proton precipitation can dominate over electron precipitation, with protons carrying the majority of the energy flux and causing the majority of the thermal and chemical changes (Gallardo-Lacourt et al., 2021), but the overall effects of proton aurora on the atmosphere are unknown.

Proton arcs also appear equatorward of the oval in the afternoon, at about 15 magnetic local time (MLT), when the IMF changes direction (North to South or West to East for example), causing geomagnetic disturbance. These subauroral proton arcs have been observed by IMAGE spanning several hours of MLT (Sakaguchi et al., 2007).

Another significant form of proton aurora is the cusp spot - when observed from space this appears as a bright roundish spot at the high-latitude side of the cusp, and is often imaged in proton aurora bands such as Lyman α. It is generally accepted to be formed due to proton and electron precipitation from lobe reconnection, under northward IMF (Han et al., 2023). On the dayside at high latitudes we also observe direct entry solar wind proton precipitation, which is *not* the cusp spot, but is located in the cusp[1]. This is accelerated proton precipitation lasting for several hours around noon MLT.

There are several more recently discovered strange auroral phenomena, which are linked to proton precipitation. Highly accelerated protons in the subauroral region can produce Isolated Proton Aurora

[1]..depending on how strongly you feel about your preferred definition of the cusp.

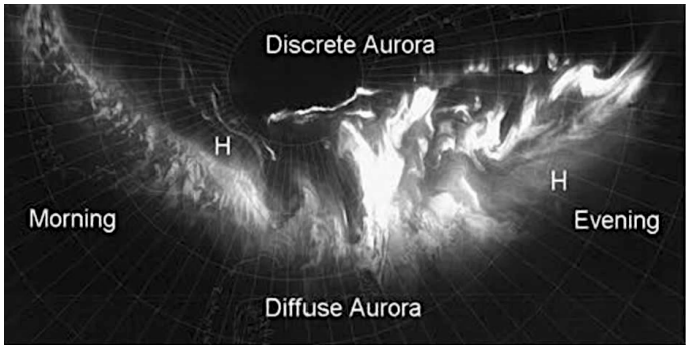

Figure 1.6: The location of the proton aurora dominated regions (marked with a H) relative to the nightside electron aurora (split into discrete and diffuse regions), showing the proton aurora is concentrated equatorward of the oval in the evening (or dusk) sector and poleward at dawn (Egeland and Burke, 2019).

(IPA), also known as blobs, shown in Figure 1.7. They are accelerated by Landau damping of EMIC waves (Kim et al., 2021), which also produce relativistic electrons capable of destroying mesospheric ozone (Ozaki et al., 2022). IPA produce a visual signature at the location of these ozone holes.

Figure 1.7: Proton blobs imaged by Katie Raymer-Woods at Dunvegan, Skye, as part of the SolarMax mission, see Chapter 7. Skywarden observation https://taivaanvahti.fi/observations/show/133800.

Blobs can sometimes appear below a diffuse red arc, the red at 230km and green at 110km (Nishimura et al., 2022), in a combination known as Red Arc with Green Diffuse Aurora (RAGDA) (Herlingshaw et al., 2024a) (shown later in Figure 7.9). This red arc is distinct from the similar Stable Auroral Red (SAR) arc which are also linked to proton precipitation from the ring current, (e.g. Cornwall et al., 1971; Rees and Roble, 1975). SAR arcs have been studied for decades, with recent interest being particularly renewed in relation to STEVE, see section 1.4.2.

Dunes are another recently discovered strange phenomenon. They appear as a soft green diffuse band southward of the main auroral arcs, filled with parallel wave-like bands (Herlingshaw et al., 2024a). They were first identified from Finnish citizen scientist photographs by Palmroth et al. (2020), and proposed to be due to atmospheric waves such as a mesospheric bore modulating the oxygen density around the mesopause. Later work by Grandin et al. (2021) using further citizen science photographs from Scotland and Norway, combined with spacecraft particle data, found that dunes are linked to particle precipitation. While it has been assumed that electron precipitation plays the core role, significant high proton flux was found close to the dunes, and identified as a possible contributor.

Proton aurora is a diverse and complex form of aurora, relatively poorly understood and often ig-

nored compared to its electron counterpart due to its invisible and often extremely diffuse appearance, complicating observations. Open questions around proton aurora include the acceleration and precipitation mechanisms in non-oval regimes, secondary electron production, proton precipitation's role in other strange auroral forms, and the effect of proton precipitation on the polar atmosphere.

1.4.2 Continuum emissions

For a more detailed background into continuum emissions see Chapters 5 and 6. A quick overview of what continuum refers to;

Continuum: A true continuum refers to an emission from a continuous process such as thermal blackbody radiation, Bremsstrahlung, or synchrotron radiation. There is no small-scale spectral structure to be resolved as photons are emitted from a non-discrete process.

Pseudo-continuum: The work presented in this thesis has shown that this is what we see in auroral studies - when molecular bands are sufficiently dense and overlapping, we see a flat raised spectrum across a large bandwidth. This structure can be resolved into individual lines and so is not a true continuum. In our field this is usually referred to as just 'continuum'.

STEVE, backronym-ed as Strong Thermal Emission Velocity Enhancement, is a white-mauve ribbon of light which lies aligned East-West southward of the auroral oval, shown in Figure 1.8. It was discovered by citizen scientists who initially mis-identified it as a form of proton aurora, calling it a proton arc, but it was later identified as the visible signature of a Sub-Auroral Ion Drift or SAID. These are strong horizontal ion flows which are driven by strong magnetospheric electric fields in the subauroral region. Spectral studies have confirmed the spectrum to be a pseudo-continuum containing also some N_2 bands. The most common theory in the field is that these strong ion drifts cause heating through translation energy transfer to N_2, this reacts with oxygen or OH to produce atmospheric nitrous oxide, NO, which emits a pseudo-continuum emission through chemiluminescent reaction with oxygen.

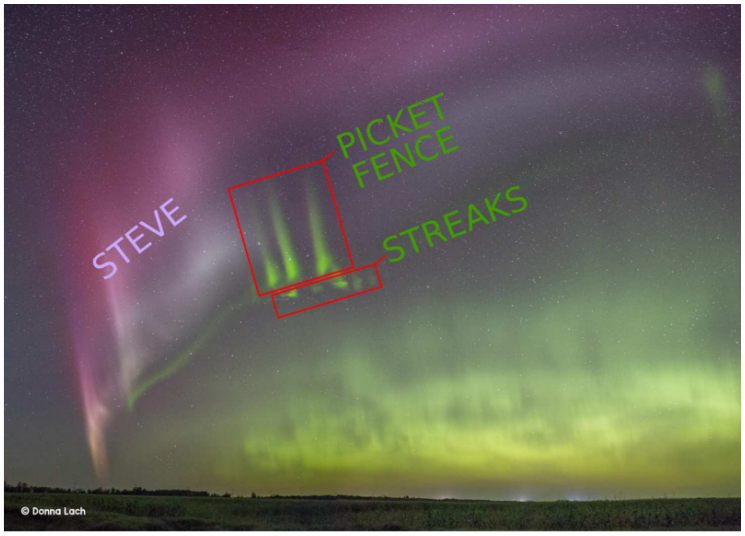

Figure 1.8: STEVE shown with picket fence and streaks, photo by Donna Lach, taken from (Herlingshaw et al., 2024a).

Continuum emissions have also now been observed in the auroral oval (Spanswick et al., 2024b). These don't have their own name yet but are usually referred to as 'oval continuum' or similar, when distinguishing them from STEVE and GHOST.

GHOST, backronym-ed as Geomagnetically-driven High-bandwidth Optical Spectrum from the Thermosphere, has been newly discovered, with the work presented in this thesis, so I will leave it as a surprise for Chapters 5 and 6.

1.4.3 Green bits

STEVE is often accompanied by bright green vertical pillar-like features, which appear usually evenly spaced below the continuum arc. These are called the picket fence, and are an active area of research. At the bottom of the picket fence, there are sometimes smaller green dots, known as streaks. These are both shown in relation to STEVE in Figure 1.8.

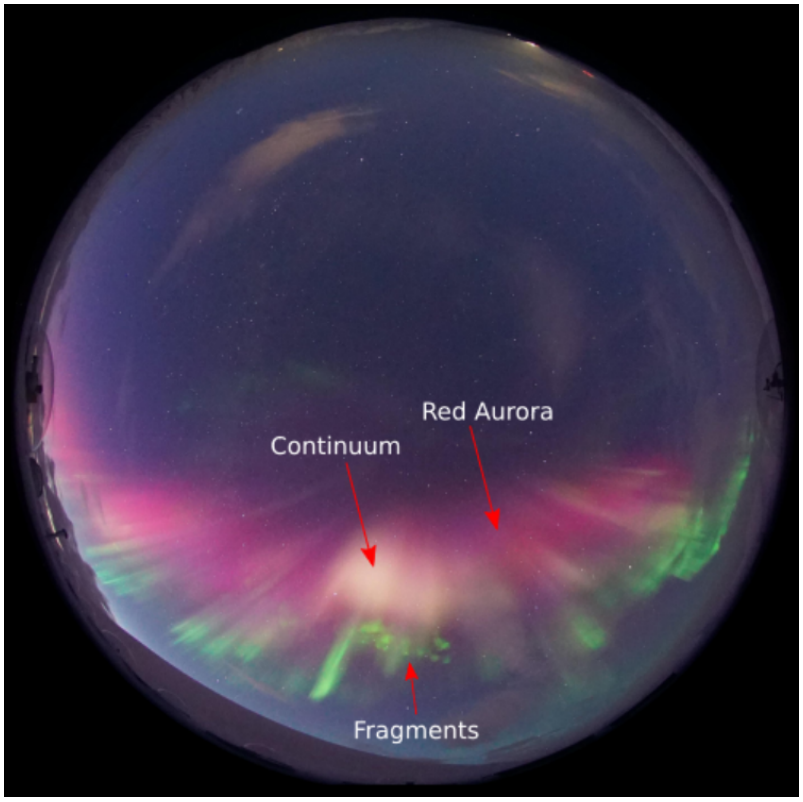

Figure 1.9: UNIS All-sky Camera image of fragments, continuum, and auroral arc, taken from Svalbard Aurora Chasers (2025)

Fragments of Aurora-like Emission or FAEs, appear as small $< 20\mathrm{km}$ dots of green emission, lasting typically under a minute. They can appear alone or form chains, and are visually quite similar to the 'streaks'. Fragments are also frequently spotted alongside continuum emissions, for example in Figure 1.9. They were first identified only recently from citizen science identifications in the Aurora Zoo project, and first published in Dreyer et al. (2021); Whiter et al. (2021).

Chapter 2

Auroral physics and chemistry

2.1 Proton aurora

Proton aurora is generated by the precipitation of auroral protons typically in the 1-100 keV range (see section 1.4.1). The mechanism is shown in a digram in Figure 2.1. The proton precipitates down the field line, travelling in a helical pattern due to the cyclotron motion. When the proton collides with an atmospheric species (ion, molecule, or atom) it can undergo charge exchange - stripping the atmospheric species of an electron and become neutralised. This neutral hydrogen atom is in an excited electronic state. Since it is now electrically neutral it is no longer bound to the magnetic field and will continue travelling close to the incident proton velocity v away from its original field line in a direction determined by its trajectory pre-ionisation. After a short period of time, the hydrogen will de-excite by emitting a photon, the proton aurora. Due to the decoupling of the hydrogen from the field before emission, proton aurora is diffuse and unstructured as the hydrogen 'spreads out' before de-excitation, this effect is increased by its larger initial gyroradius, as ρ_c for a proton in the geomagnetic field with energy 5 keV is about 200 m. Since the hydrogen is travelling with some v typically between 200-1000 kms^{-1}, the measured photon is Doppler shifted (Jones, 1974). The resulting broadened H-emission profile is therefore close to the incident velocity profile of the precipitating protons when viewed in the magnetic zenith (Galand and Chakrabarti, 2006), some emission will be to the red side indicating protons travelling upwards - this is due to reflection of protons from the magnetic bottle (Jones, 1974). Some high-energy precipitating protons can induce secondary electrons, resulting in visible green emission by the mechanism described below in section 2.2. Visibility is also improved as high-energy protons are less affected by broadening (Jones, 1974). This can be seen in Isolated Proton Aurora (IPA), which appears as diffuse green 'blobs' and is generated by secondary electrons produced by highly EMIC-accelerated protons in the subauroral region (e.g. Sakaguchi et al., 2015; Kim et al., 2021). The separation of proton and electron contributions to the auroral spectrum is an ongoing open problem in aurora physics.

2.2 Molecular auroral emissions

Traditional electron precipitation aurora involves the excitation of (relatively stationary) atmospheric constituents and is bound to the magnetic field, so is typically brighter and visible to the naked eye with sufficient electron precipitation flux. Eventually, an atmospheric species such as N_2 can be excited to a higher energy level, described by its electric state as well as its vibrational and rotational state if molecular (see section 2.3). The species will then de-excite by emitting a photon with wavelength characteristic of the emitting species. The overall spectrum is produced by the emissions of many electron-excited species in the line-of-sight and imparts information about the emitters. Is is possible to identify the emitting species, energy partition of states, temperature, altitude, and many more useful attributes by careful observation and modelling of the auroral spectrum.

In this thesis, aurora is not necessarily due to particle precipitation (or only in part), and I do not study traditional electron precipitation aurora. Therefore a broader description, could start not with precipitation but with any energising process in the ionosphere. This might be due to a strong parallel electric field, secondary electrons from strong ion-drifts, precipitation of electrons or protons resulting in many secondary electrons, shear flow causing translational excitation, high temperatures, or any other energising process. In auroral forms such as STEVE, GHOST, fragments, or picket fence, we do not yet understand the energising mechanisms, but the result is similar to traditional aurora, where we end up with an excited molecular species, which decays and emits auroral photons.

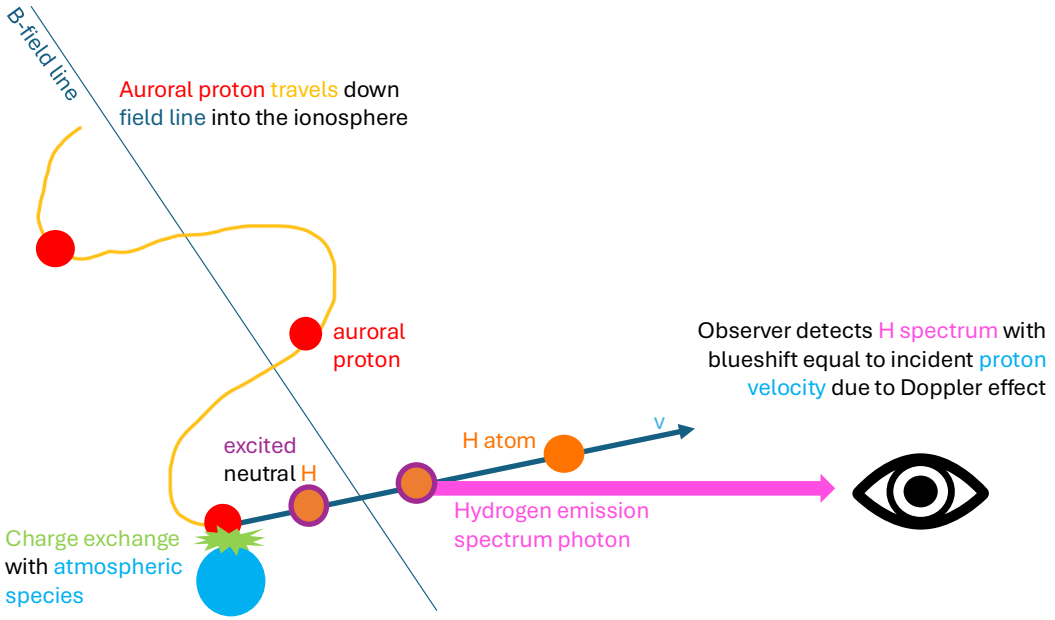

Figure 2.1: Diagram showing the process by which a precipitating auroral proton produces proton aurora.

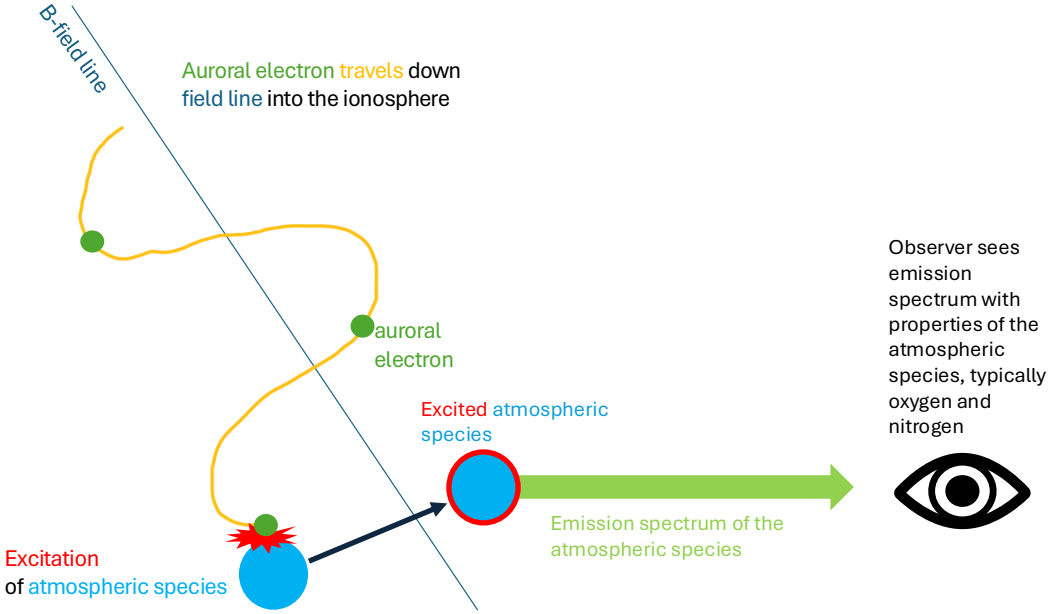

Figure 2.2: Diagram showing the process by which a precipitating auroral electron produces electron aurora.

2.3 Molecular spectroscopy

This section was written using Jokiaho (2009) and Holmen (2016) as reference. Molecular spectroscopy is complicated enough, so let's only consider diatomic molecules, which are mostly what we observe in the upper atmosphere anyway. This section will first explain the possible quantum states of a diatomic molecule. From here we can look at the possible energy levels for the electric, vibrational, and rotational degrees of freedom, giving us a way to find the molecules' emitting wavelengths. The intensity of emission from each line will be found, explaining Einstein A coefficients, temperature effects etc. on the way. We will see how much information can be gathered by resolving the molecular spectrum.

2.3.1 Diatomic molecules

The total energy of a diatomic molecule is the sum of its electric, vibrational, and rotational energies, each of which are quantised;

$$E_{tot} = E_e + E_v + E_r \tag{2.1}$$

Firstly, the *electric state* depends on which orbitals the electrons sit in. When all the electrons have the lowest energy, populating the lower orbitals, this is the ground state and is denoted with the letter X. In excited electric states, the electrons move up in orbitals, and states are denoted by the letters A, B, C,[1] ...

The electrons have *orbital angular momentum* L based on their orbital motion around the molecule, and *spin angular momentum* S based on their own rotation. The molecule therefore has some total angular momentum of electrons, which is designated Ω, where

$$\Omega = |\,\Lambda + \Sigma\,| \tag{2.2}$$

and where Λ and Σ represent the vector components of L and S along the intranuclear axis respectively. These two quantities are used to further describe the molecular state. $\Lambda \in \mathrm{N}_0 \leq \mathrm{L}$ and the corresponding molecular states are given by $\Lambda{=}\Sigma, \Pi, \Delta, \ldots$ while $\Sigma{=}\mathrm{S}, \mathrm{S}{-}1, \mathrm{S}{-}2, \ldots, {-}\mathrm{S}$ where $\mathrm{S} > 0$ and can be integers or half integers depending on whether the number of electrons (who each have spin $\mathrm{s}{=}\frac{1}{2}$) are odd or even. In molecular notation, the Λ state follows the electric state, e.g. X the ground state, which is then followed by Ω.

If $\Lambda \neq 0$, the electric energy splits into a multiplet of states. The number of states is $2\mathrm{S}+1$. Molecules with an even number of electrons, have S a whole integer and therefore are odd multiplets, singlets/triplets etc. and molecules with odd number of electrons form even multiplets, doublets/quartets. A multiplet state gives several electric energy levels very close to each other.

Finally, a homonuclear diatom can have symmetric or anti-symmetric parity. Parity refers to whether the wavefunction of the molecular orbitals change sign under inversion, essentially flipping the molecule. If an inversion changes the sign the parity is *ungerade*, if not it is *gerade*. This is marked by a u or g.

Let's look at an example notation for a molecular state;

$$X^2\Pi_{\frac{1}{2}}g \tag{2.3}$$

This tells us that the electric state is X, the ground state. The superscript ^{2} indicates that this is a doublet state. Π indicates that $\Lambda = 1$, and $_{\frac{1}{2}}$ that the total electron angular momentum Ω is $\frac{1}{2}$, so Σ must be $-\frac{1}{2}$. Lastly, the g tells us the molecule is gerade/symmetric.

2.3.2 Molecular spectra

Besides translation, our diatomic molecule has two modes of motion, it can rotate or vibrate, see Figure 2.3. The diatom can rotate around either of the axes through the centre of mass, perpendicular to the interatomic axis, these are degenerate, and can vibrate along the interatomic axis.

[1] In N_2 there are also B' and W states for annoying historical reasons (Jones, 1974)

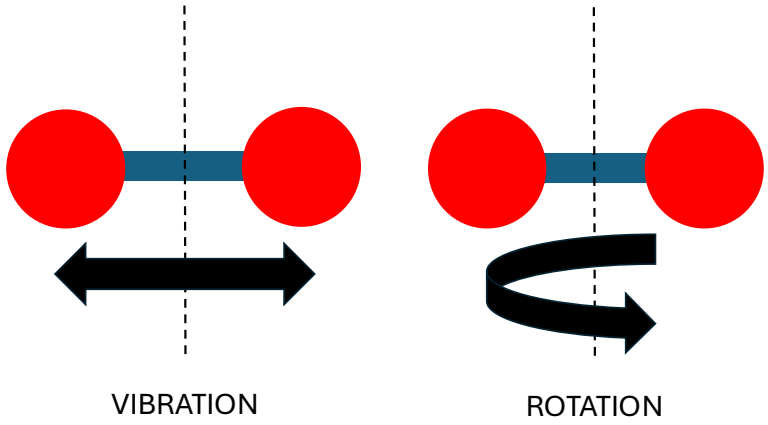

Figure 2.3: Vibrational and rotational motion of a diatom, atoms are represented as red circles, the bond as a blue line connecting the atoms along the interatomic axis, and a perpendicular axis through the centre of mass marked as a dotted black line.

We can assume that the vibration can be described as a simple harmonic oscillator, so that the displacement of each atom from equilibrium can be described as a sine wave. The equation for a simple harmonic oscillator here is;

$$E_v = h\nu(v + \frac{1}{2}) \qquad v = 0, 1, 2, \ldots \tag{2.4}$$

Where h is Planck's constant, ν the vibrational frequency, and v is the vibrational quantum number, which takes values $\in N_0$ where $v = 0$ still has some small vibrational motion. The vibrational quantum number describes the set of quantised vibrational energy states. In a transition between vibrational levels, the upper state is marked v' and the lower as v''.

Rotational motion is modelled as two point masses which we can assume here are equal, rotating around the centre of mass with some rotational frequency. The total rotational energy is given by

$$E_r = \frac{h^2 J(J+1)}{8\pi^2 I} \qquad J = 0, 1, 2, \ldots \tag{2.5}$$

for some $J \in N_0$, the rotational quantum number, which represents the molecular rotational angular momentum. We have a set of discrete quantised rotational energy levels. Transitions between rotational energy levels, J' to J'' are only allowed where

$$\Delta J = J' - J'' = \begin{cases} -1 \\ 0 \\ 1 \end{cases} \tag{2.6}$$

Different values of ΔJ correspond to different branches of lines. $\Delta J = -1$ gives the P-branch, $\Delta J = 0$ gives the Q-branch, and $\Delta J = 1$ is the R-branch. Now we should have everything we need to explain the structure of a molecular spectrum. A diagram showing a simplified schematic of eleconic, vibrational, and rotational energy levels is shown in Figure 2.4.

When an electron moves from a higher to a lower energy level, the wavelength of the photon is dependent on the change in energy, given by

$$E_{tot} = \frac{hc}{\lambda} \tag{2.7}$$

The largest energy division is in the electrical state, then vibrational, and rotational states being the most closely spaced. This translates to the resulting molecular spectrum, in which each electric transition leads to a set of vibrational bands, each containing many individual rotational lines from the P, Q, and R branches.

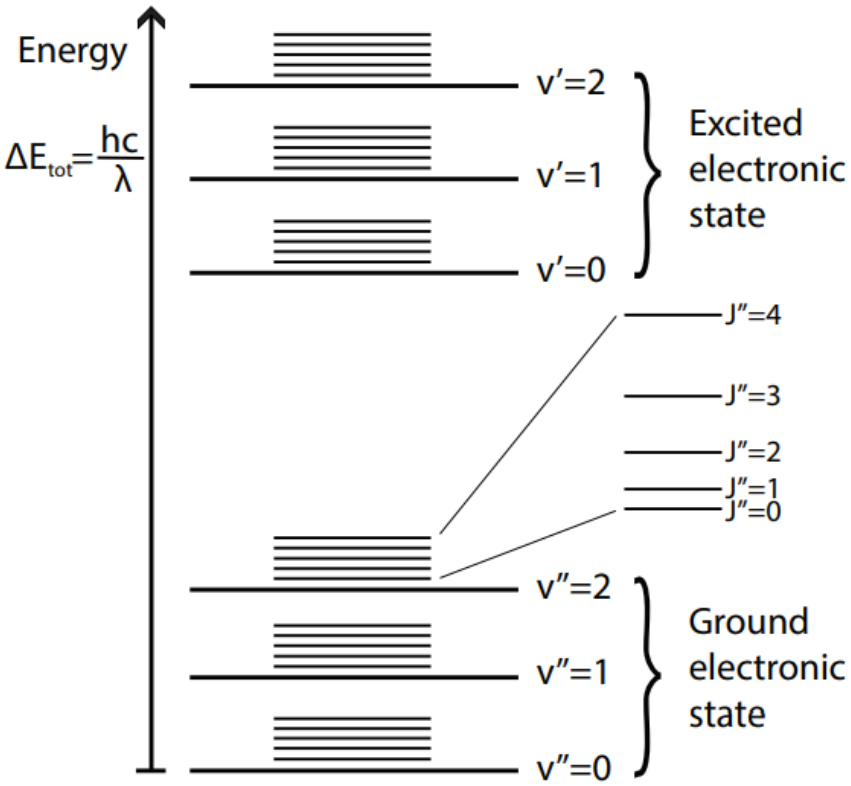

Figure 2.4: Simplified diagram showing electrical, vibrational, and rotational energy states, taken from Holmen (2016)

2.3.3 Emission rates

To predict the shape of the spectrum, the intensity of each line must also be determined. Full details are omitted here as they are outside of the scope of this work, but the basic idea is covered.

The emission rate of a spectral line can be given as

$$I_{v''J''}^{v'J'} = A_{v''J''}^{v'J'} N_{v'J'} h\nu \tag{2.8}$$

describing the energy emitted per second per unit solid angle at frequency ν, from vibrational state v' to v'' and rotational state J' to J'', and depends on the Einstein A coefficient for the transition $A_{v''J''}^{v'J'}$ and the density of molecules in the upper state $N_{v'J'}$, for a unit volume of optically thin emitting gas.

The Einstein A coefficient $A_{v''J''}^{v'J'}$, is the probability per second of spontaneous transmission from the upper state to the lower. It is determined experimentally, usually by examining the relative strength of different transitions.

The density of molecules in the upper state $N_{v'J'}$ depends on the distribution of states in the population. Here is where temperature comes in. There are many factors which describe how energy is divided among the possible vibrational and rotational states, and the P,Q,R branches. The result is that the shape of the spectrum comes from the population distribution of energy levels, which is equivalent to the temperature of the molecules. It can be split into vibrational temperature, the distribution of vibrational states, and rotational temperature, the distribution among rotational states.

Assuming thermal equilibrium, the kinetic temperature of the gas/plasma is very strongly coupled to the rotational temperature due to collisions and excitation, such that

$$T_{therm} \simeq T_{rot} \tag{2.9}$$

Therefore, the shape of the molecular spectrum can be used to determine T_{rot} which we can usually assume is close to T_{therm} of the neutral atmosphere. We determine T_{rot} by spectral fitting. Note, this

assumption is usually reasonable in the E-region up to 120km for typical auroral temperature ranges, but gets worse in the F-region (e.g. Kurihara et al., 2006; Wüst et al., 2023) as the collision time between neutrals increases beyond the radiative decay lifetime.

2.4 Plasma physics

Plasma is defined as an ionised gas in which electromagnetic forces dominate its dynamics, as opposed to short-range nearest neighbour forces which dominate the dynamics of a traditional fluid. It can be modelled either through considering the motion of a single test particle, through considering the plasma as a fluid in magnetohydrodynamics, or through kinetic theory which describes the particle behaviour through distribution functions. We will stick with test-particle descriptions in this section. Only a few plasma physics concepts are really instrumental to this thesis, but I will begin here by defining a few fundamental concepts.

If one assumes a completely ionised hydrogen plasma, comprising equal numbers of positive and negative charges, at the larger scale we can expect the plasma to be electrically neutral. The characteristic length scale at which this occurs is called the Debye length, given by

$$\lambda_D = \left(\frac{\epsilon_0 k_B T}{n e^2} \right)^{1/2} \tag{2.10}$$

linking the average energy of the charges $k_B T$, the charge number density n, and electric charge e (with ϵ_0 representing the vacuum permittivity). Therefore if you add an unbalanced charge to the plasma, the other charges will adjust to cancel it everywhere but the surrounding Debye length (in practice often a few λ_D), (Diver, 2019).

Since plasmas are electrically neutral for scales $> \lambda_D$, there must be a restoring force. If charge neutrality is disturbed this will lead to oscillations in the number density, of some characteristic frequency which we call the plasma frequency. By considering the fluid equations for electrons and assuming stationary ions, and assuming a small perturbation, we end up with a simple harmonic oscillation with frequency

$$\omega_p = \left(\frac{n_0 e^2}{\epsilon_0 m} \right)^{1/2} \tag{2.11}$$

with m the mass of the charge and n_0 the initial charge number density. Since ω_p is mass dependant we have both and ion and electron plasma frequency (Diver, 2019). Another fundamental frequency relates to cyclotron motion. When a charged particle encounters a magnetic field, inserting the B-field into the equation for Lorentz force gives circular motion around the guiding centre in the x and y planes, with a cyclotron frequency of

$$\omega_c = \frac{q B_0}{m} \tag{2.12}$$

where q is charge and m mass, again leading to species dependent cyclotron frequencies (Kontar, 2019). The particle is free to travel parallel to the field line in a helical pattern, defined by the pitch-angle, α given by;

$$\alpha = \arctan \frac{v_\perp}{v_\parallel} \tag{2.13}$$

An important physical mechanism which hinges on these concepts is the reflection of radio waves from the ionosphere. Assuming a cold plasma, the refractive index of the plasma is a function of both the radio frequency and the density dependant electron plasma frequency. Essentially, radio waves will be reflected if $\omega_{EM} < \omega_{pe}$, and transmitted if $\omega_{EM} > \omega_{pe}$. In the real ionosphere, this refractive index varies with density, temperature, and direction and will also impart a change in polarisation for magnetised plasma. This is useful when we consider ionospheric radar measurements later on.

2.4.1 EMIC waves

When $\omega_{EM} > \omega_p$ as we discussed before, electromagnetic waves can travel through plasma relatively unaffected. However, at low frequencies the wave interacts strongly with the plasma environment. In particular, close to the plasma and cyclotron frequencies, the difference between ions and electrons becomes important and various different modes of wave propagation occur. Far below the electron cyclotron frequency we find the ion-cyclotron wave (Baumjohann and Treumann, 2012).

Let's briefly look at the maths to see where EMIC waves fit into the plasma wave zoo. We will start having derived already the cold plasma dielectric tensor, see e.g. Swanson (2003), which comes from the equation of motion for a single particle in an electromagnetic field and Maxwell's equations, assuming a static magnetic field $\boldsymbol{B}_0$ and a uniform homogeneous cold plasma. Assuming a plane wave with wave vector k lying in the x-z plane, making an angle θ with the background magnetic field $\boldsymbol{B}_0 \parallel \hat{z}$;

$$\begin{pmatrix} S - n^2 cos^2\theta & -iD & n^2 cos\theta\, sin\theta \\ iD & S - n^2 & 0 \\ n^2 cos\theta sin\theta & 0 & P - n^2 sin^2\theta \end{pmatrix} \begin{pmatrix} E_x \\ E_y \\ E_z \end{pmatrix} = 0 \tag{2.14}$$

Here, the big letters stand in for the Sum, Difference, Right, Left, and Plasma terms as is traditional, and are physically related to the the cyclotron, plasma, and wave frequencies. θ is the angle between the wave vector and the z-axis. The solutions of this give us the dispersion relations of plasma waves.

For non-trivial solutions, we require the determinant of equation 2.14 to vanish, yielding the general dispersion relation for electromagnetic waves in a cold magnetized plasma. This is the cold plasma dispersion relation

$$An^4 - Bn^2 + C = 0 \tag{2.15}$$

where

$$\begin{gathered} A = Ssin^2\theta + Pcos^2\theta \\ B = RLsin^2\theta + PS(1 + cos^2\theta) \\ C = PRL \end{gathered} \tag{2.16}$$

which we can write in terms of the angle as

$$tan^2\theta = -\frac{P(n^2 - R)(n^2 - L)}{(Sn^2 - RL)(n^2 - P)} \tag{2.17}$$

For waves propagating parallel to the background magnetic field ($\theta = 0$), then the numerator must be = 0 and there are three possible solutions;

$$\begin{gathered} P = 0 \\ n^2 = R \\ n^2 = L \end{gathered} \tag{2.18}$$

These give respectively, plasma oscillations and a right and left-hand circularly polarised wave. Looking now at the left-handed wave, and substituting in the frequencies (for a single-ion plasma) we get;

$$n_L^2 = L = 1 - \frac{\omega_{pi}^2}{\omega(\omega - \omega_{ci})} - \frac{\omega_{pe}^2}{\omega(\omega + \omega_{ce})} \tag{2.19}$$

So where do we get resonance? In the low-frequency limit the electron contribution becomes approximately constant while the ion term dominates, and we get resonances at the ion cyclotron frequency ω_{ci}, which defines the EMIC wave branch (if we follow the right-handed wave solution we get the electron counterpart of EMIC - whistler waves). In a plasma containing multiple ion species (e.g. H^+, He^{++}, O^+), the ion term becomes a sum over the number of species, and each species introduces a resonance and associated cutoff in the L-mode dispersion relation. This leads to distinct EMIC wave bands below the respective ion cyclotron frequencies.

So, Electromagnetic Ion-Cyclotron (EMIC) waves are left-circularly polarised transverse electromagnetic plasma waves. They travel mostly parallel to the magnetic field close to the ion-cyclotron frequency. Though the solar wind is mostly hydrogen, it contains a small amount of heavier ions such

as He^{++} and O^{+}. Where multiple ion-species are present, EMIC waves travel in multiple bands, each close to a different ion's cyclotron frequency. EMIC waves are typically generated in the equatorial closed magnetosphere by hot plasma anisotropy but can also be generated in the outer magnetosphere, and are an important precipitation mechanism for proton aurora.

2.4.2 Trapped particles and loss processes

Particles can become trapped by magnetic mirroring, where converging field lines increase the particles' pitch-angle, causing reflection at the mirror point. Since Earth's approximate dipole field creates converging field lines where they approach Earth's surface, a population of particles is trapped, bouncing back and forth along the closed field. There are many processes by which particles can be lost from these trapped populations, resulting in precipitation down the field-lines into the atmosphere, two of which are described here which are referenced in the following work.

Pitch-angle scattering

Not all bouncing particles are trapped. If a particle's pitch-angle becomes low enough it can enter the 'loss-cone'; essentially for small α particles the magnetic mirror point can lie within the atmosphere, meaning that the particle will collide with neutrals before it is reflected, and can escape. We can consider that any particle which would reflect below an altitude of 100 km from the surface will be lost. We can use this to define a cone, where all pitch-angles below a certain threshold will be lost, and we call this the loss cone.

Plasma waves with frequency above the plasma and cyclotron frequency can alter the pitch-angle of a particle so that it is scattered into the loss-cone, leading to precipitation of particles into the atmosphere (Baumjohann and Treumann, 2012). EMIC waves can strongly resonate with protons at energies from a few keV to 100 keV, and are therefore efficient at pitch-angle scattering protons (Gabrielse et al., 2022).

Field-line curvature scattering

If the magnetic field exhibits abrupt spatial changes comparable to the gyroradius of a particle, the gyro-orbit may not remain closed. This violates the first adiabatic invariant[2] and the pitch-angle can be changed such that it enters the loss cone and the particle precipitates (Gabrielse et al., 2022)

Curvature scattering is dependent on the particle gyroradius ρ_c and the field-line radius of curvature R_c. The rate of scattering can be expressed as the ratio

$$\kappa = \frac{R_c}{\rho_c} \tag{2.20}$$

where scattering is strong for small κ. Since ions have a large gyroradius this is another important precipitation mechanism in protons. It typically occurs in the magnetotail.

[2]The invariance of magnetic moment of the particle when it experiences a change in **B**.

2.4.3 Landau damping

An important wave-particle interaction is Landau damping, by which EMIC waves can accelerate ions. Landau damping is the transfer of energy from a wave to a resonant particle with frequency $\nu = \nu_{wave} \pm \Delta\nu$ for some small $\Delta\nu$, or vice versa. A population of slightly slower particles will be accelerated by a wave which is itself slowed, while a population of faster particles will lose energy and accelerate the wave. This interaction is elastic so the total energy of the wave and particles is conserved with no dissipation (Baumjohann and Treumann, 2012; Kontar, 2019).

2.4.4 Frozen-in condition and reconnection

In sufficiently conductive magnetised plasma, particles become 'frozen-in' to the magnetic field. Essentially particles are stuck to a specific field line and cannot move across it. If an outside force acts on the field, the plasma must follow it, and if a force acts on the plasma it will drag the field-line along with it. If the plasma is not sufficiently conducting, instead of the magnetic field lines being frozen into the plasma, the field diffuses through the plasma (Diver, 2019).

When two field-lines are sufficiently close and under sufficient pressure, the field topology can change in a process called magnetic reconnection. The plasma breaks the frozen-in condition and diffuses across the field-line (Baumjohann and Treumann, 2012), allowing external plasma to enter a closed magnetic volume such as solar wind into the magnetosphere, (Dungey, 1961).

The magnetic Reynolds number, is a dimensionless quantity which describes the plasma-ness of the plasma;

$$R_m = \frac{vL}{\eta} \tag{2.21}$$

where v is the characteristic velocity of the plasma, L the characteristic scale length, and η the magnetic diffusivity. It describes the strength of the plasma coupling to the magnetic field - for low $R_m << 1$ diffusion dominates and particles can travel across field-lines. A high $R_m >> 1$ indicates that the plasma is frozen in, and reconnection can take place.

Chapter 3

Instrumentation

Figure 3.1: Kate Barton and I working on HiTIES under the dome at the KHO, taken in January 2025 by Katie Herlingshaw. The red sky enigma (Sigernes et al., 2005) is visible in the background, as ice crystals reflect sunlight from over 10° below the horizon to produce a bright pink-orange glow in the depths of polar night.

3.1 HiTIES

Figure 3.2: HiTIES view out of the dome at the KHO, taken by me in January 2025. SIF is visible in the lower right hand side of the image where the two freshly added ASK cameras are visible in silhouette. An active auroral arc sits above in the sky.

High resolution aurora spectra were acquired using the High-Throughput Imaging Echelle Spectrograph (HiTIES). The instrument is the University of Southampton's copy of the first HiTIES, whose design specifications are laid out in Chakrabarti et al. (2001). HiTIES is part of the Spectrographic Imaging Facility (SIF), located at the Kjell Henriksen Observatory (KHO), see Figures 3.1 and 3.2, at Longyearbyen on the Arctic archipelago, Svalbard at geographic latitude 78° 8' 52.8" N, and longitude 16° 2' 34.8" E. HiTIES is directed at the magnetic zenith with an 8° by 0.05° field-of-view. The instrument includes an echelle spectrograph with a mosaic filter, which is used to select multiple overlapping spectral orders, enabling observation of multiple non-contiguous wavelength bands at very high resolution. The detector is a highly sensitive Electron-Multiplying CCD (EMCCD), which is ideal for very low light imaging at the photon counting level. This means we can run at high temporal resolution. The imaging cadence is $2\mathrm{Hz}$ giving a temporal Nyquist frequency of $1\mathrm{Hz}$. However, HiTIES spectra are commonly integrated over multiple seconds to improve the signal to noise ratio when observing phenomena of an appropriately long variation timescale.

Figure 3.3 shows a simplified view of the HiTIES setup in the KHO room, showing the most important data cables, coolant system, and layout. Power, internet, lighting, and the other SIF instruments (the photometers and ASK) have been omitted for simplicity. The HiTIES spectrograph and camera are mounted on a platform, under the dome in the dark room, separated from the computer room by a blackout curtain and door. Figure 3.4 shows the optical path of the HiTIES spectrograph unit. The field-lens focusses light onto the spectrograph slit, an echelle grating splits the light beam, this is then collimated and passed through a mosaic filter and is then imaged onto the EMCCD detector chip using a 50 mm camera lens.

HiTIES is connected to a coolant system which uses purified water to cool the EMCCD chip to -70° C to reduce dark current, and the camera data cable connects directly to the SIF computer in the adjoining room, transmitting images and metadata such as chip temperature. The silverbox is located under the SIF platform - it sends a timing signal to the camera and runs the sensor array. The GPS is used to synchronise the clock in the silverbox to ensure that images are taken exactly on the second and half-second boundary. Sky brightness, dome temperature, and computer room temperature are all

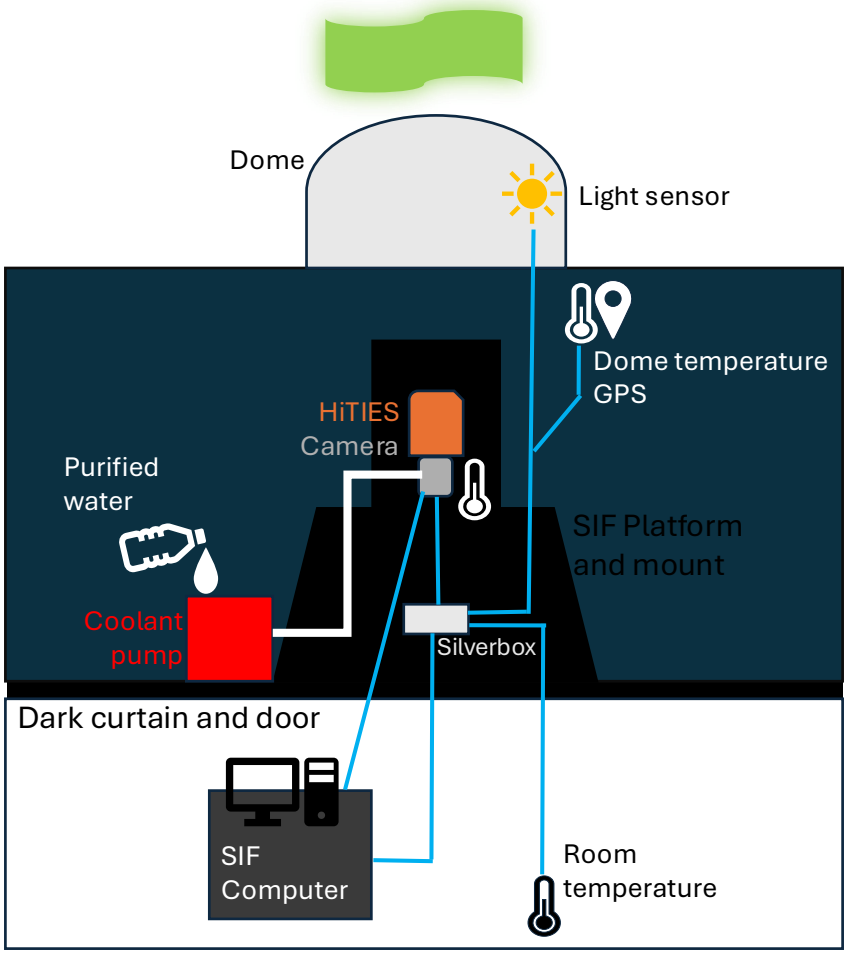

Figure 3.3: Diagram showing the layout of the HiTIES instrument and vital connections in the dome room at the KHO. Blue lines indicate data cables, the thicker white line represents the coolant hose.

monitored. HiTIES is paused when the sky is too bright, to prevent damaging the EMCCD detector.

For the observations in this thesis, HiTIES used three filter panels. The mosaic filter selects the Hα band at 649–663 nm used for observing proton precipitation, the long-lived $\mathrm{O} + 2\mathrm{p}{-}2\mathrm{d}$ emission imaged by ASK and OH(8,3) band at 728–743 nm, and OH(5,1) and OH(9,4) bands at 790–807 nm. An image of the mosaic filter with the three panels is shown in Figure 3.5. The spectral resolution is ~ 1Å and varies with wavelength.

Typically once or twice in each observing season, HiTIES flat and Hα calibrations are taken. Flat exposures are used to measure the CCD response to a bright uniform source, for absolute intensity calibration and non-uniformity correction. A flat-lamp (uniform bright white light box) is placed over the aperture which is imaged by HiTIES for 5 minutes, with corresponding background (lamp off) images taken for two minutes before and after. Since HiTIES' shutter has broken, darks throughout the season are taken from an average of the CCD response outwith the mosaic filter area as a proxy. HiTIES images are then calibrated using these flats and darks as per the following relationship;

$$Calibrated = \frac{RawImage - Darks}{Flat - Darks} \tag{3.1}$$

During calibrations, a Hydrogen gas spectrum tube is also exposed to calibrate the location of H Balmer line emissions, such as Hα at 6563Å or the Hβ line.

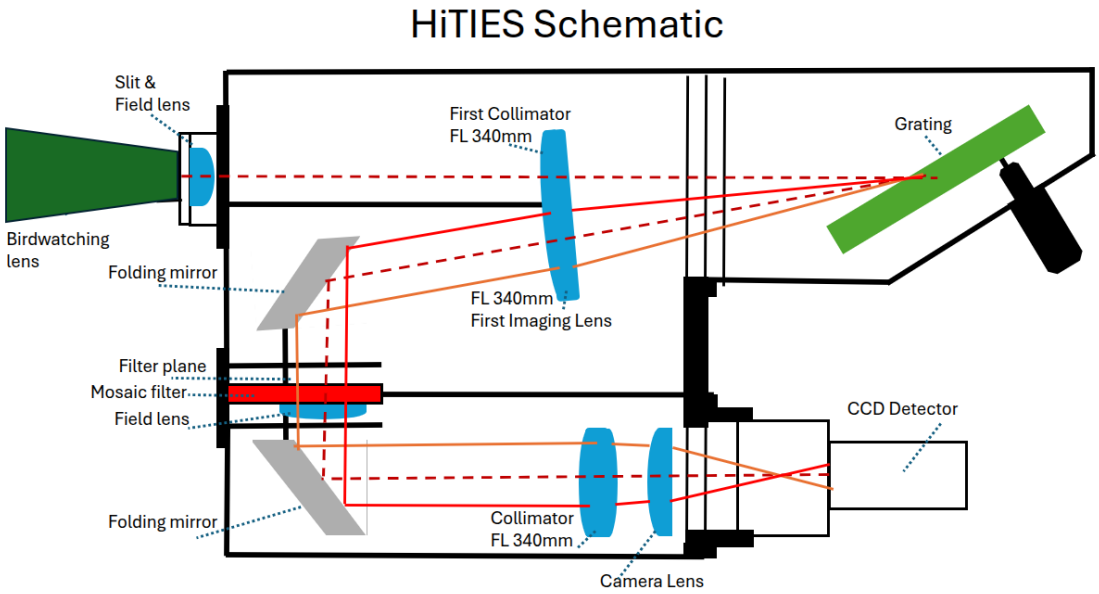

Figure 3.4: Schematic of the HiTIES spectrograph unit showing the central optical path. The light enters a large birdwatching lens, passes through the slit and the first collimator before reflecting from the echelle grating. The light then splits, passes through an imaging lens, and is reflected through the mosaic filter which selects the desired spectral order. The resulting spectrum is then collimated, enters the camera lens, and is imaged by the Electron-multiplying CCD detector. Figure reproduced from Chakrabarti et al. (2001).

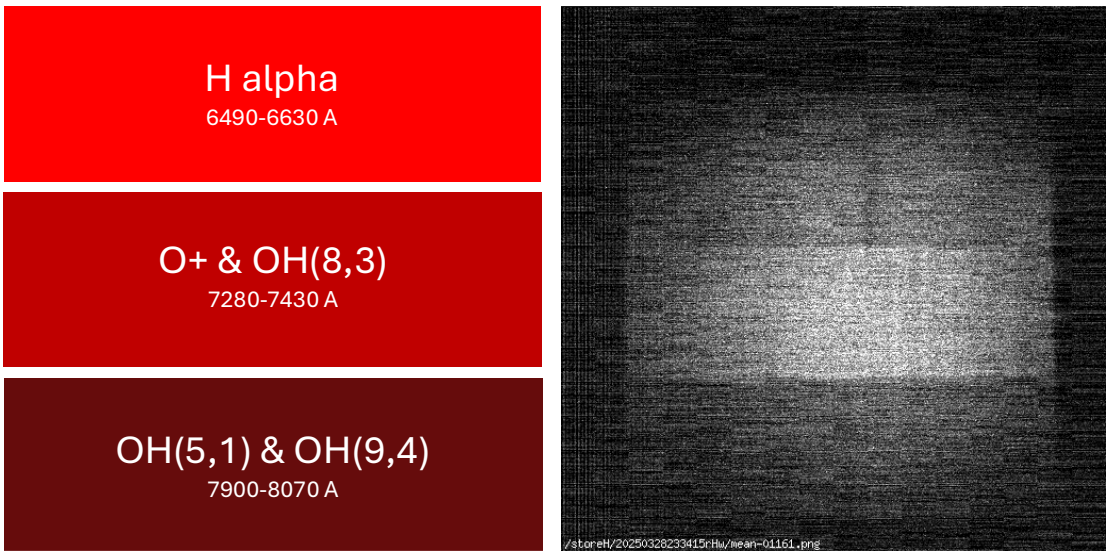

Figure 3.5: Diagram of HiTIES' mosaic filter for the observations used in this thesis (left), and real HiTIES raw image (right). The three filters are stacked vertically, each imaging a third of the slit.

3.1.1 Calibration

The most vital calibration for the HiTIES spectrograph is the wavelength calibration, i.e. the relationship between wavelength and pixel position within each mosaic panel. The calibration is different for each panel due to their different wavelengths, and varies between seasons due to changes made to the instrument setup, degradation of parts, accidental knocks etc. which requires that the wavelength calibration be repeated regularly. There are several emission sources which can be used for calibration - the hydrogen spectrum tube; absorption lines from the solar spectrum can be used; or OH airglow lines can be used. My favoured calibration spectrum is OH airglow lines as you can take a long exposure to get a clear, well defined spectrum, with a quiet dark background. OH lines are well distributed throughout the Hα panel, and they are visible in clear conditions throughout the season, allowing for calibration to be as close to the target event as possible.

First, at least 20 minutes of dark, quiet sky conditions should be found - this can be done using quicklook keograms from the SIF website. A time with no cloud, and no aurora should be chosen for the clearest calibration spectrum. This IDL code uses the Space Environment Physics group's library of routines for HiTIES, hsoft, to read in the data, average it in time, produce a spectrum, lookup the existing wavelength calibration, and plot the spectrum.

```
read_tim, '03/01/2020 21:00:00', 20/60.,  ...

av=reform(total(dseq,1)/double(n_elements(time)),[1,512,512])
spectra,3,mjs0,time[0],av,sp
get_w,mjs0,3,wl
plot,wl,sp
```

It is worth identifying spectral features on this reference spectrum before calling the calibration procedure. In particular, there is a strong Hα emission line at 6563Å from the Earth's hydrogen geocorona, which should be identified so it is not confused with an OH line. As a tip for future calibrators - the spectrum can be compared to the hydroxyl model spectrum in a programme like Inkscape by overlaying the data and models to easily identify the line correspondences, see Figure 3.6

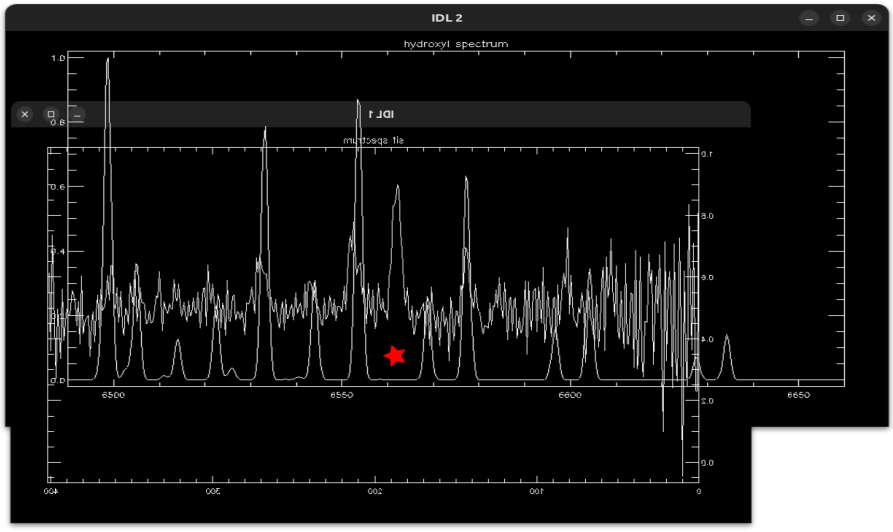

Figure 3.6: An example quick comparison between a spectrum of 20-minutes of dark sky and a model OH spectrum. The Hα geocorona line is identified with a red star. Note, the data spectrum x-axis has been flipped.

Once the OH lines have been identified, the interactive `auto_wlcal` routine can be called with appropriate settings. The inputs are the data arrays `mjs0, time, av`, the panel number, and the wavelength range `6490d,6660d`. The outputs `p0, wout` are the central pixel and calibration coefficients. The `mid, ctype, hydroxyl` keywords are used in this case. `mid` signifies that the calibration

should use the centre of the panel as the central pixel. `ctype` specifies the calibration equation to be used, in this case `ctype=2`, which adds a sinusoidal component, and the `hydroxyl` keyword sets the reference spectrum to OH instead of the solar spectrum which is the default.

```
auto_wlcal,mjs0,time[0],av,3,6490d,6660d,
    p0,wout,/mid,ctype=1,hydroxyl=2
```

`auto_wlcal` will plot the uncalibrated data as a spectrum, and a reference model OH spectrum. All clear spectral lines in the spectrum should be left-clicked, when finished the far left of the data spectrum can be clicked. This will highlight all the chosen lines, and the corresponding lines in the model spectrum can be selected. Once all the lines have been matched, a polynomial best fit is used to get the calibration coefficients. `auto_wlcal` will then plot the calibrated spectrum and model spectrum together, and plot the calibration equation so the fit can be checked. Once a good fit has been found, the calibration coefficients can be entered into the `wavelengths.lut` look-up table in the SIF code-base, hsoft.

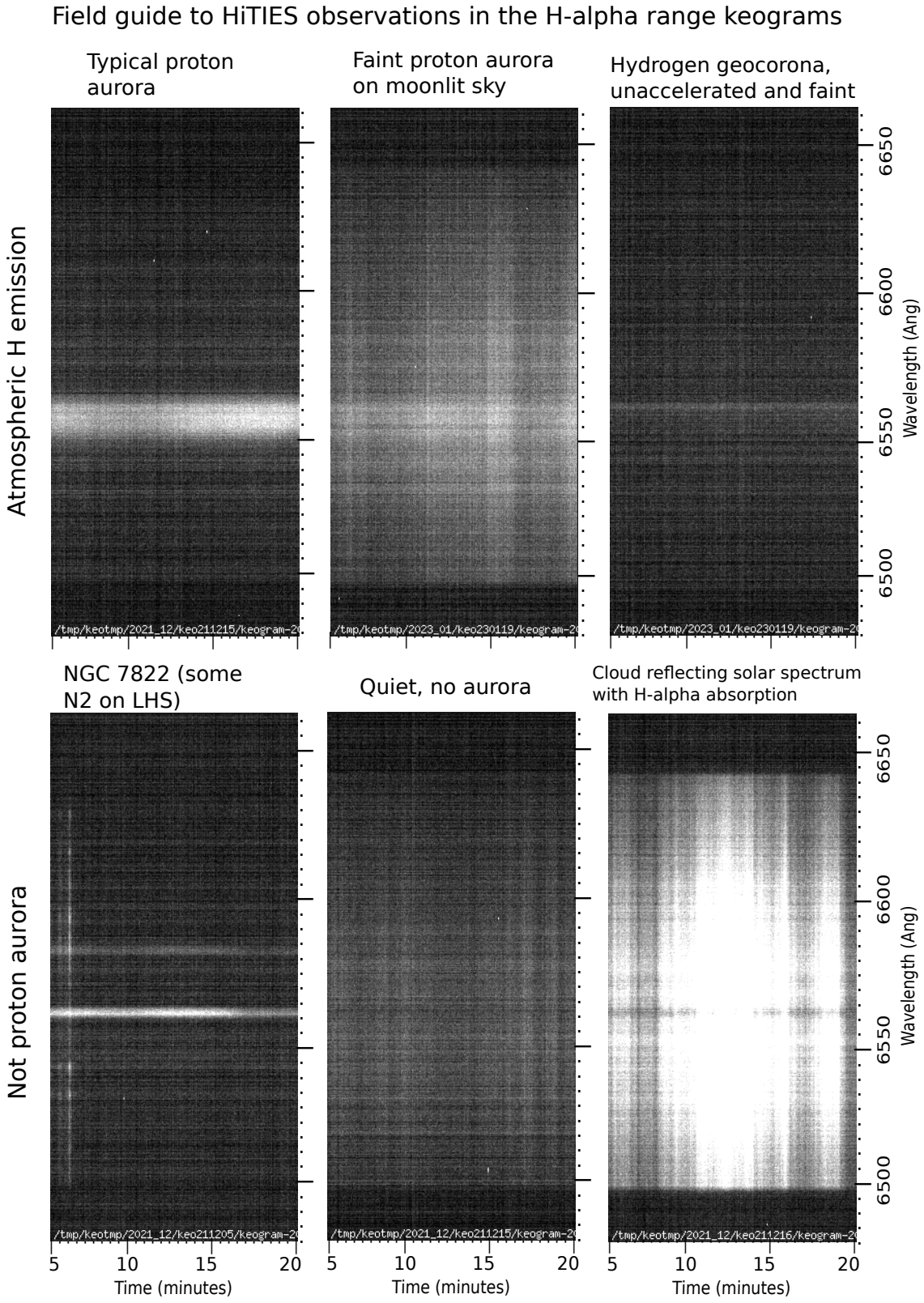

Figure 3.7: This 'field-guide' shows some common observations from the HiTIES instrument in the H-α panel in keogram form i.e. a row of pixels from each frame of the spectrograph stacked horizontally left to right, with time on the horizontal and wavelength on the vertical axis.

3.1.2 HiTIES observations

Proton Aurora

The proton aurora observations used in this study are explained in the 'field-guide' in Fig.3.7, including a set of six keograms i.e. stack plots of intensity along the wavelength axis in time, where each plot shows 20 minutes of observations. Each keogram gives an example of different typical observations from the HiTIES instrument and is included here to demonstrate how proton aurora was identified. The top row shows three examples of proton Hα emission, the most clear and bright on the left and the fainter example in the middle are both auroral proton emission. The top right proton spectrum could be from Hα airglow or geocorona. The bottom row shows typical non-proton aurora keograms. From left to right, the first is a spectrum from the nebula NGC 7822, see Section 3.1.2. The second is a quiet panel with no auroral emission, and the third is an example of sun or moonlit sky/cloud signal (the Hα absorption line comes from the solar spectrum).

There are several 'types' of proton aurora visible with HiTIES. The first, already shown, is the most typical observation. This is dayside precipitation within the polar cap but not in the cusp. This precipitation is characterised by a broad, well accelerated and often bright band of proton precipitation which varies slowly, on a timescale of ~ 30 minutes. If present, this dayside proton aurora typically appears early in the morning, stays relatively constant throughout the day, and drops off between 12 and 15 UT. Note, there is no such thing as 'typical' aurora and there are far more exceptions than events that fit this pattern.

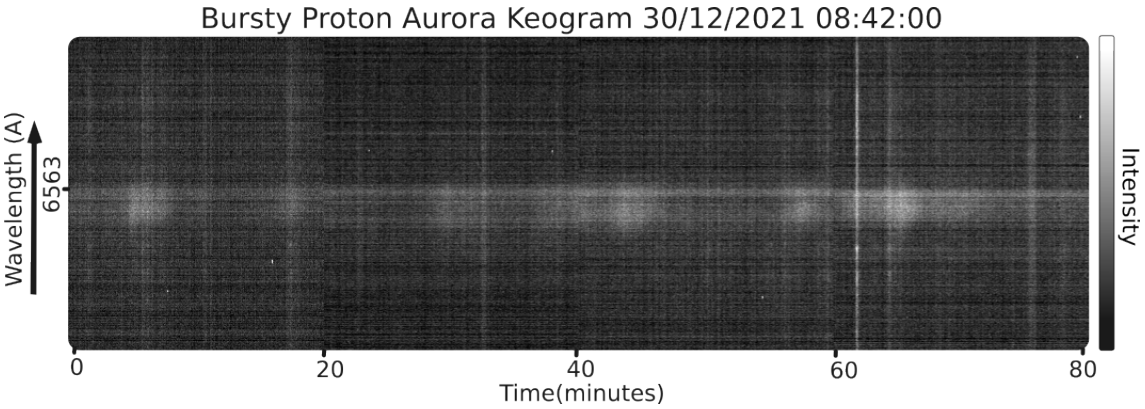

Figure 3.8: Example keogram of bursty proton aurora, throughout the 80 minute period there are many bright 'bursts' of precipitation lasting about 5 minutes each.

The second type is patchy proton aurora, see Figure 3.8 - this occurs on the dayside and is characterised as patchy or bursty. Bright, brief bursts of proton and electron precipitation are observed varying together, with bursts lasting $\sim 3-10$ minutes. This patchy proton aurora indicates that the cusp is overhead, and we are observing reconnection footprints (Moen et al., 1998; Deehr et al., 1998). It can also be linked to poleward moving auroral forms.

Occasionally, the nightside proton auroral oval is visible over Svalbard. Since the nightside proton oval is equatorward of the electron oval, nightside proton aurora observations require a low Kp and poleward expansion to be visible. This proton aurora typically varies on short-timescales and its dynamics closely follow the oval expansion and contraction. This type of proton aurora is usually observed during the evening during substorm expansion, lasting less than ~ 30 minutes. Example shown in Figure 3.9.

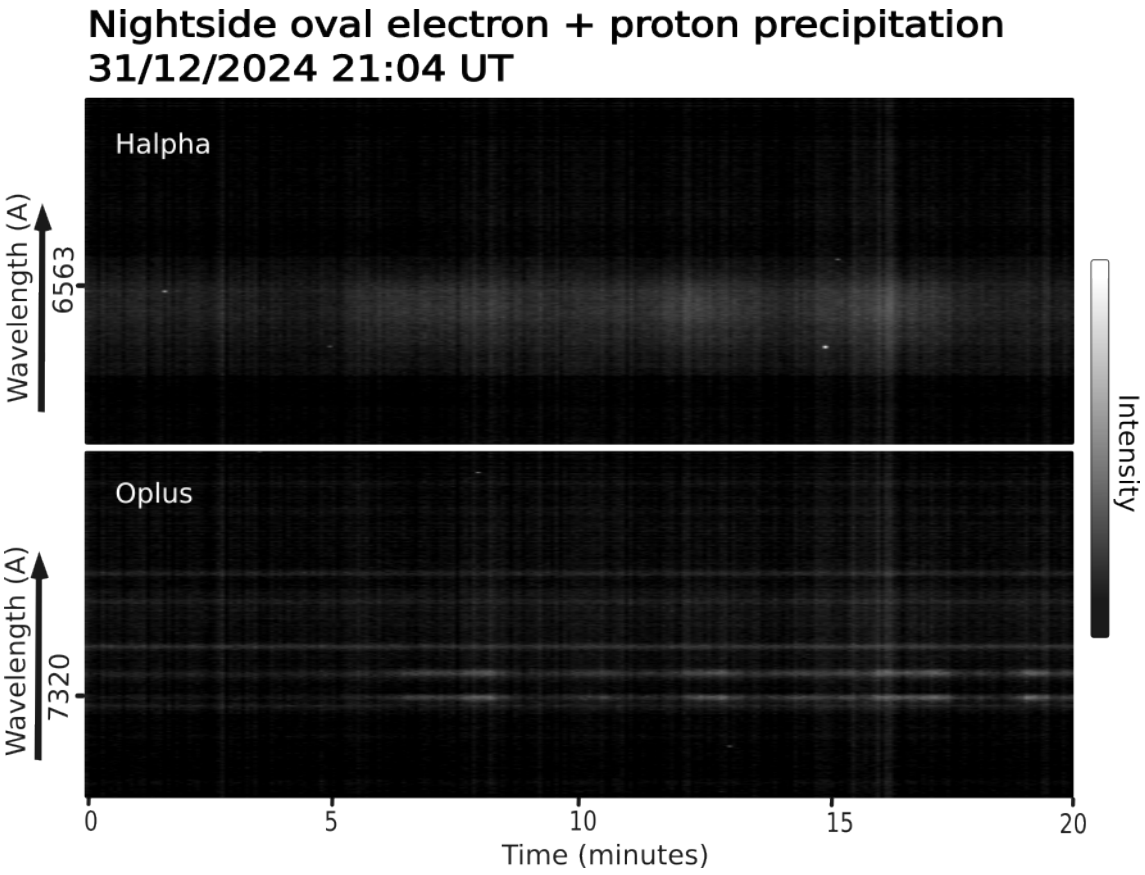

Figure 3.9: Example keogram of nightside oval proton aurora. It is identified by a quickly varying proton precipitation signature (top) on the nightside, corresponding to variations in the electron O+ auroral signature (bottom).

Continuum

Continuum emission can be observed with HiTIES - this thesis presents the first observations of continuum emission in the poleward region, as published in Partamies et al. (2025). Continuum is difficult to identify as it is difficult to separate from cloud when looking only at keograms. To positively identify continuum, ideally co-located all-sky images and video should be used. I tend to use the University Centre in Svalbard (UNIS) All-sky Sony keograms, which are colocated at the KHO and can be accessed at https://kho.unis.no/Keograms/. Continuum should be identified from comparing all-sky and keograms to identify any spectra that look like clouds, while the all-sky shows clear skies with aurora. Continuum should be first identified from the all-sky images where it appears a pale mauve/pink colour (due to the red dayside soft precipitation in the background). An example of continuum in the Sony All-sky camera is shown in Figure 3.10. The spectrum should be plotted to look for identifying features. If there is Hα in absorption, the spectrum is reflected sunlight from cloud and is not continuum emission. The continuum emission spectrum, as shown for the Hα panel in Figure 3.11, shows a fairly flat/uniform continuum spectrum with molecular emission lines throughout.

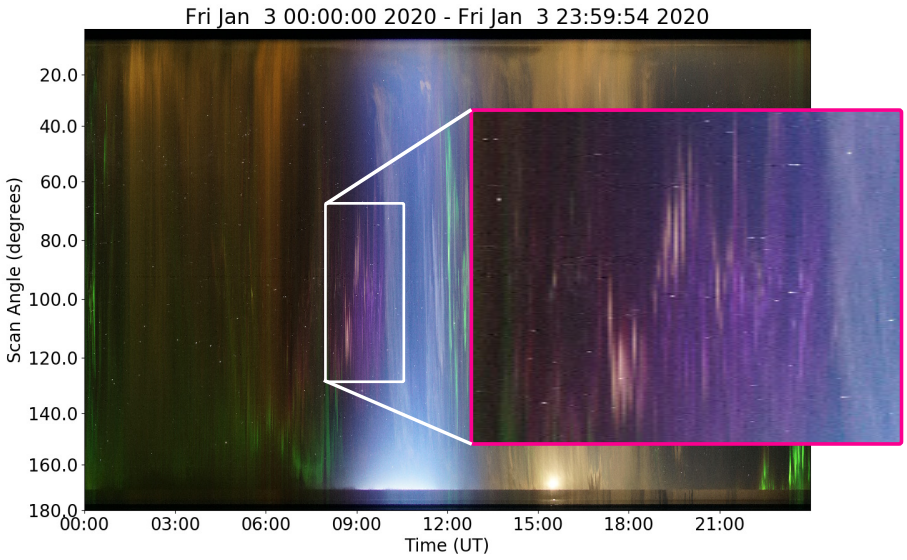

Figure 3.10: 24-hour Sony All-Sky keogram from 3 Jan 2020, showing a day of data and zooming in on the bright continuum emission in the morning from 08:30 - 09:30 UT. The continuum appears pale pink/orange and is located around the zenith. No clouds are visible in the all-sky at that time. Keogram taken from KHO website https://kho.unis.no/Keograms.

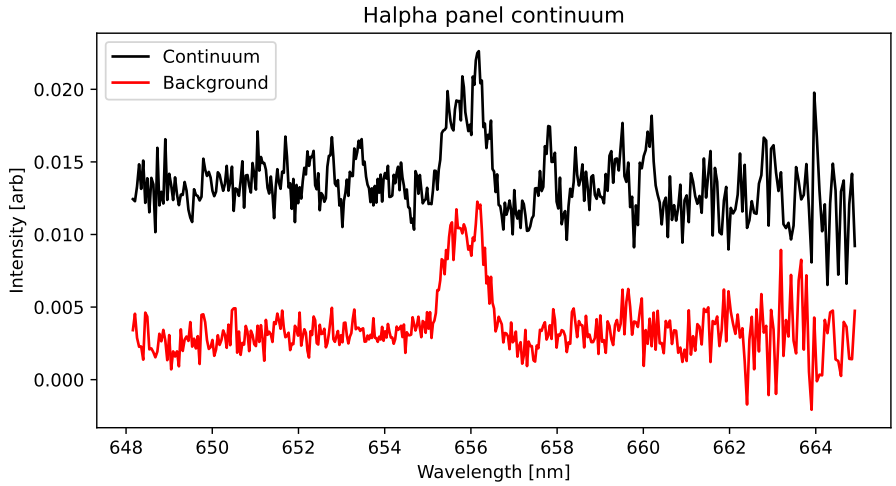

Figure 3.11: Example continuum spectrum from HiTIES from 3 Jan 2020 (black), compared with a background reference spectrum taken just before (red). Proton aurora emission is seen around 656 nm, and many molecular vibrotational emission lines can be seen.

NGC 7822

The hydrogen nebula NGC 7822, commonly known as the question mark[1], see Figure 3.12, is a circumpolar star-forming nebula, consisting of mainly H+. It is visible in the HiTIES Hα panel for ~ 30 minutes every day of the season unless blocked by clouds, moon or sunlight. It has a rotational period of one sidereal day so shifts about 5 minutes earlier each day, this is also how we identified it as an astronomical object. At the beginning of the season, e.g. late November or early December, it is seen at 18 UT, by January will have shifted around to 15 UT, and finally in February is no longer visible as it lies in the daylit sky. The exact location and times can be easily found using free astronomy software such as Stellarium[2]. The spectrum can be seen in Figure 3.7 in the bottom left panel. We have identified the spectral features as the Hα line at 6563 Å and the N II 6584 Å line, by comparison with the literature (Lozinskaia and Sitnik, 1977) and the NIST Atomic Spectra Database[3].

Figure 3.12: Lovely picture of the NGC 7822 nebula, showing the nebulae gases, dust, and young stars, with its question mark shape. Credit: Davide De Martin & the ESA/ESO/NASA Photoshop FITS Liberator - http://www.spacetelescope.org/projects/fits_liberator/fitsimages/davidedemartin_6/.

[1] An apt name, since it confused us for weeks.
[2] https://stellarium.org/
[3] https://physics.nist.gov/PhysRefData/ASD/lines_form.html

3.2 The Meridian Imaging Svalbard Spectrograph

The Meridian Imagine Svalbard Spectrograph (MISS[4]; Martinez 2024) is used to confirm continuum spectra over Svalbard in Chapters 5 and 6. MISS is a wide-view imaging spectrograph located at the KHO, which has been operational since the 2018-2019 season. It measures a low-resolution ($\sim 1\text{nm}$) spectrum over the entire optical range along the geomagnetic North-South meridian with an angular resolution of $\sim 1^{\circ}$, and with a cadence of 4 frames per minute. The instrument, shown and detailed in Figure 3.13, includes a fisheye objective lens, slit, collimator, tunable air-spaced transmission grating and prism, and finally a 34mm objective and Atik 414EX camera - an off-the-shelf astrophotography camera with a CCD detector and inbuilt chip cooling. MISS is used in this thesis to identify GHOSTs by their pseudo-continuum spectrum, taking advantage of its much larger field-of-view than HiTIES.

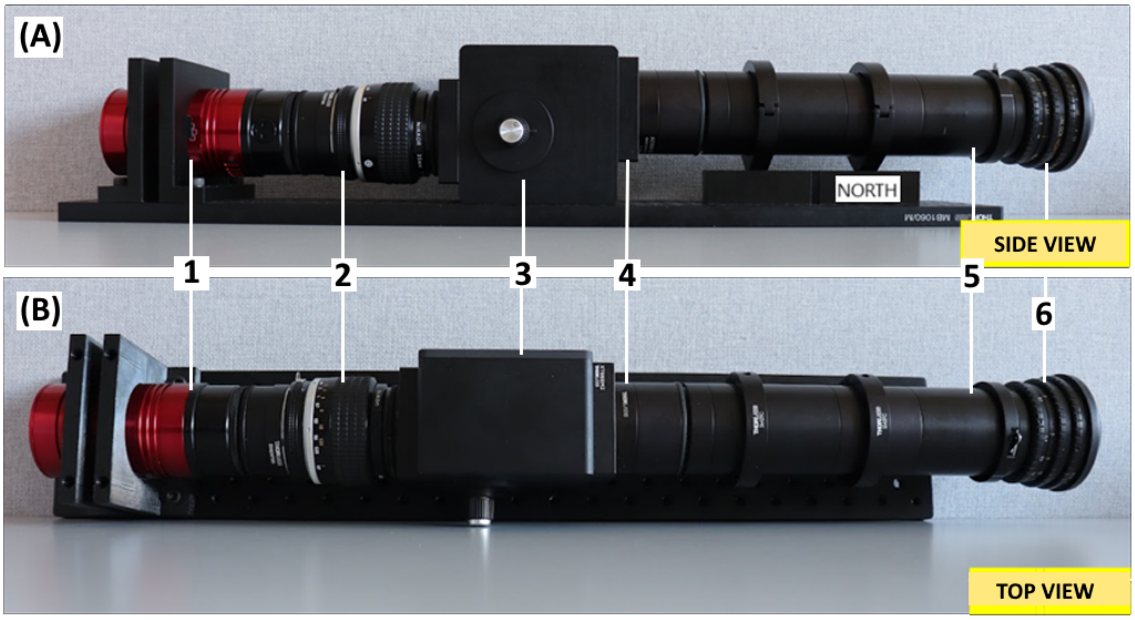

Figure 3.13: Meridian Imaging Svalbard Spectrograph (MISS) assembled.Panel (A) Side view. Panel (B) Top view. (1) Atik 414EX camera head, (2) Nikkor 35 mm objective, (3) Air spaced tunable transmission grating and prism (tGRISM) house, (4) Thorlabs 200 mm collimator lens, (5) Slit tube housing with field lens, and (6) Peleng Fisheye objective, taken from the KHO website (see footnote).

[4] https://aurora.unis.no/Instruments/MISS.html

Figure 3.14: Image of the 2-Axis Search Coil Magnetometer: KHO website https://kho.unis.no/Instruments/SearchCoilmagn.html

3.3 2-Axis Search Coil Magnetometer

A 2-Axis Search Coil Magnetometer, shown in Figure 3.14, was used to identify Pc1 magnetic pulsations in this thesis. The magnetometer is colocated with HiTIES at the KHO and is owned and operated by Augsburg College and University of New Hampshire. A search-coil magnetometer measures variation in magnetic flux through induction. Figure 3.15 shows a diagram for a single axis search-coil magnetometer. A solid ferromagnetic bar is surrounded by a conducting solenoid connected to an AC power supply. When the magnetic field component along the bar axis changes, this induces an electric field due to Faraday's law, which thereby increases the measured output voltage. Therefore, changes in magnetic field can be measured along a single axis. A 2-axis search-coil magnetometer combines two together, in this case they are aligned with magnetic north-south and east-west. The KHO 2-Axis Search-Coil Magnetometer is sensitive to 150 microvolts/nT * Hz with a dynamic range of ± 2.26 nT and has a sampling rate of 10 Hz. It uses a GPS signal to time measurements with an accuracy of 39 msec. By Fourier-transforming the voltage timeseries, the power spectrum of different magnetic variation frequencies can be plotted in time, as in Figure 3.16. In this case the north-south axis is shown. Auroral noise is broadband and is highlighted in pink. In yellow, Pc1 pulsations are shown. Pc1 refers to the frequency band of the pulsations, 0.1-1 Hz and these pulsations are caused by EMIC waves. The data is processed by the instrument owners and is accessed by an online portal at http://mirl.sr.unh.edu/projects_ulf.html.

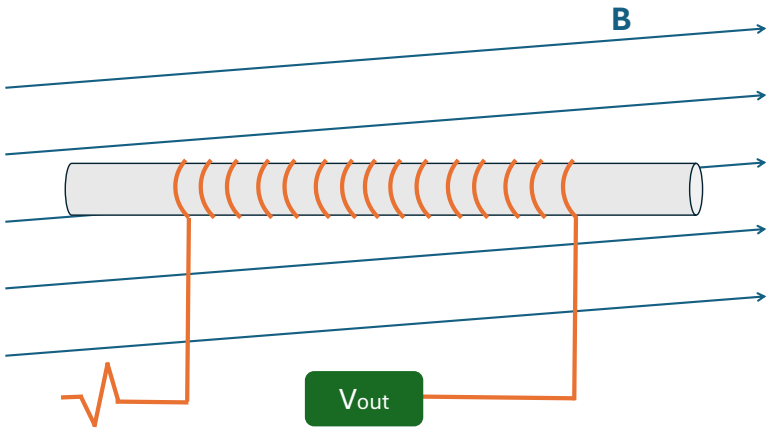

Figure 3.15: Diagram showing the simplified setup of a single-axis search-coil magnetometer, reproduced from Plank (2024).

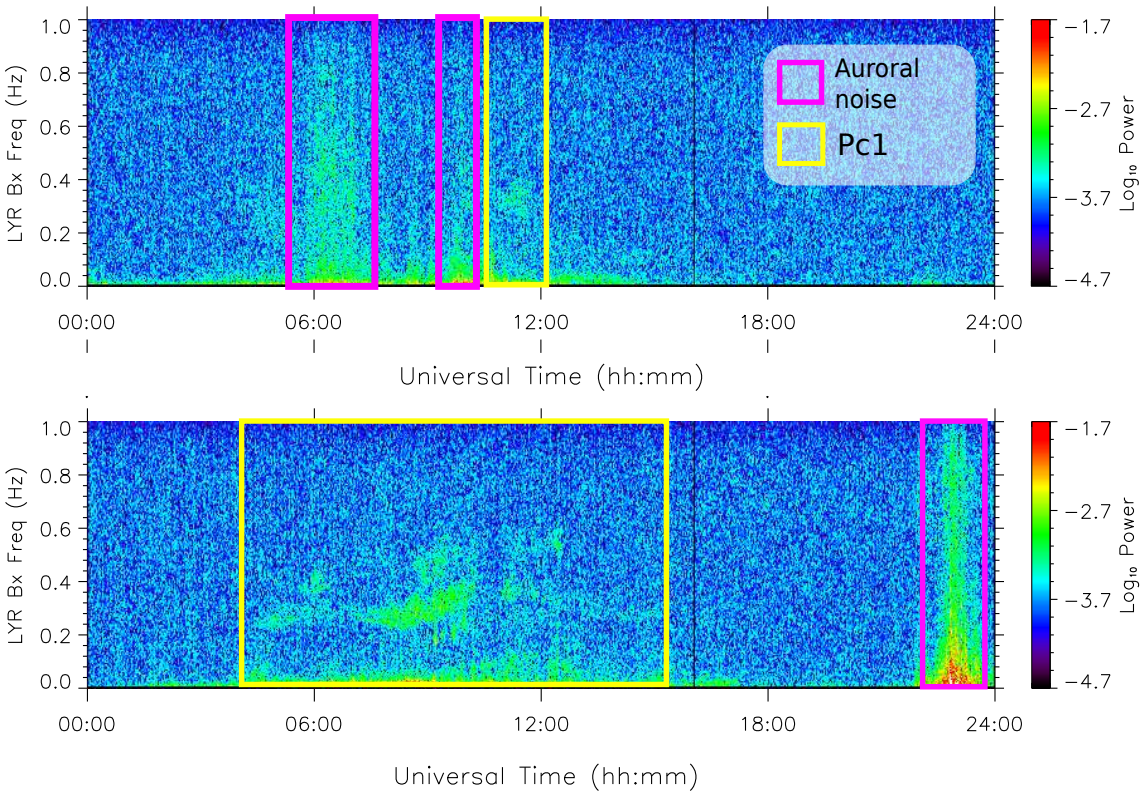

Figure 3.16: This field-guide shows two examples of 24 hour magnetometer data, showing broadband auroral noise in the pink boxes, and Pc1 pulsations in the yellow.

3.4 EISCAT

The European Incoherent SCATter (EISCAT) Scientific Association is an international ionospheric radar facility, involving multiple Incoherent Scatter Radar (ISR) sites in northern Scandinavia and Svalbard. The EISCAT Svalbard Radar (ESR), see Figure 3.17, was used during this thesis to provide profiles of ionospheric plasma parameters in an approximately shared volume with HiTIES and other KHO instruments. The ESR is located 600 m north of the KHO on Svalbard. It consists of a stationary 42 m parabolic dish antenna pointed in the field-aligned direction, and a steerable 32 m dish. ESR operates in the 500 MHz frequency band with a transmitter peak power of 1000 kW. The data are typically integrated to a time resolution of at least ~ 1 min to gain sufficient signal-to-noise.

Figure 3.17: The 32m (left) and 42m (right) parabolic dish antennae of the ESR, with red sky enigma.

ISRs work by transmitting high-power radio waves[5] into the ionosphere and detecting the weak backscatter from free electrons in the plasma. ISRs operate at a frequency above the plasma and cyclotron frequency, but low enough to observe the collective behaviour of electrons, and they measure fluctuations in density that match the wavelength of the radar, Langmuir and ion-acoustic waves. The backscattered signal power spectrum contains features that depend on various ionospheric parameters which affect the density and velocity distribution of the particles, providing detailed measurements of the height profiles of electron and ion density, electron and ion temperature, ion composition, and plasma velocities.

Grand Unified Incoherent Scatter Design and Analysis Program (GUISDAP, Lehtinen and Huuskonen 1996) is a piece of software which performs most of the EISCAT signal analysis, and has been used to analyse the raw data from the ESR for all data presented in this thesis.

[5] Coherent when transmitted, incoherent on return.

Chapter 4

Proton acceleration by EMIC waves

Abstract
In order to test the hypothesis that EMIC waves are responsible for the acceleration of auroral protons, we have used spectrograph measurements of proton aurora over Svalbard alongside co-located magnetometer measurements of Pc1 pulsations. The observational evidence only supports a weak association between proton aurora and Pc1 waves in this region, by three different methods. Firstly, accelerated protons and Pc1 pulsations are only slightly correlated in time. Secondly, the proton energy spectrum does not change between Pc1 activity and quiet times. Finally, no imprint of the EMIC wave is found in periodicity of the intensity and blue-shift of the proton Hα line, unlike in flickering electron aurora where intensity fluctuations are caused by EMIC waves. We find no evidence that EMIC waves are the *primary mechanism* responsible for accelerating auroral protons in the high-latitude dayside, at least based on the considered ground-based data of proton aurora and magnetic Pc1 pulsations. The link between the two phenomena is less significant than would be expected if most or all of the proton precipitation in the high-latitude dayside was precipitated and/or accelerated by EMIC waves.

Attribution
This work was completed in collaboration with Dan Whiter and Betty Lanchester of the University of Southampton, and Hyomin Kim of the New Jersey Institute of Technology. This chapter was submitted to JGR: Space Physics and to EGU journals and is available as a preprint, see Dayton-Oxland et al. (2024). RD collected, analysed, and interpreted the data, and wrote the manuscript in consultation with DW, HK, and BL. DW conceived the research idea, supervised the project, and contributed to the interpretation. HK contributed to the understanding of magnetometer data. BL contributed to the interpretation. This work has been improved based on the comments of anonymous reviewers.

4.1 Introduction

When observed in the high Arctic under the high-latitude dayside, proton aurora originating directly from the solar wind can be observed. The high-latitude dayside proton aurora is typically observed with a blue-shifted spectrum with super-solar wind velocities of 430 - 1400 $\mathrm{km\,s^{-1}}$ (Lummerzheim and Galand, 2001; Galand et al., 2001) compared to around 400 $\mathrm{km\,s^{-1}}$ in the slow solar wind (Hundhausen, 1970), indicating that some acceleration process occurs within the high-latitude dayside (Galperin, 1963). This acceleration process is typically assumed to be by Landau damping of ElectroMagnetic Ion Cyclotron (EMIC) waves (Engebretson et al., 2013; Xiao et al., 2013; Khazanov et al., 2015; Ozaki et al., 2018). However, there are no observational studies of the mechanism by which auroral protons are *accelerated* in the high-latitude dayside. This paper presents observations of accelerated proton aurora and $0.1 - 1$Hz Pc1 pulsations from Svalbard and shows that there is only a weak temporal link between the two phenomena, and no evidence of acceleration, contrary to expectations.

EMIC waves are left-circularly polarised electromagnetic plasma waves that propagate quasi-parallel along magnetic field lines, oscillating transversely to the magnetic field. The wave-particle interactions of EMIC waves are one of the main precipitation mechanisms for protons trapped in the magnetosphere by scattering protons into their loss-cone, resulting in proton aurora *equatorward* of the auroral oval. EMIC waves are typically generated at equatorial latitudes as a result of a fundamental plasma instability (e.g. due to anisotropy or ion beam instabilities) and propagate along field-lines to their foot-points at higher latitudes, where they manifest as structured (see Matsuda et al., 2018) geomagnetic Pc1 (period of 0.2-1Hz; Glaßmeier (2007)) pulsations at the ground (Varlamov et al., 2021; Yahnina et al., 2000; Francia et al., 2020). However, EMIC waves in Svalbard are generally observed as unstructured Pc1

pulsations, suggesting that their origin lies in the outer magnetosphere (Menk et al., 1993; Mursula et al., 1994; Safargaleev et al., 2004; Engebretson et al., 2009; Regi et al., 2017). Bräysy and Mursula (2001) reports that 75% of EMIC waves detected in space are detected as conjugate Pc1 pulsations on the ground. This is the first study to our knowledge investigating auroral proton acceleration in this high-latitude dayside regime.

EMIC waves have been observed to cause the precipitation of protons in several studies (e.g. Xiao et al., 2013; Ozaki et al., 2018; Liang et al., 2022; Tian et al., 2023). The cusp contains a minimum magnetic potential, creating a magnetic bottle within which protons with high field-perpendicular velocities can become trapped. Xiao et al. (2013) used in-situ Cluster measurements to suggest that EMIC waves are capable of violating the invariance of the magnetic moment and scattering protons into the atmosphere, leading to high-latitude dayside proton aurora.

Outwith the high-latitude dayside region, Kim et al. (2017) showed travelling convection vortices to generate EMIC waves coincident with proton auroral precipitation. In the night-side auroral oval, proton aurora is understood to be caused by precipitation from the plasma sheet and ring current (Spasojević et al., 2013). EMIC wave scattering is also associated with detached proton auroral arcs, i.e. low-latitude bands of proton aurora detached from the main auroral oval. Magnetic Pc1 pulsations consistent with EMIC waves have been detected near detached subauroral proton arc events (Immel et al., 2005; Sakaguchi et al., 2007) and isolated proton aurora (IPA) (Sakaguchi et al., 2015; Nomura et al., 2016; Kim et al., 2021; Nakamura et al., 2021; Ozaki et al., 2021; Liang et al., 2022; Ozaki et al., 2022; Nakamura et al., 2022). Geomagnetic Pc1 pulsations associated with a substorm have been observed occurring during a proton arc and Strong Thermal Emission Velocity Enhancement (STEVE) event (Varlamov et al., 2021). EMIC/Pc1 waves have also been observed associated with energetic proton precipitation on the dayside on Svalbard on closed-field lines at the poleward boundary of the auroral oval by Engebretson et al. (2013), during a travelling convection vortex (TCV) event. Engebretson et al. (2013) is the only observation of EMIC related proton precipitation from Svalbard in the high-latitude dayside to our knowledge.

Field-line curvature scattering (FLCS) is also a significant source of proton precipitation, when the scale size of the field-line curvature and the proton gyroradius are comparable, Ma et al. (2022). The equatorward boundary of the FLCS driven energetic proton precipitation, sometimes called the isotropic boundary (IB), has been empirically modelled in Ma et al. (2022), and typically ranges from about 50°latitude, up to close to 78°North. This FLCS is the largest contributor to the proton auroral oval.

Periodic flickering of a wide wavelength band assumed to be an isolated proton aurora (IPA) was reported as evidence of EMIC acceleration by Ozaki et al. (2018) (akin to flickering electron aurora (Whiter et al., 2010)). They present a $1\mathrm{Hz}$ periodic modulation in photometer measurements correlated with Pc1 observations; however, they do not show a method for separating IPA from contamination by electron precipitation. In addition, their conclusions do not necessarily apply to the high-latitude dayside region.

This study compares observations of the proton Hα auroral emission with observations of Pc1 pulsations in the high-latitude dayside. We do not observe any temporal link between proton aurora and Pc1 waves or any effect from Pc1 waves on the velocity spectrum of the protons. We did not observe any periodic flickering in the Hα auroral emission line.

4.2 Instrumentation and Observations

This work uses observations taken during the 2021-2022 observing season, from 4th December 2021 - 31 January 2022. Periodicity studies were carried out on proton aurora events with concurrent Pc1 observations on 10 December 2021 and 13 December 2021. Observations during February and March were not used since daylight limits and time-biases dayside observations.

The Hα spectrum is taken using HiTIES, see Chapter 3, extracted from the EMCCD image of the Hα panel in the mosaic filter by integrating the pixel intensity in the spatial direction (along the slit). The spectrum is then calibrated using flat-field images taken on 4 December 2021, and dark-field images taken every 20 minutes. The wavelength of the spectrum is calibrated using the OH airglow spectrum and the solar spectrum. An example observation of the proton aurora spectrum with HiTIES is shown in Fig.4.1.

A 2-axis search-coil magnetometer (Engebretson et al., 2009), co-located with HiTIES at the KHO, Svalbard was used to observe Pc1 pulsations. It consists of two sensors aligned with magnetic N-S and E-W. The Pc1 geomagnetic pulsations are observed in the 0.1 - 1 Hz range, and are used as a proxy for EMIC waves (Paulson et al., 2017; Francia et al., 2020). The search-coil data was processed by the instrument owners.

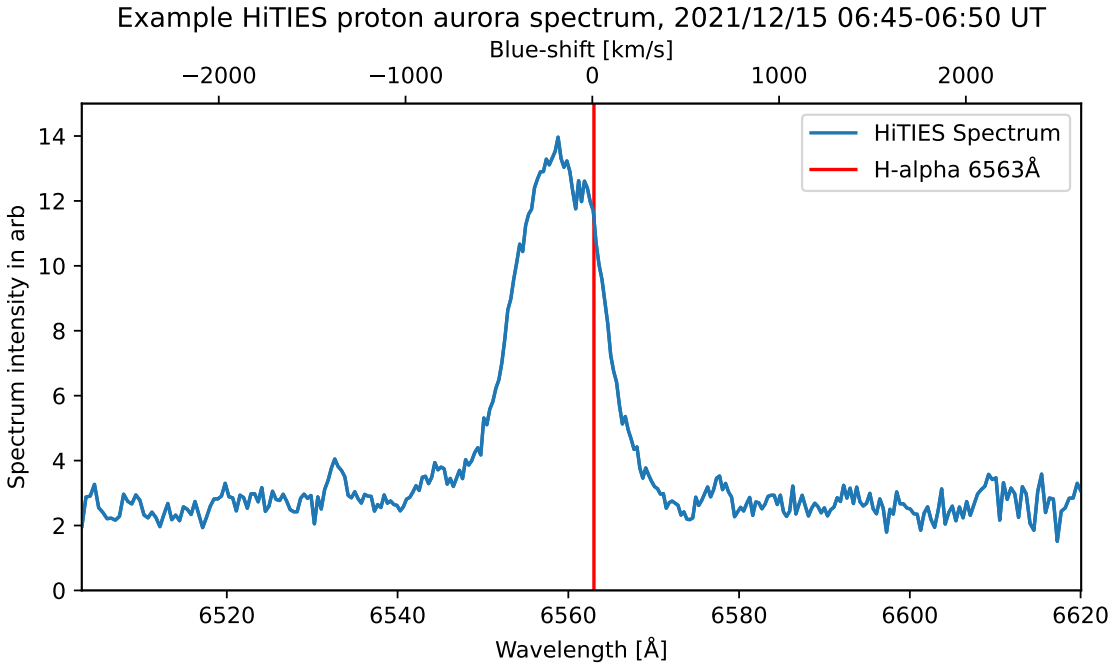

Figure 4.1: An example Hα spectrum as measured by the HiTIES instrument, where the vertical red line signifies the stationary Hα wavelength at 656.3nm. The broad Hα line is clearly visible above the background showing its usual blue-shifted peak. The median velocity from the blue-shift of this spectrum is around 300$\mathrm{km\,s^{-1}}$, with the fastest end identifiable from the background around 700$\mathrm{km\,s^{-1}}$.

4.3 Methods and Results

Three methods were used to analyse the proton aurora Hα spectrum and magnetometer data. A 'field guide' to show the method of identification of proton aurora is shown in Figure 3.7. EMIC waves are identified by an enhanced unstructured signal in the Pc1 band as measured by the 2-axis search coil magnetometer. Fig.4.2 shows an example of unstructured Pc1 from EMIC waves between 05-16 UT. This event is considered unstructured as it lacks the typical pearl-like structure seen in structured Pc1/EMIC observations. The December 2021 event shown is used in the spectra comparison and periodicity methods described below. The first, section 4.3.1, is a comparison of when Pc1 and proton aurora occur, to determine whether the occurrences are statistically linked. Section 4.3.2 is a comparison of the spectrum (i.e. velocity profile) of the incident protons during Pc1 events and during Pc1-quiet times to determine whether the Pc1 waves are linked to an increase in proton acceleration. The third method, section 4.3.3, is to search for periodic flickering in the proton aurora, as this has previously been identified as a signature of EMIC acceleration in electron aurora (Whiter et al., 2010) and proton aurora (Ozaki et al., 2018).

4.3.1 Co-occurrence

We present a statistical study of the contingency of proton aurora and Pc1 pulsations, i.e. the likelihood that they are correlated based on how often they occur together vs. separately. Identifying proton aurora and Pc1 enhancements for the entire December/January period of the 2021/2022 observing season, we

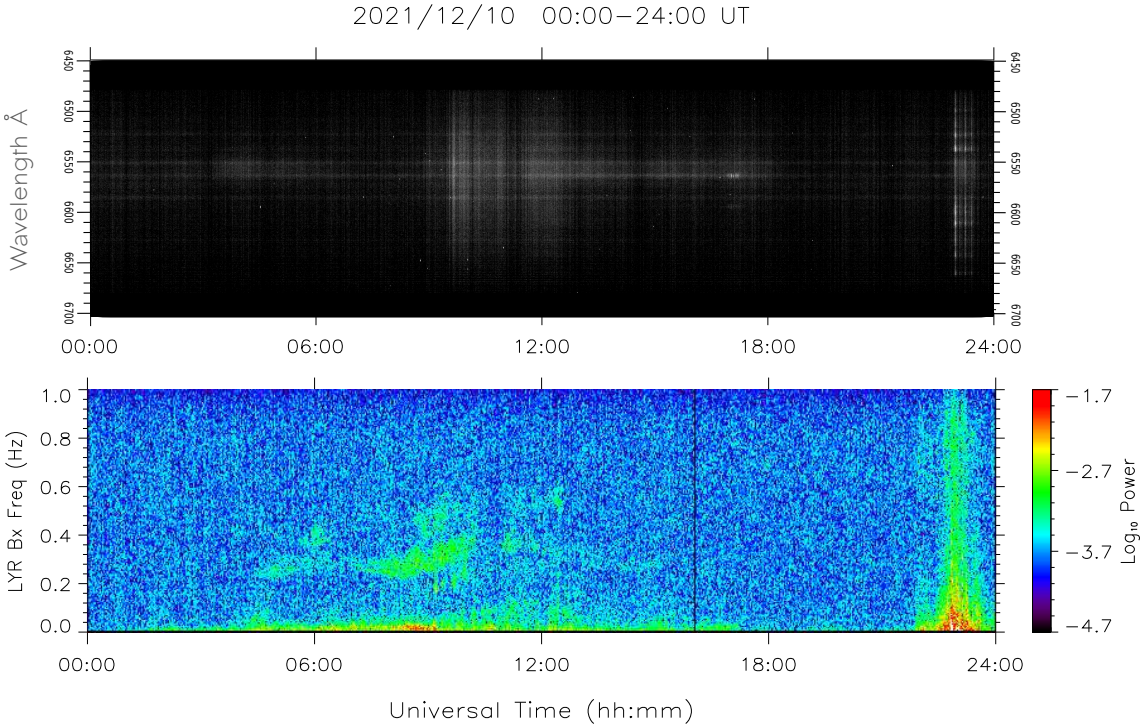

Figure 4.2: An example overview of data for 10 December 2021. The first panel shows a keogram of HiTIES Hα observations over 24 hours. Around 6563Å there is proton aurora visible from 03-06UT, from 10-13UT there is cloud and more proton aurora until 1830UT. At 1730UT Hα emission from the nebula NGC 7822 is visible. There is N_2 auroral emission at 2245 to 2330 UT. The bottom panel shows the same 24 hours of measurement from the search-coil magnetometer displayed as a spectrogram of B_x. This shows Pc1 pulsations from 5 UT to 16 UT, and auroral broadband noise at 23 UT (coinciding with the N_2 optical signature), from magnetometer observation of Pc1 enhancements during 10 December 2021.

obtain occurrences for proton aurora and Pc1 pulsations. The proton aurora and Pc1 enhancements were identified manually; see the identification process in the Field Guide, Appendices Fig.3.7. The occurrence relationship between the proton aurora and Pc1 is first tested with the odds ratio - this is a simple statistic which quantifies the strength of association between two events.

For some occurrence table of events A and B;

	B=1	B=0
A=1	p_{11}	p_{10}
A=0	p_{01}	p_{00}

the Odds ratio is;

$$OR = \frac{p_{11}p_{00}}{p_{10}p_{01}}$$

.

The proton aurora and Pc1 pulsation contingency table is found in Table 4.1. By comparing the number of 10 minute long time-intervals during the observing season where Pc1 and proton aurora are observed it is clear that while proton aurora is quite common, Pc1 observations are relatively rare. This finding already suggests that Pc1 pulsations are not likely to be the only acceleration mechanism since they are observed together in only 65 of the 10-minute intervals across a 2-month observing season. The disparity in quantity of proton aurora observations vs Pc1 waves is visualised in Figure 4.3. From this it is reasonable to conclude that since Pc1 waves are not present in the vast majority of proton aurora observations, the ground-based evidence does not support the theory that EMIC waves cause the majority of proton precipitation in this region.

	Pc1 present	No Pc1
Proton aurora present	65	1108
No proton aurora	53	1677

Table 4.1: Contingency table showing the number of 10-minute intervals of observation during the 21/22 Dec-Jan observing period with Pc1 waves and proton aurora. Odds ratio = 1.856.

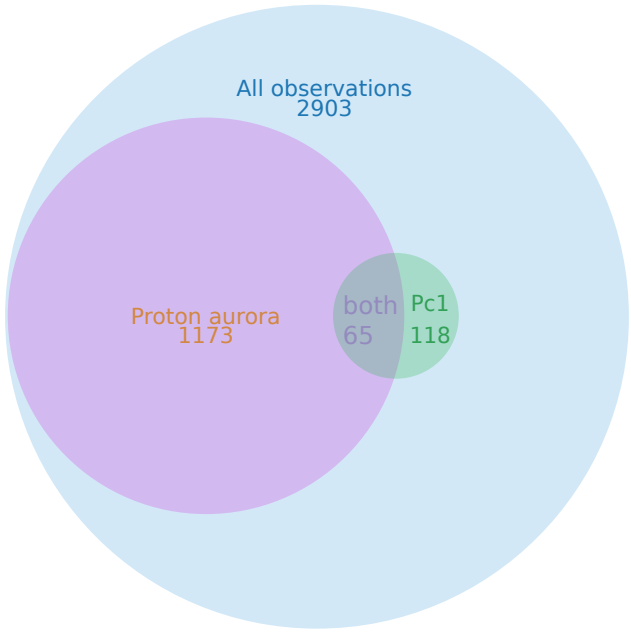

Figure 4.3: Venn diagram showing the number of observations where proton aurora and Pc1 waves are present.

Times when proton aurora is not visible due to scattered sunlight or bright clouds have been discounted from the statistics. Times when Pc1 band is obscured by auroral noise, typically only for short periods during substorms, have been discounted. Only dayside (6 hours either side of local magnetic noon) observations have been considered, see Figure 4.4. We tested different definitions (hours either side of 10UT) of the dayside to ensure our definition did not affect the results of the Odds ratio test. Below 6 hours there is no significant increase in Odds ratio with increasing hours of daylight. Above 6 hours, i.e. including nightside data, the correlation quickly increases. This is expected as Pc1 and proton aurora are both seen primarily in the dayside at this latitude. A total of 448 hours of data were excluded from both datasets throughout the observing season, representing $\sim 30\%$ of the total data, primarily due to bright cloud.

The Odds ratio is calculated to examine whether proton aurora and Pc1 have any temporal relationship, as a statistic of the correlation in time. If Pc1 (EMIC) waves were the responsible acceleration mechanism for auroral protons, a positive time correlation would be expected between accelerated proton aurora and Pc1 pulsations. The Odds ratio for this table is 1.856. Investigating the distribution of log Odds ratios for 1000 random shuffles of the dataset, we can plot the significance of the proton aurora and Pc1 simultaneity, in Figure 4.5.

We can see that the proton/Pc1 Odds ratio sits over the 3σ line, suggesting some temporal correlation between Pc1 and proton aurora. This is definitely a small temporal correlation, the 'odds' of proton aurora happening when Pc1 is present are ~ 1.8 times the odds without Pc1, but since there is a 10-minute buffer in the definition of 'coincedent' it is much more slight than one might expect if Pc1 waves were causing proton precipitation all or most of the time.

Overall, the temporal coincidence of proton aurora and Pc1 waves does not support EMIC waves as the principal precipitating mechanism for protons. However, it is likely that when EMIC waves are present they do cause precipitation.

Figure 4.4: Line plot showing the resulting Odds ratio and maximum bootstrap value for the Proton/Pc1 dataset, with the x-axis being the number of hours either side of local noon in the definition of dayside. Plot shows that including non-dayside events (hours > 6 from local noon) creates a false link, as Pc1 pulsations and proton aurora are seen primarily in the dayside at this latitude.

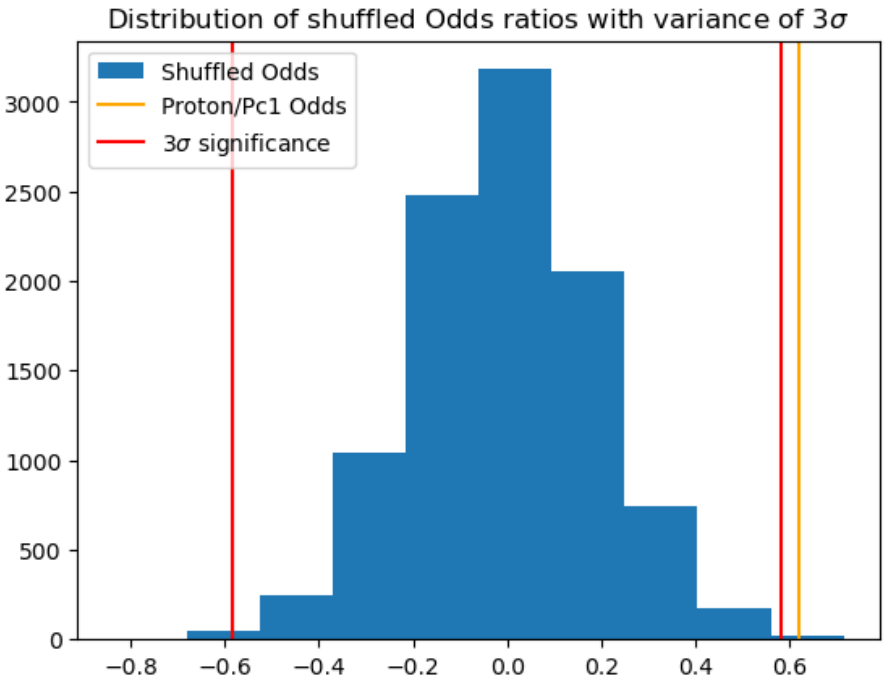

Figure 4.5: Distribution of the log of Odds ratios for 1000 randomly shuffled versions of the proton/pc1 dataset. Random shuffle Odds ratios form a Gaussian distribution around 0 as expected, the proton/pc1 Odds ratio is marked with a vertical orange line, this sits slightly above 3σ.

4.3.2 Spectrum comparison

The second piece of evidence we present is a comparison of the average proton aurora spectrum during Pc1 pulsations, and when there are no Pc1 pulsations. 200 minutes of proton aurora observations during Pc1 and 200 minutes of proton aurora without Pc1 were averaged throughout the December 2021 observing season. This time was chosen to minimise computing time while providing a sufficiently large dataset. The spectra were normalised for comparison. OH airglow contamination was removed by fitting and subtracting synthetic spectra, using a least-squares-fit algorithm (with temperature dependence). Synthetic spectra for temperatures 150 - 250 K were generated and fit to the Hα panel background, excluding the Hα emission from 6540 - 6570 Å. There is Hα geocorona visible in the spectra at the rest wavelength, which we ignore. Since the majority of emitting particles travel quasi-parallel to the magnetic field-line (Galperin, 1963) and we point to the magnetic zenith, the line-of-sight velocity determined from the Doppler shift of the proton spectrum can be used as an indication of the characteristic energy of the incident precipitation.

The average proton aurora spectra for Pc1 and no-Pc1 times are compared in Fig.4.6. The full width at half maximum (FWHM) and peak wavelength of the Hα spectrum is very similar during either Pc1 or no-Pc1 times. There may be a small additional acceleration on the blue wing of the spectrum with Pc1, incidicating that when Pc1 are present they can accelerate a small proportion of the precipitating protons. This acceleration is not enough to explain the total proton acceleration. Similarly to the previous section, we conclude that EMIC waves cannot be the primary acceleration mechanism, but are capable of some acceleration when present.

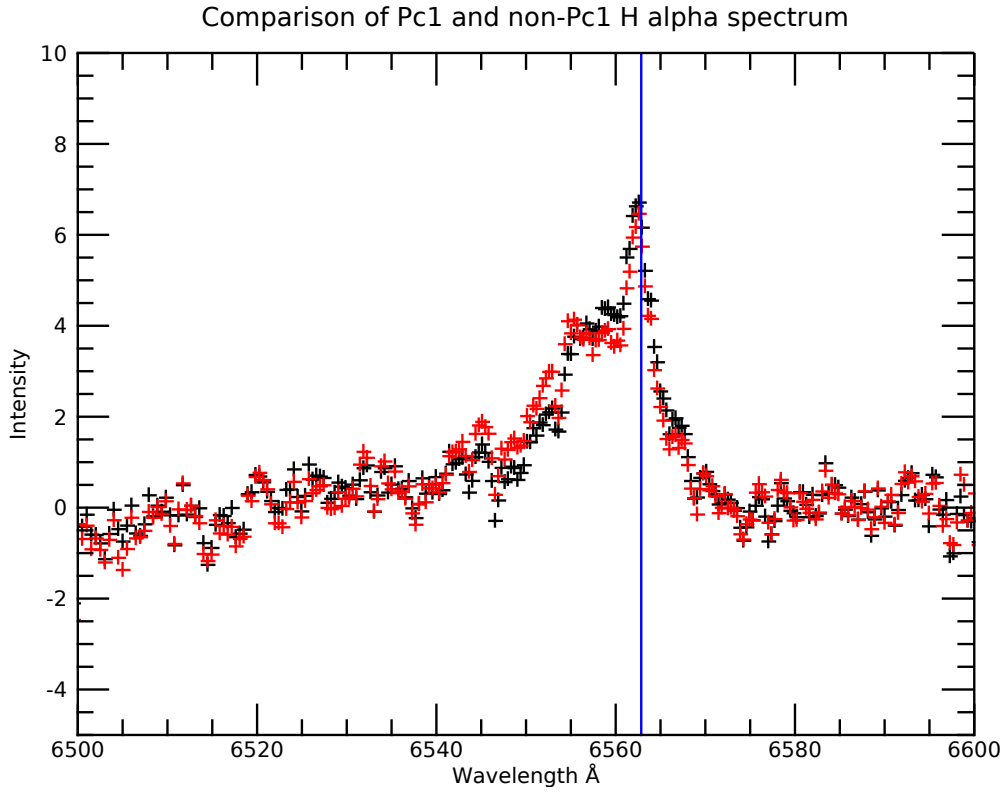

Figure 4.6: Comparison of 200 minutes of proton aurora during Pc1 waves in red, and 200 minutes of proton aurora when the Pc1 band is quiet in black, The rest wavelength of Hα, 656.3nm is marked with a blue vertical line. The plot shows no change in acceleration of the proton aurora when Pc1 is present or not present.

4.3.3 Periodicity

The integrated intensity and mean blue-shift are calculated for the spectra at each time step during proton aurora events with concurrent Pc1 waves, generating two time series each 60s long. The timeseries backgrounds were removed by subtracting a linear fit, effectively a high-pass filter on the intensity variation (as we are looking for a 1-10s periodic signal, related to the Pc1 frequency as described in Ozaki et al. (2018); Whiter et al. (2010)). A range of different days during the December 2021 period were chosen, specifically those where Pc1 pulsations were also measured and where the proton spectrum was quite bright. The timeseries were analysed using autocorrelation and Fourier transform methods to identify any periodic oscillations that might show flickering aurora such as the flickering electron aurora observed by Whiter et al. (2010) or the flickering observed by Ozaki et al. (2018). The significance of the autocorrelation results was tested using a bootstrapping method.

Example autocorrelation and Fourier transforms performed on the time series of the proton aurora photon flux during 10th, 13th, and 15th December 2021 do not show any periodic signal over each day of data. Pc1 band magnetometer plots during these times are shown in Fig.4.2. Figure 4.7 shows the results of performing an autocorrelation of the proton aurora intensity timeseries of each minute of data in a 60 minute period on 10 December 2021 during which Pc1 enhancement and accelerated proton aurora were observed together. The red horizontal lines in these figures represent missing data when the HiTIES shutter is closed to acquire dark calibration images. Bootstrapping of the timeseries by recording the maximum autocorrelation value for each lag over 10, 100, 1000, and 10000 random permutations of the aurora intensity timeseries gives a minimum statistically significant amplitude of around 0.2. None of the autocorrelation plots generated over the observing season during Pc1 pulsations show structures that exceed this threshold, so we can conclude that there are no significant periodic signals.

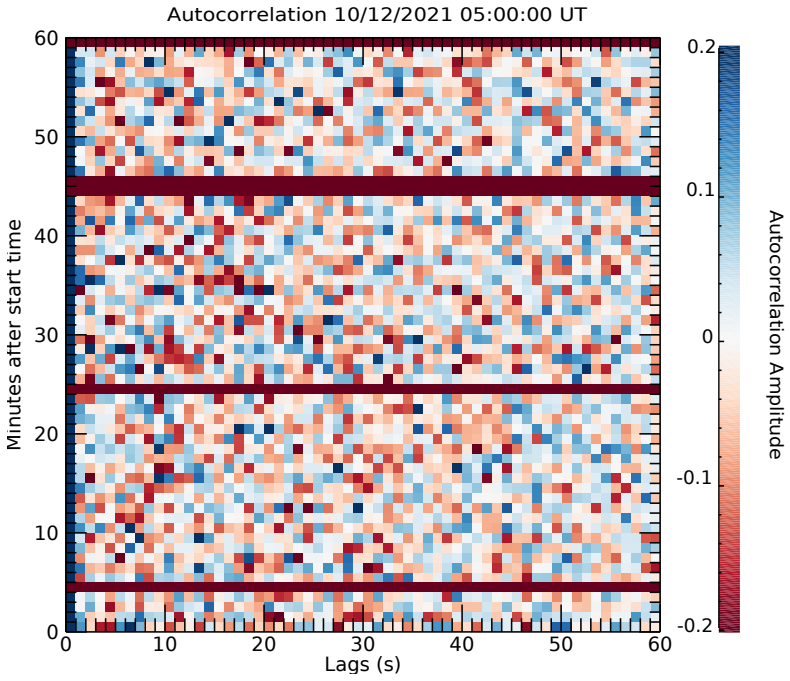

Figure 4.7: Autocorrelations on the proton aurora Hα total intensity during Pc1 activity shown in Fig.4.2. The x-axis is the autocorrelation test lags up to 60 seconds, and the y-axis is the minutes after the start time. Each row moving upwards is an intensity autocorrelation on a minute of data, with the amplitude shown by colour, red is negative and blue positive. Periodic signals would show up as vertical repeating structures of red and blue lines. No such signals appear. The dark red horizontal bands represent missing data. Note the colorbar is set so that the maximum range is equal to the minimum significant value, so no structure within these colorbars is significant.

4.4 Discussion

In this study we analyse ground-based observations of proton aurora and Pc1 pulsations in the high-latitude poleward dayside, and do not find any significant link between the two phenomena. This result questions whether EMIC waves are the primary precipitation and acceleration mechanism for proton aurora in this region.

To relate the results of this study which concern Pc1 and proton aurora to EMIC waves, we must assume that EMIC waves nearly always cause Pc1, and Pc1 are nearly always caused by EMIC waves. While the two have been closely related (Varlamov et al., 2021; Francia et al., 2020; Yahnin and Yahnina, 2007; Yahnina et al., 2000), there is a possibility that high-latitude dayside EMIC waves do not always propagate down to cause Pc1 pulsations. Therefore it is possible that EMIC waves do accelerate auroral protons in the high-latitude dayside, but do not cause Pc1 pulsations. Bräysy and Mursula (2001) show that 75% of EMIC waves detected in space were also detected at the ground as Pc1 pulsations in Sodankylä. This implies that were EMIC waves present, we would observe them in 75% of cases - but this cannot account for our paucity of Pc1 measurements compared to proton aurora events. From our results it seems clear that although it is possible that EMIC waves are capable of accelerating high-latitude dayside protons, it cannot be the primary acceleration mechanism as we did not measure any change in the proton acceleration during measured Pc1 pulsations. Pc1 are also too infrequent to be causally linked to accelerated proton aurora (we would expect the magnetometer to detect Pc1 over a much larger area than the small field of view of HiTIES, so could even expect Pc1 to be more frequent than accelerated proton aurora if they were in fact linked).

Dayside oval proton aurora is likely FLCS-driven, so it is the most likely alternative precipitation mechanism. Differentiating the different regimes of proton aurora in this region, the proton auroral oval, cusp spot, and polar cap precipitation, would be valuable. In Svalbard, typically we are in the polar cap throughout the daytime, so we expect mostly open/direct-entry proton precipitation and cusp proton precipitation, so this should not affect the precipitation study too much. It's a non-trivial additional piece of work and would be valuable in future.

Our results indicate a need for an alternative explanation for *acceleration* of protons in the high-latitude dayside. Since the proton aurora spectrum is accelerated almost all of the time, transient and infrequent events are unlikely candidates. The most obvious alternative mechanism is other forms of ion-acoustic or electrostatic wave (Xiao et al., 2013), though they suffer the same transience as EMIC waves.

Magnetic reconnection is known to accelerate protons (e.g. Phan et al. 2000; Gosling et al. 2005). Reconnection occurs in the high-latitude nightside, but since this geometry requires northward IMF it is not frequent enough to be a good candidate for high-latitude dayside proton aurora.

Turbulent reconnection is also capable of accelerating ions and is an ever-present feature of the bow-shock (Gingell et al., 2020), however the amount of turbulence varies with different IMF regimes (quasi-parallel vs. quasi-perpendicular shock; Plank and Gingell 2023) so we would expect variation with IMF conditions. Since this process is time-varying it is not a good candidate.

We do not currently have a favoured alternative explanation, this requires future work to narrow down possible mechanisms. Further study should look at the different proton aurora signature under varying solar wind, open/closed field, and cusp hours.

4.5 Conclusions

We present three different analyses of spectrograph observations of proton aurora and co-located magnetometer ground-based observations, in order to investigate whether EMIC waves are the accelerating mechanism of proton aurora. Our analyses show no or only a weak link, implying that EMIC waves are not the primary acceleration mechanism responsible for energetic auroral protons in the high-latitude dayside, at least based on the considered ground-based data of proton aurora and magnetic Pc1 pulsations.

The first analysis is a study of the co-occurrence of Pc1 pulsations with accelerated proton aurora. Throughout the December and January of the 2021/2022 observing season, there is only a small temporal link between Pc1 pulsations and accelerated proton aurora. Although accelerated proton aurora is common, Pc1 pulsations were only present during proton aurora in 65 10-minute intervals

during the two months, so only around 5% of the time. The second analysis is a comparison of the average proton aurora spectrum with and without the presence of Pc1 waves. It shows that there is no significant difference in acceleration during Pc1 pulsations than at Pc1-quiet times. The final piece of evidence is that accelerated proton aurora in the high-latitude dayside shows no flickering (intensity modulation) during any of our Pc1 events, or at other non-Pc1 times.

Three separate methods have failed to find a strong link between auroral proton acceleration and Pc1 pulsations, contrary to the prevailing assumptions. This implies that another mechanism is responsible for the majority of acceleration of auroral protons in the high-latitude dayside.

Chapter 5

First observations of GHOST

Note: Geomagnetically-driven high-bandwidth Optical Spectra in the Thermosphere (GHOST) is the new name of continuum emissions in the poleward dayside region as described in the following paper. The text has been left as published.

Published in;

Partamies, N., **Dayton-Oxland, R.**, Herlingshaw, K., Virtanen, I., Gallardo-Lacourt, B., Syrjäsuo, M., Sigernes, F., Nishiyama, T., Nishimura, T., Barthelemy, M., Aruliah, A., Whiter, D., Mielke, L., Grandin, M., Karvinen, E., Spijkers, M., and Ledvina, V. E.: First observations of continuum emission in dayside aurora, Ann. Geophys., 43, 349–367, https://doi.org/10.5194/angeo-43-349-2025, 2025.

Abstract

We report the first observations of continuum emission at the poleward boundary of the dayside auroral oval. Spectral measurements of high-latitude continuum emissions resemble those of Strong Thermal Emission Velocity Enhancement (STEVE), with light characterised by colours such as white, pale pink or mauve. The emission enhancement spans the entire visible wavelength range. However, unlike STEVE, the high-latitude dayside continuum emission events tightly follow the auroral particle precipitation often forming field-aligned rays and other dynamic shapes. Some dayside emissions appeared as wide arcs or cloud-like structures within the red-emission dominated dayside aurora. Our spectral measurements further suggest that the broad band continuum emission may extend into the near-infrared regime. Similar to the STEVE emission, low-Earth orbit measurements of plasma flow in the region of continuum emission show a strong horizontal cross-track velocity shear. Ground-based radar and optical observations provide evidence of both plasma and neutral heating, as well as upwelling, in connection to the continuum emissions. We conclude that the interplay of different heating mechanisms may be an important factor in generating high-latitude continuum emissions.

Author Contribution

NP, **RDO** and KH conceptualised the study, selected the events and wrote most of the manuscript; BGL wrote the introduction and high-latitude continuum comparison with STEVE observations; TN provided DMSP data and helped with its interpretation; **RDO** and DW provided high-resolution spectra, analysed proton precipitation data and helped with the interpretation of the continuum spectra; IV analysed ESR data for this study and helped with its interpretation; TN provided IR spectra for the continuum and helped with the interpretation of the continuum spectrum; MB contributed to the interpretation and modelling of the continuum spectra; FS helped with the technical interpretation of MISS data and run the instrument calibration for this work; MiS provided the MISS data access, helped with cleaning, plotting and wavelength calibration of those data; AA provided the FPI data and assisted the analysis; MaS provided and processed the photo of a FA continuum; LM calculated the solar elevation angle and shadow heights. All authors have participated in the discussions of the observations, the interpretation of the results and editing of the manuscript.

5.1 Introduction

Continuum emissions in the night sky have been observed for decades. One of the earliest reports by citetMeinel1953 describes continuum emissions observed in wavelengths between 390 nm and 480 nm. In nightglow studies, in particular, continuum emission has been recognized as a well-known emission type (Noll et al., 2024b). In recent years, continuum emissions have also gained interest in the auroral community following the discovery of a new optical phenomenon known as Strong Thermal Emission Velocity Enhancement or STEVE (MacDonald et al., 2018). STEVE appears as a mauve-white arc just equatorward of the auroral oval in the sub-auroral ionosphere. STEVE is narrow ($\sim$0.5° latitudinal extent) and spans several hours in magnetic local time (MLT) (Gallardo-Lacourt et al., 2018a). Satellite observations have identified STEVE as the optical manifestation of extreme sub-auroral ion drifts (Archer et al., 2019a). Initially, STEVE was identified to occur during active geomagnetic conditions, consistent with storm-time conditions. However, more recent observations have reported STEVE during quiet geomagnetic conditions, raising questions about the generation mechanism of these intense sub-auroral ion drifts and the role of the magnetosphere in the process (Gallardo-Lacourt et al., 2018a; Martinis et al., 2022; Gallardo-Lacourt et al., 2024; Nishimura et al., 2024). Interestingly, particle detectors onboard low-Earth orbit satellites have determined that STEVE is not related to particle precipitation, suggesting that STEVE emissions could be generated locally in the ionosphere (Gallardo-Lacourt et al., 2018b; Nishimura et al., 2019). Consistently, field-aligned current (FAC) measurements by satellites have confirmed the presence of a downward FAC collocated with STEVE observations (Archer et al., 2019a; Nishimura et al., 2019). A more recent report on STEVE-like pale emissions located poleward of the green morning sector aurora (Nanjo et al., 2024) suggests that strong gradients at the boundary of Region-1 and Region-2 currents are critical for generating strong ion flows and heating.

These significant discrepancies with traditional auroral processes prompted further research into STEVE's spectral characteristics. Gillies et al. (2019) determined STEVE's spectrum for the first time using a spectrograph from the Transition Region Explorer (TREx) array capable of analyzing emissions between 400 nm and 800 nm. These analyses revealed a continuum emission with elevated intensities at all measured wavelengths, solidifying the understanding that STEVE is not produced by particle precipitation but potentially by local ionospheric processes. Further analysis of STEVE's spectrum and optical properties supports these findings (Mende and Turner, 2019; Gillies et al., 2023).

One of the most intriguing questions in STEVE research is understanding the processes involved in its generation and unusual spectrum. Harding et al. (2020) used a simple photochemical model to demonstrate that the fast sub-auroral ion drifts (SAIDs) measured alongside STEVE observations could excite nitrogen molecules into vibrationally excited states. This then results in nitrogen oxide that combines with ambient oxygen to produce NO_2 and a spectrally continuous emission. Additionally, feedback-unstable magnetosphere-ionosphere interactions have been evaluated as possible generation mechanisms for STEVE (Mishin and Streltsov, 2019), challenging the photochemical mechanism proposed by Harding et al. (2020). Currently, there is no consensus on how these continuous emissions are created, and measurements are scarce. Future missions, such as NASA's planned Geospace Dynamics Constellation (GDC) and Dynamics missions, could help elucidate the physical mechanisms at play in STEVE from the magnetosphere–ionosphere coupling perspective.

Recent studies have revealed the presence of auroral structures with continuous emissions within the auroral oval, different from STEVE. Using the TREx colour imagers (RGB) and spectrograph array, researchers have identified these emissions, which would otherwise be overlooked or mistaken for single-wavelength emissions in panchromatic cameras. In the absence of full spectral measurements, continuum emissions could easily be misinterpreted as enhancements of individual emission lines, or a combination of individual emission lines and certain conditions of background sky illumination on the same line-of-sight. Interestingly, these new observations of continuum emissions are closely associated with auroral dynamics and precipitation. Events captured by the TREx RGB cameras, when compared to spectrograph data, not only confirmed the presence of continuum emissions but also uncovered embedded auroral emissions within the same region (Spanswick et al., 2024b). While more events are needed to understand the frequency, spatial distribution and other characteristics of these continuum emissions, they appear to be not uncommon within the auroral oval but rather overlooked due to the instrumentation designed to measure specific wavelengths.

This study reports the first observations of continuum emissions detected around the polar cap boundary over Svalbard (78°N) in arctic Norway. The continuum emission events reported in this paper

occurred within the dayside aurora, but we also show events in the afternoon and nightside aurora, which are likely to be continuum emissions. Our observations align with those of Spanswick et al. (2024b) in that they follow the particle precipitation and auroral dynamics. They may also be influenced by strong gradients at the poleward boundary of the auroral oval, as reported by Nanjo et al. (2024), and could even associated with strong plasma flow shears, similar to STEVE.

In the following sections, we describe our observational setup (Section 2) and our four sample events (Section 3). The sample events were chosen based on the data coverage and their MLT occurrence to demonstrate the variety of different ionospheric conditions in which continuum emissions may appear. Sections 4 & 5 are dedicated to the discussion of the results and conclusions, respectively.

5.2 Data and instrumentation

As the continuum emission is enhanced across the entire visible wavelength range, the best way to observe it is with instrumentation covering the whole spectral range. We use a full-colour all-sky camera (ASC) and an imaging spectrograph. In full-colour images, the color of the continuum emission does not correspond to any known individual emission line. An example of this can be seen in Figure 5.1a as an arc-like region of pale pink colour. To confirm the correct identification of the continuum emission, spectral measurements are necessary. An example of the visible range spectra, collected along the local magnetic meridian and corresponding to the centre column of the all-sky image (white rectangle), is shown in Figure 5.1b. The spectra around the scan angle of 120 (indicated by the black rectangle) show enhancement at auroral emission wavelengths of 428, 558 and 630 nm, as well as across all the displayed wavelengths from 400 to 700 nm.

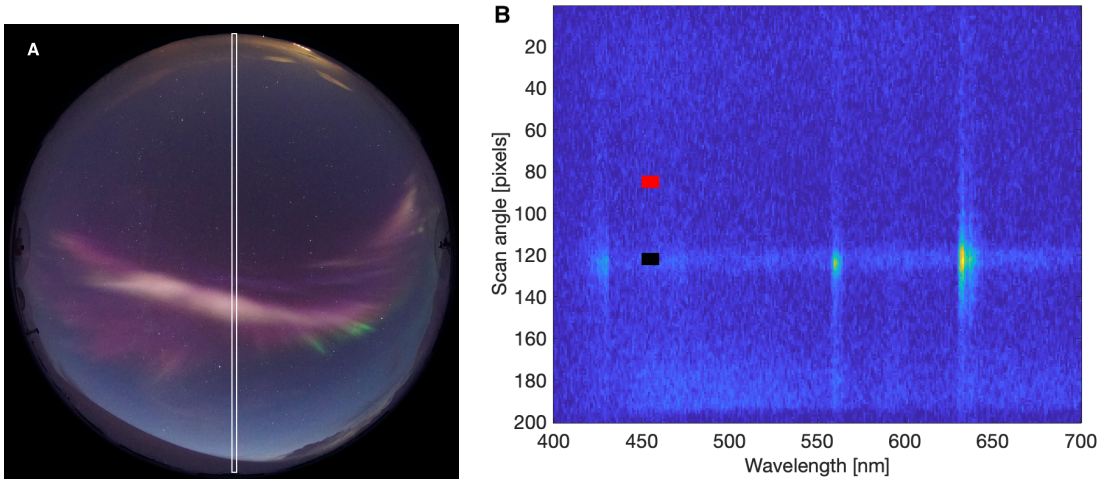

Figure 5.1: A: A full-colour all-sky image from Kjell Henriksen Observatory (KHO), Svalbard, exemplifying the pale pink continuum emission as an arc-like structure in the middle of red-dominated auroral emission. The image is take on 3 January 2020 at 08:48:56 UT. North is to the top and east is to the left of the image. The white rectangle marks the location of the spectrometer field-of-view in the image. The Sun was located at an elevation angle of about -13° relative to the horizon with an azimuth of 149° (SSE). The ionosphere above about 160 km altitude was sunlit. B: Spectra measured by Meridian Imaging Svalbard Spectrograph (MISS) at 08:49 UT. Spectra across the visible wavelength range at 400–700 nm are collected along the magnetic meridian. The continuum emission in the image corresponds to the spectral enhancement at the scan angles of about 120, marked by the black square. An empty sky reference scan angle is indicated by the red square at the scan angle of about 90.

Kjell Henriksen Observatory (KHO, 78°N) hosts a full-colour mirrorless camera (Sony α7S, for details, see e.g. Dreyer et al. (2021)) as well as a the Meridian Imaging Svalbard Spectrograph (MISS) described in a recent KHO science review by Herlingshaw et al. (2024b). The camera has been in operation since 2015, but has been preceded by another full-colour DSLR since 2008. The current

imaging cadence is about 12 seconds with a nighttime exposure of 4 seconds. The full pixel resolution of the images is 2832×2832.

The MISS spectrograph, installed in late 2019, provides a spectral image along the magnetic meridian every minute. The optics incorporate a 0.1 mm slit, which provides a roughly one degree wide field-of-view along the meridian. The spectral resolution capability is 1.5 nm. However, due to the internal optics being out of focus, the spectral resolution of the data used in this study was deteriorated to about 5 nm, which still works well for the purpose of this study. The data are wavelength calibrated using the three strongest auroral emission lines at 428, 558 and 630 nm as references, with a second-order polynomial fitted to the wavelength regions in between. The CCD background has been subtracted based on pixel values outside the slit region (cropped out of the displayed data), and no absolute intensity calibration is done for these data.

Additional spectral information has been gathered from the Near-InfraRed Aurora and airglow Camera (NIRAC) that measures molecular nitrogen ion emission of N_2^+ Meinel (0,0) band at 1 μm (Nishiyama et al., 2024). This emission is primarily prompted by electrons penetrating down to about 100 km altitude, which corresponds to precipitating electron energies up to 10 keV. The emission can also be generated above 140 km by charge exchange between molecular nitrogen (N_2) and atomic oxygen (O^+). NIRAC's field-of-view is 84×68° and the nominal temporal resolution is 20 seconds.

High-resolution spectra have been obtained by the High-Throughput Imaging Echelle Spectrograph (HiTIES, Chakrabarti et al. 2001), located at the KHO. The instrument includes an Echelle spectrograph grating, an electron-multiplying charged coupled device (EMCCD) detector, and a mosaic filter which is used to select multiple overlapping spectral orders, enabling observation of multiple non-contiguous wavelength bands at high resolution (< 0.1 nm). The mosaic filter selects the H-alpha band at 649–663 nm used for observing proton precipitation, O^+ green line / OH(8,3) band at 728–743 nm, and OH(5,1) band at 790–807 nm. HiTIES is directed at the magnetic zenith with an 8° by 0.05° field-of-view. The imaging cadence is 2 Hz, giving a temporal resolution of 0.5 seconds. The spectra in this study have been spatially and temporally integrated to improve the signal-to-noise ratio. The background has been subtracted based on pixel values outside of the filter mosaic, and the data are not calibrated for absolute intensity. Dark frames are taken every 20 minutes and flat fields are taken at the beginning of the observing season.

The EISCAT Svalbard Radar (ESR) (Wannberg et al., 1997b) is located about 1 km north of KHO, and provides profiles of ionospheric plasma parameters within the zenith region of the Sony camera field-of-view. The data consist of height profiles of electron density, electron and ion temperature and ion velocity as a standard set of parameters along the radar beam with a temporal resolution of one minute. The radar experiment that was run during one of our events was `ipy`, which has a height resolution of about 4–5 km in the ionospheric E region. In this study, we only use data from the non-steerable parabolic antenna (42 m in diameter), which measures plasma profiles along the geomagnetic field direction.

The Fabry-Perot Interferometer (FPI) at KHO can determine the neutral winds and temperatures in the thermosphere at the heights of red auroral and airglow emission (630.0 nm), which typically has a peak emission at around 240–250 km (Aruliah and Griffin, 2001). The winds and temperatures are based on Doppler shift and Doppler broadening of the observed emission. The FPI has well-separated look directions towards zenith, north, east, south and west at an elevation angle of 30°. The wind and temperature estimates have a temporal resolution of 8 min. The line-of-sight wind measurements can be converted to horizontal estimates by assuming that there is zero vertical wind. In this study, we only use the zenith line-of-sight location to estimate the neutral upwelling.

The Defense Meteorological Satellite Program (DMSP) F17 satellite flew over one of our continuum emission events. In our analysis, we use the horizontal cross-track plasma flow measurements from F17 (Cornelius and Mazzella, 1994). These data are archived in the Coupling Energetics and Dynamics of Atmospheric Regions (CEDAR) madrigal database. The geomagnetic disturbance level for our continuum emission events was 2–4 at Kp index range, and the magnetic local time (MLT) in Svalbard is approximately UT+3h. We use the OMNIWeb solar wind and interplanetary magnetic field (IMF) measurements to assess the solar wind driving conditions for our events (Papitashvili and King, 2020).

5.3 Continuum emission observations

5.3.1 Dayside continuum on 3 January 2020

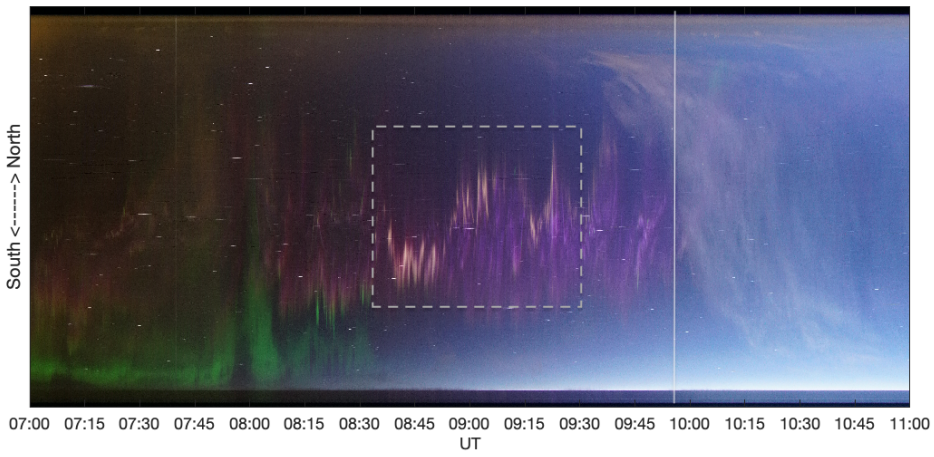

Figure 5.2: Keogram of Sony images at 07–11 UT on 3 January 2020. The y-axis is a slice through the sky from magnetic South (bottom) to magnetic North (top). The most intense pale pink continuum emission is seen in the time period of 08:30–09:30 UT indicated by the rectangle. Appearance of a thin cloud layer is marked by vertical line.

Figure 5.2 shows a full-colour keogram compiled of the all-sky images captured by the Sony camera at 07–11 UT on 3 January 2020. The first 1.5 hours display a combination of red emission overhead and diffuse green towards the southern horizon. The most intense pale pink continuum emissions are seen in the time frame of 08:30–09:30 UT (rectangular region in the figure), where during the first half-hour they appear particularly intense and wide. At 09:03–09:14 UT the continuum emission structures were very thin, but another wide continuum emission was observed at around 09:15 UT, and a continuum-bracketed corona was seen at around 09:21 UT. From about 09 UT until about 10 UT the dominant emission colour in the aurora is pink due to resonant scattering (Shiokawa et al., 2019), and the last hour is obscured by thin clouds (right of the vertical line). Some individual thin arcs including the pale colour of the continuum emission took place earlier and later but the structures were too thin to be differentiated from the background in our spectral measurements.

The left panel of Figure 5.1 shows an example of a pale pink arc-like structure captured with an all-sky during the first intense period of the continuum emission. The image is taken at 08:48:56 UT. No auroral structures can be seen poleward of the continuum emission, and therefore this continuum emission was located at the poleward boundary of the auroral oval. This pale pink structure crossed the centre meridian of the images. The MISS spectrograph measured a clear emission enhancement across the entire wavelength region at 08:49 UT (right panel in Figure 5.1). We compare the continuum emission spectrum at the meridian location of the black square in Figure 5.1 to a reference spectrum that is taken from the north side of the continuum and auroral emissions (meridian location of the red square in Figure 5.1). The reference spectrum location is chosen so that there is no obvious emission in the sky as seen in the all-sky image. The reference spectrum is represented by the red curve in Figure 5.3 and only shows mild enhancements at 558 and 630 nm. The continuum spectrum (black curve in Figure 5.3) shows strongly enhanced auroral emission lines at 428, 558 and 630 nm in addition to elevated brightness counts throughout the measured wavelength range.

At the time the image and spectra in Figures 5.1 and 5.3 were captured, the solar elevation angle was estimated to be about -13°. This places the shadow height at about 160 km making all dayside

auroral emission sunlit, which explains the purple hue of the auroral display due to resonance scattering. The shadow height estimates for the dayside events displayed in this study have been calculated by the following geometry with the assumption of a spherical Earth: $h = R_{\mathrm{E}}/\cos(\theta - 90) - R_{\mathrm{E}}$, where h is the shadow height, R_{E} is the radius of the Earth (6371 km), and θ is the solar zenith angle in degrees.

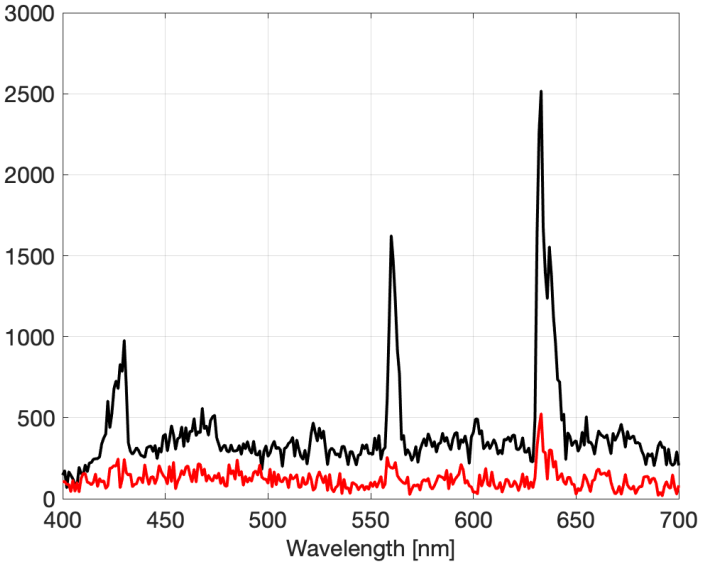

Figure 5.3: Continuum spectrum (black) and an empty-sky reference spectrum (red) measured by MISS at 08:49 UT on 3 January 2020. The y-axis values are counts summed over scan angles around the continuum maximum (118–128) and scan angles of 80–90 for the reference spectrum. The solar elevation angle was about -13° and the ionosphere above about 160 km altitude was sunlit.

In the continuum spectrum in Figure 5.3 (black curve), we can identify some specific spectral features. The blue auroral emission at around 428 nm, which is the signature of sunlit aurora, is strongly enhanced. Another milder enhancement at about 470 nm is also most likely from the N_2^+ first negative band with the nominal wavelength of 471 nm. At about 520 nm, a 10 nm wide feature may consist of both the atomic nitrogen line at 520 nm and the N_2^+ first negative band at 522 nm. Further in the long wavelength regime, a narrower emission signature at around 600 nm can be due to an enhancement of O_2^+ band at 602.6 nm (Chamberlain and Oliver, 1953; Chamberlain, 1961).

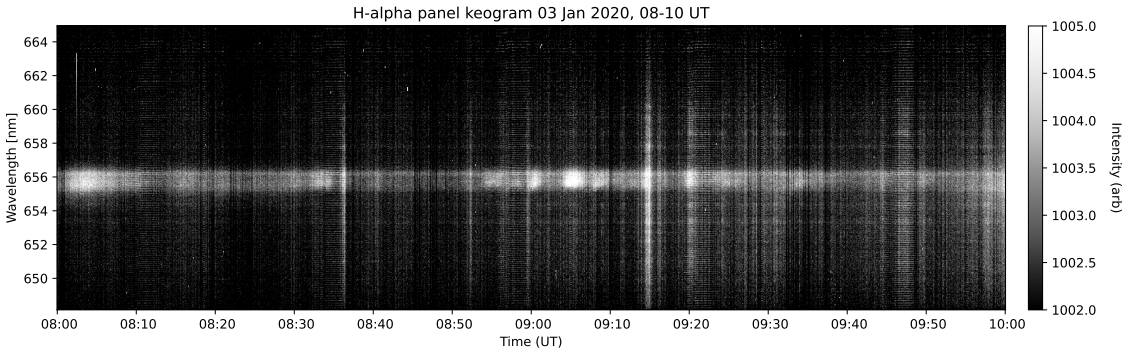

Figure 5.4: HiTIES data on 3 January 2020: the y-axis is the spatially integrated spectrograph slit, in 0.5 s second increments along the x-axis. The keogram shows proton precipitation Doppler shifted over ~ 1nm from the rest Hα wavelength at 656.3 nm, occurring in short bursts during the event. The continuum emission crosses the spectrograph slit, and is visible as a vertical bright line at, for instance, 09:15 UT.

The HiTIES spectrum for the proton band (Hα) shows an increase in the proton emission during the continuum event, as seen in Figure 5.4. The proton precipitation is visible as a wide, bright band of proton aurora. It is blue-shifted from the Hα rest wavelength at 656.3 nm due to the downward velocity of the precipitating protons. The proton aurora brightens in short bursts throughout the event, including a bright burst as the continuum passes through the HiTIES slit at 09:15 UT at the centre of the ASC field-of-view (image in the top panel of Figure 5.7). This variation may be temporal or spatial, though it is not possible to determine which. High-resolution spectra of the continuum from HiTIES at 09:15 UT are shown in Figure 5.5 and compared to a reference spectrum taken at 09:11 UT, when only proton aurora emissions were within the instrument's field-of-view. These spectra show clearly the continuum nature of the emission in the observed bands, as well as some specific emission features. The background features are proton aurora (top panel), O^+ aurora (centre panel) and OH airglow (centre and bottom panels), these emission lines do not appear to be affected by the presence of the continuum. From the OH panel we can see that the continuum is also present in the very near-infrared. Since these data are not calibrated for absolute intensity, we can instead use the relative intensity of the continuum compared to the background to observe that the continuum becomes less bright towards the longer wavelengths, i.e. tapering off towards the infrared.

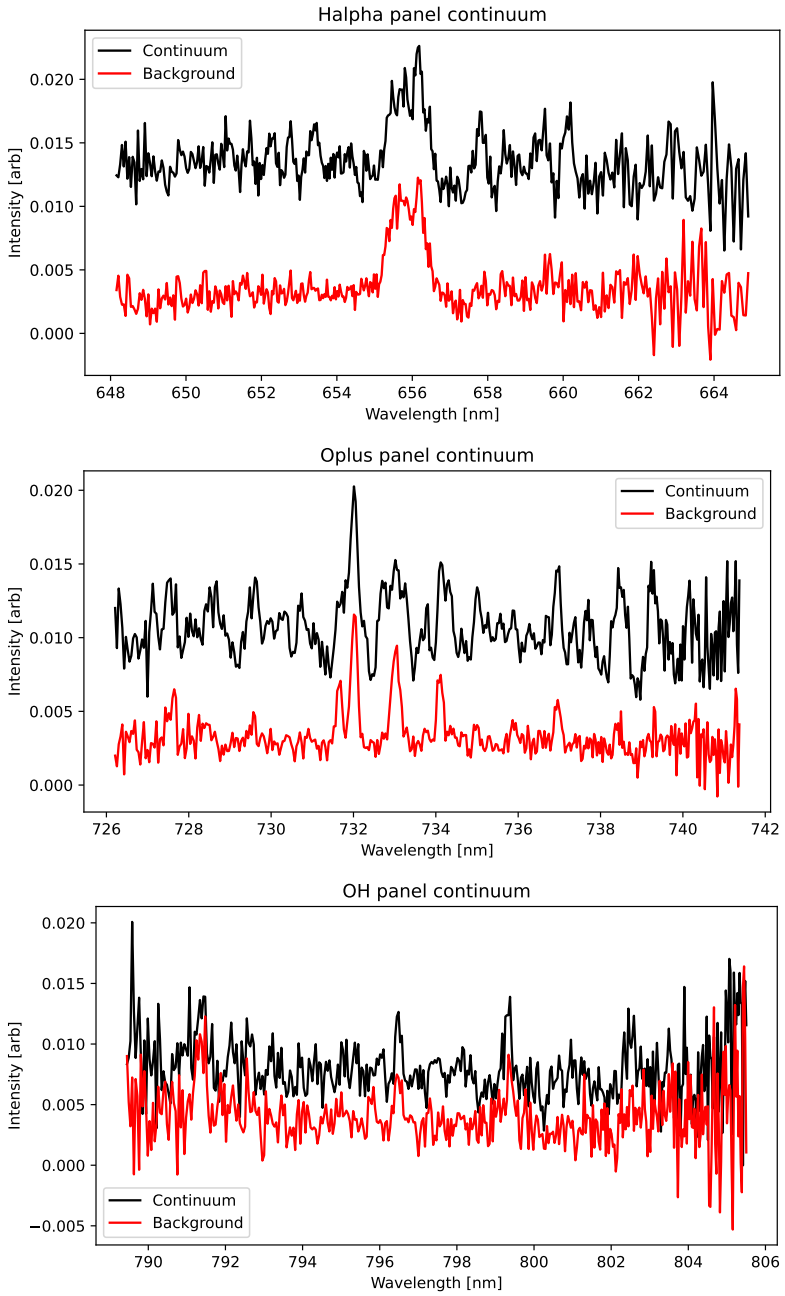

Figure 5.5: High-resolution HiTIES spectra of continuum (black) of 3 January 2020, at 09:15 UT, compared to background (red) taken from 09:11 UT same date. The measured intensity in arbitrary units is plotted against the wavelength in nm.

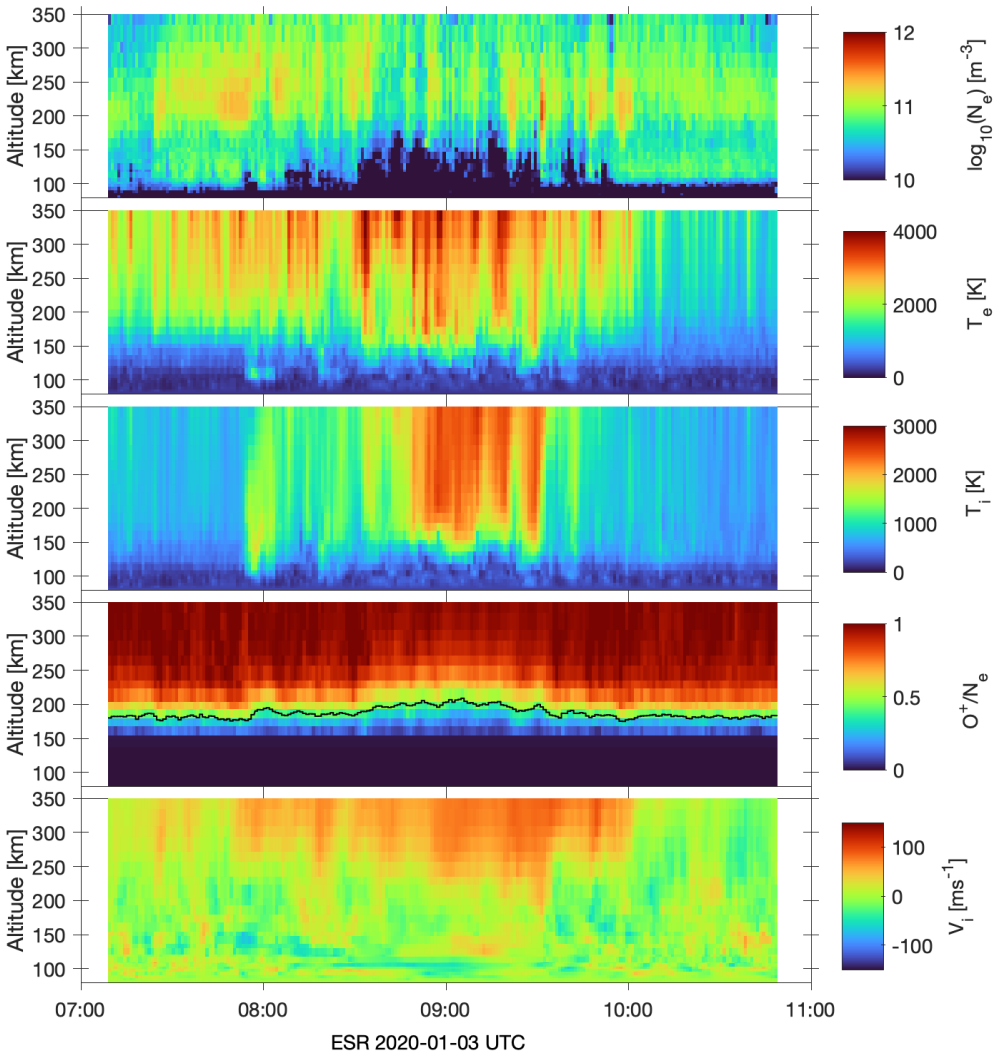

Figure 5.6: EISCAT Svalbard Radar (ESR) data on 3 January 2020. Electron density (top), electron temperature (2nd), ion temperature (3rd), ion composition ratio (4th) and ion drift velocity (bottom) as a function of time and height are analysed by Bayesian filtering method (BAFIM) using chemical Flipchem model.

At the time of the main continuum emission observations (08:30–09:30 UT), EISCAT data shows transient enhancements of electron density which were mainly limited to the F-region (top panel in Figure 5.6). E-region electron density was very low, making all E-region observations highly uncertain. Particle heating can be seen as electron temperature increases at and above 150 km (2nd panel). Ion heating is also mainly concentrated in the F-region heights above about 150 km (3rd panel). Ion heating is interpreted as Joule heating, which generally requires horizontal electric field. It is not obvious if the heating is directly related to the particle precipitation and to the pale pink emission that is drifting into the EISCAT beam, or if the timing is just a coincidence. The EISCAT data were analysed with a Bayesian filtering method (BAFIM, Virtanen et al. (2021)) with an inclusion of an F-region chemical model Flipchem (Virtanen et al., 2024). This chemical model inclusion allows a variable ion composition ratio (4th panel) and therefore produces more reliable electron and ion temperatures. Ion upflow is seen to correspond the ion heating (bottom panel), mainly above 200 km.

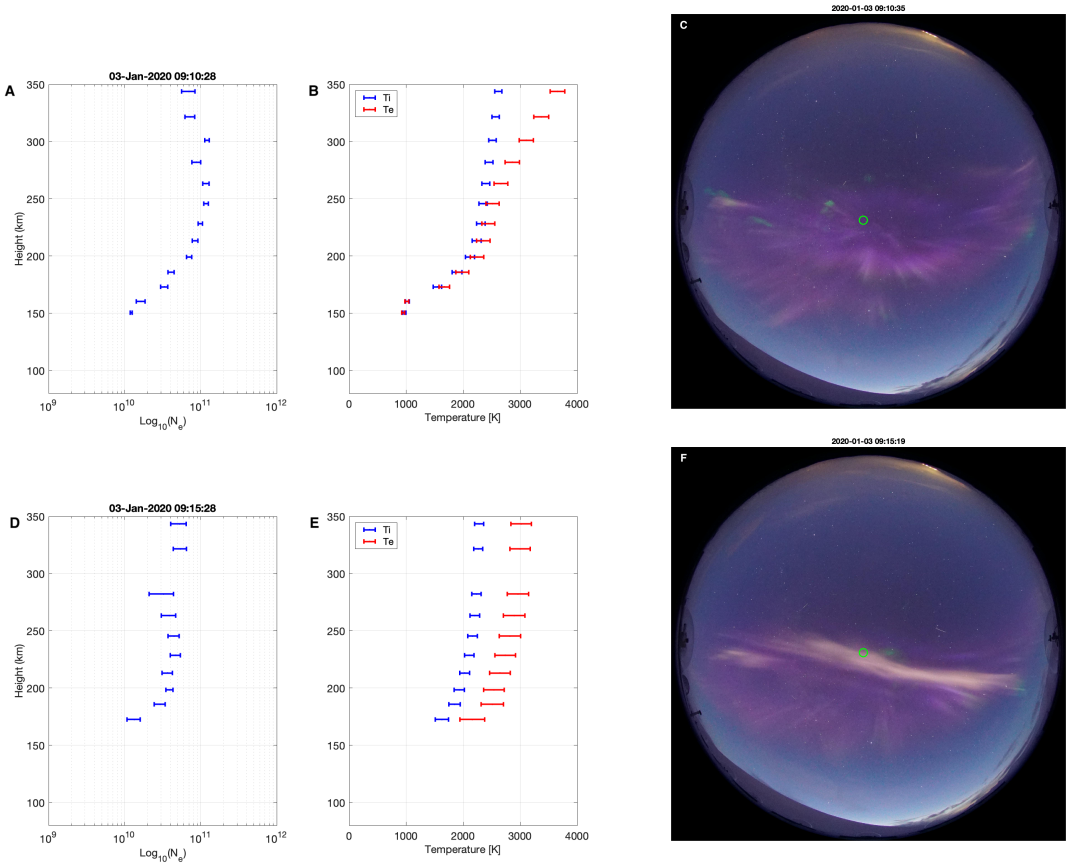

Figure 5.7: A & D: Electron density profiles measured by ESR at 80–350 km on 3 January 2020. The scale is logarithmic and all electron densities below $10^{10}\mathrm{m}^{-3}$ have been omitted as uncertain. B & E: Ion (blue) and electron (red) temperature profiles (in K) for the same height range and the same time instants. All temperature values corresponding to heights of omitted electron densities have been excluded. C & F: All-sky images taken closest to the ESR measurements. ESR profiles times are 09:10:28 UT (A & B) and 09:15:28 UT (D & E). The corresponding image times are 09:10:35 UT (C) and 09:15:19 UT (F). At 09:15 UT the Sun was located at an elevation angle of about -12° relative to the horizon with an azimuth angle of 155° (SSE). The ionosphere was sunlit above the altitude of 145 km. The green circle in the images marks the approximate pointing direction of the radar beam at 150 km altitude.

Individual ionospheric profiles and images captured at 09:10:30 and 09:15:30 UT are shown in Figure 5.7. These are close to the times the HiTIES spectra was taken for the background and the continuum emissions in Figure 5.5. Initially (a–c), the radar beam points (green circle in panels c and f) into faint red emission region corresponding to mildly increased electron density above 200 km. Later

(d–f), the beam points into the continuum emission. The electron density profile within the continuum is less enhanced in the F region than in the non-continuum profile. The same applies to the ion temperature (blue curves in b and e). Both time instances comprise soft electron precipitation. However, electron temperature is enhanced by about 500 K at about 200–250 km at the time of the continuum (e) as compared to the non-continuum profile (b).

FPI measurements of red emission can be used to estimate thermospheric neutral temperatures and winds at the heights of red emission.

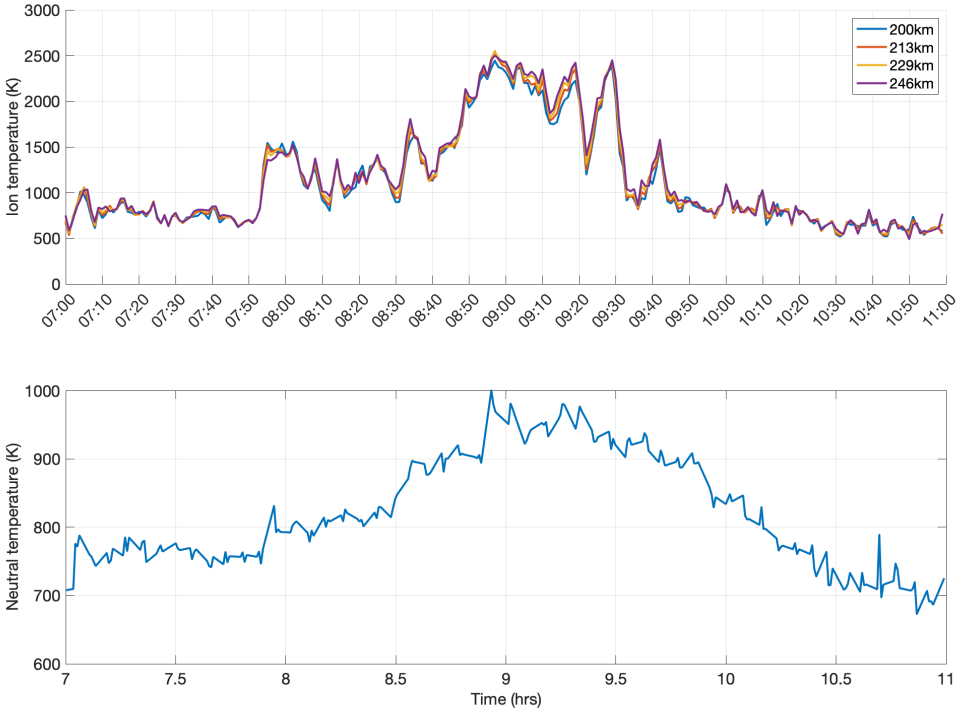

Figure 5.8: F region ion temperature measurements by ESR (top panel) at the heights of 200, 213, 229 and 246 km on 3 January 2020. Thermospheric neutral temperature measured by FPI (bottom).

Figure 5.8 shows the comparison between the EISCAT measurements of F-region ion temperature time series from the heights of 200, 213, 229 and 246 km (top panel) and the thermospheric neutral temperature measured by FPI (bottom panel). FPI temperatures are estimated in the vertical line-of-sight direction, which is the closest direction to the field-aligned ion temperature measurements. The temporal correspondence between the two is very good. There is more variability in the ion temperature but the initial enhancement takes place at the same time (at about 07:52 UT). The initial temperature for ions and neutrals is similar (around 700–750 K), the temperatures peak closely at the same time (at about 08:56 UT) and decay during the same time period, although the neutral temperature decay takes about an hour longer (until about 10:30 UT). The maximum temperature for ions is about 2.5 times higher than the neutral maximum temperature, in agreement with Aruliah et al. (2010), who pointed out that the neutral temperature provides the lower boundary for the ion temperature variability.

The FPI data also shows neutral upwelling in the vertical line-of-site direction in the time frame of ion upflow, as shown by Figure 5.9. The radar measurements are displayed for four consecutive heights in the range of the strongest heating and upflow. The neutral upflow reaches higher speeds than the ions by about 40 m/s, but only for a very short period (about 10 min) just before 09:00 UT. The neutral upflow correlates best with ion upflow at 246 km height, which is a likely height for the red auroral emission to occur. The enhanced ion drift continues for about half an hour after the neutral flow had decayed. Observed upflow speeds and temperature enhancements are similar to previous upflow

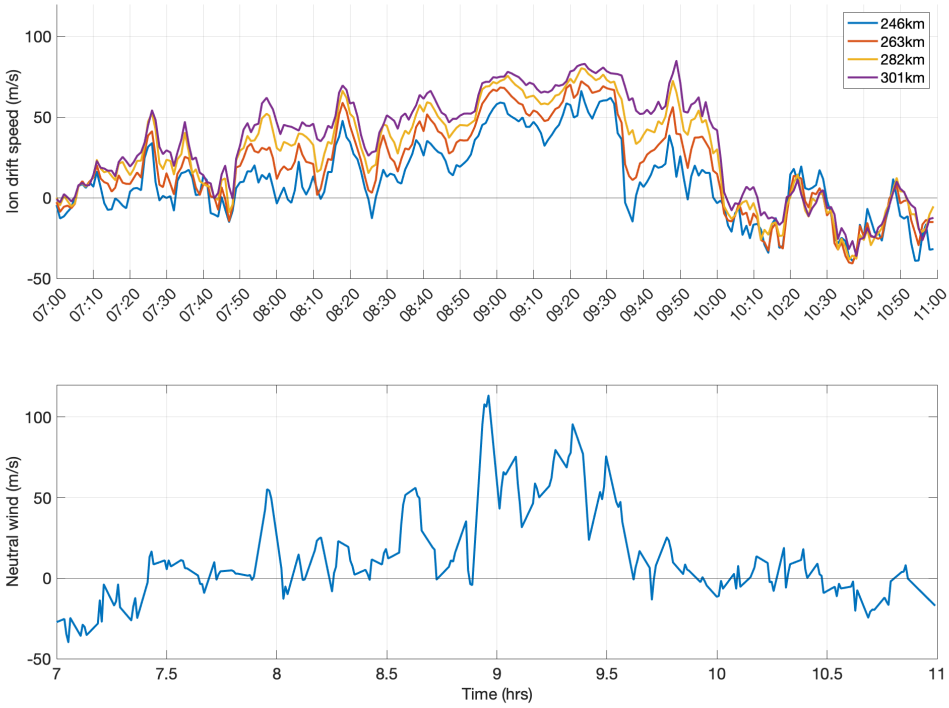

Figure 5.9: F-region ion drift speed measurements by the ESR (top panel) at the heights of 246, 263, 282 and 301 km on 3 January 2020. Thermospheric neutral upflow speed (vertical line-of-sight) measured by the FPI (bottom). Positive speed is upwards in both measurements.

measurements at polar cap boundary of the auroral oval during moderate geomagnetic activity (e.g. Innis et al., 1997). Also, neutral and plasma upflow have been observed to correlate in the vicinity of auroral activity (e.g. Shinagawa et al., 2003). The flow and heating observations during the continuum emission are therefore not exceptional or extreme.

The DMSP F17 spacecraft flew over the region of continuum emission at 08:39–08:40 UT at an altitude of about 800 km. Its footpoint locations are plotted on the ASC image taken at 08:40:05 UT in Figure 5.10a. This image is selected as it is the closest in time to the DMSP overpass. The thin white line linearly connects the footpoint locations at 08:39 and 08:40 UT. The image is converted to geographic coordinates assuming an emission height of 150 km, which is at the bottom of the heated height range measured by EISCAT. The continuum emission moved southwest in the time between the two DMSP footpoint locations, so the spacecraft is estimated to have crossed the continuum at 08:39:40 UT (northeastward of the location seen in the image). This time is marked by a vertical line in the plot of velocities and temperatures measured by DMSP in Figure 5.10b and c. Figure 5.10b shows the vertical (red) and horizontal cross-track velocity (blue), where the positive directions are upward and sunward (northwest here). Figure 5.10c shows the ion (red) and electron (blue) temperatures. The ion temperature varies around 2000 K and the electron temperature around 4000 K, which are in agreement with the EISCAT measurement some 400 km further down (Figure 5.6). While the magnitude of the vertical flow measured by DMSP may not be reliable, the flow direction is upwards (positive). The horizontal cross-track flow measured by DMSP experiences a strong shear from negative (southeast) to positive (northwest) over the time of the continuum overpass. The cross-track shear flow converges towards the region of continuum emission, which is in agreement with the upflow measured by EISCAT.

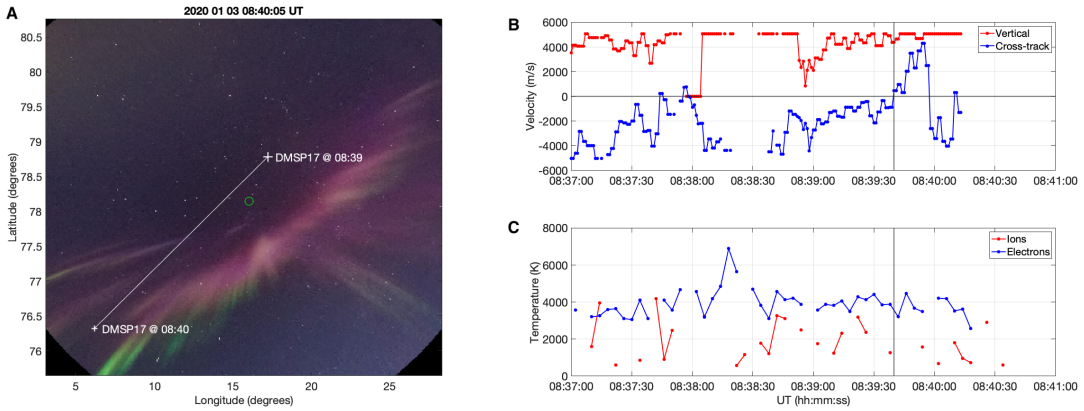

Figure 5.10: A: DMSP F17 overpass through the arc-like continuum emission. The white crosses mark the footpoint locations of the spacecraft at 08:39 and 08:40 UT. The time-wise closest ASC image at 08:40:05 UT has been plotted on geographic coordinates with the height assumption of 150 km and a linear lens model. B: DMSP measurements of vertical (red) and cross-track (blue) velocities during the overpass at 08:37–08:41 UT. Positive flow directions are upward and sunward (northwest here). C: DMSP measurements of ion (red) and electron (blue) temperatures during the overpass. The time of the estimated continuum crossing is marked by a vertical line at 08:39:40 UT.

5.3.2 Morning continuum on 11 February 2024

Another continuum emission event was observed over Svalbard on 11 February 2024, but this time in the morning sector. During this event, solar wind density peaked extremely high ($\sim 40/cm^3$) right after 02:00 UT when optical instruments were in the dawn sector. Some continuum-like thin structures were visible as early as 02:29 UT. Strong red emission could be observed despite variable cloudiness from about 02:40 UT onwards. The first obvious continuum signatures were measured in the emission spectra at 05:23 UT on the southern part of the sky. These were wide arc and cloud-like structures of pale pink emission within bright pink sunlit aurora (Figure 5.11). By about 06:00 UT the region of auroral emission had returned to the southern horizon and by 06:30 UT it had become undetectable due to daylight. As long as any emission colours were visible, the continuum emission was also present.

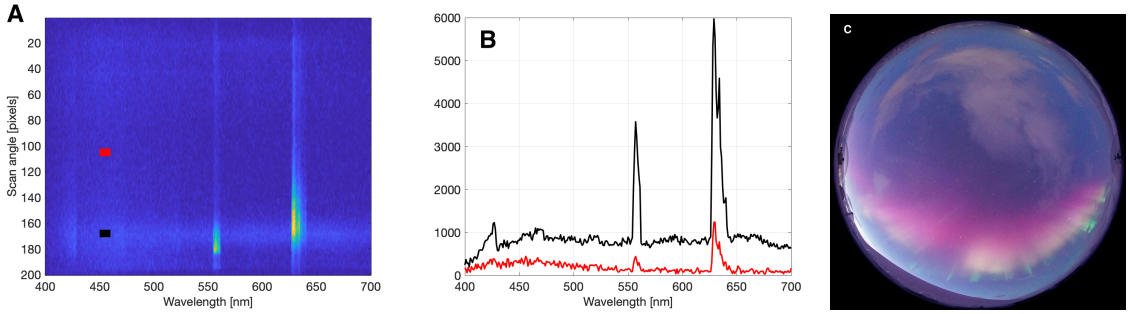

Figure 5.11: A: MISS spectrogram data at 05:46 UT on 11 February 2024 with the meridian locations of the reference spectrum (red) and the continuum spectrum (black). B: Continuum spectrum (black) and an empty sky reference spectrum (red) measured at 05:46 UT. The y-axis values are summed counts over scan angles of 163–173 for the continuum and over scan angles of 100–110 for the reference. C: ASC image taken at 05:46:03 UT. North is to the top and east to the left of the image. The solar elevation angle was -12° relative to the horizon with an azimuth of 102° (ESE) and the sunlit boundary of the ionosphere was at 142 km.

The MISS spectrograph data shows a particularly big difference (~800 counts) between the continuum (black) and the background (red) for this event. This is illustrated by the continuum emission and reference spectra at 05:46 UT in Figure 5.11a and b. The sky is lighter in the region of the contin-

uum emission than in the region of the reference spectrum due to the increasing daylight towards the southern horizon (Figure 5.11c). Some of the spectral difference at the short wavelength end of the spectrum (<500 nm) can therefore be due to the daylight, while the broad band enhancement is due to the continuum. Most of the individual emission bands that were identified in the spectrum of the previous event are visible in this case as well, except the enhancement of the O_2^+ band at 602.6 nm.

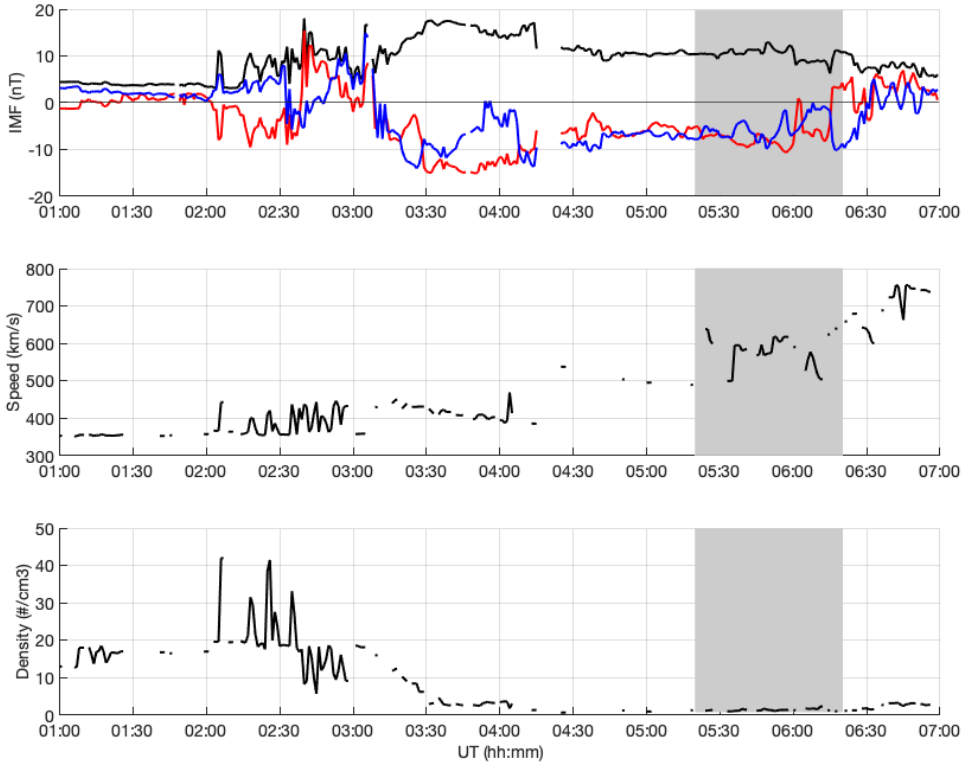

Figure 5.12: Solar wind and IMF parameters on 11 February 2024, propagated to the bow shock. *Top:* IMF magnitude (black), By (red), and Bz (blue) in nT. *Middle:* Solar wind speed in km/s. *Bottom:* Solar wind proton density in the number of particles per cm^3. The shaded region indicates the time period of most intense continuum emission observations.

Prior to and during the continuum emission observations, the IMF Bz was negative (around -10 nT) for an extended period of time (see Figure 5.12). The solar wind speed increased from about 400 km/s to about 700 km/s during the time period of the continuum emission observations. The proton density in the solar wind peaked at values above 30–40 cm^{-3} previously but declined to values below 10 cm^{-3} before the strongest continuum emissions were observed in the dawn sector.

5.3.3 Afternoon continuum on 1 December 2023

Strong red auroral emission was observed on 1 December 2023, particularly in the afternoon. Most of the continuum emission structures were either off the meridian / zenith or were very thin structures. The spectral comparison between the continuum and the background sky, such that was done for the previous events, was therefore not possible. The colour of the observed emission, however, strongly suggests the structure was a continuum emission. The thin continuum-like structures appeared as early as about 08:30–10:00 UT, while more clearly field-aligned structures were seen at about 15:00–16:00 UT. Some of the continuum-like rays were captured by photographers.

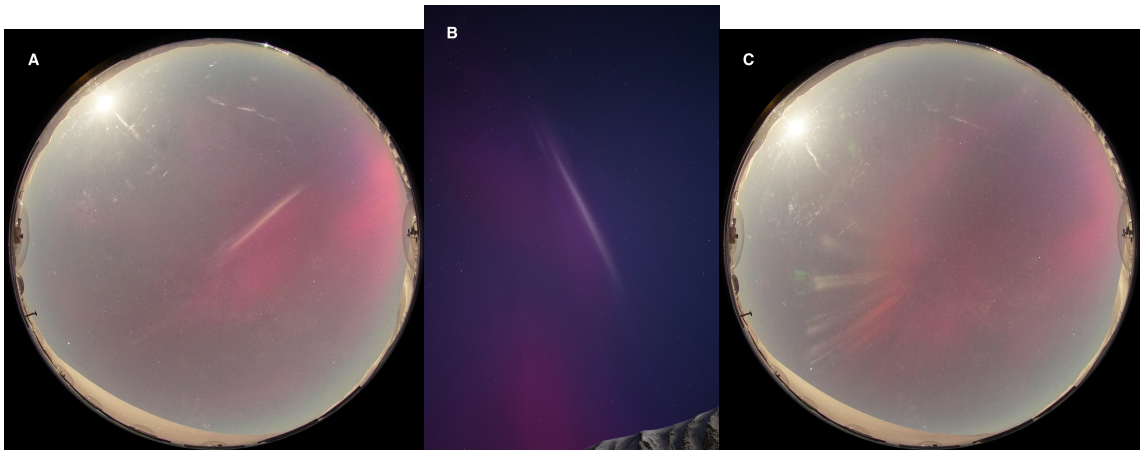

Figure 5.13: Example Sony images of the afternoon continuum taken on 1 December in 2023 at 15:11:58 UT (A) and 16:00:56 UT (C). The thin arc in panel A was shown to be a field-aligned structure based on the photograph taken independently in the same region and on the same minute by Marjan Spijkers (B). The photo was taken with 8-second exposure time and viewing the sky towards west. Pale bundles of field-aligned rays are seen in the image C. North is to the top and east to the left in ASC images (left and right). At 15:11:58 UT the Sun was located at an elevation angle of -17° with an azimuth of 243° (WSW). The ionosphere was sunlit above an altitude of 284 km.

The photograph in Figure 5.13b was taken independently by a citizen scientist and captured the same thin structure observed in Figure 5.13a. This photo provides a side view into the thin continuum emission clearly showing the field-aligned orientation of the thin pale structure. The all-sky images show the thin continuum emission persisting for a minute, from 15:11:10 to 15:12:10 UT. Similarly the pale pink rays seen in Figure 5.13c were clearly visible in the ASC images for about a minute.

The infrared camera NIRAC also detected the thin emission structure, which overlaps with the continuum-like field-aligned structure in the left panel of Figure 5.13. The NIRAC image displayed in Figure 5.14 shows no enhancements related to the surrounding red emission (630 nm) but an enhanced thin structure of the continuum at 1.1 μm.

This demonstrates that the wide spectral enhancement of the continuum emission may not be limited to the visible wavelength range but may extend deep into the infrared regime. During this event, NIRAC was operated at 5-second cadence. This infrared emission from molecular nitrogen is likely to be caused by charge exchange from atomic oxygen ion as it is likely occurring in the F-region together with the surrounding red emission.

Prior to and during the continuum emission observations the IMF magnitude was relatively stable and high (around 20 nT) as seen in Figure 5.15. The Z-component of the IMF was strongly negative (about -20 nT) until about 13:20 UT. The solar wind speed was above 500 km/s throughout most of the time prior to and during the continuum emission. The proton density in the solar wind varied primarily above 20 cm^{-3}, reaching the peak values above 50 cm^{-3} between around 11:00–13:00 UT.

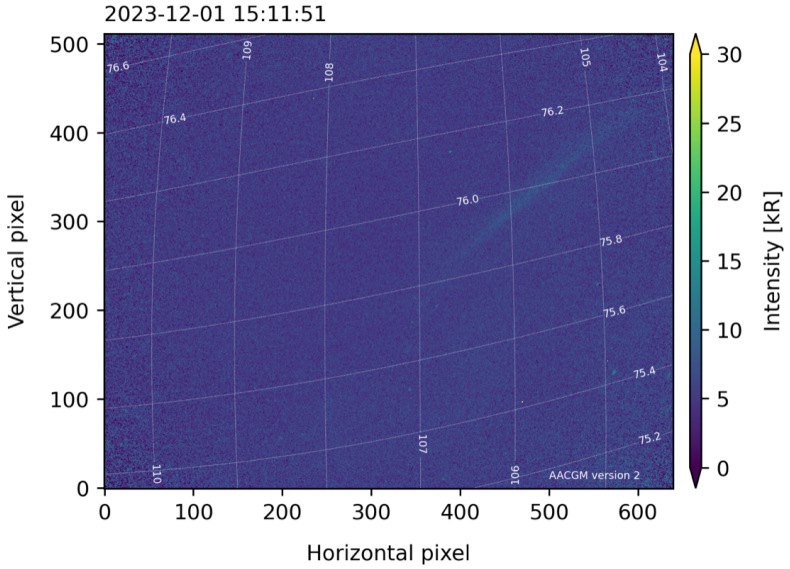

Figure 5.14: An infrared image of the thin structure in the images of Figure 5.13. No red emission at 630 nm is seen but the continuum structure is clearly visible at 1.1 μm. The white grid indicates the geomagnetic coordinates.

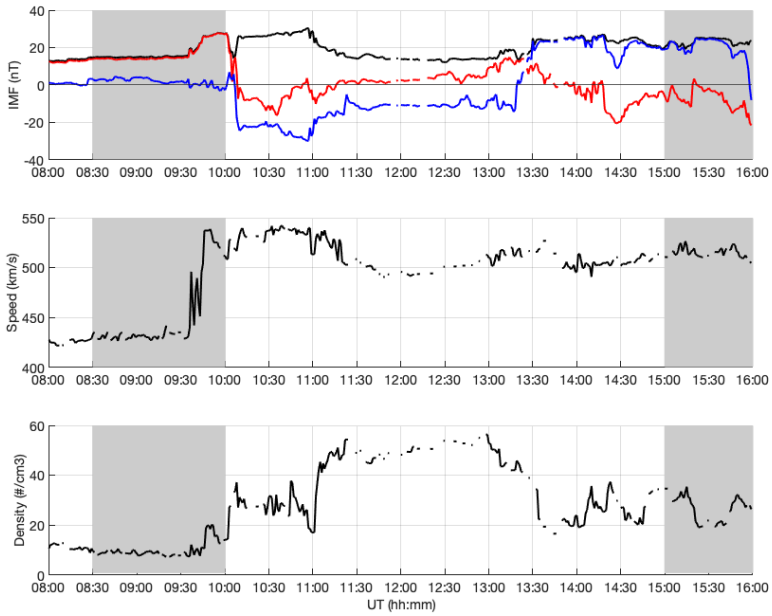

Figure 5.15: Solar wind and IMF parameters on 1 December 2023, propagated to the bow shock. *Top:* IMF magnitude (black), By (red), and Bz (blue) in nT. *Middle:* Solar wind speed in km/s. *Bottom:* Solar wind proton density in the number of particles per cm^3. The shaded regions indicate the time periods of most intense continuum emission observations.

5.3.4 Nighttime continuum on 8 February 2019

Continuum-looking arc-like features were observed in the ASC images close to the zenith/centre meridian several times during the first hour of the day on 8 February 2019. As seen in the example images in Figure 5.16, these events are faint and narrow structures and therefore hard to detect even for a trained human observer. The meridian imaging spectrograph was not able to resolve the continuum from the background sky spectrum, but the colour of the emission cannot be explained by any other known emission than the continuum.

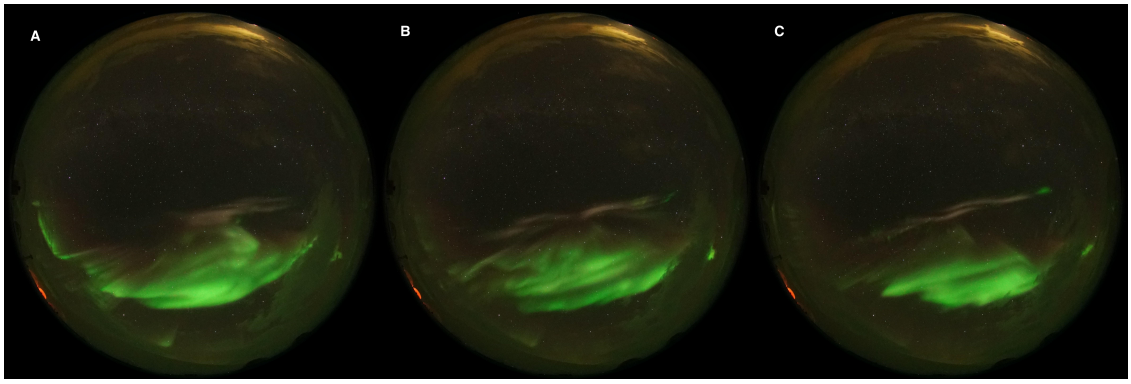

Figure 5.16: Example images of our only nightside continuum event on 8 February 2019. This continuum emission lasted for about 10 minutes and showed a temporal evolution like any auroral event. Images are taken at 00:26:55 (A), 00:27:55 (B) and 00:28:43 UT (C). North is to the top and east to the left in the images. The Sun's elevation angle was -26° relative to the horizon and the shadow height was above 700 km.

The thin continuum-like structures developed in the image data for about 8 minutes (from about 00:26 until 00:34 UT). The solar wind prior to and during the event was slow (about 400 km/s) with a moderate density of 4–5 cm^{-3}. The IMF Z-component varied between -4 and +2 nT (data not shown).

5.4 Discussion

In this study, we present the first continuum emission observations captured near the poleward boundary of the dayside auroral oval. We described two spectrally confirmed, intense continuum emission events on 3 January 2020 and on 11 February 2024, in the noon and dawn sector respectively. Additionally, we show nighttime and afternoon events, not confirmed by spectral measurements, but are classified as continuum emission based on their pale pink colour showing visual similarities to the spectrally confirmed events. The afternoon sector event mainly manifested itself as thin field-aligned structures of continuum-like emission. An example of a nighttime continuum-like emission event appeared as a narrow arc at the poleward boundary of the green aurora.

Auroral conditions similar to those seen on 1 December 2023 with strong red-dominated emission and thin continuum-like emission structures were visually found at least on 12, 21, 23–27 and 30 November 2022; 1, 6 and 7 November 2023; 2–3, 6 and 15–16 December 2023, as well as 6 February 2024. These are all likely to be continuum emissions, in which case, this type of emission is not a rarity at high latitudes. It rather seems infrequent to see it so strong and wide that it is unambiguously visible in the spectrograph data and keograms. The observed pale pink emission moves with the auroral particle precipitation and often appears as field-aligned rays that may evolve quickly in time. Because the individual continuum emission structures last typically of the order of a minute or less, the mismatch in the timing between the ASC images and the spectra plays a role in the number of spectrally confirmed observations.

Interestingly, during each of the continuum emission events shown in this study, Fragmented Aurora-like Emissions (FAEs) occurred nearby (such as in top panel of Figure 5.7). Fragments were first described by Dreyer et al. (2021) as localised emission regions, which lack the field-aligned extent. While there is no commonly established generation mechanism for fragments, the authors concluded that

fragments were not caused directly by particle precipitation but that local instabilities would play a key role in producing the observed emission. Not all fragment observations align with observations of continuum emissions, but vice versa seems to be true, suggesting that the strong ionospheric heating may lead to favourable conditions for fragment formation.

The behaviour of the continuum emission of STEVE is different from our observations of the high-latitude continuum emission. STEVE typically appears before the magnetic midnight, relates to the substorm recovery phase, and lasts for about an hour (Gallardo-Lacourt et al., 2018a). In contrast, our examples of continuum emissions are transient structures with lifetimes of minutes, distributed across different magnetic local times, from midnight to dayside cusp hours and late afternoon. Apart from the midnight event, our continuum emissions take place in time sectors multiple hours away from substorm activity. While the STEVE continuum is often seen as a narrow horizontal arc, our events show variable morphological structures from thin to wide arcs, perturbed arcs and field-aligned rayed structures. However, field-aligned rays are sometimes observed as a fine-structure of STEVE too, so the rayed continuum emission structure is not fully absent, just perhaps not as frequent in STEVE as it is among the events reported in this study. The dynamic behaviour of the continuum emission events reported here is similar to the continuum emission events found embedded in the auroral oval (Spanswick et al., 2024b). Also similar patchiness is seen in our continuum emission events as reported by Nanjo et al. (2024). One of the structures reported here was related to a strong flow shear measured at low-Earth orbit, comparable to the extreme sub-auroral ion drift associated with STEVE (MacDonald et al., 2018; Archer et al., 2019a). It remains to be discovered if strong flow shears are also commonly associated with high-latitude continuum emissions.

According to Nishiyama et al. (2024), the molecular nitrogen Meinel band in the infrared range can be excited by charge exchange with atomic oxygen ions. In particular, the excited D state of the atomic oxygen may be an important source of ionised molecular nitrogen emission in the infrared range (N_2^+ Meinel band). If this IR band was an extension of the continuum, the measurements of this emission would support atomic oxygen ions having an important role in the continuum process, whether they were produced by particle precipitation or enhanced through ion upflow. Furthermore, spectral measurements between the proton bands and the N_2 Meinel band deeper in the infrared would be helpful to confirm if the continuum emission truly extends all the way to over 1100 nm, or if the continuum emission and the enhanced IR Meinel band measurements coexist due to another reason during this particular event. As indicated in the discussion of Figure 5.3, the observed broad-band spectral enhancement may build up from contributions of many thermally excited species. Further work on spectral measurements in combination with emission modelling is required to fully reveal the contributions of different emitting species. Also careful examination of the heating and energy transition processes are needed to fully resolve which conditions are required for the continuum emission to appear and how wide of a wavelength region it can involve.

During the continuum event on 3 January 2020, the ESR measured the strongest ion heating above about 200 km and electron heating above about 250 km. Ion temperatures reached about 2500 K at 150–350 km heights during our continuum event, which is similar to the values that have been measured during the STEVE continuum (Archer et al., 2019b; Liang et al., 2019). The heating-induced emission that was proposed to explain STEVE emission is based on availability of vibrationally excited molecular nitrogen that produces NO, which further reacts with atomic oxygen to result in NO_2 and light (Harding et al., 2020). The brightness of the resulting NO_2 continuum was deemed sensitive to neutral heating and upwelling. In our case the upward ion drift is strongest above 150 km. The electron precipitation during the observed continuum emission occasionally reaches 150 km. This places both enhanced electron density and the upward moving ions in the height range typical for the red-dominated auroral emission. More detailed observations and modelling of this region is required to judge if the observed heating and upwelling can produce enough NO_2 continuum to explain the observed emission.

During the afternoon of 1 December 2023, when thin field-aligned continuum emissions were observed, the ESR measured particle precipitation and heating of the same order of magnitude as those seen during the continuum on 3 January 2020 in Figure 5.6 (electron temperatures up to about 3000–4000 K and ion temperatures up to about 2000 K at 300 km). However, no continuum emission was observed within the radar beam or in the vicinity. This may either suggest that an additional local heating mechanism is needed to produce the continuum, or that particle and Joule heating are required to reach down to at least 200 km altitude before sufficient atmospheric composition is available for the

production of the continuum emission.

A common driver for the two strong dayside continuum emission events as well as the afternoon continuum described in this study may be the high solar wind particle density during or before the event of continuum emissions. Kataoka et al. (2024) studied the storm on 1 December 2023, which had a moderate Dst but very intense red auroral emission seen at exceptionally low latitudes. They concluded that high solar wind density (pressure) drives the strongly red-dominated auroral emission by compression of the magnetopause. This intense red emission was observed in our continuum events as well. For our nighttime continuum event, the driver is less obvious. This event is also much less prominent than the dayside events. While large numbers of particles from the solar wind entering the magnetosphere–ionosphere system could indeed heat the upper atmosphere, the ionospheric and solar wind driving conditions for the events presented in this study are very different. Therefore, further research is required to resolve the necessary conditions to facilitate continuum emission.

5.5 Conclusions

We present the first observations of high-latitude dayside continuum emissions. The events, which were confirmed to be continuum emissions by spectral measurements, were seen at the polar cap boundary of the dayside auroral oval. We additionally presented visually identified continuum-like events across other MLT sectors. These events were classified as continuum based on the observed emission colour, which cannot be explained by any other known emission. All continuum (and alike) emission events shown in this study involve a range of different ionospheric conditions. For the one event for which ESR, FPI and DMSP data are available, we see enhanced temperatures in both electron, ion and neutral particle populations. These temperature increases suggest both precipitating particles and Joule heating to be present. We also identified a strong horizontal plasma flow shear in the region of the continuum emission, which may further contribute to the heating and upflow of ions and neutrals.

Our measurements reveal that a number of different emission lines and bands contribute to the broadband continuum emissions. Even emission structures in the near and far infrared were observed, which suggest multiple emitting species to be responsible for the observed spectral enhancements.

Resolving the exact spectral structure and chemical constituents of the continuum will require further investigations, involving both observations and modelling. Also, understanding the required ionospheric conditions for continuum emission will be examined in the future with more observational evidence.

Chapter 6

Hot N_2 mechanism for GHOST

Published in;

Dayton-Oxland. R, Ball, F., Whiter, D., Samaddar, S., Partamies, N., Barthemely, M., Herlingshaw, K. Karvinen, E. *GHOST aurora - continuum emission produced by hot* N_2, EGUsphere Preprint https://doi.org/10.5194/egusphere-2025-5317. 2026.

Abstract

We investigate the origin of the continuum emissions observed in the poleward dayside aurora discovered in Chapter 5, known as GHOST, and propose that they arise from highly excited, hot, neutral and ionised N_2. Using spectral modelling and fits to ground-based measurements of high-resolution GHOST spectra, we demonstrate that vibrationally and rotationally excited N_2 and N_2+ bands can reproduce the observed structured continuum without requiring emission from NO. Spectral fitting indicates that GHOST events coincide with extreme ion heating and high neutral temperatures. Background conditions from additional events indicate that strong ionospheric flows are typically present, which could help to provide the necessary energy input for producing hot neutral and ionised N_2. Proton aurora and EISCAT measurements indicate that two of our three events are located in the cusp. These results suggest that the combination of strong flow, heating, particle precipitation, and cusp conditions produce thermally excited N_2 populations which could account for the continuum-like spectrum of GHOST.

Author contribution statement

RD led the study, performed the preliminary spectral identification, and identified events. **RD** and FB jointly developed the main concepts of this study. **RD**, FB, SS, and NP wrote most of the manuscript. FB analysed the background conditions. DKW carried out the spectral fitting of HiTIES data, and assisted in developing the main concepts. SS performed the spectral modelling. NP identified events, analysed MISS spectra and all-sky images. MB investigated contributions from NO_2. KH and EK contributed to the discussion and development of the study. All authors contributed to the discussion, interpretation, and the preparation of the manuscript.

6.1 Introduction

While atmospheric continuum emissions have been known to the field of airglow for decades (Meinel, 1953; Sternberg and Ingham, 1972; Noll et al., 2024a), they had not been observed and studied in aurora and aurora-like emissions until the recent discoveries of STEVE (MacDonald et al., 2018), nightside continuum in the aurora (Spanswick et al., 2024a; Nanjo et al., 2024), and continuum structures in the poleward dayside (Partamies et al., 2025). In this study we call the continuum emission structures within dynamic aurora GHOSTs (backronym-ed as Geomagnetic High-bandwidth Optical Spectra from the Thermosphere) due to their pale, ghostly appearance, and to differentiate the particle precipitation related continuum from the plasma flow driven continuum, like STEVE. To be exact, continuum should only refer to a true continuum spectrum, like that produced by thermal blackbody radiation or Bremsstrahlung, a completely non-discrete mechanism. However, other studies in the airglow and aurora fields have referred to molecular pseudo-continuum as 'continuum', or used both interchangeably. All mentions of continuum here are addressing molecular pseudo-continuum.

Similar spectral properties and visually similar emission to STEVE observations were found within the dayside aurora over Svalbard, Arctic Norway in Chapter 5. The chapter described two dayside auroral

events where the dayside red emission was accompanied by white or pale pink continuum emission. These emission structures lasted for tens of minutes but, unlike the STEVE continuum, they followed the dynamics and the evolution of auroral structures. Spectral evidence from a co-located spectrograph was presented for the two dayside events. In addition, similarly coloured emission structures were reported in the afternoon and nightside aurora without simultaneously measured spectra. Along with the optical observations, the dayside continuum emissions in Chapter 5 were observed by the EISCAT incoherent scatter radar, Fabry-Perot Interferometer and an overpassing Defence Meteorological Satellite Program (DMSP) satellite. They provided evidence on enhanced plasma and neutral gas heating and upwelling, as well as a strong horizontal shear flow across the emission structure for one of the events. These parameters were deemed comparable to the heating and shear flow observed in connection with STEVE.

Independently, continuum emission was found within the dynamic nightside aurora over Rabbit Lake in Canada (Spanswick et al., 2024a). This study reported 30 continuum emission events captured by the Canadian Transition Region Explorer (TREx) RGB all-sky camera and meridian imaging spectrograph. The continuum emission conditions were quantified to be at least about 20 R/nm brightness level across the visible wavelength range. An integrated luminosity at 502–507 nm was used as an indicator for continuum emission, as it is a wavelength region where the ionosphere does not include strong auroral or airglow emission lines. The sizes of these emission structures ranged from 20 to 500 km with lifetimes of minutes and less. Compared to the dayside events the nightside continuum emission structures appeared more white/gray (or less pink) and more transient.

The largest continuum emission structures in Chapter 5 occurred within dayside aurora in sunlit ionosphere with shadow heights around 160 km. The auroral emission in those conditions is predominantly red with a purple hue, these colours are generally understood to be from atomic oxygen and molecular nitrogen emission. Dayside blue emission is primarily due to resonance scattering, in which upwelling of molecular nitrogen into the sunlit heights allows it to absorb and emit at its characteristic blue light at $428\mathrm{nm}$ (Shiokawa et al., 2019).

STEVE is driven primarily by Subauroral Ion Drift (SAID) events (MacDonald et al., 2018), with extreme ion drift velocity and electron temperature in the highest 5% and 3% compared with non-STEVE SAID events, corresponding to about 3 km/s and 4000–10000 K (Archer et al., 2019a). Similarly in GHOSTs, Partamies et al. (2025) report high cross-track shear velocity of 4 km/s in each direction from the DMSP satellite, and high ion (2500–3000 K) and electron (3000–4000 K) temperatures measured by EISCAT Svalbard radar.

Spectral studies of STEVE show an enhanced emission brightness across the entire optical range and slightly into the infra-red. Gillies et al. (2019) present TREx spectrograph data of a STEVE showing elevated continuum emission from 400–800 nm, supported by Liang et al. (2019). Even with the strongest auroral emission lines at 428, 558 and 630 nm subtracted, the total brightness of the continuum emission across the wavelength range gave twice as high values as the background sky.

Airglow continuum emissions have long been attributed to the nitric oxide mechanism

$$\mathrm{NO} + \mathrm{O} \rightarrow \mathrm{NO_2} + \mathrm{h}\nu \qquad \{1\}$$

(e.g. Meinel 1953). This same mechanism has also been considered for STEVE, initially suggested by Gillies et al. (2019), further developed in Harding et al. (2020); Mende et al. (2019); Mishin and Streltsov (2022); Nanjo et al. (2024), and recently disputed by Liang and Donovan (2024). The NO continuum mechanism has also been considered as a potential mechanism for GHOST emission (Chapter 5), who presented high-resolution (sub-Ångström resolution) spectra evidencing the continuum's molecular structure for the first time. Spanswick et al. (2024a) also considered NO to explain their observed continuum, which they use to rule out FeO and NiO as potential species. They further presented a comparison of the continuum emission brightness with expected $\mathrm{NO_2}$ brightness at discrete points. In conclusion they suggested that the $\mathrm{N_2}$ 1P, 2P and $\mathrm{N_2}+$ 1N bands may be embedded in the continuum spectrum.

All the previous studies have focused on the NO reaction because it does produce a pseudo-continuum emission, i.e. broadband emission which appears close to a true continuum, but contains discrete structure, indicating it is composed of many densely packed emission lines. However, the production of enough NO for the observed continuum brightness leads to challenges. In the case of STEVE, Harding et al. (2020) presented two NO production pathways;

$$\mathrm{N_2[A^3\Sigma_u^+] + O \rightarrow NO + N(^2D)} \quad \{2\}$$

$$\mathrm{N_2[X^1\Sigma_g^+(v > 11)] + O \rightarrow NO + N} \quad \{3\}$$

where v is the quantum vibrational number. Reaction 2 requires $\mathrm{N_2}$ in the upper state of the Vegard-Kaplan band system (A), requiring energies $> 6\mathrm{eV}$, while Reaction 3 requires ground state $\mathrm{N_2}$ with vibrational level higher than 11, which has a lower energy requirement of $3\mathrm{eV}$, and so was considered more likely.

Liang and Donovan (2024) calculated the vibrational excitation of $\mathrm{N_2}$ molecules by collision with drifting ions, specifically the vibrational-translational energy transfer. Under typical SAID conditions, the resulting density of $\mathrm{N_2^*}$ was found to be too low to produce enough NO to explain the observed STEVE brightness. Within the airglow community, the NO mechanism has been questioned by Bates (1993) and Evans et al. (2010), who have pointed out discrepancies between the proposed chemistry and the observed spectra, suggesting that the spectrum results from metastable oxygen and FeO respectively.

NO requires high energy to produce and is strongly reactive. The problems with the NO mechanism suggest that an alternative continuum producing mechanism is possible. In this work we will argue that sufficiently heated $\mathrm{N_2}$ itself is capable of producing (pseudo-)continuum emissions which explain the observed spectra well.

6.2 Instrumentation and data

We use full-colour all-sky camera (ASC) data from Kjell Henriksen Observatory (KHO, 78.25°N, 16.04°E, Herlingshaw et al. (2024b)) on Svalbard in arctic Norway for identifying GHOST events. This ASC is a Sony α7s mirrorless DSLR, which has been in operation since late 2015. The raw data has a pixel resolution of 2832×2832. Nighttime images with 4-second exposure time have been taken at a cadence of 12 seconds throughout the winter seasons, which on Svalbard extend from the beginning of November until the end of February. Images are captured when the Sun is below the horizon. The continuum emission in these images looks white, pale pink or orange, none of which matches the normal auroral emissions of green, red and blue light. For context, an animation of GHOST evolution for each event is provided in the supplementary material.

We acknowledge that white or gray colour in full-colour images can be caused by overlapping green and red emission along the same line-of-sight. We therefore collect spectra from a co-located Meridian Imaging Svalbard Spectrograph (MISS) to confirm our GHOST observations. MISS images a meridian slit (approx. 1 degree wide) to provide spectral information from 400 to 700 nm with a resolution of about 5 nm until late 2024, and 1.5 nm since then. A full spectrum was recorded every minute until late 2024, and every 15 seconds since then.

The High Throughput Imaging Echelle Spectrograph (HiTIES, Chakrabarti et al. 2001) is used to obtain high-resolution spectra of the GHOST emissions, see Chapter 3. It uses the 3-panel mosaic filter, selecting Hα, O+, and $\mathrm{OH^*}$ emissions in the red.

The EISCAT Svalbard Radar (ESR, Wannberg et al. 1997a) provides ionospheric plasma measurements and is approximately co-located with KHO. We use the ESR run presented in Partamies et al. (2025), but present analysis of the data from the 32m steerable dish instead of the field-aligned one. At the time of the GHOST appearance, the steerable ESR dish was pointed poleward at an elevation of 30 degrees.

We also use Super Dual Auroral Radar Network (SuperDARN, Greenwald et al. 1995) measurements to look at the background ionospheric convection, location of the cusp and convection cells with respect to the locations of the GHOSTs.

Finally, Interplanetary Magnetic Field (IMF) measurements are taken from the OMNIWeb (King and Papitashvili, 2005), which provides data from multiple satellites propagated to the bow shock.

6.3 Events

6.3.1 Event 1: 3 January 2020, bright large GHOST

The first event studied here is the spectrally confirmed continuum emission event which filled the zenith from 08:30 to 09:30 UT on the 3rd January 2020, presented in Chapter 5. During this rather long time, GHOST structures were seen to appear and disappear in the ASC field of view, and temporally and structurally evolve and follow the red emission caused by auroral precipitation in the cusp. During this GHOST evolution, the ionosphere was sunlit above about 160 km, which led the red emission to be accompanied by blue resonance scattering.

6.3.2 Event 2: 28 February 2020, thin isolated GHOST

The second event is an arc-like GHOST identified in ASC images and confirmed by spectral measurements from MISS. This event occurred as an isolated individual continuum structure that persisted about 15 minutes at 03:05–03:20 UT. Unlike other high latitude GHOSTs, this structure occurred in vicinity of primarily green aurora and a few hours earlier in the magnetic morning (before cusp) compared to the GHOST Event 1. The spectral measurements of this event show an increasing continuum brightness towards longer wavelengths (bottom left panel in Figure 6.1). The ionospheric shadow height during this event was about 170 km.

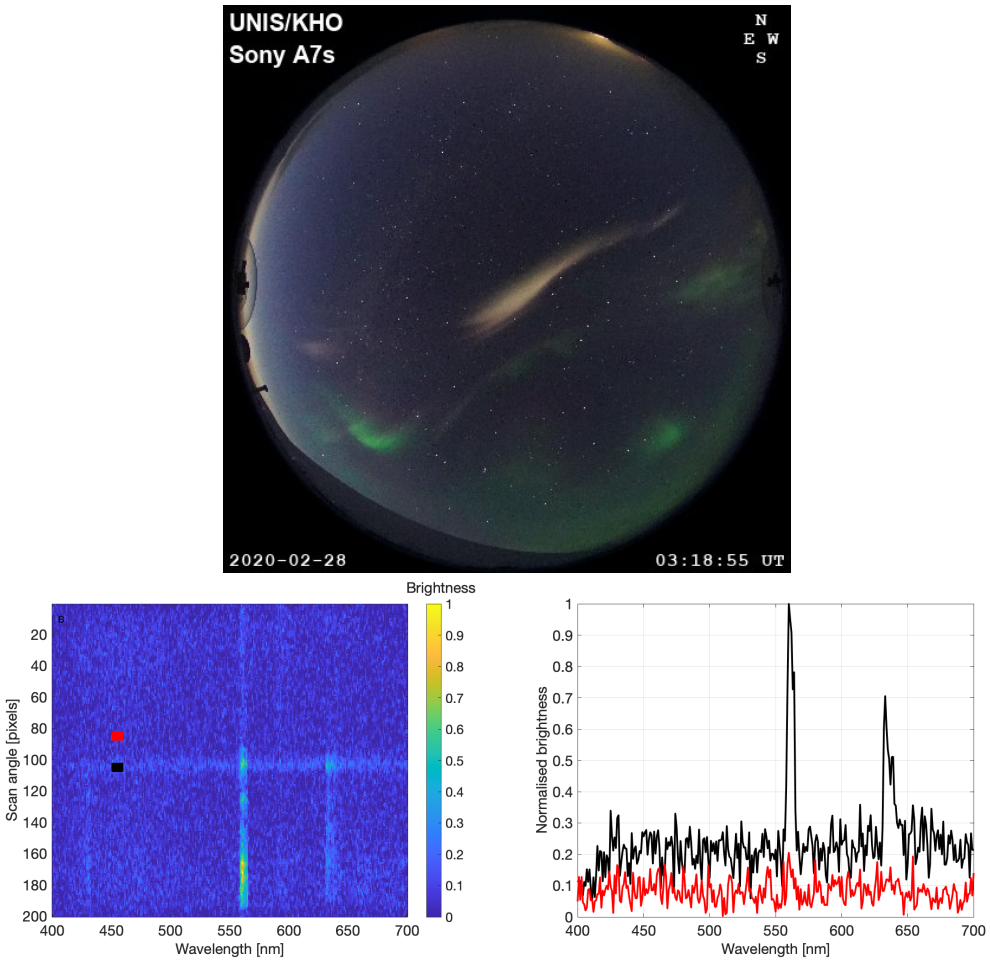

Figure 6.1: GHOST in all-sky image (top) encircled by a gray oval, simultaneous spectrogram along the meridian slice of the image (bottom left) and spectra at the meridian location of the continuum emission (black) as well as an empty sky (red) north of continuum (bottom right).

6.3.3 Event 3: 30 December 2021, GHOST conditions

The last event was first identified from the presence of bursty proton aurora, shown in Figure 6.2, and was confirmed by all-sky images and HiTIES spectra. Sparse patches of white GHOST visually appear in ASC images from 09:12 to 09:33 UT against a typical cusp sky, and HiTIES spectra measure sparse, fairly dim continuum from 09:22 to 09:50 UT. None of the GHOST structures were seen in the meridian line for long enough to be captured by MISS. The visual occurrences in the ASC images off the meridian line had the same colour as the GHOSTs seen in Events 1 and 2, as shown by the example images in Figure 6.3. Based on these images and the HiTIES measurements shown in Figure 6.4, this event clearly has the correct conditions for GHOST emissions to appear, but it is missing some factor to produce the large GHOST event at the zenith, such as in Event 1. The high resolution spectra of NO_2, for example as shown in Smalley et al. (1975) at very low temperatures, does not show any clear coincidence with the Hα HITIES spectra shown in Figure 6.4, or compared with previous high-resolution spectra of GHOST reported in Chapter 5.

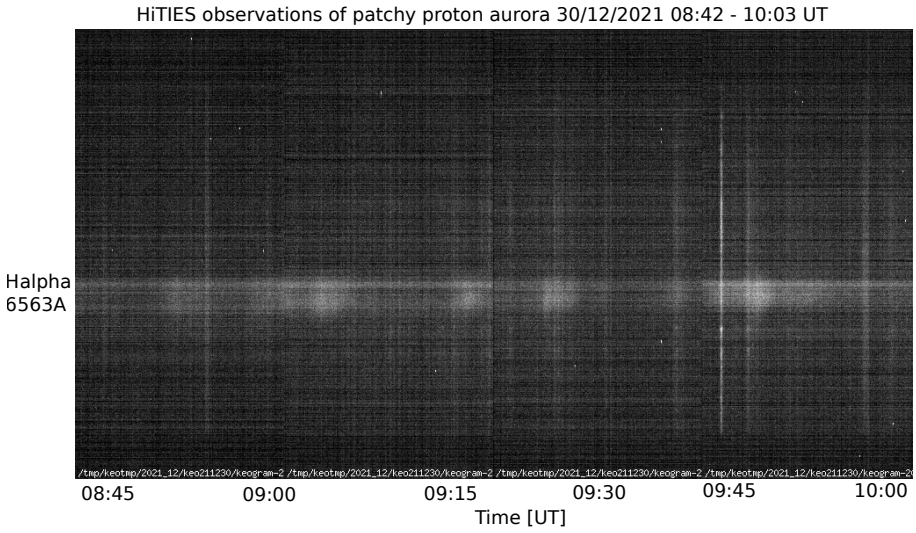

Figure 6.2: Keogram of HiTIES observations of proton aurora from 08:42 to 10:03 UT on 30/12/2021 during GHOST event 3. Bursts of proton aurora appear as broad bright blobs, blue-shifted from the Hα wavelength at 08:50, 09:00, 09:17, 09:28, and 09:47 UT

Figure 6.3: ASC images of the GHOST structures towards the west horizon during Event 3 taken at 09:15:30, 09:22:50 and 09:24:01 UT. The regions of continuum emission are marked by the gray ovals.

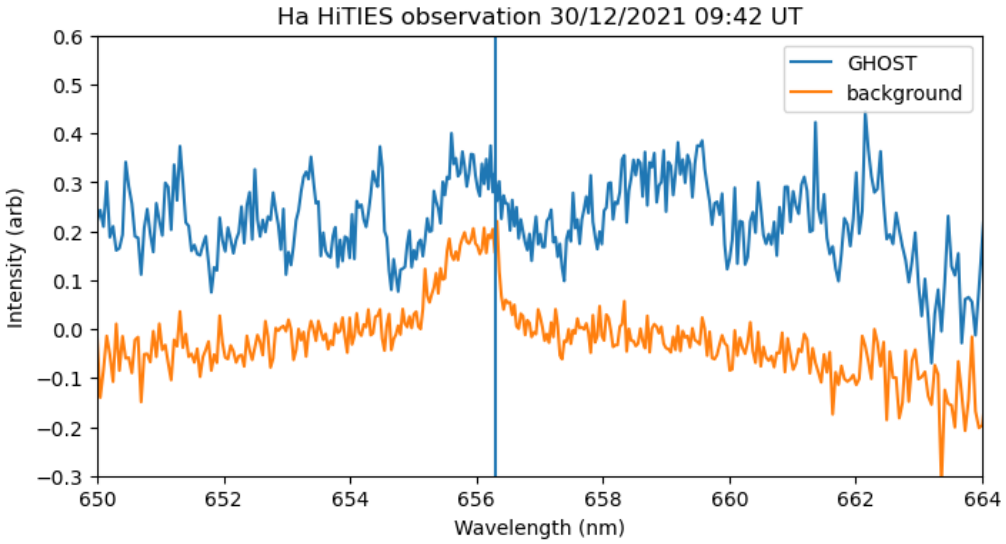

Figure 6.4: Spectrum showing GHOST-like emission (blue) against a background spectrum (orange) in HiTIES on 30/12/2021 taken at 09:42 UT. The Hα rest wavelength at 656.3nm is marked with a blue vertical line, and proton aurora is visible in both the GHOST and background spectra.

6.4 Spectral modelling

In order to investigate the origin of the continuum spectrum, we model synthetic spectra of various species known to be abundant in the polar atmosphere with emission within our measured spectral range, N_2, N_2^+, O_2^+, and O^+ auroral emission and OH^* airglow. We model only the shape of the emission spectrum for each species based on temperature, and do not model precipitating flux or specific atmospheric conditions.

The spectral fit uses emissions from excited states of N_2 and ionization states of N_2^+, containing several key vibrational bands, that emit photons in the optical range. The emissions from excited states of N_2 used in this study are the First Positive band (N_2 (1P), decay from the excited electronic $B^3\Pi_g$ to $A^3\Sigma_u^+$ states, Naudé (1931)), Infra-red Afterglow (IRA, emissions from $B'^3\Sigma_u^-$ to $B^3\Pi_g$ states, Carroll and Sayers (1953),Carroll and Rubalcava (1959)), and Vegard-Kaplan (VK) band emissions (from excited ($A^3\Sigma_u^+$ state to ground state $X^1\Sigma_g^+$ of N_2, Vegard (1930), Kaplan (1934)). Meinel band emissions from excited $A^2\Pi_u$ to ground $X^2\Sigma_g^+$ state of N_2^+ ion (Meinel, 1950), and the O_2^+ First Negative (1N, $b^4\Sigma_g^-$–$a^4\Pi_u$) band system are also included in the synthetic spectra.

The total energy of N_2 molecule is the sum of its electronic (T_e), vibrational (G_v) and rotational (F) energies. The synthetic spectra of the four aforementioned emissions were constructed after substantial literature review of the latest available vibrational and rotational constants. For each electronic state, the model includes vibrational levels from 0 to 22. The model includes their vibrational $G(v)$, and rotational $B(v)$ and $D(v)$ (Laher and Gilmore (1991)) constants given by fitting of the following standard polynomials. The vibrational energy level is obtained from the coefficients of the polynomial fit given by Equation 6.1

$$G(v) = w_e\left(v+\frac{1}{2}\right) - w_e x_e\left(v+\frac{1}{2}\right)^2 + w_e y_e\left(v+\frac{1}{2}\right)^3 + w_e z_e\left(v+\frac{1}{2}\right)^4 \quad (6.1)$$

The other two constants of rotational-vibrational interactions are obtained similarly from Equations 6.2 and 6.3

$$B(v) = B_e - \alpha_e\left(v+\frac{1}{2}\right) + \gamma_e\left(v+\frac{1}{2}\right)^2 \quad (6.2)$$

$$D(v) = D_e + \beta_e \left(v + \frac{1}{2}\right) + ... \tag{6.3}$$

The empirically defined constants w_e,$w_e x_e$,$w_e y_e$,$w_e z_e$, α_e,γ_e, D_e,β_e, etc. of the polynomial fits in Equations 6.1, 6.2, 6.3 are primarily obtained from the NIST database (Huber and Herzberg, 2025).

The vibrational and rotational constants are then used to obtain the rotational levels for each vibrational band. The rotational energy for each level J is obtained from the above constants from Equation 6.4

$$F_v(J) = B_v J(J+1) - D_v[J\,(J+1)]^2 \tag{6.4}$$

The level J is the total angular momentum and is associated with a particular electronic and vibrational motion of the molecule. For each electronic transition, there are several 'branches' (from upper J' to lower J'' levels), for example, the ${}^{P}Q$,${}^{P}P$,${}^{R}R$ and the ${}^{R}Q$ branches of the VK band (Herzberg, 2013; Yonker, 2005), which can be observed in the emission spectra. Theoretically, these rotational branches can be evaluated from quantum mechanical selection rules. The model uses these selection rules to derive the rotational transitions from the upper to the lower J levels. The rotational branches of the Meinel band calculated here are in agreement with the extensive study of Benesch et al. (1980) and the recent Zhang et al. (2015). The rotational structure of N_2 (1P) have been previously modelled by Jokiaho (2009). The selection rules for the rotational branches of the IRA are similar to those of N_2 (1P), since both are ${}^3\Sigma - {}^3\Pi$ transitions and are compiled from Herzberg (2013) and Carroll and Rubalcava (1960).

The intensities of each emission line are given by the theoretical relation based on the r-centered approximation (Nicholls and Stewart, 1962; Laher and Gilmore, 1991) as shown in Equation 6.5.

$$I_{v'v''J'J''} = \frac{64\pi^4\lambda^4 N_{v'} c}{3Q_r}\phi|\mathbf{R_e}(\overline{r}_{v'v''})|^2 q_{v'v''}\zeta_{J'J''} exp\left\{-\left(F_v(J') + G(v')\right)\frac{hc}{kT}\right\} \tag{6.5}$$

where, h is Planck's constant, c is the speed of light, k is Boltzmann's constant, and T is the temperature. The $F_{v'}(J')$ and $G(v')$ are calculated from Equations 6.4 and 6.1 respectively. Q_r is the rotational partition function and is equal to $1 + 3e^{-2B_v hc/kT} + 5e^{-2B_v hc/kT} + ...$ For sufficiently large T or small B_v, Q_r can be approximated by $\frac{kT}{hcB_v}$ (Herzberg, 2013).

The intensity of radiated emission by a population density of $N_{v'}$ in the upper vibrational level v' can be related to the expected value of the electronic transition moment at the r-centroid $|\mathbf{R_e}(\overline{r}_{v'v''})|$ and the Franck-Condon factor, $q_{v'v''}$ which is the overlap integral, indicating the strength of vibrational transition (Gilmore et al., 1992). These values are obtained from Gilmore et al. (1992), which tabulate the above values for 22 vibrational levels of all four emissions studied here. Similarly, the Hönl-London factors, $\zeta_{J'J''}$ in Equation 6.5 determine the relative likelihood of the transition from the upper J' to the lower J'' rotational branches within a vibrational band of emission. In this study, the Hönl-London factors are obtained from Schadee (1964).

Finally, ϕ is the statistical weight which is $\frac{2}{3}$ for odd J' and $\frac{1}{3}$ for even J' for N_2 (Yonker, 2005).

There are a large number of free variables involved in the fitting, consisting of the intensity and rotational temperature of the OH, $N_2$1P, N_2IRA, N_2VK, N_2^+ M and O_2^+ 1N band systems, as well as the intensity of the O^+ $(^2D - -^2P)$ doublet and ratio of populations in the $J = 1/2$ and $J = 3/2$ levels of the ^2P upper state. To avoid making any assumptions about the vibrational distribution of GHOST emitting species, the populations of the upper vibrational levels of each molecule are independent free parameters. To reduce the number of free parameters, it is assumed that all N_2 bands have the same rotational temperature, and the N_2^+ and O_2^+ bands also have the same rotational temperature (but this can be different to the neutral N_2 rotational temperature).

The synthetic spectrum is fit to the data by minimising the root-mean-square (RMS) of the residuals between the two. Since there are many free parameters, there are many local minima in the parameter space, and so a gradient descent or similar algorithm is unlikely to find the global minimum (i.e. best fit). We therefore use a simulated annealing technique, first outlined in Kirkpatrick et al. (1983), which can escape local minima to find the global minimum, but is time and computing intensive. This method is an iterative process. In each iteration, a random neighbouring state to the current state (i.e. similar set of parameter values) is selected and tested against the data. This new state is accepted if it provides an improved fit to the data, but can also be accepted if it provides a worse fit, according to a parameter

called the annealing temperature, enabling the escape from local minima. The probability of accepting a worse state is initially high, but reduces with each iteration as the annealing temperature is reduced (system "cools"). The process ends either when no new state is accepted for 90 iterations or when a total of 3000 iterations (accepted or not) has been reached. The whole process is repeated 3 times, and the state with the lowest RMS from the full set of up to 9000 iterations is then chosen as the best fit to the data. This method was first used to fit synthetic spectra to HiTIES data by Price (2021).

6.5 Results

Spectral fitting of the HiTIES data shows the breakdown of different components of the spectrum, for different types of aurora observed on 03 Jan 2020, close to the GHOST event.

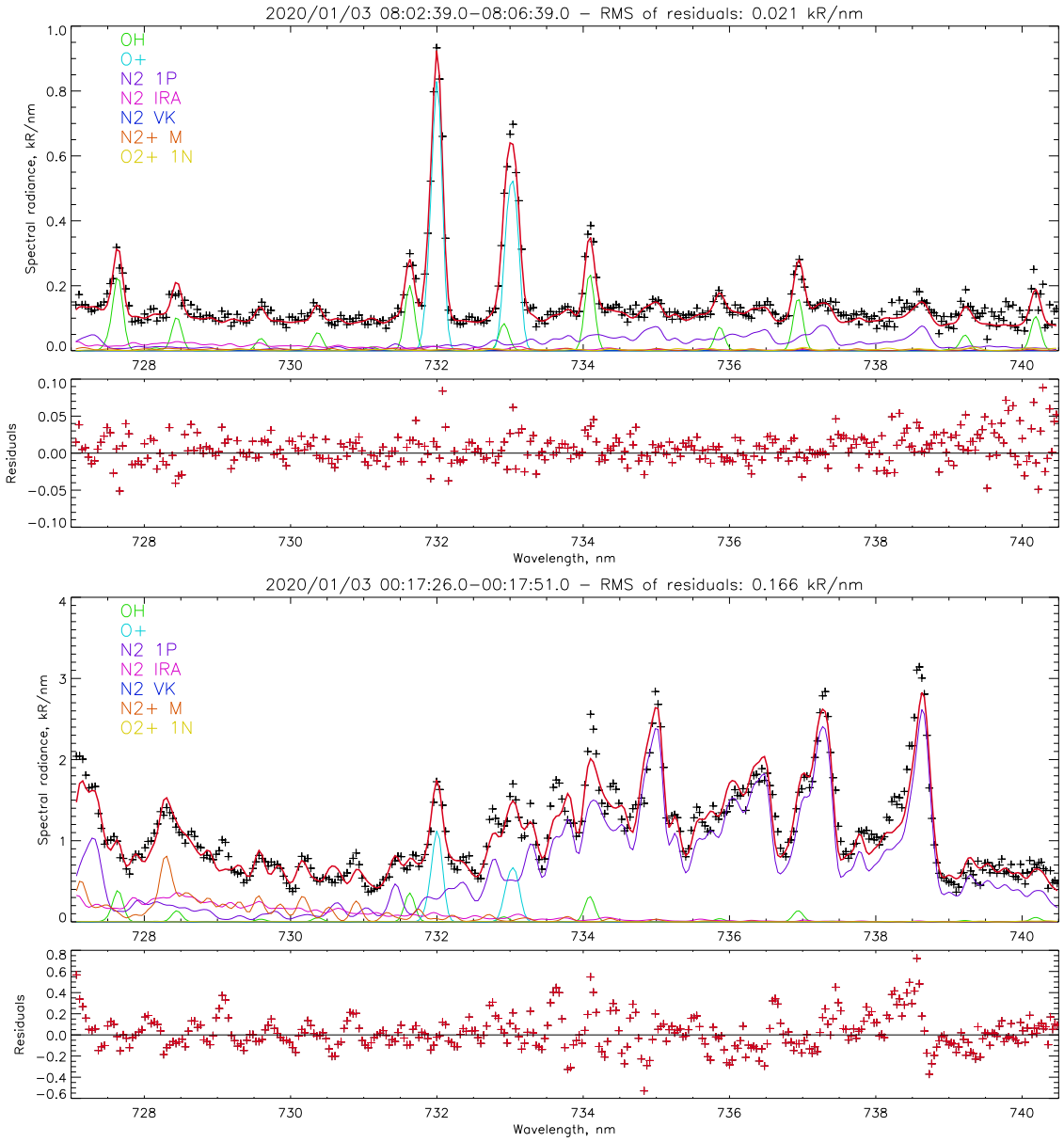

Figure 6.5: HiTIES spectrum of low-energy precipitation (top) on 03 Jan 2020 at 08:02 UT, and high-energy precipitation at 00:17 UT (bottom) deconstructed into its spectral components; OH (green), O^+ (cyan), N_2 1p (purple), N_2 IRA magenta), N_2 VK (blue), N_2^+ M (red) and O_2^+ 1N (yellow). Residuals plotted below.

First, low energy precipitation from 08:02 UT is shown in Figure 6.5 (top). The spectral modelling shows typical auroral conditions on Svalbard, where the $O^{+2}D{-}^{2}P$ doublets are dominant. These are produced in the F-region by low energy precipitation. OH airglow and a small amount of N_2 1P are also visible here. High-energy precipitation is shown in Figure 6.5 (bottom). The fitting shows a typical high-energy spectrum, with N_2 1P being the dominant component. These results give a baseline of what is typically expected during 'normal' aurora.

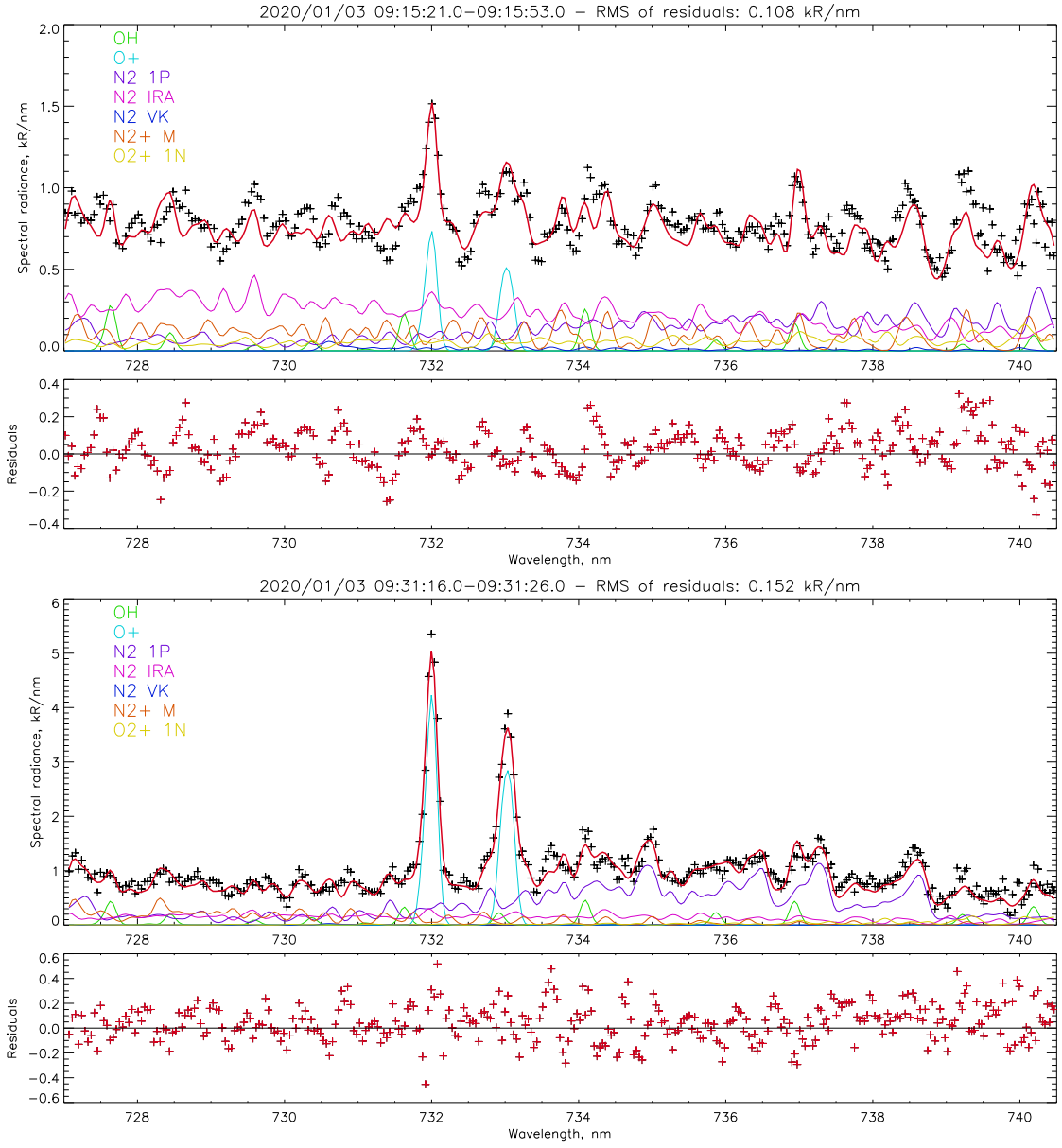

Figure 6.6: HiTIES spectrum of GHOST continuum (top) and low-energy precipitation with possible continuum contribution (bottom), deconstructed into its spectral components; OH (green), O^+ (cyan), N_2 1p (purple), N_2 IRA magenta), N_2 VK (blue), N_2^+ M (red) and O_2^+ 1n (yellow). Residuals plotted below.

Next, we present the results of fitting the confirmed continuum GHOST spectrum in Figure 6.6 (top). There is still O^+ and N_2 1P, but the N_2 IRA band system is significantly enhanced. The N_2^+ Meinel and O_2^+ first negative are also enhanced as compared to the N_2 1P. N_2^+ M seems to be especially important for the shape of the spectrum. Although N_2 IRA is normally weak, it does have vibrational bands through much of the visible and near infrared, at least above ~ 520 nm, and N_2^+ M could also

cover the whole visible range if there is enough population in the high vibrational levels. The fitting of N_2 and N_2^+ explains the full brightness of the continuum without any indication of the presence of NO.

Besides the enhanced N_2 IRA in the continuum, another key difference to normal aurora is the rotational temperature. In the normal nightside high energy aurora the N_2 temperature was found to be 278 K, and the ion temperature (N_2^+ and O_2^+ rotational) came out at 162 K. This value has a high uncertainty due to the emission being relatively weak, but it nonetheless gives a good magnitude estimate. In contrast, the continuum gave an N_2 rotational temperature of 881 K and an ion temperature of 2927 K, consistent with EISCAT ion temperature measurements above 150 km presented in Chapter 5.

Close to the continuum event, some 'normal' N_2 aurora was fitted, as shown in Figure 6.6 (bottom). In this spectrum, though N_2 1P is dominant, there is an increased contribution from N_2 IRA and N_2^+ M. This could be continuum-like emission, representing the 'missing link' between normal aurora and GHOST. It could result from temperatures in between the typical values and the extreme heating found in GHOST events.

These results indicate that the continuum emission is linked to strong heating. As 881 K is not that unusual in the cusp thermosphere (Skjæveland et al., 2017), it alone is therefore unlikely to be enough to thermally excite the N_2 IRA (or we would expect it to be detected regularly). Assuming the GHOST emission peaks in the E-region, we are seeing an extreme temperature for this altitude, consistent with the extreme heating associated with GHOST, measured in Partamies et al. (2025). The high rotational temperatures generally flatten all band systems, which would make the spectrum more continuum-like at all wavelengths. Strong heating in the thermosphere leads to expansion and upwelling of the atmosphere which can potentially increase drag on satellites, shortening mission lifetimes - this has been measured occurring frequently in the cusp measured by the CHAMP satellite, see Skjæveland et al. (2017); Lühr et al. (2004).

There is some structure visible in the residuals of Figure 6.5 (bottom) and both fits from Figure 6.6. This indicates that some of the components of the spectrum are not being well fitted — this could be due to a single temperature being assumed, whereas in reality the spectrum is made up of the entire integrated line-of-sight column and would thus contain multiple temperatures affecting the shape of the rotational spectrum for the N_2, N_2^+, and O_2^+ species.

6.6 Background conditions

We also consider the global magnetospheric conditions during the GHOST events in order to begin to identify any possible background conditions needed for GHOSTs to occur. GHOSTs have been observed at various magnetic local times (MLT), see Chapter 5. In this chapter, the first and third events occur in the dawn–noon sector (9-12 MLT), and the second event occurs in the midnight–dawn sector (3-6 MLT). The IMF conditions for all three events can be found in Figure 6.7 and are discussed with the event descriptions below. Global ionospheric plasma convection patterns from the SuperDARN radar network can be found in Figure 6.8. The figure includes one convection map for each of our three GHOST events with vectors colour-coded by the flow velocity. Due to radar distribution, there is minimal scatter and therefore minimal data available above Svalbard, however convection maps are still presented in order for discussion of the polar cap equipotential cells and global convection behaviour during the GHOST events.

6.6.1 03/01/2020

During Event 1, the ESR 32 metres dish was operating with an elevation of 30° pointed north. This enabled ESR to capture pulsed ionospheric flows (PIFs) (also sometimes referred to in literature as poleward moving radar auroral forms) which themselves are the ionospheric signatures of energetic flux transfer events (FTEs) at the dayside magnetopause, evidencing reconnection (Goertz et al., 1985). These are seen in Figure 6.9 as ion velocity enhancements appearing at ∼350 km and moving further in range in the radar beam at about 08:30, 09:00, 09:30, 09:45 UT. This would place the GHOST event from 8:30-9:30 UT firmly in the cusp ionosphere.

Chapter 5 also reported observation of patchy or pulsing proton aurora during this Event 1. Previous work on patchy proton events on Svalbard has concluded that they are evidence of flux transfer due

to reconnection (Moen et al., 1998; Deehr and Lummerzheim, 2001), which also locates this event within the cusp. It is further interesting to note that the IMF is mostly Bz-negative throughout the observation interval, an IMF orientation which leads to the most energetic reconnection and therefore most energetic precipitation into the cusp ionosphere.

Supplementary material of this event includes a video in which the GHOST is seen flowing eastwards. This eastwards flow is consistent with cusp flow in the dominant negative By regime (Burch et al., 1985; Lockwood et al., 1989), which is consistent with IMF conditions in Figure 6.7. Dominant By conditions are also visible in the modelled equipotential polar cap cells in Figure 6.8, which would place the convection throat over Svalbard.

Finally, we note that this is the brightest and largest of the three GHOST events studied, suggesting that the prevailing conditions were especially favourable.

6.6.2 28/02/2020

The morning sector GHOST on the 28/02/2020 occurs at about 03 UT (about 06 MLT), and we do not see any patchy protons or other reconnection signatures at that MLT, as expected as we are not in the cusp. However, similar to the previous event, referring to the middle panel in Figure 6.7 the event takes place during a period of dominant By with negative Bz. It is interesting to note that there appears to be stronger ionospheric return flows in SuperDARN (Figure 6.8) than cross polar-cap flows at this time. With the expected polar cap asymmetry under dominant By conditions as outlined in Cowley and Lockwood (1992), and judging by the contour lines of the equipotential polar cap cells as seen in the middle panel of Figure 6.8, it is possible that Svalbard is located underneath a similar strong return flow. In supplementary material provided, the GHOST in event 2 is seen flowing eastwards, this would be consistent with a strong return flow over Svalbard, however without SuperDARN radar backscatter it is hard to say that this is the cause of GHOST flow direction. It is noted that Event 2 is thinner compared to its Event 1 counterpart.

6.6.3 30/12/2021

Event 3, like event 1, takes place in the sunlit dayside ionosphere. Also similar to event 1, there are patchy proton aurora during the 30/12/2021 event visible in Figure 6.2, consistent with cusp conditions and energetic dayside reconnection. Referring to the bottom panel of Figure 6.7, like Events 1 and 2, Bz was negative throughout the event, but unlike event 1 the By component was not dominant throughout. Again, there is no backscatter from SuperDARN radars near Svalbard, as seen in Figure 6.8, for this event. The convection map shows cross-polar cap flow originating from dayside reconnection, but unlike in Event 1, there does not appear to be strong dominant By influence on the polar cap convection cells. Indeed, looking at Figure 6.7, By is only slightly dominant for the period of time prior to the GHOST observation and is not dominant during the observation period of the GHOST from 9:12 - 9:33 UT.

From the supplementary material, the GHOST is seen flowing westwards. It is interesting to note the By is opposite polarity from Event 1, which would be consistent with opposite-direction flow. The GHOST is noted to be thin and off-zenith.

6.6.4 Summary of Background Conditions

Examining the background conditions from across the three events presented in this work, a certain number of factors can be identified as possibly having an effect on the appearance of the GHOST. These factors across the events, as well as the type of GHOST observed, are presented in Table 6.1

Event	Type of GHOST	GHOST Flow Direction	By Polarity	By Dominance?	Bz	Cusp	Energetic Dayside Reconnection	Sunlit
03/01/2020	Fat	East	-ve	Yes	-ve	Yes	Yes	Yes
28/02/2020	Thin	East	-ve	Yes	-ve	No	N/A	No
30/12/2021	Thin (off-zenith)	West	+ve	No	-ve	Yes	Yes	Yes

Table 6.1: Summary of GHOST events presented in this paper and their associated background conditions.

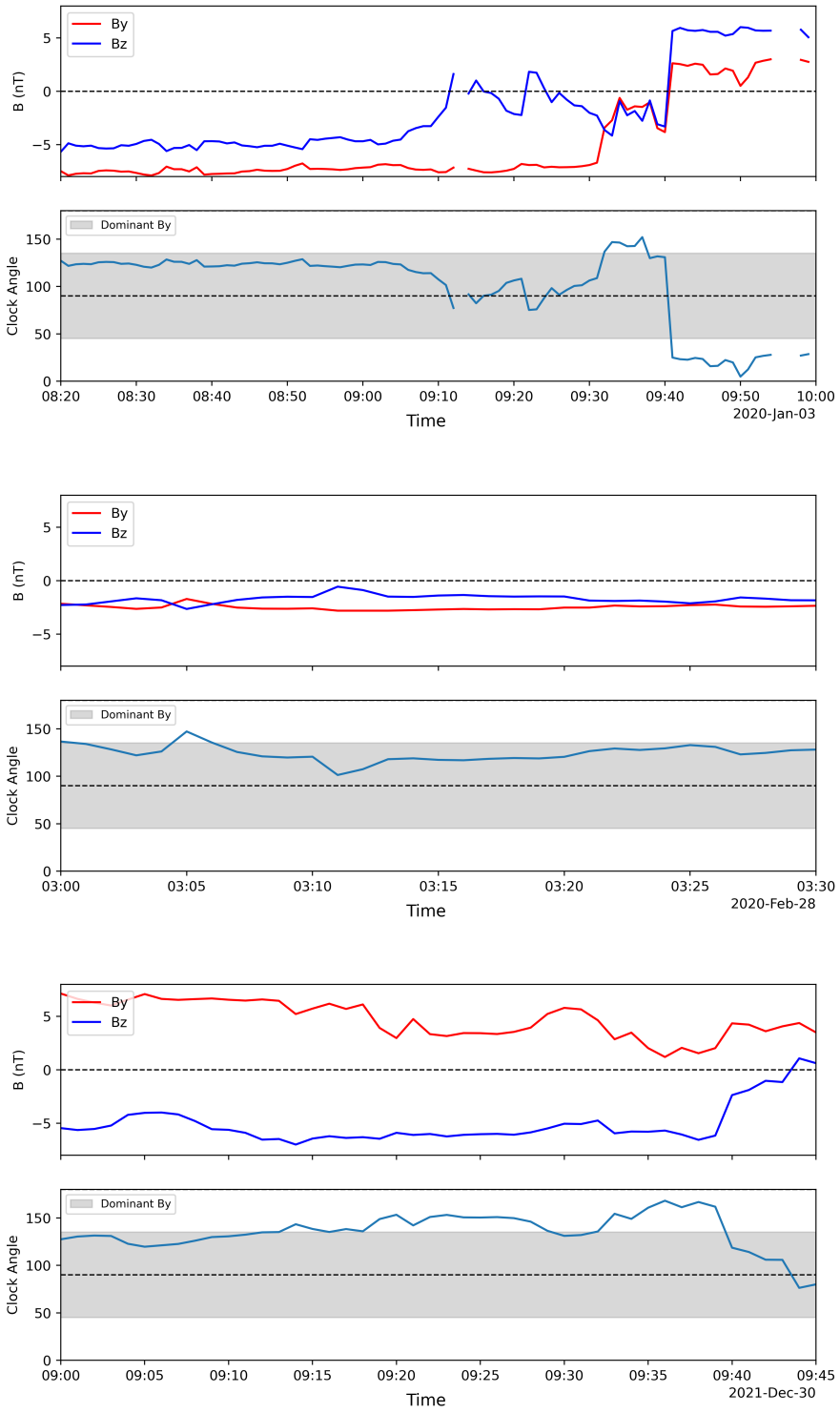

Figure 6.7: IMF conditions on the 03 Jan 2020 (top), 28 Feb 2020 (middle), and 30 Dec 2021 (bottom), showing IMF Bz, By, clock angle, and the associated clock angle region where By is dominant. By dominance is defined as the range of clock angles of the solar wind with angles between 45 and 135°.

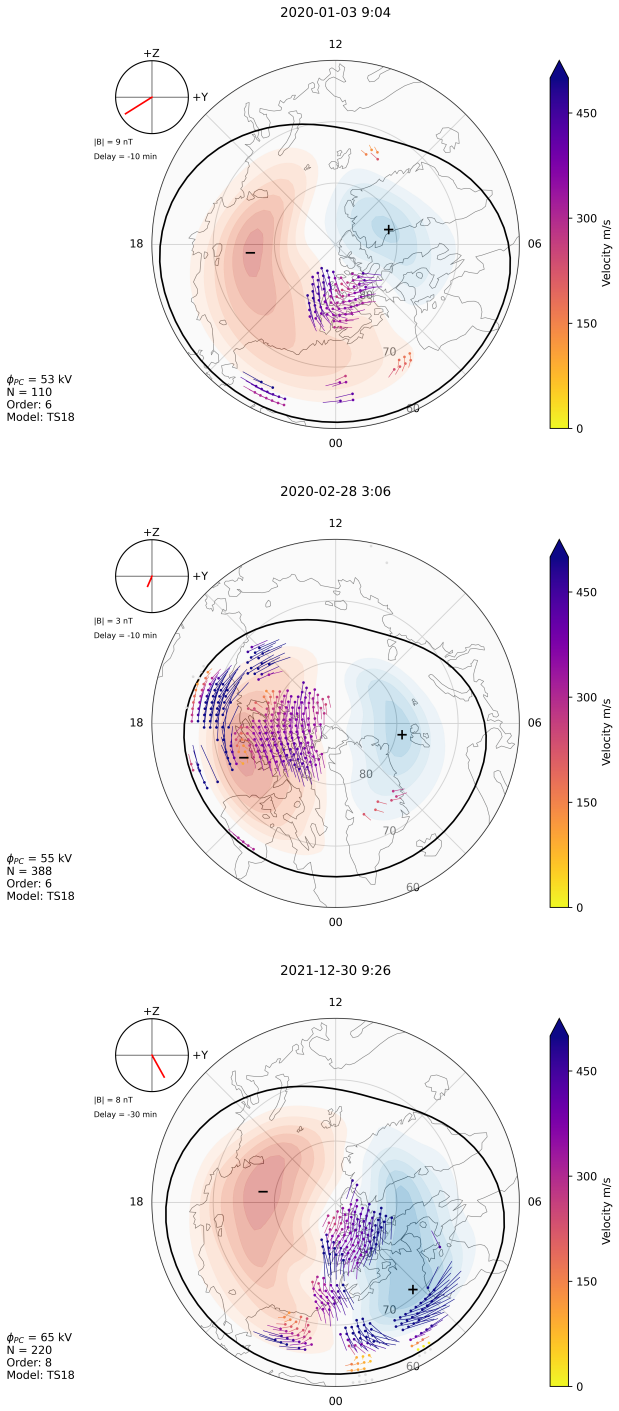

Figure 6.8: SuperDARN global polar cap convection map data from times during the GHOST events on 03 Jan 2020 (top) and 21 Feb 2020 (middle) and 30 Dec 2021 (bottom). Flow velocity vectors are shown by ball and stick plots with colour maps. Equipotential polar cap cells are blue (negative) and red (positive). The Heppner-Maynard boundary representing the equatorward edge of the ionospheric convection pattern is shown in black.

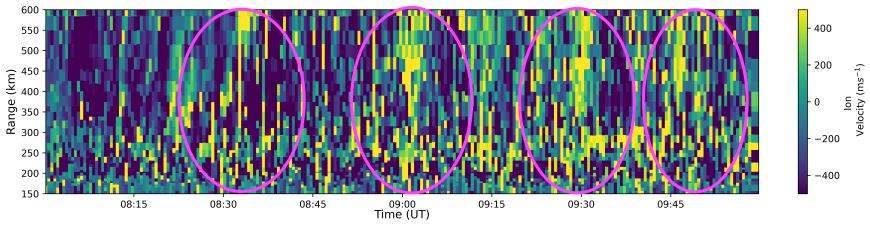

Figure 6.9: ESR 32m data at 30 degree elevation (pointed poleward) from 08:00-10:00 UT on 03/01/2020. PIF signatures are identified (circled in pink) in the ion drift velocity as slanted increases in the ion velocity moving further in range (and thus poleward) with time.

6.7 Proposed mechanism

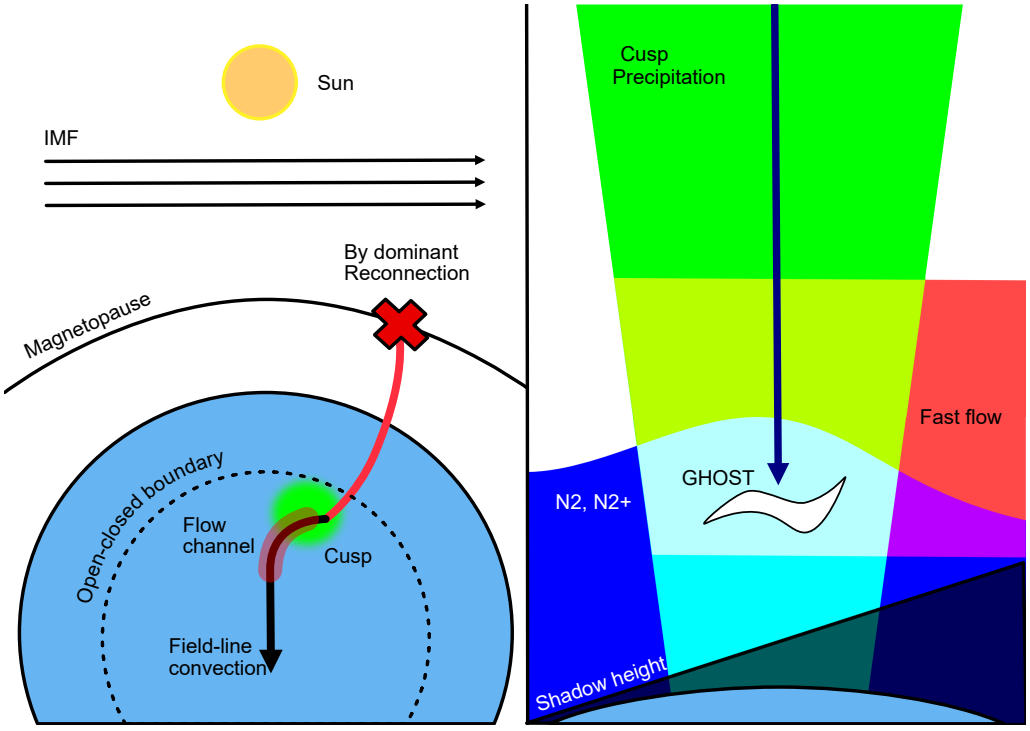

Figure 6.10: Cartoon of proposed continuum mechanism showing how the background conditions evidenced could combine to produce GHOST conditions. The left panel (view from above into the polar region) shows how the solar wind conditions result in flow channels close to local noon. The right panel (view from the dusk side into the vertical cross-section of the cusp ionosphere) shows how the cusp location, flow channel, and upwelling of N_2 combine, each contributing to prime the ionosphere to produce GHOST emissions.

We propose that the GHOST continuum emission requires an ionosphere that is primed with upwelling, heating, and rotational and vibrational excitation of N_2, N_2^+ and O_2^+. When precipitation collides with this primed ionosphere, pseudo-continuum made up of the higher electric excitation states of N_2, N_2^+ and O_2^+ is emitted. Figure 6.10 shows a cartoon of the combination of background conditions observed, as discussed here.

The cusp regions are important to this priming due to the steady input of the low energy electrons, which can efficiently heat the ionosphere. The largest known GHOST events, such as Event 1 in this study and another dayside event reported in Chapter 5, occurred co-located and simultaneously with cusp signatures such as patchy proton events, poleward moving auroral forms, and FTE signatures. As the cusps heat the dayside ionosphere with the low-energy electron precipitation, it causes upwelling of molecular ionospheric species to altitudes higher than the shadow height.

The cusp region GHOST occurrences also place the GHOST processes in the sunlit ionosphere, which is seen as an enhanced glow of the blue emission from molecular nitrogen ions, the resonance scattering. Above the shadow height, sunlight contributes to the ionisation of the upwelled species. Particularly the abundance of N_2^+ tends to peak around the height of about 160 km, because below that the lifetime of this ion sharply decreases (Hunten, 2003). The sunlit ionosphere therefore together with the upwelling has been deemed as an important ingredient for the GHOST background conditions.

The known large and persistent GHOST events take place during By dominant, southward IMF. This is true for the Events 1 and 2 in this study, as well as for another dayside event discussed in Partamies et al. (2025) (~06 UT on 11 February 2024). Under By-dominant IMF conditions the cusp will either be dawnward (as depicted in Figure 6.10) or duskward of noon. After reconnecting, field-lines must therefore convect meridionally noonwards before they convect across the polar cap from noon to midnight. These conditions produce strong east-west flow channels on the dayside, providing

strong frictional heating. A horizontal shear flow was observed in connection to the GHOST aurora in Partamies et al. (2025), suggesting that this additional frictional heating may also play a key role in setting the GHOST conditions.

The brightest, largest and longest-lived GHOST aurora observed so far appear during these ideally primed conditions where the ionosphere is hot, expanded, and sunlit. We propose that the combination of these heating sources allows the N_2 to reach high enough temperatures to produce a (pseudo-)continuum spectrum by exciting the N_2 IRA, N_2^+ M, and O_2^+ 1N bands. These bands are present throughout the whole visible range. The upwelled N_2, N_2^+ and O_2^+ in this scenario can be abundant enough to produce the observed brightness of the broadband emission.

6.8 Conclusions

GHOST emissions produce a pseudo-continuum, visually similar to STEVE and other continuum auroral features. Previous studies have suggested that the NO mechanism is responsible for observations of GHOST pseudo-continuum, but it faces significant challenges to have a high enough rate of production of NO to explain the observed brightness.

The high-resolution spectra observations shown in this study are the first attempt to unpick the continuum spectrum at a resolution where the rotational structure is visible. Fitting shows that the continuum spectrum can be deconstructed into N_2 first positive as expected, but with a significant contribution from the N_2 infra-red afterglow band, the N_2^+ Meinel band, and the O_2^+ first negative. The infra-red afterglow and Meinel bands have not been considered in previous studies, and produce emission throughout the visible range. We propose that a combination of these high energy, vibrationally excited states could be a possible explanation for the continuum emissions within the auroral oval, without the need for high levels of NO.

To determine the origin of the energy required to produce these highly energised molecules, we look at the background conditions common to GHOST events. Extreme ion temperatures and high neutral temperatures are evidenced by spectral fitting, supported by measurements reported in Partamies et al. (2025). We find that soft cusp precipitation and daylit ionosphere conditions are present in the brightest GHOST events. IMF conditions with dominant By and southward Bz are also identified as possible contributors, as these conditions result in strong high-latitude global flows and direct energetic reconnection flow into the ionosphere respectively. We suggest that these are the origins of strong flow and shear conditions identified by DMSP measurements in Partamies et al. (2025).

We propose that the combination of upwelling, heating, and shear flow provides the energy needed to excite these higher states of N_2, N_2^+, and O_2^+, to produce the observed pseudo-continuum. This provides a unified explanation of GHOST and other auroral emissions, and we provide evidence of a possible in-between state. Combined heating factors resulting in excited N_2 could potentially be investigated as contributors to the spectrum of STEVE and other auroral continuum emissions.

Future work should include more detailed modelling, including a temperature altitude profile rather than a single rotational temperature, and exploring the full observed range of continuum wavelengths. Statistical studies exploring GHOST occurrence and strength with solar wind, ionospheric flow, and cusp conditions would be valuable, particularly in investigating the shear flow and heating thresholds required to produce continuum. The emission altitude could be constrained by multi-instrument and/or citizen science imaging of GHOST.

Chapter 7

Citizen Science

Abstract This chapter looks at citizen science in the field of aurora, presenting the benefits, challenges, and wider outlook for both scientists and citizen scientists. As a core member of the Auroral Research Coordination: Towards Internationalised Citizen Science (ARCTICS) Working group, I have participated in several pieces of research and citizen science projects, including the global aurora observation campaign SolarMax, involving citizen scientists and the spacecraft mission Fram2. The scientific outputs of the collaboration which I most directly contributed to are outlined, as well as my involvement in the Fram2 mission. ARCTICS also published a handbook and field-guide for aurora citizen science as a free online text - the sections which were written primarily or jointly by me have been copied here.

7.1 Introduction

Citizen science refers, in general, to the active participation of those who are not professional scientists in the scientific process, i.e. the conception of studies, collection of data, testing of hypotheses, analysis, interpretation, and communication of results. Typical examples of citizen participation in auroral science are taking photographs, time-lapses, videos, contributing written accounts of observation sessions, classifying auroral data, identifying new or unusual features, and any other form of active involvement. Grandin et al. (2025) presents a detailed summary of citizen contributions in auroral science.

The following framework initially from Shirk et al. (2012) is given here in Table 7.1, with examples of how citizen scientists in aurora physics can interact with professional science.

Citizen science is valuable to both the scientific and citizen communities, and provides great benefits to both. For scientists, citizen science can provide data which is not captured by scientific instruments, for example to provide observations where there is no scientific cameras operating. Citizen scientists can volunteer to do time-intensive work such as image classification which would be impractical for scientists to do themselves, such as in the Zooniverse[1] projects AuroraZoo or Sunspot Detectives. Citizen scientists can also contribute significant observing experience, for example they might have seen hundreds of events of a certain auroral feature and can identify common features or typical progression. Experienced observers can also identify new auroral features which have been missed by scientists - STEVE and FAEs being good examples.

The first, most obvious benefit to citizen scientists in participating in these kind of projects is for enjoyment - from the least to the most experienced aurora photographer, people are going out on cold clear nights to watch and photograph the aurora because it is a beautiful natural phenomenon that they want to see! Citizen science projects not only give citizen scientists the opportunity to learn more about the aurora, but to learn about space, the sun, the earth, physics, chemistry, and more. Directly engaging with a science project can allow for deeper understanding of the science, and exposure to more complex aspects of aurora science than they might have otherwise experienced. Another huge benefit to citizen scientists is in forming communities. Citizen science projects can facilitate communities to form both in-person and online. Through participation in citizen science projects, people have an opportunity to contribute to a large project, have their work appreciated, and their voices heard. A good citizen science project should be a fulfilling experience for all involved. Overall, citizen science projects can be an enjoyable opportunity to engage more deeply in an existing interest, contribute to something meaningful, learn new science, form new communities, gain confidence in learning new skills, and gain new experiences (Collins et al., 2022; Land-Zandstra et al., 2021). This section drew inspiration from testimonies from Donna Lach, Canada, and Marjan Spijkers, The Netherlands, in Section 2.4 Testimonials in the Aurora Handbook Herlingshaw et al. (2024a).

[1] https://www.zooniverse.org/

Type	Definition	In aurora science	Real example
Contract	Communities ask professional researchers to conduct a specific scientific investigation and report on the results	Asking scientists to investigate an unusual observation	MacDonald et al. (2018) - First discovery of STEVE
Contributory	Designed by scientists and for which members of the public primarily contribute data	Submitting aurora observations to a survey, for a campaign, or to a database such as Skywarden or Aurorasaurus	(Grandin et al., 2024) - Survey based study on May 10 Superstorm
Collaborative	Designed by scientists and for which members of the public contribute data but also help to refine project design, analyze data, and/or disseminate findings	Scientists and citizen scientists working together to create campaigns, analyse and interpret the images	The SolarMax mission - https://www.solarmaxmission.com
Co-Created	Designed by scientists and members of the public working together and for which at least some of the public participants are actively involved in most or all aspects of the research process	Usually small group of photographers or other citizen scientists working closely with a small group of researchers on a paper	Discovery of FAEs (Whiter et al., 2021), relationship of proton blobs and SAR arcs (Nishimura et al., 2022)
Collegial	Non-credentialed individuals conduct research independently with varying degrees of expected recognition by institutionalized science and/or professionals.	Aurora chaser groups who investigate little-known phenomenon among their community	The Giant Blue Ray Aurora group https://www.facebook.com/groups/823832301812745

Table 7.1: A framework for the 5 main types of citizen science Shirk et al. (2012) with examples of each in aurora science.

In addition to these direct advantages, citizen science is an excellent vehicle for outreach i.e. a way for scientists to communicate their research to the public. Outreach is vital to encourage the next generation of scientists, to raise the profile of science in the public eye and to teach scientific literacy - vital in a world where science distrust and misinformation is negatively impacting society. In addition, increasing awareness and trust in science could influence the public to vote for science-friendly government, or policy-makers to make scientifically supported policy (Bonney et al., 2009).

Despite its importance, outreach can have a negative perception within science institutions. Johnson et al. (2014) studied 133 US scientists in physics and biology. In physics, respondents reported that outreach was too time consuming, not part of their duties, a low-status task which is not viewed favourably in promotions, and even a threat to one's reputation. They also found that overall, women were more involved in outreach (75% of respondents) compared to men (46% of respondents). One reason cited was a feeling of responsibility to be 'visible' as a woman in science to encourage more women into the field. There is in fact a large body of research on the feminisation of the outreach role in science. Johnson et al. (2014) identify that performing outreach duties has become a feminised role in physics in particular, and note how outreach is part of a process of 'occpuational ghettoisation' Roos and Reskin (1992), i.e. women's entry into physics has resulted in internal stratification, where women tend to occupy roles which offer less reward, and are less valued within the occupation, such as outreach. This is summarised in an essay on the need for a feminist approach to sci-comm (Lewenstein, 2019);

> "..the positive interpretation is that women are a lot smarter than men and have figured out that science communication is a lot more interesting than science itself." Unfortunately, and less ironically, there's a less positive interpretation, which is that science communication is a ghetto for women: lower paid, less status, less stability than science itself."
> - Bruce Lewenstein, (Lewenstein, 2019)

A similar story results from a study of Australian science communicators (Beasley-Hall et al., 2024), who reported that the most common demographic were women in early-career positions. A plurality of respondents 28.9% described sci-comm work as 'not at all' valuable to their career progression, and 84.6% of those who answered 'not at all' were women. Despite this, 87.2% expressed a desire to continue contributing to sci-comm. In summary, outreach alone is often undervalued, and has suffered the occupational ghettoization process. Women undertake the majority of outreach, and can face informal sanctions such as diminished career progression, reputation, and respect.

But what about citizen science? A search of the literature shows a gap in research on demographics of scientists conducting citizen science studies, which would have been interesting to compare to other forms of public engagement. However, there has been many studies on the demographics of the participants which generally agree that citizen scientists are slightly more likely to be western, male, white, educated, and of higher socio-economic status (Pateman et al., 2021; Strasser et al., 2023; Blake et al., 2020). Alternatively, a study of Zooniverse participants found that participants were diverse and that people with experience of discrimination (gender, race, sexuality etc.) were more motivated to take part in citizen science (Unterfrauner et al., 2024).

So do scientists see citizen science as negatively as outreach? A case-study citizen science project showed that scientists were primarily motivated by scientific output and funding opportunities, and scientists were found to be reluctant to believe that the public could make worthwhile contributions (Golumbic et al., 2017). However, a 4 year study of New Zealand scientists found that scientists identified more positive benefits of citizen science with increased participation, and identified expanded data collection, public engagement/education, and funding, as key benefits (Carson and Rock, 2024), while both studies identified data quality as a concern. Lewandowski et al. (2017) and Collins et al. (2022) report that both scientist and citizen scientist confidence in their abilities to learn and apply science skills limit citizen science projects from their full potential, and both encourage deliberate project design to ensure data quality, and encourage both parties.

Since citizen science involves two-way interaction between scientists and the public, it could be a more palatable way for scientists to engage in outreach as there is a direct career benefit (research papers, publicity, new data sets, funding). Since citizen science can produce these tangible career progression benefits, it could also help women in science to avoid the 'outreach ghetto'. Overall, with carefully designed projects to ensure quality, citizen science could encourage scientists to view engaging with the public more positively, resulting in more public engagement overall.

7.2 ARCTICS

The Auroral Research Coordination: Towards Internationalised Citizen Science (ARCTICS) group[2] is a working group of the International Space Science Institute (ISSI), to which I have been a core member throughout my PhD. ARCTICS has created an international aurora citizen science collaboration with the goal of overall improving cooperation between the two communities, coordinating global campaigns, and leveraging citizen scientist contributions to produce new science. The initial goal outputs of the ARCTICS group were;

1. Peer-reviewed research papers
2. A review of citizen science contributions in aurora and aeronomy
3. A handbook for scientists and citizen scientists, providing guidance on engaging in citizen science
4. A living dataset of citizen scientist events to be used for space physics and aeronomy research

Three years after the start of the ARCTICS group, we have achieved each of these aims. Here I will expand on my contributions to these aims and further work done as part of the ARCTICS group. Studies of continuum emissions such as STEVE have been a core topic in ARCTICS, leading to the discovery of GHOST. My contributions to the study of GHOST were presented earlier as their own research chapters in Chapters 5 and 6.

I contributed to Grandin et al. (2024), an ARCTICS study of citizen science observations of the May 10 2024 geomagnetic storm, sometimes named the Mother's Day or Gannon storm[3]. Figure 7.1 illustrates the central thesis of this study - that some scientific results are only possible with citizen science. In this case, the coverage of aurora observatories is limited to the typical auroral oval region, typically above 60°of geomagnetic latitude. The May 10 2024 superstorm was so strong that aurora was seen down to 30°geomagnetic latitude, with our most equatorward sighting in India[4]. Our results show that in a large geomagnetic superstorm, scientific instrumentation is not available at the geomagnetic latitudes needed to observe the aurora. This result supports the importance of citizen science and the need for an international aurora citizen science project, to collect important citizen observations in a way that is accessible to scientists. In this study, we used Skywarden[5] to collect publicly available citizen observations from Canada, France, Sweden, and Finland. We can see the benefit here of having a website where citizen science observations are free for scientific use, as this data is easy to retrieve (directly on the site or using the Skywarden API) and is actively monitored and quality checked. The other main citizen data source for this study was a short survey, asking for the time and location of aurora and technological disturbances during the storm, as well as the colour and form of the aurora and the type of disturbances. My part in this study was in the initial conception, a small part of the writing, input on the text, and dissemination of the study within the UK through mailing lists, personal social media, direct communication, and word of mouth.

I have also contributed to a study of Fragmented Aurora-like Emissions (henceforth, fragments, e.g. Whiter et al. (2021)) 'around the world', in preparation at time of writing. This study collects citizen observations of fragments from outwith Svalbard, from Skywarden and observations which have been sent in individually. The study will explore the distribution of fragments in time, geographic/geomagnetic coordinates, in relation to the auroral oval, solar wind conditions etc. and represents the first effort to form a statistical picture of fragment occurrences. Since fragments are small and short-lived, typically around 20 km in scale with duration less than a minute (Dreyer et al., 2021), they can be easily missed in all-sky cameras. Citizen science photographs (even better, video) can give the resolution needed to positively identify fragments over the entire auroral region. My contribution to this study has been in group fragment identification. A small group of us went through every observation individually and confirmed or questioned the fragments in the image. Fragments can easily be confused with picket

[2] https://collab.issibern.ch/arctics/

[3] I propose it should be named the Migratory Birds Storm in honour of the UN's international day of migratory birds, which is a more international, neutral, and fun way to name geomagnetic storms.

[4] Aurora observation in India is confirmed by aurora photographs taken by Vincent Ledvina - ARCTICS member, professional aurora chaser, and PhD student in aurora physics, who was in north India on holiday at the time.

[5] taivaanvahti.fi

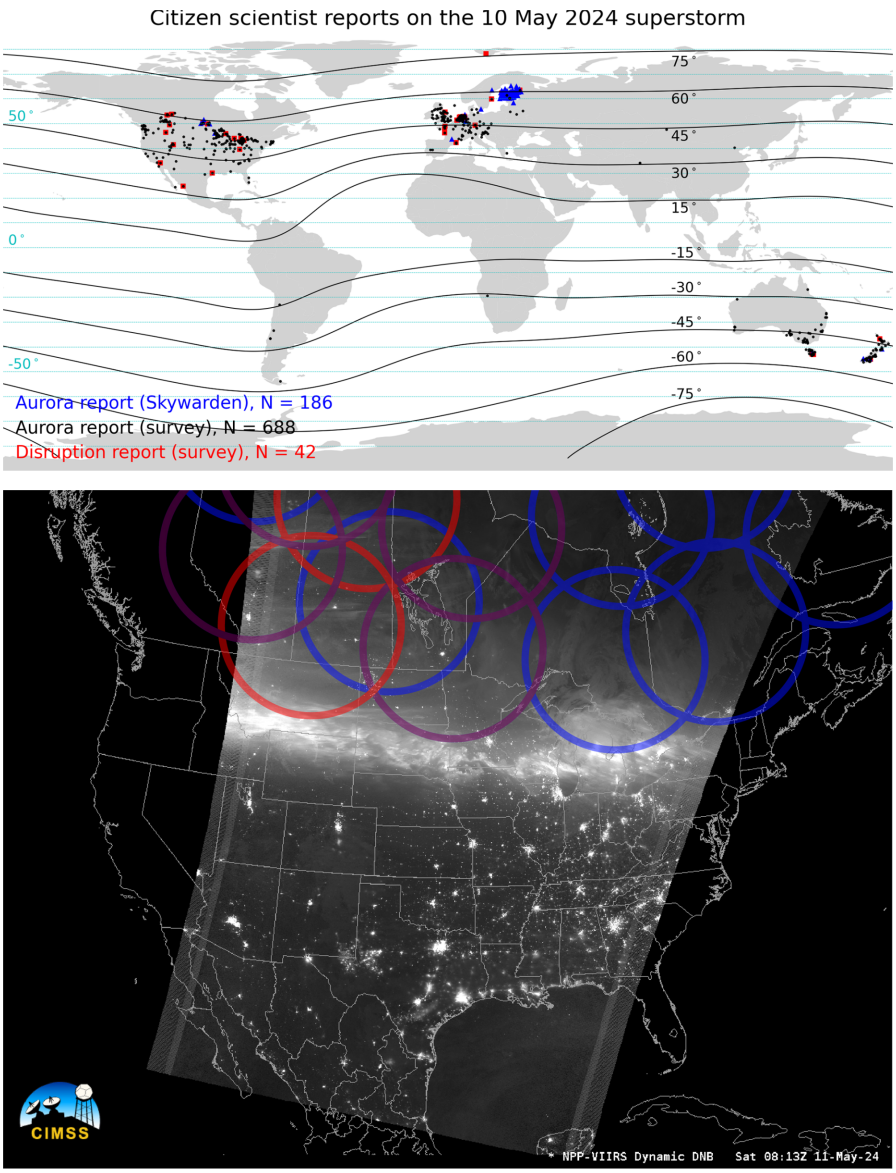

Figure 7.1: (Top) Map of citizen science reports on the 10 May 2024 geomagnetic susperstorm, taken from Grandin et al. (2024). Map shows the global coverage of reports from Skywarden (blue), aurora sightings from survey respondents (black) and technological disruptions observed by survey respondents (red), overlaid with parallels of geomagnetic latitude. Since this event occurred during northern hemisphere summer, aurora was not visible above the 65th geographic parallel, where the sun was only 5°below the horizon. (Bottom) Map of the auroral oval and scientific instrumentation during the May 10 2024 storm over the continental US. Image from the Visible Infrared Imaging Radiometer Suite (VIIRS) Day/Night Band (DNB) onboard the Suomi NPP satellite, showing a section of the auroral oval at 08:13 UT on 11 May 2024. FOVs of THEMIS (blue) and TREx (red) ASIs are overplotted. Co-located TREx and THEMIS ASIs are shown in purple. It is evident that the auroral oval was located too far south for observation with any of the scientific instruments.

fence or green lens flares, so each observation needs to be scrutinised to ensure only true fragments are included in the study.

The living dataset of citizen scientist events to be used for space physics and aeronomy research, has been based around Skywarden - this site was chosen as it already exists as a place to report observations of all atmospheric phenomena, upload images which are freely accessible to science, tag specific features, is accessible with API, and is moderated by experienced citizen scientists. The site is Finnish and most popular in Finland, but has a growing user base in Canada, Sweden, and Norway. We decided to promote Skywarden as the gold standard reporting website for our citizen science campaigns. Skywarden was used as the primary data collection for all of our citizen science efforts, in particular the SolarMax mission.

7.2.1 Fram2 and the SolarMax mission

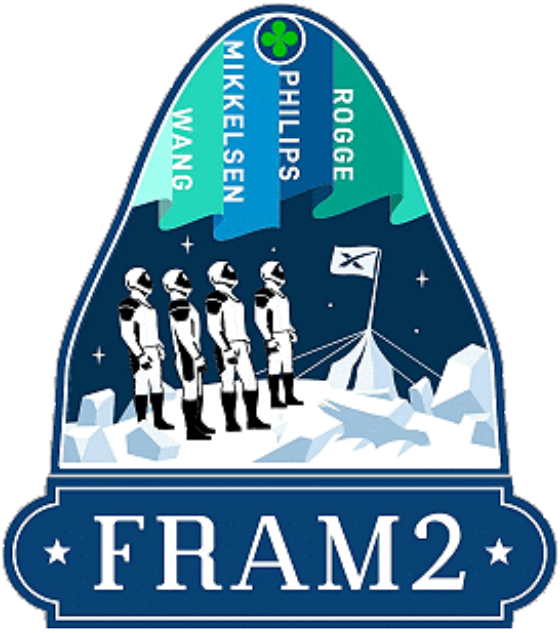

Figure 7.2: Fram2 mission patch depicting the four astronauts on a polar expedition under the aurora.

The Fram2 mission, Figure 7.2, was a private manned spaceflight, aboard SpaceX's Dragon capsule, which took place from 1st - 4th April 2025 over 3 days, 14 hours. The mission was the first ever human spaceflight over the poles and involved various programmes of science research, one being the study of 'weird' auroral emissions through the SolarMax mission. Vehicle commander, film director, and 3D cinematographer Jannicke Mikkelsen would take videos of any aurora they passed over, focused in particular on locations where citizen scientists were actively photographing the same features from below (Wall, 2025; Next Spaceflight, 2025; Warren, 2025).

The SolarMax mission (Herlingshaw, 2025) was, to our knowledge, the largest aurora photography campaign to date. The goals were to collect a global dataset of aurora images, video, and timelapse for the duration of the Fram2 flight, the first priority to capture four specific features; STEVE, picket fence, GHOST, and fragments. All other auroral forms were the second priority. The SolarMax mission is now an ongoing collaboration between astronaut Jannicke Mikkselsen, Katie Herlingshaw, and the ARCTICS working group, to use this unique dataset for aurora science.

The SolarMax mission resulted in 123 observations on Skywarden from 7 countries throughout the auroral region, including 5 observation sets from the UK, see Figure 7.3. Many observations contain the maximum of 8 files, in photographs, videos, and time-lapses, representing a substantial dataset well spread in geography and time throughout the mission. In addition to this citizen science dataset, scientific instruments were encouraged to run in campaign mode, for example the EISCAT radars UHF and VHF ran throughout the darkness hours for the duration of the mission. In addition

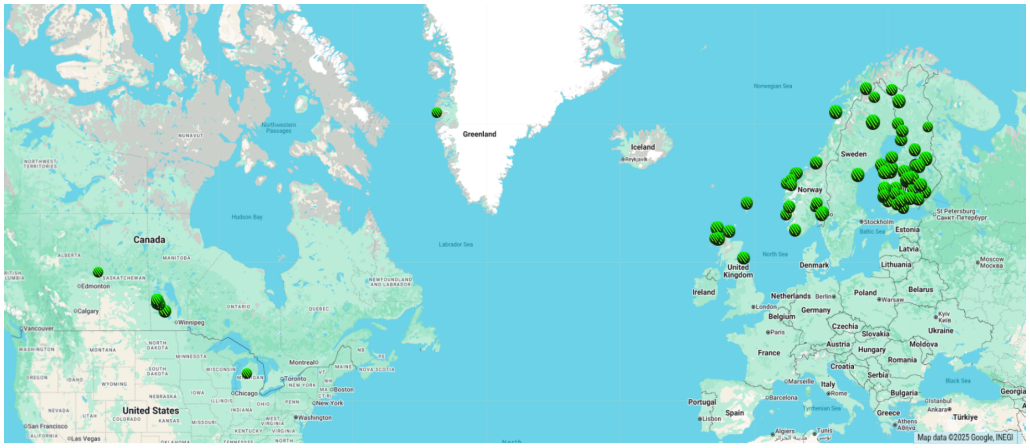

Figure 7.3: Map of all 123 SolarMax mission observations published to Skywarden, tagged as #SolarMaxMission, 5 of which are from the UK, Map Data ©2025 Google.

to the typical accessible network of all-sky cameras, some all-sky cameras in Antarctica were run in an auroral campaign mode and have provided excellent data and many conjunctions with the Fram2 Dragon capsule.

During the SolarMax mission I ran one of two UK aurora monitoring hubs, the other being Glen Wheatley who runs the Northern Lights UK Facebook page[6] (with 27.8k members at time of writing). I monitored UK observations through Aurora Alerts UK[7], a website which monitors ongoing substorms and provides a map of current aurora sightings. Citizen scientists can provide real-time updates of observing conditions at their location which are used to produce a map of aurora presence, visibility, and cloud cover. In addition to Aurora Alerts UK, I used Facebook to monitor recent aurora image uploads from a total of 10 groups including Northern Lights Alert, Northern Lights UK, Scotland's Scenery, Isle of Harris, Smartphone Astrophotography, Aurora Hunters UK & Iceland, Scotland's Aurora Watch Help & Advice, Shetland Aurora Hunter, and Argyll Auroras. I also monitored webcams throughout the UK. Using this data I was able to send alerts through the SolarMax mission to Jannicke on board Fram2, and to disseminate information about the SolarMax mission to citizen scientists. After the capsule splashdown I also used social media to collect observations and encourage people to submit their data to Skywarden.

Aurora science is a fortunate field in that there exists already a large network of aurora chasers, professional aurora guides, photographers, and aurora tourism. Facebook is commonly used to create communities around aurora chasing, from the smaller local scale up to large global groups. For example, the Northern Lights Alert Facebook group (a global group for sharing aurora sightings) currently has 1.4 million members. Since Argyll Auroras is based in my home county where I have a large network, and is well placed in a fairly northern dark sky area, see Fig 7.4, I decided to actively participate in this Facebook group to encourage participation in SolarMax. Argyll Auroras has 11.9k members at time of writing, representing 13.5% of the total population of Argyll, so this Facebook group was a great way to engage directly with a significant portion of Argyll's population and over a large geographic region with a significant spread in latitude - 6,907 km^2 ranging from the tip of Kintyre at 55.29°N to the Island of Coll at 56.70°N (Statistics.gov.scot, 2023). Through Argyll Auroras I was able to obtain many photos of Isolated Proton Aurora (IPA) blobs which were visible all over the UK, send alerts with the Fram2 overpasses, and share information on STEVE and picket fence with good engagement.

There are thousands of publicly available webcams that can be used as aurora observation tools and for data collection. During the SolarMax mission, I monitored several publicly accessible webcams, taking screenshots regularly. The main webcams I used to monitor aurora visible from Scotland, were the Shetland Webcams[8], due to their availability, and location at the extreme north of the UK. Several northward looking webcams were suitable for aurora monitoring, particularly Cliff Cam 3, Cliff Cam 2,

[6]https://www.facebook.com/groups/829182728558596
[7]https://aurora-alerts.uk/
[7]https://gostargazing.co.uk/light-pollution-map/
[8]https://www.shetlandwebcams.com/

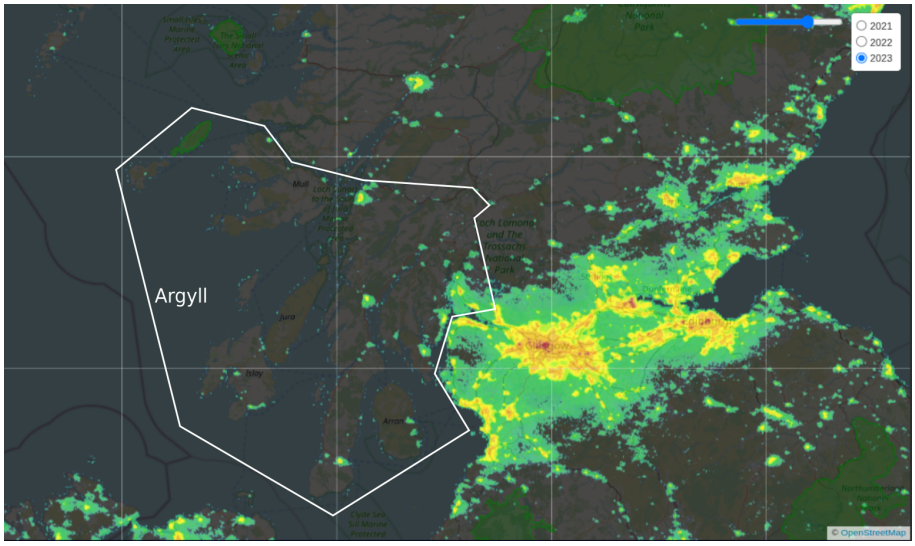

Figure 7.4: Map of light pollution over Argyll & Bute, Scotland, taken from Go Stargazing (2025), based on data from the Visible Infrared Imaging Radiometer Suite (VIIRS) instrument aboard the NASA/NOAA satellite, taken in 2023. Argyll & Bute county outlined in white.

Burrafirth, and Eshaness Lighthouse. Cliff Cam 3 and Burrafirth were chosen for monitoring as they had suitable camera settings for observing aurora, wide north-facing field of view, and are located at the northern and southern tips of Shetland, giving a geographical separation of ~ 100km, Figure 7.5.

The webcams were invaluable throughout the SolarMax mission to provide the astronaut, Jannicke, with alerts on UK auroral activity throughout. The screenshots taken were also submitted to Skywarden, Observation number 134658[9], and two examples are shown in Figure 7.6. My observations with the webcams included images from the expansion, breakup, and recovery phases of a substorm, and included both active auroral features such as pillars, enhanced aurora, and beads, as well as diffuse features such as omega bands and patchy aurora. At least one of the images of auroral pillars was taken while Fram2 was overhead and had been alerted, so it is a potential conjunction to investigate in the future.

The SolarMax mission brought together astronauts, scientific instrumentation, and a wide network of citizen scientists to create a global campaign. By combining data from space, ground-based instruments, photographs, videos, webcams, and real-time social media posts, we were able to capture a valuable dataset of auroral activity across a large range in geography and time. The mission also served as a fantastic example of how citizen science can directly support and enhance space-based observations, and vice versa. With so many contributors across different platforms, and conjunctions between ground and space still to investigate, SolarMax is an example for future collaborative efforts in aurora research.

[9]https://www.taivaanvahti.fi/observations/browse/map/6581950/observation_id/desc/0/100
[10]https://taivaanvahti.fi/observations/show/134658

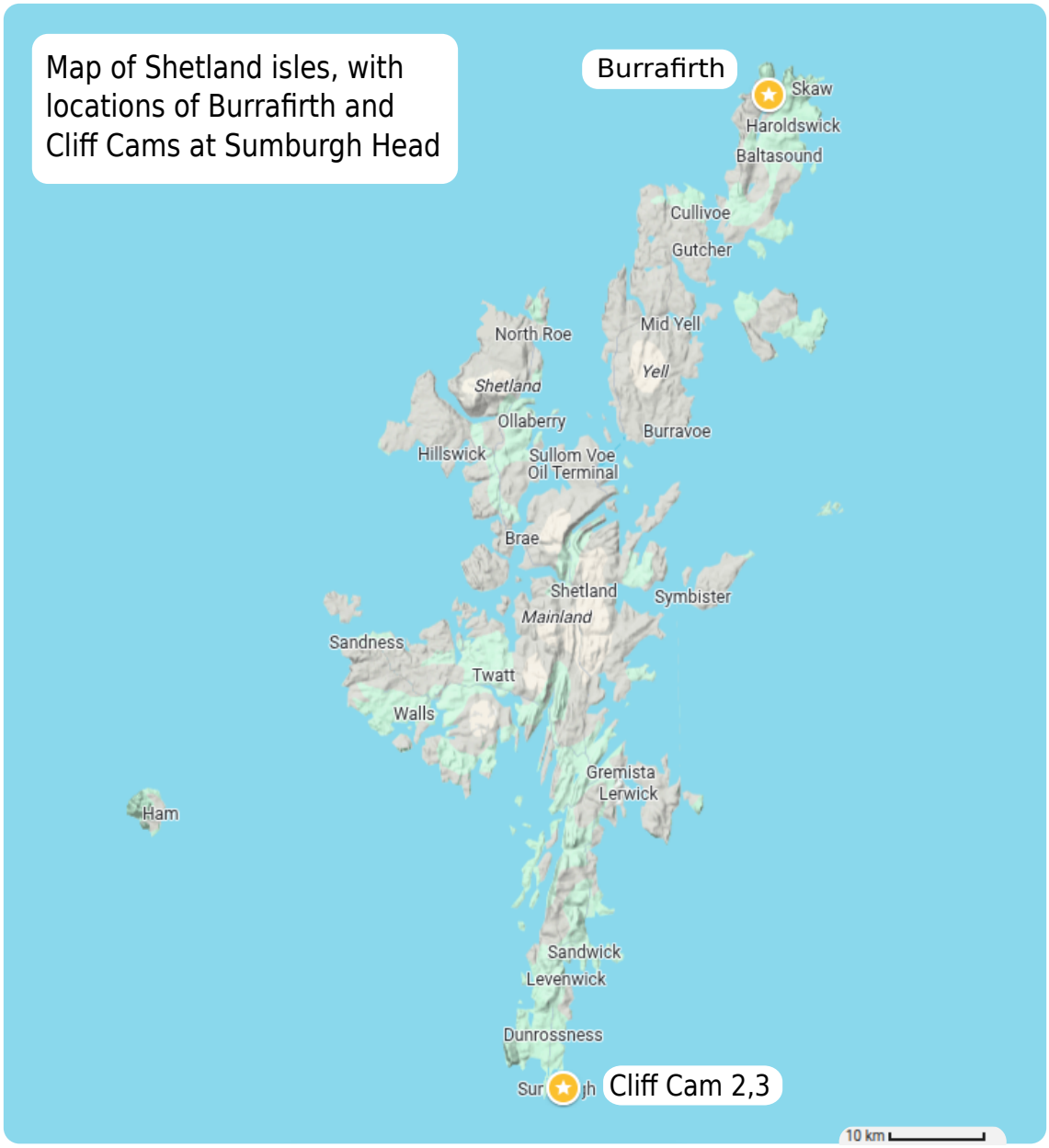

Figure 7.5: Locations of Shetland Webcams, Map Data©2025 Google

(a) Enhanced aurora - Burrafirth 60.80°N

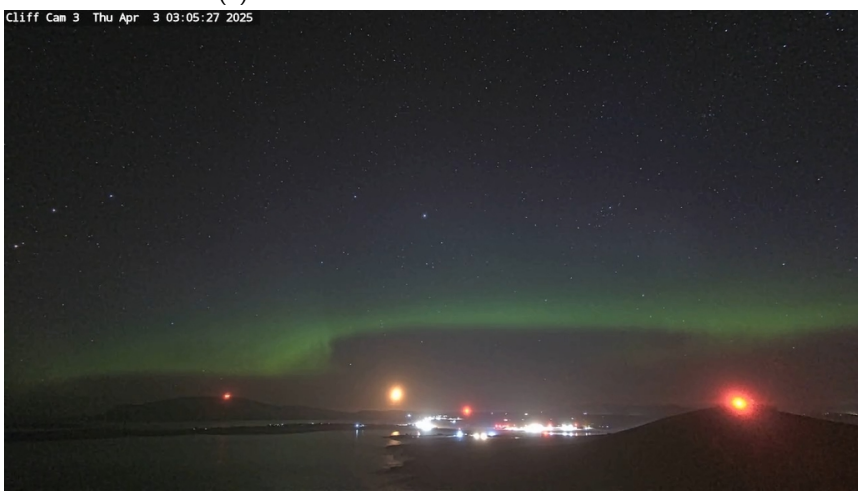

(b) Omega bands - Cliff Cam 3 59.85°N

Figure 7.6: Screenshots from the publicly available Burrafirth webcam, used with permission from Shetland Webcams. Submitted to Skywarden, Observation number 134658[10], as part of the SolarMax mission.

7.3 Aurora Handbook for Citizen science

This section includes the sections of the Aurora Handbook for Citizen Science (Herlingshaw et al., 2024a) which were written primarily or jointly by me - I also contributed in smaller ways to other sections (not replicated here), and other authors assisted with editing my sections. My contributions to the field guide were primarily in image selection and discussion of contents. Other authors represented in this section are Noora Partamies of the University Centre in Svalbard, and citizen scientists Eero Karvinen, Donna Lach, and Chris Ratzlaff, who I collaborated with on certain sections, marked at the start of each section as contributors.

7.3.1 Welcome

Contributors: Rowan

Welcome to the **Aurora Handbook for Citizen Science**, a guide intended to bridge the gap between professional and citizen scientists who observe the aurora. Our objective is to empower the citizen community with the knowledge and tools to contribute meaningfully to auroral science, and to enable professional scientists to fully utilise the data and expertise of citizen scientists. By bringing together these two groups we aim to foster a strong collaborative relationship, and to use our shared data and expertise to advance our understanding of the aurora, a phenomenon which captivates and inspires us all.

Citizen Scientists

A **citizen scientist** *is someone not engaged professionally to work on a project as a scientist, who contributes to scientific research as a volunteer or other collaborator (paid or unpaid). They can be school students, teachers, families, retirees (including retired scientists), researchers contributing outwith their own field, independent researchers, or other members of the general public.*

Citizen scientists can collaborate with professional scientists at different levels – they may collect and/or analyse data for the project (contributory citizen science), or they may collaborate with professional scientists on many different parts of the project (collaborative citizen science). They may also design the project with professional scientists from the ground-up (co-created citizen science). Other types of citizen science projects may be initiated by a community, with scientists acting as external consultants (contractual citizen science), and additionally independent researchers may collect their own data, or conduct their own research, and ask professional scientists for advice or assistance (collegial citizen science). Historically, auroral citizen science projects have included members of the wider community in many of these ways. This Handbook will help you anticipate what to expect in your collaborations with professional scientists.

Scientists

A **scientist** *is a trained expert who is paid and employed at an institution to study the natural world. It is their profession to employ the scientific method to analyse the natural world and publish their results through reputable, peer-reviewed journals.*

As a professional scientist, you have many opportunities to leverage observations made by citizen scientists of phenomena associated with aurora. This Handbook will help you anticipate what to expect in your conversations with citizen scientists and how to seek the data you are looking for. For example, suggesting "your photos will get exposure" will often result in a negative response. Instead suggesting their work will "contribute to emerging science" and that they will be "included as a co-author" will receive a more favourable response.

Both

Combining the communities of citizen scientists and professional scientists in studying aurora creates a unique opportunity to leverage the strengths of each group. Citizen scientists, with their diverse

geographical locations and dedication to observation, provide a resource that would be difficult for professionals to gather alone. Professional scientists, in turn, offer the expertise needed to interpret these observations and draw conclusions. Together, they form a partnership where the data collected by citizens support scientific research, leading to new discoveries, more thorough studies, quicker advancements, and a better understanding of auroral phenomena.

7.3.2 Why Study the Aurora?

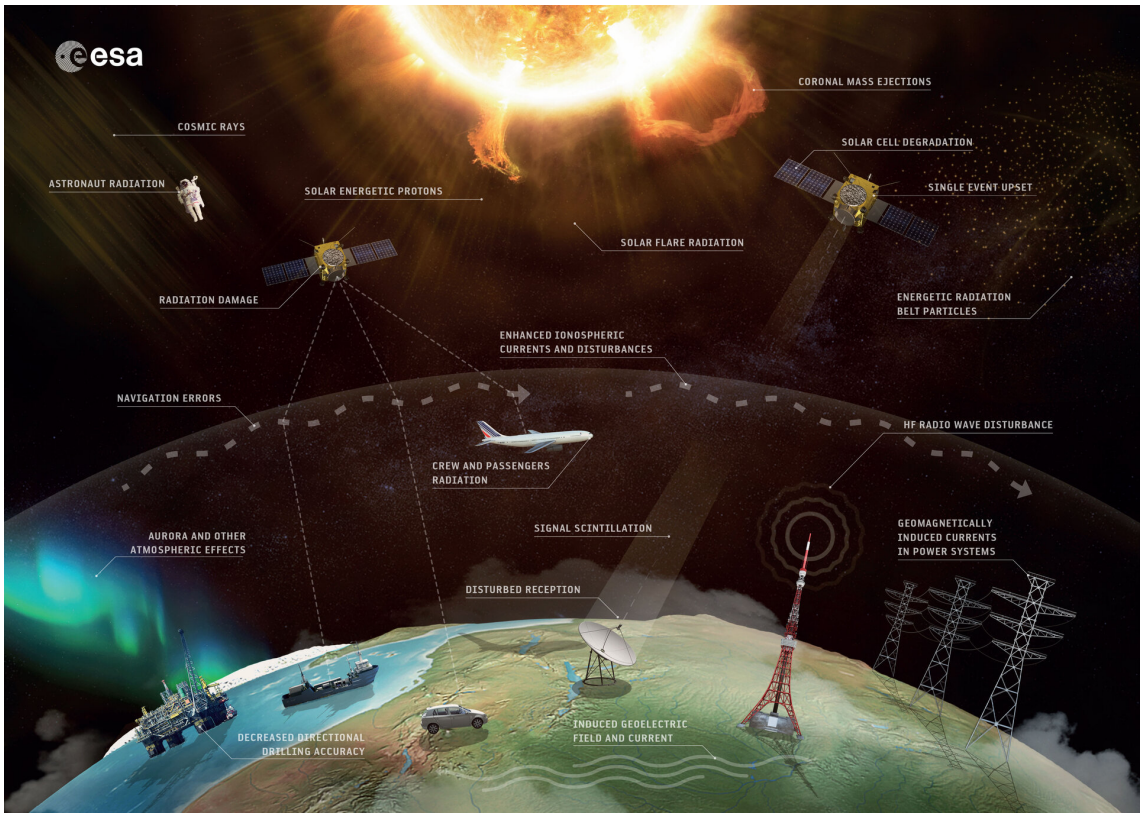

Figure 7.7: Examples of space weather impacts on society. Image credit: ESA/Science Office, ESA Standard Licence.

Contributors: Rowan

So why research the aurora? What insights can it offer us?
Firstly, **the aurora provides a natural laboratory for studying plasma physics**. Plasma is an ionised gas made of free electrons and ions that respond strongly to electromagnetic fields. It makes up about 99% of the visible matter in the universe and is not well understood compared to the other three states of matter (solid, liquid, gas). The magnetic environment of the Sun and Earth consists of a complex plasma environment where we can observe complicated plasma processes. One very important method of understanding these plasma processes is by measuring the auroral emissions which result from them. Insights which help us to understand the range of different auroral forms and behaviours can be applied across the rest of plasma physics, from stars, supernovae and interstellar space in astrophysics, to lightning, fire, and fusion reactors, all the way to spacecraft ion-thrusters or the humble neon sign. Plasma is all around us, both in scientific research and day-to-day engineering, and aurora research provides a vital laboratory to help us fully understand it.

The aurora is also closely linked to **space weather**, such as solar storms. Understanding the aurora can improve our ability to predict space weather and the Earth's magnetic reaction to it. This is crucial for protecting satellites, communication systems, and power grids from solar-induced disturbances that can have significant impacts on modern technology and infrastructure. These effects are shown in Figure 7.7.

Even closer to the ground, the aurora interacts with the **Earth's atmosphere**, influencing its chemical composition and temperature. By studying the aurora, researchers gain insights into atmospheric processes, including how energy is transferred from the Sun to the Earth's atmosphere and how it affects atmospheric chemistry. The aurora can also offer clues about the effects of **climate change** on the upper atmosphere. Changes in the Earth's upper atmosphere can be observed in the aurora and other atmospheric light emissions. By studying these interactions, scientists can better understand the broader impacts of climate change on the atmospheric system.

7.3.3 Continuum Emissions

Contributors: Rowan, Noora

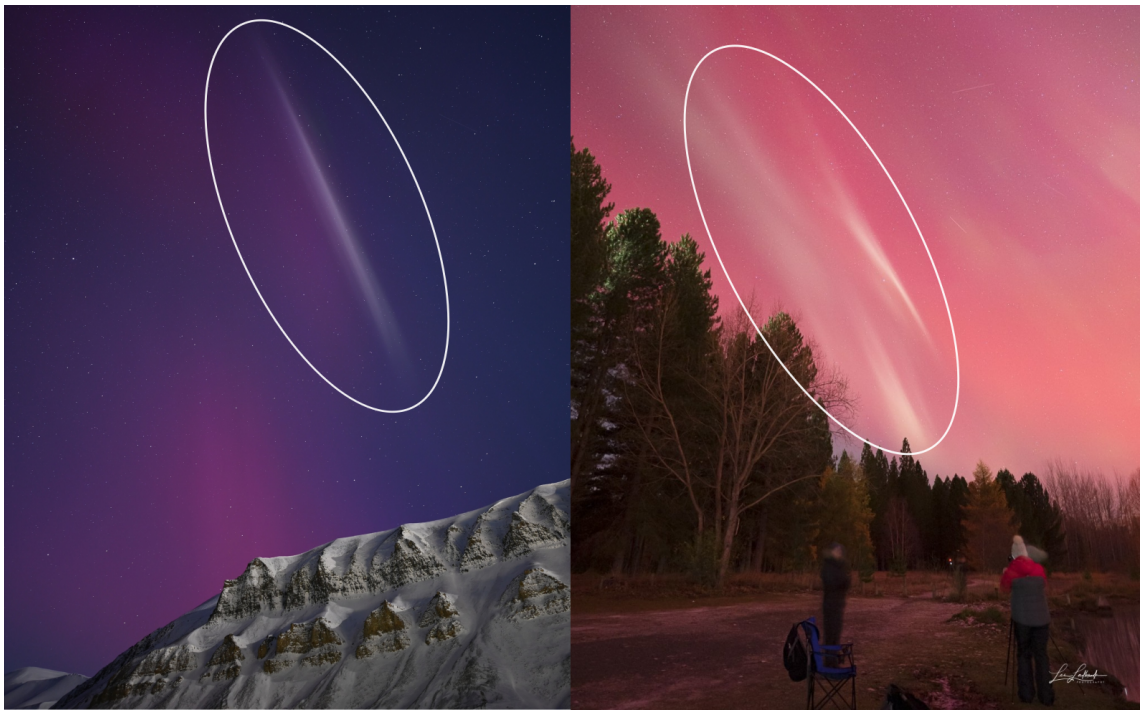

Figure 7.8: (Left) Image of aurora over Svalbard with faint red emission background and a thin white-ish stripe of continuum emission that is aligned with the magnetic field direction. Image credit: Marjan Spijkers. (Right) Image over New Zealand showing stripes of white-ish continuum emission with a pink/red background. Image credit: Les Ladbrook.

Continuum emissions have been recognised for decades, but recently, the mauve/grey/white emissions have attracted renewed interest in relation to STEVE Gillies et al. (2019). These emissions are made up of all the different colours in the visible wavelength range, which combine together to appear off-white. They have been identified as characteristic of STEVE, primarily occurring at the equatorward edge of the auroral oval. However, observations in 2024 from Tromsø (Nanjo et al., 2024) indicate that STEVE-like conditions may also exist polewards of the green aurora. Both types of continuum emissions typically manifest as thin arcs of pale light. These emissions have been observed within dynamic aurora and at the poleward edge of the auroral oval, and they are seen to change in brightness and shape in step with the nearby aurora that is created by particle precipitation. The precipitation-induced continuum emission structures can take on various shapes and evolve rapidly, similar to dynamic aurora. Examples of continuum emissions are shown in Figure 7.8.

Some typical **characteristics of continuum emissions** can be summarised as follows:

- **Colour and Shape:** Pale mauve/grey/white colour. They can appear as thin or wide arcs or more rayed structures.
- **Brightness:** Variable.

- **Location:** Polewards, within, and equatorwards of the auroral oval. Continuum emissions have also been seen at high latitudes in the dayside aurora, so they are not necessarily a nightside feature like STEVE.
- **Size:** Variable. They can be fine scale ray-like features, thin ribbons like STEVE, or thick arcs.
- **Duration and Stability:** Variable. The thinner, more dynamic emissions typically last seconds to minutes, while the arc-like features can last hours.
- **Other Helpful Information:** It is worth noting that the colour of the continuum emission in colour images depends on the background illumination of the sky, including the aurora. There are therefore different shades of pale.

The actual generation mechanism for continuum emissions is not known, but it is likely that ionospheric heating by particle precipitation and/or strong plasma flows play an important role. The variety of different conditions where continuum emissions occur suggests that a combination of different mechanisms might work together to produce a favourable environment.

The only bullet-proof evidence of continuum emission is a scientific measurement showing the brightness over a range of measured wavelengths. However, many photos provide relatively convincing observations even without these measurements.

7.3.4 Proton Aurora

Contributors: Rowan, Eero

Most proton precipitation (protons raining into the Earth's atmosphere from near-Earth space) results in proton aurora, which is diffuse and invisible to the naked eye. Sometimes protons may also contribute to weak visual emission by releasing enough "secondary electrons". A secondary electron is taken off an atmospheric atom or molecule when a precipitating proton carries enough energy to ionise it. This electron then follows the magnetic field direction downwards and can excite atmospheric constituents in the same way as a precipitating particle coming from space, leading to auroral emissions. The auroral structures associated with secondary electrons are sometimes called proton blobs, proton patches, or isolated proton arcs. They appear equatorward of the main auroral oval, often around dusk, and typically show up as green emissions that are separate from the main oval.

During 2015–2022, Finnish and Canadian citizen scientists documented several events of isolated, green proton structures with a faint red arc above the proton blob structure. Both the red arc and the green aurora were aligned with the emissions happening at different altitudes: red at about 230 km height and green at about 110 km Nishimura et al. (2022). This combination of the red and green proton aurora is called Red Arc with Green Diffuse Aurora (RAGDA). An example of this scene is shown in Figure 7.9.

Although the red arc in RAGDA is not a SAR arc, sometimes proton precipitation can trigger a SAR arc or leave one behind after the proton activity fades out. During this transition, distinguishing between the different arcs based on their cause can be visually challenging.

Some typical **characteristics of proton aurora** can be summarised as follows:

- **Colour and Shape:** Red or green diffuse aurora in arcs or blobs.
- **Brightness:** Dim.
- **Location:** Equatorwards of the auroral oval.
- **Size:** Variable but arcs can be elongated over thousands of kilometres.
- **Duration and Stability:** RAGDA can typically last for tens of minutes to hours but the proton blobs have shorter lifetimes.
- **Other Helpful Information:** A useful guideline is that only RAGDA displays diffuse rayed structures in the red arc, and SAR arcs lack the diffuse green emission blobs seen beneath RAGDA.

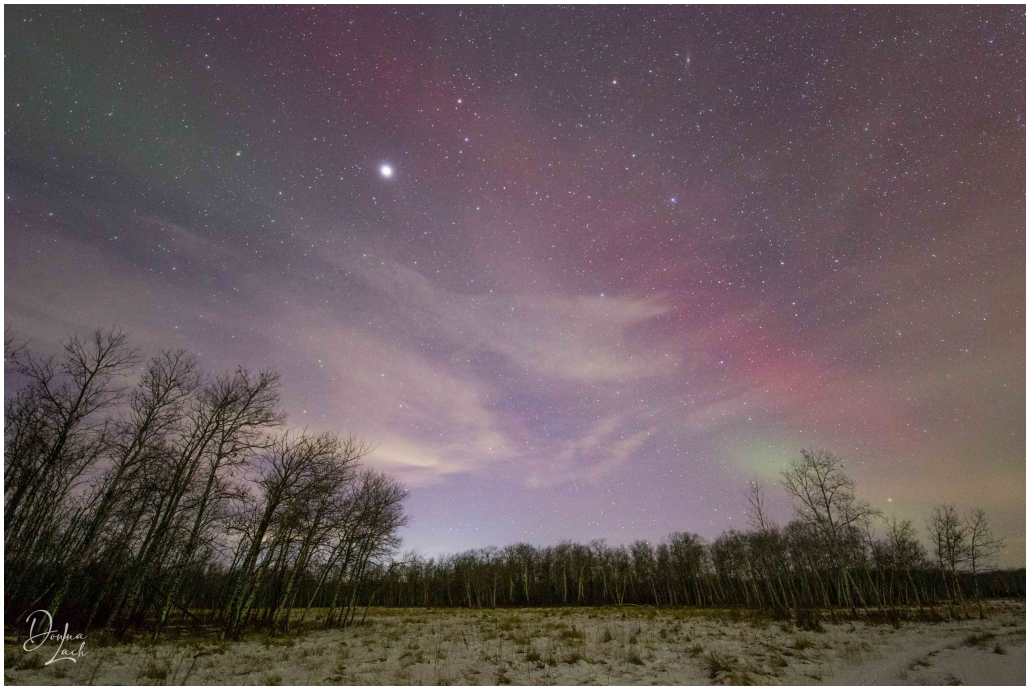

Figure 7.9: Diffuse emissions of red and green close by form RAGDA in the subauroral latitudes. Image credit: Donna Lach.

7.3.5 Classification Platform for Fine-scale Aurora

Contributors: Rowan

If you do not want to or perhaps cannot take your own aurora photos, but like to look at them and classify them and still contribute to science then there is a project you might be interested in. In the Aurora Zoo project hosted by Zooniverse, citizens can classify and investigate images and video of fine-scale auroral features. The scientific goals of Aurora Zoo are to firstly, understand how different small-scale shapes and movements in the aurora are formed, and secondly to understand what conditions are needed for these different shapes and movements to happen. As well as classifying short clips of aurora video data, the forum feature can be used to point out unusual or new features. As an example, citizen scientist analysis using Aurora Zoo contributed to the discovery of fragments (Whiter et al., 2021).

The videos in Aurora Zoo are taken by the ASK (Auroral Structure and Kinetics) instrument, based on Svalbard and operated by the University of Southampton. ASK differs from a typical camera as it focuses on only a small area of the sky and uses highly sensitive sensors such that we are able to video rapid dynamics at up to 50 frames per second. It has collected data in the high Arctic since 2007. To get involved in Aurora Zoo click here[11] or go to Zooniverse.org and search for Aurora Zoo.

7.3.6 Reciprocity, Attribution, & Payment

Contributors: Rowan

Reciprocity and attribution ensures that contributions are acknowledged and valued. This section outlines the principles that guide fair exchange and recognition in sharing data and findings. By embracing reciprocity and practicing proper attribution, the aurora community strengthens trust and encourages ongoing collaboration, advancing our collective understanding of auroral phenomena. Different forms of reciprocity, kinds of content licences, advantages and disadvantages of payment for images, and procedures for authorship and acknowledgement are explained in this section.

[11] https://www.zooniverse.org/projects/dwhiter/aurora-zoo

Forms of Reciprocity

Contributors: Donna, Rowan

Reciprocity is the practice of exchange for mutual benefit. Reciprocity of some form should be present in the relationships between scientists and citizen scientists, to build and maintain lasting positive relationships within our communities. If a citizen scientist is freely sharing their photos and observations, reciprocity by the scientist can, for example, be:

- **Acknowledgement and Credit:** Such as being listed as a coauthor of a scientific publication (see 7.3.6).
- **Feedback and Communication:** Take the time to provide project updates during and after a project. Answer any questions that need clarification so that the citizen scientist can understand the impact of their work. A failure to do this could lead to a disengagement of the citizen scientists and they may lose enthusiasm to make further contributions.
- **Connection to Scientific Community:** Allows for conversations with the scientific community regarding their observations. Inviting the citizen scientist to participate in analysis and discussions fosters a sense of ownership in the research process and deepens understanding.
- **Event Involvement:** Makes connections to involve the citizen scientist in conferences/meetings, outreach, and news, media or science communication events. This provides a platform for them to share their experiences and insight and opens opportunities for them to expand their network and participate in future citizen science projects.
- **Funding:** Consider the pros and cons of financially reimbursing citizen scientists (listed in 7.3.6). Consider if your funding source allows for this and if it is appropriate in your situation. Funding can also be used to indirectly offer reciprocity, for example, opportunities for relationship building, planning community events, supporting community experts, or gifts/prizes/equipment for involvement in projects.
- **Targeted Research Development:** Scientists may have their own research targets to hit for their funding providers. However, if it is possible to incorporate topics or apply for funding for topics that are important to the citizen scientists and target their priorities, then their insights on the topic can be incorporated into the project and motivations for contributions will be high. This could lead to more rewarding collaborations for the citizen scientists where they are involved in the development of the project goals, the project itself, and the project results.

Authorship and Acknowledgement

Contributors: Rowan, Chris

Authorship on a scientific publication is a good example of a reciprocity. If citizen science data are used in scientific publication, the original photographer should be offered co-authorship on the submitted manuscript. They can then decide themselves if that is how they would like to be credited. They also should be credited in any figure caption or in-line reference to the photographs studied, according to their content licence conditions (see 7.3.6).

Citizen scientists should be kept up-to-date on the use of their data, and informed of any publications. Large groups of citizen scientists, e.g. survey respondents, should be given the opportunity to provide their details for acknowledgement. Individual journal guidelines should be followed in relation to acknowledgements. Large groups may still be listed as co-authors[12], or listed fully in the appendices or acknowledgement section, particularly if the journal does not allow large author groups.

[12]The current record for number of authors on a scientific publication is 15,025 according to Guinness World Records!

Payment for Data

Contributors: Rowan, Donna

This is a complicated issue to which there are no straightforward answers. Here follows a discussion based on the positives and limitations of financial compensation for citizen scientists' images.

The choice of whether to pay citizen scientists for their photos is a complicated area with no simple guidelines. In some ways, offering payment may enhance data quality and inclusion, while in others the projects may thrive within a volunteer-driven, open-access framework. Scientists need to carefully balance financial limitations with ethical considerations, ensuring that contributors feel appreciated, whether through financial compensation, recognition, or other means of acknowledgment. Each situation will require individual assessment. Below we highlight some of the advantages and disadvantages of payment for citizen scientist's photos.

Advantages to paying citizen scientists:

- Citizen scientists put a huge amount of effort, money, labour, and time into photographing the aurora and creating data of scientific use. Offering monetary compensation acknowledges the value of their labour and their contribution to research while at the same time showing respect for intellectual property.

- If they are paying for the data, scientists could request certain aspects which make the data higher quality, and potentially encourage more people to collect the data. The citizen scientists could also invest more in equipment that would help them capture even better photos. All of these would lead to higher-quality data and results for research over longer time spans.

- Offering payment could also encourage those in remote or lower-income areas to take part in citizen science and make participation more equitable, allowing a broader demographic the possibility to be involved.

Disadvantages to paying citizen scientists:

- Many scientist and citizen scientist projects are based on open-access data. Citizen science is traditionally a voluntary activity, where participants are interested in and passionate about the topic and enjoy taking part in it and contributing to scientific progress. Introducing payments could shift the focus from collaboration to compensation and cause a distortion in the purposes of those participating. Paying for data could undermine the existing culture of openness and the willingness of participants to freely share data, which could change the communities themselves.

- Scientists research budgets are also limited. They may find it difficult or even impossible to provide financial compensation for multiple reasons. As they are in the public sector, funding is limited and tightly protected, and typically not able to be used to purchase content, in particular data. If scientists should pay for every image used, then they may not be able to carry out their research or it could significantly limit the scale of the research.

- Some scientists think that other forms of reciprocity, such as those listed in 7.3.6 are a more appropriate and budget-friendly way to recognise contribution from citizen scientists, rather than financial compensation.

Attribution & Content Licensing

Contributors: Rowan

Licensing images and videos is vital to protect citizen and professional scientists and photographers. Citizen scientists are recommended to add a licence to images posted online, and scientists are recommended to confirm a licence whenever you request images. Here is a list of some broad groups of licence types with a simple definition. The Creative Commons licences give six standardised licences of

different types, able to be used by companies and individuals for any form of creative content[13].

To add a licence to your photo or folder/directory of content, the convention is to copy and paste or download a standard licence from online (they are freely available) and include it within the folder as a text file named LICENCE. Following this convention ensures that your licence is easy to find and reference. It is then the responsibility of anyone who accesses your content to follow the terms of the licence and ensure that derivative products are licensed accordingly. If you have a website or social media page and want to apply a licence to all images you post, you can add a statement to the footer, bio, or dedicated copyright page. This can state, for example, "All images on this website are licensed under a Creative Commons Attribution-NonCommercial 4.0 International Licence (CC BY-NC 4.0) unless otherwise noted". The different types of licences will be described below.

Permissive licences allow almost any use of the content. This can include commercial use, adapting, distributing, or adding to the content in any medium or platform. Permissive licences typically require attribution to the author. CC-BY is an example of a permissive licence.

Copyleft licensing is a form of open access which requires any derivative content to also be open-access. This is often used to prevent commercial use or profiting from your open-access content. However, copyleft licences can be restrictive and can (ironically) stop scientists from being able to freely use and share the data. CC BY-SA is an example of a copyleft licence.

Restrictive licences typically ensure accreditation to the author, while restricting any commercial, derivative, or adaptive use of the content. Restrictive licences are not recommended for scientific use as they make it very difficult to share scientific results and are not compatible with open-access policies, e.g. CC BY-NC-ND.

Public domain means that the copyright has been completely given up by the author, or that the licence has expired. This allows anyone to use, commercialise, adapt, change, or derive products from the content with no conditions to attribute to the author, e.g. CCO.

If you wish your content to be used freely/open access for scientific use, in most cases it is recommended to use the **Creative Commons CC-BY** licence, which is an example of a permissive licence. This will allow scientists to use the data in e.g. presentations, scientific articles, and publications, and will also ensure attribution to the content author. Many universities and journals require CC-BY open-access licensing for published content, which will necessitate CC-BY for compatibility with open-access policies.

Creators who do not wish their content to be shared, reproduced, or used for commercial purposes, should directly engage with scientists to agree on the best form of licensing agreement. Many photographers have standard image licences, including royalty agreements. For considerations on payment for photos see 7.3.6.

We strongly recommend using a standard licence on all intellectual property and content. However, in the case that a citizen scientist does not wish to use a licence for their photos it is recommended that they come to an individual agreement. They should express their expectations for use of their photos when communicating with the scientist and sharing their photos. When communicating with a scientist and sharing photos that are not licensed, an agreement can look something like this:

1. Photo is sold - Photo (identifier) has been purchased by (scientist name) from (citizen scientist name) and therefore has ownership and rights to use in study and publication.
2. Photo is shared - (scientist name) has been granted the rights to use (identifier) photos for scientific study. The owner of the photo (citizen scientist name) retains ownership and copyrights. If this photo is used for study in the scientific process and/or published, (citizen scientist name) will be listed as owner of the photo and contributor to the study. The citizen scientist will be contacted at the conclusion of the study to confirm whether or not the photos were used.

[13] For clear explanations, examples, and licence text, see https://creativecommons.org/share-your-work/cclicenses/.

When soliciting photos, observations, survey responses, or any other type of intellectual content from the public, it is recommended as standard to include both a General Data Protection Regulation (GDPR) statement detailing how any personal data will be stored, alongside a licence agreement.

Chapter 8

OH* airglow and proton aurora

Abstract

Energetic proton precipitation causes proton aurora over Svalbard, but its effects on the chemistry and heat economy of the atmosphere are not well observed. Temperature and intensity changes in the OH layer have been observed during auroral electron precipitation (Enengl et al., 2021), but no studies have yet investigated the effect of auroral proton precipitation. HiTIES observes proton precipitation in the H-alpha wavelength as well as the $\mathrm{OH}^*(8{-}3), (9{-}4), (5{-}1)$ airglow vibrotational bands. These OH bands can provide an estimate of temperature and species density, which can be compared to the H-alpha profile and luminosity as a measure of proton aurora energy and flux. This chapter presents preliminary work using HiTIES to compare the proton aurora with the OH^* airglow spectra.

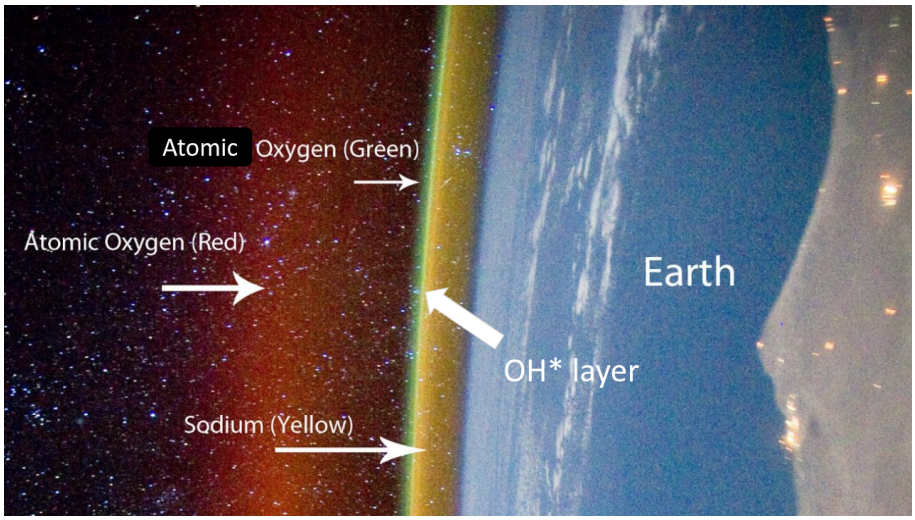

Figure 8.1: Image of the limb of Earth's atmosphere from space, labelled with the main visible airglow bands and location of the OH* layer.

8.1 Introduction

Airglow is the name given to natural atmospheric light produced by chemical reactions in the upper and middle atmospheres. Sunlight deposits energy which is stored as chemical energy, and later released as airglow photons. Due to the stratification of species in the atmosphere, there are many distinct layers of airglow. The tallest layers, usually visible in astronaut images of Earth, are produced by atomic oxygen in the thermosphere, but at lower altitudes we find the thin sodium layer and the hydroxyl layer, see Figure 8.1.

This thin layer of excited hydroxyl molecules, hereafter OH^*, is situated close to the mesopause altitude at 87km, with a depth of 8km. OH^* in this layer is produced by two principal reactions, producing different vibrotational states. The ozone-hydrogen reaction

$$\mathrm{O_3 + H \rightarrow OH^*}\,(v \geq 9) + \mathrm{O_2} + 3.34\,\mathrm{eV} \qquad \{4\}$$

and the perhydroxyl-oxygen reaction

$$\mathrm{O} + \mathrm{HO_2} \rightarrow \mathrm{OH}^* (v \geq 6) + \mathrm{O_2} \cdot \quad \{5\}$$

Lower vibrational states of OH* are then populated by radiative cascade. The vibrational branches from the states $v = 7, 8, 9$ can only be produced by the ozone-hydrogen reaction, while both the ozone-hydrogen and the perhydroxyl-oxygen reaction contribute to states $v \leq 6$. Globally, the ozone-hydrogen reaction 4 is dominant. However, in Svalbard, in the winter, the photodissociation rate is very low as the pole lies in darkness for months. This leads to a build-up of $\mathrm{HO_2}$, and the relative rate of the two production mechanisms becomes about equal (Holmen, 2016).

OH^* undergoes several loss processes. The dominant loss process is through quenching, reacting with atomic oxygen:

$$\mathrm{OH}^*(\mathrm{v}') + \mathrm{O} \longrightarrow \mathrm{H} + \mathrm{O_2} \cdot \quad \{6\}$$

Energy can also be lost during interaction with a molecule such as O, $\mathrm{O_2}$, or $\mathrm{N_2}$:

$$\mathrm{OH}^*(\mathrm{v}') + \mathrm{M} \longrightarrow \mathrm{OH}^*(\mathrm{v}'^{-}1) + \mathrm{M} \cdot \quad \{7\}$$

And finally, the production of airglow through radiative emission results in loss of OH^*:

$$\mathrm{OH}^*(\mathrm{v}') \longrightarrow \mathrm{OH}^*(\mathrm{v}'') + \mathrm{h}\nu \cdot \quad \{8\}$$

Since the OH* emission line ratios are dependent on the rotational temperature of the OH* molecule, and assuming thermal equilibrium, atmospheric temperature can be extracted from the OH* emission spectrum. This method is laid out well in Wüst et al. (2023) and references therein. The different vibrational states of OH* are separated in altitude from $100\mathrm{m}$ up to several km, so the different vibrotational bands of OH* emission lines sample populations from slightly different altitudes within the OH* layer (Wüst et al., 2023), see Figure 8.2. This figure also demonstrates the varying density of OH^* producing species in this altitude region.

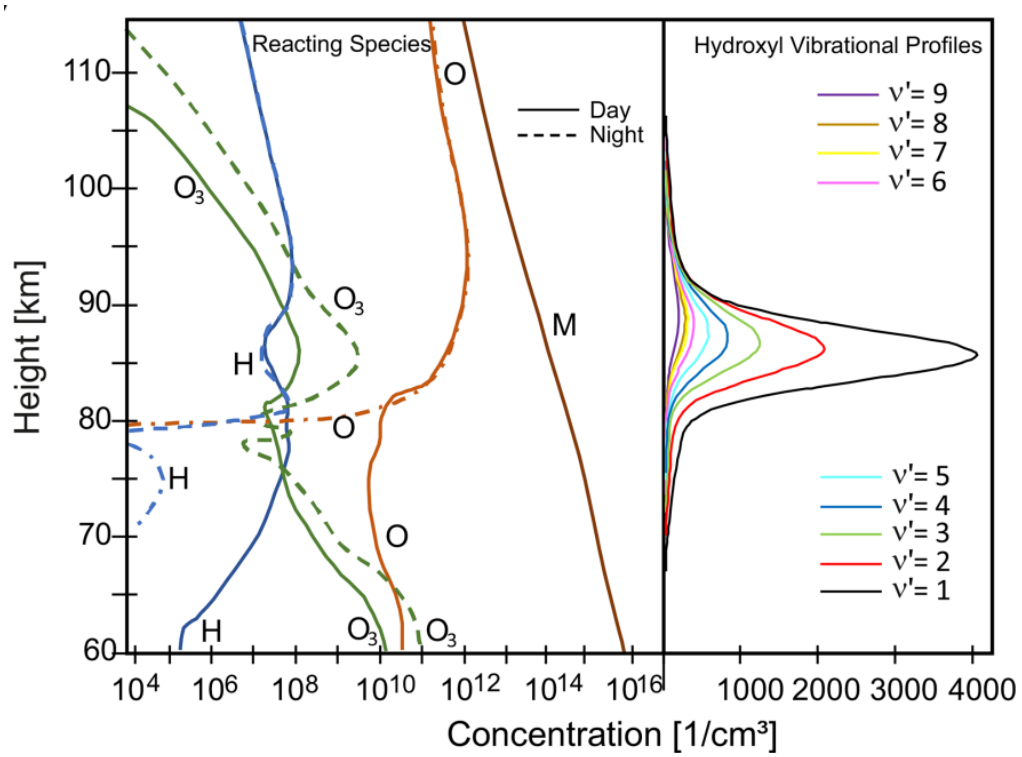

Figure 8.2: Left panel: vertical profiles of the major-reacting species in the OH photochemical scheme for daytime (solid) and nighttime (dashed) conditions between 60 and 115 km height, M denotes a collisional partner. Right panel: modelled OH^* profiles for v' = 1–9, taken from Wüst et al. (2023).

The altitude of the OH^* layer makes it particularly interesting, as it lies around the position of the mesopause, defined as the point where atmospheric temperature stops decreasing with altitude, and begins to rise again. This point varies significantly, with seasonal and diurnal variation, so the OH^* layer is embedded in a highly variable temperature gradient, see Figures 8.3 and 8.4. Depending on the location of the mesopause, the temperature can be either increasing or decreasing with altitude through the OH^* layer (Enengl et al., 2021).

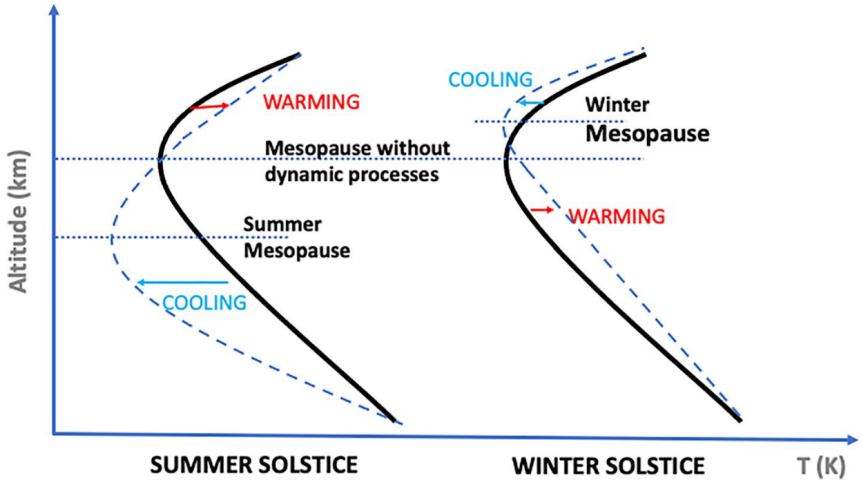

Figure 8.3: Schematic of the mesopause altitude variation at high latitudes during summer solstice (left) and winter solstice (right). The black curved lines represent the temperature profiles without considering the dynamic processes. The blue dashed curved lines represent the temperature profiles including the dynamical effects, from (Wang et al., 2022)

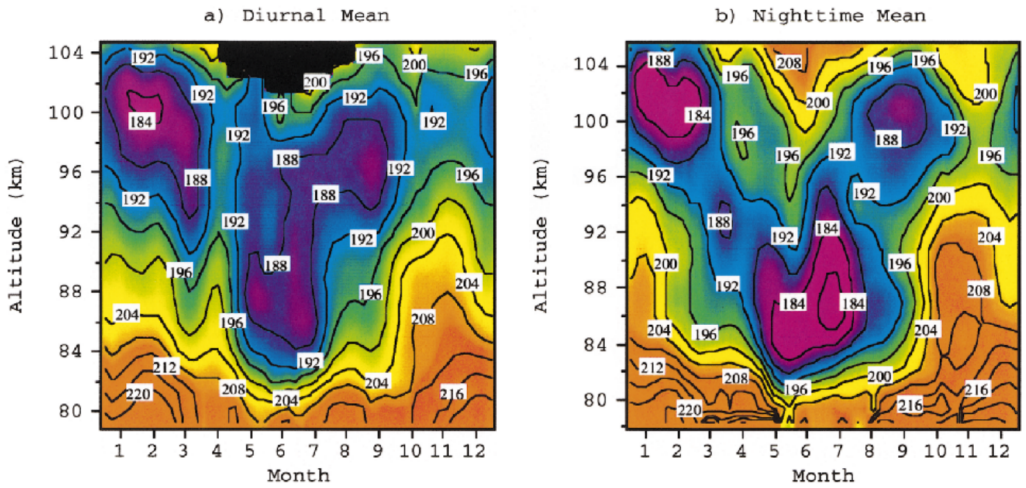

Figure 8.4: Contour plot of the mesopause region annual temperature structure using (a) data covering the complete diurnal cycle and (b) data covering just the nighttime period, from (States and Gardner, 2000)

The OH^* layer is thin, allowing remote sensing of a fairly specific altitude, in an area of significant interest. The mesopause region is impossible to measure in-situ with weather balloons, planes, or satellites, leaving us with only sounding-rockets. Remote sensing is therefore essential in understanding this layer of the atmosphere, its energy budget, physical processes, and chemistry.

8.1.1 Energetic particle precipitation at the mesopause

The effect of energetic particle precipitation (EPP) at the upper mesosphere lower thermosphere (UMLT) region is complicated. EPP can cause direct heating through collisions or Joule heating, but can also affect the atmospheric chemical composition through ionisation, dissociation and excitation. Differences in chemical composition leads to changes in the energy budget of the UMLT region. EPP has been observed to lead to heating, cooling, or no change in the mesospheric temperature (Tyssøy et al., 2010).

In Tyssøy et al. (2010), energetic proton precipitation is measured by the medium energy proton and electron detectors (MEPED) on board three NOAA satellites. Precipitation as low as $30\mathrm{keV}$ is shown to affect atmospheric temperatures up to ~ 20K at an altitude of $110\mathrm{km}$ including high-Arctic latitudes 78°- 82°. $30\mathrm{keV}$ is the minimum observable limit of MEPED, so even lower energy protons could also be present. The authors suggest cooling may be due to the production of odd hydrogen atoms destroying ozone. Ozone is the main absorbing species of solar UV radiation so a reduction in ozone would cause a cooling effect at this altitude.

Enengl et al. (2021) present the effect of energetic electron precipitation (EEP) as measured by the ESR on the OH airglow layer in Svalbard. Statistical and superposed epoch analysis shows that EEP was followed by a $10\mathrm{K}$ temperature reduction in the OH* rotational temperature. The authors suggest that EEP destroys the high altitude part of the OH* layer, reducing the mean emission height and therefore sampling the atmospheric ambient temperature at a lower altitude. The variation in the mesopause altitude means that this lower altitude could be either cooler or warmer depending on the local mesosphere temperature gradient, a possible explanation for the inconsistency described in Tyssøy et al. (2010).

8.1.2 Solar energetic protons and the ozone layer

High energy proton precipitation (tens to hundreds of MeV) during solar proton events (SPEs) is well known to deplete ozone in the stratosphere by the production of excess odd hydrogen and nitrogen through observations and modelling (e.g. Kalakoski et al., 2023; Nilsen et al., 2021; Jackman et al., 2001; Häkkilä et al., 2025). SPE causes ionisation of atmospheric oxygen and nitrogen species which react with water vapour, producing odd hydrogen and nitrogen molecules $\mathrm{HO_x}$ and $\mathrm{NO_x}$ (Solomon et al., 1981; Conway et al., 2000), which then reacts with ozone, leading to large but temporary (up to 70%) depletion in the ozone layer (e.g. Jackman et al., 2001; Kalakoski et al., 2023). However, the precipitation energy is significantly higher during SPEs than in high-latitude proton aurora, which has a characteristic energy of ~ 10 keV, several orders of magnitude less. Szeląg et al. (2022) shows that while temperature effects of SPEs in the stratosphere are usually masked by underlying variability, modelling shows a cooling effect of up to 3K.

8.1.3 The effect of proton aurora on the UMLT region

Electromagnetic Ion Cyclotron (EMIC) wave driven Isolated Proton Aurora (IPA) is related to destruction of the ozone layer in Ozaki et al. (2022), though the authors do not consider the proton precipitation itself to be the destruction mechanism. The authors suggest that ultra-relativistic electrons resonant with the EMIC wave directly ionise the O_3. High latitude dayside proton aurora is not typically EMIC driven, see Chapter 4, so this mechanism is unlikely to occur over Svalbard. Though proton precipitation accounts for 15% of the energy deposition in the auroral zone it is often discounted, not being the dominant energy source. However, proton precipitation can lead to several orders of magnitude increase in electron density and Hall and Pedersen conductivities in the E-region (Yuan et al., 2014).

8.2 Potential mechanisms

8.2.1 Production of HOx and NOx

Odd hydrogen and nitrogen have been observed to be produced by solar energetic protons and precipitating electrons, which have typically much higher energy than auroral protons and so can penetrate as low as the stratospheric ozone layer. $\mathrm{HO_x}$ and $\mathrm{NO_x}$ react strongly with $\mathrm{O_3}$, destroying high altitude

ozone. Less ozone is therefore available to produce OH^* through reaction 4. Auroral protons are not typically considered a main producer of NO_x and HO_x, but are capable of penetrating down close to the OH^* layer at 30-100keV, so it might be possible with a large amount of accelerated proton aurora to cause dimming in the upper parts of the OH^* layer, leading to a dimming of the observed spectrum, and either cooling or heating depending on the local temperature gradient. 'Normal' auroral protons are much more common than SEP protons, particularly on Svalbard, so over a long period the accumulated event of auroral protons could be as significant as SEP events, or even more so, we don't know yet.

8.2.2 Joule heating

Since proton precipitation is linked to an increase in conductivity, it is likely to contribute to Joule heating in the E-region. Measurements of Joule heating are typically quite limited spatially and temporally, and recent work indicates that Joule heating is significantly underestimated by traditional large-scale measurements (Krcelic et al., 2023). Further, the effect of proton aurora on the atmosphere is poorly understood, including the Joule heating input. Joule heating in the E-region due to energetic proton precipitation could increase the temperature of the OH* layer.

8.3 Observations and method

HiTIES spectra were taken on the 09, 10, and 11 January 2022 during hours with no cloud or bright moonlight. The spectra were processed to obtain the integrated intensity of proton aurora in the Hα panel, a background was fitted and subtracted for each spectrum, and integrated intensity was calculated for a set window around the Hα rest wavelength and blueshifted wing. The difference between the centre of mass of the spectrum and the Hα wavelength was calculated as a rough proxy for the proton precipitation energy.

Three OH^* vibrational bands were measured in HiTIES. The $OH^*(8,3)$ band which lies in the $O+$ panel, and the $OH^*(9,4)$ and $OH^*(5,1)$ which lie in the OH^* panel. By modelling the OH spectrum, fitting can return the rotational temperature by using the `synth_oh` IDL software from the group's `hsoft` codebase. The fitting was done using IDL's native `curvefit` routine.

8.4 Preliminary Results

8.4.1 OH temperatures

Fitting from the $OH^*(8,3)$ and $OH^*(5,1)$ bands indicated rotational temperatures of 199K and 149K respectively. The lowest temperature of the mesopause is typically reported at -100° C or 174K, so at least $OH^*(5,1)$ T_{rot} is not accurate, indicating a need to improve the fitting. The first step should be to include water vapour. This can reduce the intensity of the OH^* lines, and so should be accounted for, particularly when clouds are present - it can be modelled following work in Chadney et al. (2017).

8.4.2 Comparison of proton aurora and OH temperature

Despite the problem with absolute estimation of temperature, I proceeded with some fitting of just the $O+$ panel's $OH^*(8,3)$, since changes in temperature should be preserved even if the absolute value is off. I stuck with the $(8,3)$ as the fitting was resulting in more reasonable temperatures.

A few preliminary results are shown in Figure 8.5, showing integrated proton intensity against the results of spectrally fitting the $OH^*(8,3)$ band in the $O+$ panel. From first glance, it appears that T_{rot} and Hα intensity track well together. Reasons for this could be to do with some background sky brightness, for example clouds moving over the spectrograph, which affects both the Hα intensity and the OH fitting. The next steps in this work would be improving the fitting and intensity algorithm to ensure that the background conditions are handled more thoroughly. Since these measurements are from different parts of the spectrum, the proton aurora should have no effect directly on the OH^* spectrum fitting.

Another reason for the observed correlation between Hα intensity and OH^* temperature could be due to the rotation of Svalbard through different regions of the ionosphere - through the morning hours

Svalbard passes through the dayside proton precipitation oval, the polar cap and the cusp. The neutral temperature is naturally changed by different ionospheric conditions through these regions. This means that proton aurora coincident with a change in temperature could be due to entering the cusp for example, so this should be ruled out. In addition, effort should be made to account for the natural diurnal variation of OH^*.

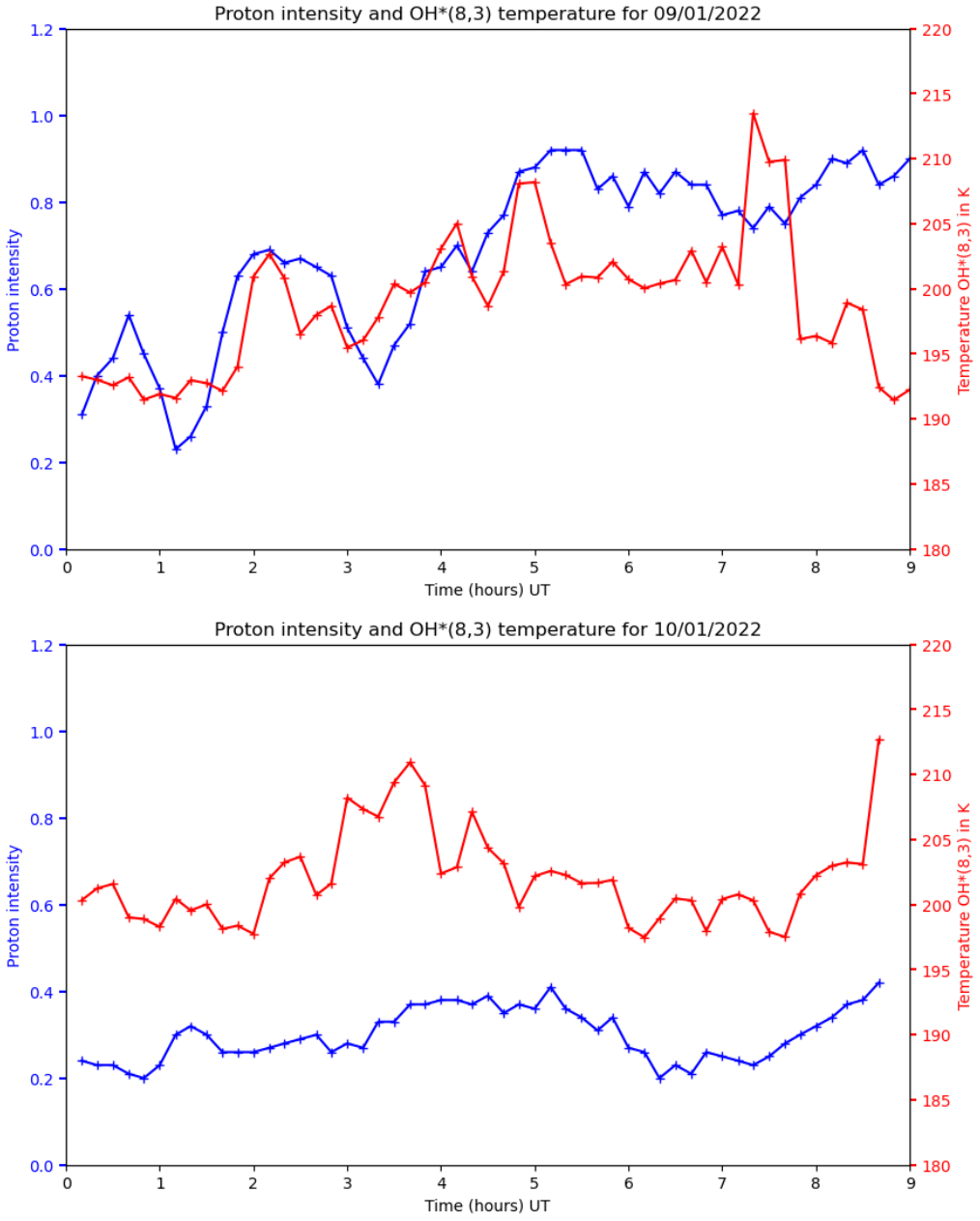

Figure 8.5: Plot of proton intensity (blue) and OH*(8,3) rotational temperature (red) against time in UT, on the 09 and 10 January 2022

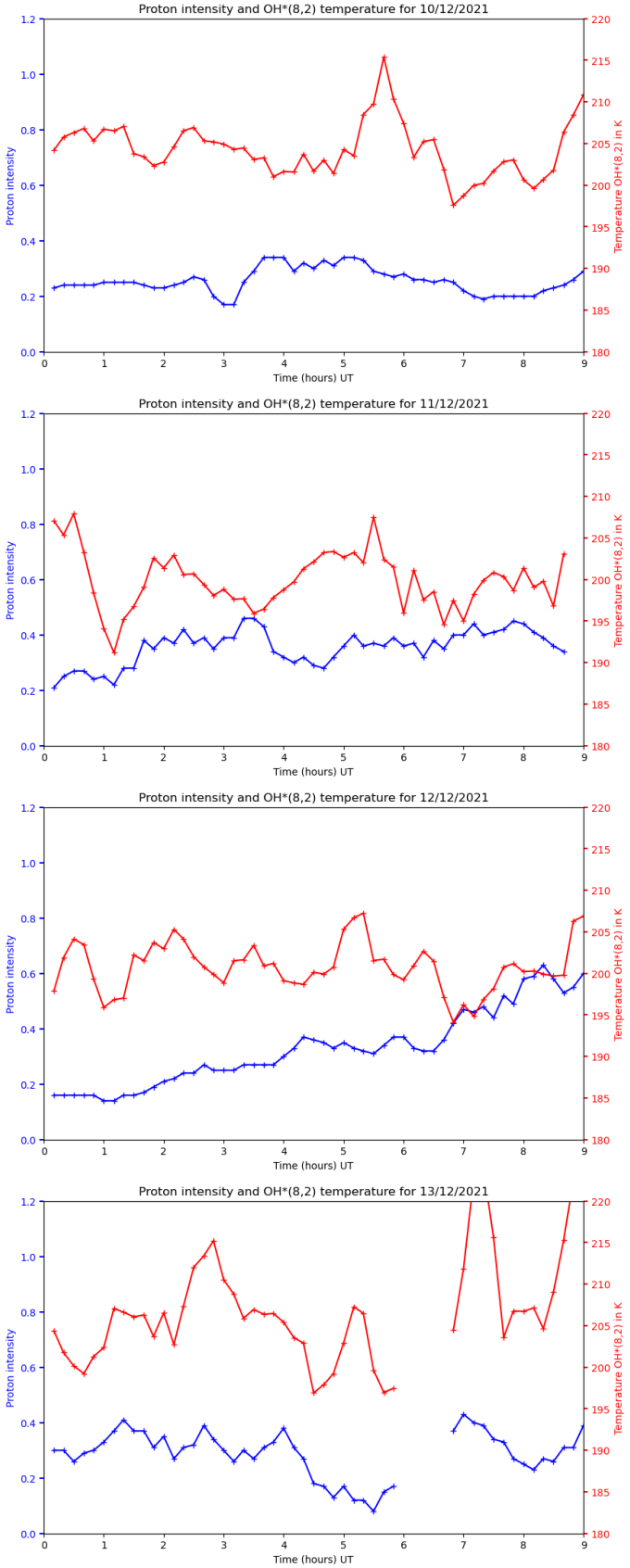

Figure 8.6: More preliminary plots of OH*(8,3) rotational temperature (red) plotting with proton intensity (blue) in time in UT, on the 10 11 12 and 13 December 2021.

8.5 Future work

This work represents the thinking, planning, and start of a study on the proton aurora and its effect on OH rotational temperature.

The next steps should be to conduct a superposed epoch analysis, stacking observations in a window around precipitation onset. Compared with electron precipitation, proton precipitation onset is usually slow, taking perhaps half an hour to fade in, so there is a challenge in deciding on a reasonable definition of precipitation onset. An easy option would be once the precipitation reaches some threshold above background intensity, for example 10%. Several methods should be tested.

A much larger amount of data should be processed to provide a high number of events for statistical study. Some amount of parallelisation could be implemented in the processing, as the current pipeline is quite slow, which would allow many more events to be analysed.

The different vibrational bands originate in different parts of the OH^* layer, see Figure 8.2, and so sample the rotational temperature at slightly different heights. It could be interesting to use these different bands to test the hypothesis described in Enengl et al. (2021), that the heating/cooling effect is due to destruction of the higher altitude layers. If this were the case, the $\mathrm{OH}^*(9,4)$ and $(8,3)$ would decrease in intensity, while the $\mathrm{OH}^*(5,1)$ band would be less affected.

In addition, the $\mathrm{OH}^*(9,4)$ and $\mathrm{OH}^*(8,3)$ are only produced by the oxygen-hydrogen reaction 4, while the $\mathrm{OH}^*(5,1)$ state can be produced by reaction 4 and the perhydroxyl reaction 5. Changes in the intensity ratio between the upper and lower vibrational levels could be expected if there was a change in the rates of these production mechanisms, for example due to the destruction of O_3.

8.6 Summary

This chapter explores the potential impact of auroral proton precipitation on the OH^* layer near the mesopause, a region of high variability and scientific interest. While previous studies have examined how energetic electron precipitation influences OH^* rotational temperature and emission, the effects of proton aurora remain largely unknown. Using HiTIES observations of Hα emission as a measure of proton precipitation alongside OH^* vibrational bands, preliminary results suggest a correlation between proton auroral intensity and changes in OH^* rotational temperature, though instrumental and background effects cannot yet be ruled out. Proposed mechanisms include ozone depletion reducing OH^* production, and enhanced conductivity driving Joule heating, both of which could alter apparent OH^* temperatures. Early fitting challenges highlight the need to refine methods such as including water vapour absorption and handling natural variability, but the work establishes a foundation for future statistical studies. Expanding the dataset and examining different vibrational bands could help test whether proton aurora modifies the vertical structure of the OH^* layer, potentially distinguishing chemical from thermal effects.

Chapter 9

Conclusions

The aim of this research was to utilise high-resolution spectral data to answer open questions in the studies of several types of strange auroral phenomena. Those questions were firstly, do observations of high-latitude dayside proton aurora show signs of acceleration or precipitation by EMIC plasma waves. Next, what is the nature these continuum aurora we have found, what does the data tell us, and can we use the data available to point to any mechanism responsible. Finally, is there any effect from proton aurora on the polar mesopause region? These questions all target strange, or understudied auroral forms, observed in Svalbard mostly on the dayside. High-resolution spectrography was used to attempt to answer these questions.

To conclude the work on proton aurora, based on work shown in Chapter 4, EMIC waves are probably not playing an important role in the dayside proton aurora. The clearest evidence is that Pc1 pulsations are so rarely observed over Svalbard in the dayside, while accelerated proton precipitation is a near daily occurrence. Several additional methods find only perhaps a small contribution from EMIC waves in the acceleration profile of the proton aurora, in the occurrence statistics of proton aurora, and no periodicity was found in the proton aurora signal, contrary to findings in subauroral EMIC accelerated proton aurora. What then is causing the acceleration of proton aurora in the Svalbard dayside? A few suggestions have been offered, but none of the other mechanisms considered were found probable. A limitation of this work is that the different proton aurora regimes are not well defined and separated - separating cusp aurora from dayside oval and dayside polar cap would hopefully make any patterns much clearer, but it would be non-trivial and would require simultaneous observations with more instruments e.g. EISCAT and SuperDARN, so the sample size would be more limited. I think the main conclusions of this work still stand however, and EMIC waves are not a significant mechanism for Svalbard dayside proton aurora, of any type. Future work should carry out more rigorous identification of the proton precipitation origin, and a broader statistical study on patterns in proton precipitation energy through each MLT would be valuable. In the meantime, the findings presented here will be useful to anyone studying the Svalbard regime, as EMIC-driven ion precipitation can probably be ruled out, for example, as a relativistic electron indicator.

This thesis presents the discovery, identification, and subsequent investigations of an entirely new auroral form, GHOST, in Chapter 5. This was a highly collaborative project, involving many scientists and citizen scientists, which was very fun to be part of. My contribution to the primary discovery was obtaining and identifying continuum in the high-resolution data. This is the first (to my knowledge) continuum spectrum at this high a resolution, and confirms that the continuum is a structured pseudo-continuum, as expected. This first piece of work also identified proton aurora during the continuum - from which we initially thought perhaps proton aurora is an ingredient in the continuum production mechanism. After further investigation we could later confirm that the patchy protons were a reconnection signature. This is great because it confirms continuum occurs in the cusp[1], and that there is active reconnection. The contribution of protons to the energy input for continuum is an open question.

Next, in Chapter 6, a study on the mechanism of GHOST is presented. While the initial fitting, realisation about N_2 and overall main idea of the study is my own work, this was again a highly collaborative effort which owes a huge amount to my co-authors. For the first time we can resolve individual rotational lines for the continuum spectrum, providing evidence that the continuum mechanism might just be very hot N_2 rather than NO as suggested by .e.g. Harding et al. (2020) in the case of STEVE continuum. N_2 appears to have gone unconsidered so far as the spectrum is quite well known and well modelled in *typical* auroral conditions, so is easily disregarded. However, in the GHOST ionosphere there is extreme shear flow, extreme ion temperatures, and quite high neutral temperatures, which could result in a highly atypical energisation of N_2 (and other abundant molecules). This work is the

[1]Depending on how specific your cusp definition is

first to add in the additional electronic excitations of N_2 from the Infra-red Afterglow band system, as well as the N_2+ Meinel and O_2+ First positive band systems. Fiona Ball and myself spent many hours working to understand how the background conditions could fit together, and eventually the picture presented in Figure 6.10 began to emerge. From comparing the background conditions during different GHOST events, we postulate that the cusp soft precipitation, daylight, and strong ionospheric flow due to dominant By solar wind conditions, all combines to produce GHOST conditions (high temperature, excited $N_2(+)$) in the ionosphere, which can be enhanced by additional precipitation. While we just don't have the evidence yet to confirm to what extent this picture is accurate, it should give us a nice starting point in trying to figure out some of the initial questions we have about GHOST. I think this potential mechanism study should generate a lot of good science, as we have answered and opened new questions. How can we quantify the strength of a GHOST event for a start. Then, is the N_2 emission idea correct? What are we missing in the spectrum and what species or states are there? How does spectral fitting of N_2 perform over the rest of the optical range? Then, is the flow/shear necessary and can both the initial polar cap and return flows induce enough shear? Can our energy inputs be modelled and what level of excitation is actually achievable? The list seems fairly endless from here. I think this study has started a very interesting discussion in the field, and to me is the most significant scientific output of this thesis.

Chapter 7 presents my contribution to the ARCTICS ISSI Working Group and SolarMax mission. I have contributed to ongoing citizen science projects, new studies based on citizen science data, and the handbook for citizen science. Citizen science has in general been a through-line of this work; both the first and second GHOST studies utilise citizen science, both in the contributed photographs shown in Chapter 5, and in contributing to the study as a whole in Chapter 6. From my work in this area, and the recent discoveries of GHOST, STEVE, fragments, picket fence, streaks, dunes, and proton blobs, I think that professional aurora science has a significant blind spot (or spots). Aurora citizen scientists are an extremely valuable resource, often with thousands of hours of observing experience, and their insight and data often fills the gaps where we aren't looking. Citizen scientists provide many observations from the sub-auroral region where dunes, blobs, STEVE, RAGDA, and SAR arcs can be seen, and where professional aurora science lacks instrumentation. Locations such as the north of Scotland, Atlantic islands, and southern Scandinavia could benefit from increased instrumentation to study some of these strange aurora. Professional instrumentation is also highly specialised to image only in known wavelengths, such as the green and red lines, and so has missed auroral continuum emissions such as GHOST and the oval continuum for decades. The newer generations of mirror-less/DSLR cameras are capable of providing excellent quality images and time-lapses of aurora, which have significantly closed the gap between the capabilities of professional and amateur equipment. But many of the questions opened by these citizen observations can only be answered by professional instrumentation. Maybe we need a subauroral HiTIES for example, as high-resolution spectra of STEVE, could be a game-changer in understanding its production mechanism. Professional level spectrography of dunes would also be very interesting to see. To me, citizen science is one of the most exciting areas of modern aurora physics, and I hope to see increased participation on the professional science side.

Finally, I have started some work on the effects of proton aurora on the polar atmosphere in Chapter 8. The effect of auroral precipitation on the atmosphere, in general, is a significant open question in the field, and I think continuing this study, or something similar, would be very interesting. From the preliminary work, it's not possible to conclude much, but there is a promising start here for somebody to pick up.

Overall, I have probably opened more questions than I have answered, which, to me, is a good contribution to the field of aurora science.

9.1 Future work

In this section I lay out a series of directions for future studies.

9.1.1 GHOST

Further spectral modelling/fitting

To investigate whether the hot N_2 continuum mechanism is able to explain the observed spectrum, further modelling at other wavelength ranges would be very valuable. The Vegard-Kaplan bands should be increasingly relevant towards the shorter wavelengths (corresponding to lower, easier to excite, vibrational energy levels), so we might expect it to be a larger part of the spectrum. Other bands and species could be added from the known available species in the upper atmosphere. Fitting should first be carried out in the other two available HiTIES panels, the Hα and OH. If continuum events can be found earlier enough, data with the 4-panel HiTIES mosaic filter might also be available, which would allow us to look at some of the blue wavelengths around Hβ. Otherwise, the older 3-panel filter with Hβ and N_2+ panels at $\sim 450\text{nm}$ could be run for a season to see if the mechanism fits in this shorter wavelength region. The MISS spectrograph at UNIS already has many low-resolution spectra of continuum - similar modelling could be run over a large, coarse, area to test whether we can reproduce the spectrum over the entire wavelength. This would be a larger modelling effort, and it would be harder to separate the contribution of different species without the shape of the rotational spectra to use.

Citizen scientist identification

Citizen science identifications of GHOST would be extremely useful to build up a wider event base. If GHOST does prove to be a dayside/cusp only phenomenon, only Svalbard locals will be capable of imaging it. However, other GHOSTs have been identified more in the nightside, poleward of the auroral oval. Northern areas of Norway, Finland, Russia, and Greenland could be capable of imaging this, particularly during high Kp geomagnetic conditions. The main problem is positively identifying GHOST, and not confusing it with other 'white' appearing aurora in RGB cameras, which can be observed due to overlap of green and red aurora.

Ionospheric flow

SuperDARN and EISCAT could be used to study the flow conditions during GHOST. The background conditions presented in both Chapters 5 and 6 have indicated that strong ionospheric flow could be providing an important part of the energy needed to produce GHOST continuum emissions, in particular during flux transfer events under By-dominated IMF conditions. I would like to use SuperDARN measurements of events identified in the All-sky and MISS spectrograph from Svalbard, to study flow conditions, similar to a recent STEVE + SuperDARN study by Macho et al. (2024). The SuperDARN radars in northern Canada and Finland are ideally located for studying high latitude flow, including just north of Svalbard. I would also look to use optical measurements from around the Arctic, including by citizen scientists, to increase the number of identified GHOST events and to provide the best possible conjunction between radar and optical measurements.

Energy calculations

A more theoretical study would be valuable looking at the total energy possibly generated by the mechanisms outline in Chapter 6. This would be a large and complex effort. Following methodology in e.g. Liang and Donovan (2024) it should be possible to calculate the maximum energy from the shear flow measured in DMSP, and how much excitation could be expected from this contributor. Even back of the envelope calculations based on the temperatures measured in EISCAT would be valuable to see what levels of excitation we can expect. Ongoing work by Brian Harding, (who presented the NO idea for STEVE continuum emission in Harding et al. (2020)), looks at the excitation level achievable in STEVE, and the results of this work could be very informative in applying similar methods to GHOST.

The goal of this work would be to find some upper and lower bounds on the energy needed to produce excitation of the level found in spectral fitting, and investigate whether the proposed mechanism works.

Comparison with STEVE and oval continuum

There are currently three parallel investigations looking into three different continuum regimes. The subauroral STEVE, the auroral 'oval continuum', and the 'super'-auroral GHOST. Shear flow seems to be important for both STEVE and GHOST, and precipitation seems to be important for GHOST and oval continuum. A review of the known features of all three forms, identifying where they overlap and contrast, would be a very useful piece of work for all three. The study could compare all known data sources, comparing appearance, magnetospheric conditions, appearance of picket fence/streaks/fragments, ion/electron diagnostics from ISR measurements, temperatures, and any other interesting things that come up.

Statistical study

Once enough GHOST events are detected, a statistical study is a clear course of action. The occurrence and strength of the event can be compared in MLT, solar wind conditions, and any other feature space available. This could confirm whether strong GHOST events are always located in the cusp, and identify other patterns in the occurrence of non-cusp GHOST. It is also the only solid method of determining whether the solar wind, shadow height, and cusp parts of the mechanism presented in this work, are truly needed or just coincidental.

Satellite and communications risk

Due to the identification of strong ion and neutral heating in GHOST, there could be an increased risk to satellites through enhanced neutral density at Low-Earth Orbit, and to RF communication during GHOST events. One could directly study the total electron content (TEC) and GNSS scintillation for a start.

9.1.2 Proton aurora

Effect on the polar atmosphere

As outlined in Chapter 8, there is plenty of further work to do in exploring whether the OH airglow layer shows any effect due to proton precipitation. Starting with a superposed epoch analysis, and perhaps including comparisons of the different observed bands, it would be interesting to see if there is any measurable difference in the behaviour of OH^* in different vibrational states.

9.1.3 Other high-resolution spectra work

High-resolution spectrograph data would be valuable for study of fragments. I have previously attempted to get a high-resolution spectrum, but it was unsuccessful. Fragments are rare, small, and short-lived, and none of the events identified by others passed through the HiTIES spectrograph slit. Still, new fragment identifications from AuroraZoo or otherwise should be checked in HiTIES if possible. Observations of fragments have found emission in the 5577ÅO and 6730Å$\mathrm{N_2 1P}$ wavelengths through narrow band filter measurements, but not at the 4278Å$\mathrm{N_2+}$ or the 7774ÅO wavelengths (Dreyer et al., 2021). High-resolution spectra in HiTIES could give more detailed insight into the $\mathrm{N_2 1P}$ emission, and could help constrain the energy and temperature of the fragments.

9.1.4 Short projects

I have come up with a few short studies which could be good for a master's or summer student;

Planeterella spectrum

The planeterella is a copy of Birkeland's original experiment, consisting of a vacuum chamber containing two charged metal spheres. When evacuated and powered with high-voltage, current flowing between the spheres produces emission from excited neutrals, simulating aurora. Southampton and UNIS in Svalbard both own one of these. It would be a fun short project to take the planeterella up to the KHO, and point some of the spectrographs at it. Probably both MISS and HiTIES would be best. The remnant atmosphere producing the light emission is the same composition as normal atmosphere at sea level, so 78% N_2 and the rest mostly O_2, though the gas composition can also be changed using a gas pipette bladder. Spectra could also be compared at different voltages, concentrations etc. The planeterella can produce a pale mauve colour emission similar to GHOST, and it would be interesting to see the spectrum of this emission.

OH temperature map

During my PhD I have produced some code for creating maps of airglow temperature from the All-sky airglow camera at KHO, but didn't get as far as properly calibrating it. A flat-field image could be taken at KHO, to improve the calibration. I have it set up to take darks from the corner pixels, which should be adequate. Cross-calibration can be done with comparison to airglow temperatures from HiTIES, or several other instruments at KHO. Once calibrated, the OH temperature map should be projected over the map of Svalbard. The resulting map could be made into a live data product, both with updating maps and keograms. This could be used for viewing gravity waves, mesospheric bores, and perhaps auroral effects. There is no such map available yet, so it would be interesting to see what appears.

Bibliography

Archer, W. E., Gallardo-Lacourt, B., Perry, G. W., St.-Maurice, J. P., Buchert, S. C., and Donovan, E.: Steve: The Optical Signature of Intense Subauroral Ion Drifts, Geophysical Research Letters, 46, 6279–6286, https://doi.org/10.1029/2019GL082687, 2019a.

Archer, W. E., Maurice, J.-P. S., Gallardo-Lacourt, B., Perry, G. W., Cully, C. M., Donovan, E., Gillies, D. M., Downie, R., Smith, J., and Eurich, D.: The Vertical Distribution of the Optical Emissions of a Steve and Picket Fence Event, Geophysical Research Letters, 46, 10 719–10 725, https://doi.org/10.1029/2019GL084473, 2019b.

Aruliah, A. L. and Griffin, E.: Evidence of meso-scale structure in the high-latitude thermosphere, Annales Geophysicae, 19, 37–46, https://doi.org/10.5194/angeo-19-37-2001, 2001.

Aruliah, A. L., Griffin, E. M., Yiu, H.-C. I., McWhirter, I., and Charalambous, A.: SCANDI- an all-sky Doppler imager for studies of thermospheric spatial structure, Annales Geophysicae, 28, 549–567, https://doi.org/10.5194/angeo-28-549-2010, 2010.

Bates, D. R.: Cause of terrestrial nightglow continuum, Proceedings of the Royal Society of London. Series A: Mathematical and Physical Sciences, 443, 227–237, https://doi.org/10.1098/rspa.1993.0141, 1993.

Baumjohann, W. and Treumann, R. A.: Basic Space Plasma Physics: Revised Edition, Imperial College Press, https://doi.org/10.1142/p015, 2012.

Beasley-Hall, P. G., Papadelos, P., Hewitt, A., Lassaline, C. R., Umbers, K. D. L., and Guzik, M. T.: Sci-comm "behind the scenes": Gendered narratives of scientific outreach activities in the life sciences, https://doi.org/10.1101/2024.02.28.582614, 2024.

Benesch, W., Rivers, D., and Moore, J.: High resolution spectrum of the N2+ Meinel system to 11 250 Å, Journal of the Optical Society of America, 70, 792–799, 1980.

Blake, C., Rhanor, A., and Pajic, C.: The demographics of citizen science participation and its implications for data quality and environmental justice, Citizen Science: Theory and Practice, 5, https://doi.org/10.5334/cstp.320, 2020.

Bonney, R., Cooper, C. B., Dickinson, J., Kelling, S., Phillips, T., Rosenberg, K. V., and Shirk, J.: Citizen science: A developing tool for expanding science knowledge and scientific literacy, https://doi.org/10.1525/bio.2009.59.11.9, 2009.

Bräysy, T. and Mursula, K.: Conjugate observations of electromagnetic ion cyclotron waves, Journal of Geophysical Research: Space Physics, 106, 6029–6041, https://doi.org/10.1029/2000ja003009, 2001.

Burch, J. L., Reiff, P. H., Menietti, J. D., Heelis, R. A., Hanson, W. B., Shawhan, S. D., Shelley, E. G., Sugiura, M., Weimer, D. R., and Winningham, J. D.: IMF By-dependent plasma flow and Birkeland currents in the dayside magnetosphere: 1. Dynamics Explorer observations, Journal of Geophysical Research: Space Physics, 90, 1577–1593, https://doi.org/10.1029/ja090ia02p01577, 1985.

Carroll, P. and Rubalcava, H.: Near Infra-Red System of Nitrogen, Nature, 184, 119–120, 1959.

Carroll, P. and Rubalcava, H.: Rotational Analysis of the 5-1 Band of the B'-B System of N2, Proceedings of the Physical Society, 76, 337, 1960.

Carroll, P. and Sayers, N.: The Band Spectrum of Nitrogen: New Studies of the Triplet Systems, Proceedings of the Physical Society. Section A, 66, 1138, 1953.

Carson, S. and Rock, J.: How do New Zealand Scientists perceive the benefits and limitation of Citizen Science?, New Zealand Science Review, 79, https://doi.org/10.26686/nzsr.v79.8344, 2024.

Chadney, J. M., Whiter, D. K., and Lanchester, B. S.: Effect of water vapour absorption on hydroxyl temperatures measured from Svalbard, 35, 481–491, https://doi.org/10.5194/angeo-35-481-2017, 2017.

Chakrabarti, S., Pallamraju, D., Baumgardner, J., and Vaillancourt, J.: HiTIES: A High Throughput Imaging Echelle Spectrogragh for ground-based visible airglow and auroral studies, Journal of Geophysical Research: Space Physics, 106, 30 337–30 348, https://doi.org/10.1029/2001JA001105, 2001.

Chamberlain, J. W.: Physics of the Aurora and Airglow, Academic Press, 1961.

Chamberlain, J. W. and Oliver, N. J.: Atomic and molecular transitions in auroral spectra, Journal of Geophysical Research, 58, 457–472, https://doi.org/10.1029/JZ058i004p00457, 1953.

Collins, S. A., Sullivan, M., and Bray, H. J.: Exploring scientists' perceptions of citizen science for public engagement with science, Journal of Science Communication, 21, https://doi.org/10.22323/2.21070201, 2022.

Conway, R. R., Summers, M. E., Stevens, M. H., Cardon, J. G., Preusse, P., and Offermann, D.: Satellite observations of upper stratospheric and mesospheric OH: The HO(x) dilemma, Geophysical Research Letters, 27, 2613–2616, https://doi.org/10.1029/2000GL011698, 2000.

Cornelius, J. R. and Mazzella, Andrew J., J.: The topside ionospheric plasma monitor (SSIES, SSIES-2 and SSIES-3) on the spacecraft of the Defense Meteorological Satellite Program (DMSP), user's guide. Volume 2: Programmer's guide for software at AFSFC, Scientific Report No. 4 RDP, Inc., Waltham, MA., 1994.

Cornwall, J. M., Coroniti, F. V., and Thorne, R. M.: Unified theory of SAR arc formation at the plasmapause, Journal of Geophysical Research, 76, 4428–4445, https://doi.org/10.1029/JA076I019P04428, 1971.

Cowley, S. W. H. and Lockwood, M.: Excitation and decay of solar wind-driven flows in the magnetosphere-ionosphere system, Annales Geophysicae, 10, 103–115, 1992.

Dayton-Oxland, R. A., Whiter, D., Kim, H., and Lanchester, B.: No statistical link between proton aurora and Pc1 pulsations in the high-latitude dayside, ESS Open Archive, https://doi.org/10.22541/essoar.169945307.73073056/v2, 2024.

Deehr, C. and Lummerzheim, D.: Ground-based optical observations of hydrogen emission in the auroral substorm, Journal of Geophysical Research: Space Physics, 106, 33–44, https://doi.org/10.1029/2000JA002010, 2001.

Deehr, C. S., Lorentzen, D. A., Sigernes, F., and Smith, R. W.: Dayside auroral hydrogen emission as an aeronomic signature of magnetospheric boundary layer processes, Geophysical Research Letters, 25, 2111–2114, https://doi.org/10.1029/98GL01535, 1998.

Diver, D.: Plasma Theory & Diagnostics 1, University of Glasgow, Lecture Series, 2019.

Dreyer, J., Partamies, N., Whiter, D., Ellingsen, P. G., Baddeley, L., and Buchert, S. C.: Characteristics of fragmented aurora-like emissions (FAEs) observed on Svalbard, Annales Geophysicae, 39, 277–288, https://doi.org/10.5194/angeo-39-277-2021, 2021.

Dungey, J. W.: INTERPLANETARY MAGNETIC FIELD AND THE AURORAL ZONES, 1961.

Eather, R. H.: Auroral proton precipitation and hydrogen emissions, Reviews of Geophysics, 5, 207–285, https://doi.org/10.1029/RG005i003p00207, 1967.

Egeland, A. and Burke, W. J.: Auroral hydrogen emissions: A historic survey, History of Geo- and Space Sciences, 10, 201–213, https://doi.org/10.5194/HGSS-10-201-2019, 2019.

Enengl, F., Partamies, N., Ivchenko, N., and Baddeley, L.: On the relationship of energetic particle precipitation and mesopause temperature, Annales Geophysicae, 39, 795–809, https://doi.org/10.5194/ANGEO-39-795-2021, 2021.

Engebretson, M. J., Moen, J., Posch, J. L., Lu, F., Lessard, M. R., Kim, H., and Lorentzen, D. A.: Searching for ULF signatures of the cusp: Observations from search coil magnetometers and auroral imagers in Svalbard, Journal of Geophysical Research: Space Physics, 114, https://doi.org/10.1029/2009JA014278, 2009.

Engebretson, M. J., Yeoman, T. K., Oksavik, K., Søraas, F., Sigernes, F., Moen, J. I., Johnsen, M. G., Pilipenko, V. A., Posch, J. L., Lessard, M. R., Lavraud, B., Hartinger, M. D., Clausen, L. B., Raita, T., and Stolle, C.: Multi-instrument observations from Svalbard of a traveling convection vortex, electromagnetic ion cyclotron wave burst, and proton precipitation associated with a bow shock instability, Journal of Geophysical Research: Space Physics, 118, 2975–2997, https://doi.org/10.1002/JGRA.50291, 2013.

Evans, W. F., Gattinger, R. L., Slanger, T. G., Saran, D. V., Degenstein, D. A., and Llewellyn, E. J.: Discovery of the FeO orange bands in the terrestrial night airglow spectrum obtained with OSIRIS on the Odin spacecraft, Geophysical Research Letters, 37, https://doi.org/10.1029/2010GL045310, 2010.

Fairfield, D. H.: Average and unusual locations of the Earth's magnetopause and bow shock, Journal of Geophysical Research, 76, 6700–6716, https://doi.org/10.1029/JA076I028P06700, 1971.

Feldstein, Y. I.: A quarter of a century with the auroral oval, Eos, Transactions American Geophysical Union, 67, 761–767, https://doi.org/10.1029/EO067I040P00761-02, 1986.

Francia, P., Regi, M., Lauretis, M. D., Pezzopane, M., Cesaroni, C., Spogli, L., and Raita, T.: A case study of correspondence between Pc1 activity and ionospheric irregularities at polar latitudes, Earth, Planets and Space, 72, 1–12, https://doi.org/10.1186/s40623-020-01184-4, 2020.

Gabrielse, C., Kaeppler, S. R., Lu, G., Wang, C. P., and Yu, Y.: Energetic particle dynamics, precipitation, and conductivity, Cross-Scale Coupling and Energy Transfer in the Magnetosphere-Ionosphere-Thermosphere System, pp. 217–300, https://doi.org/10.1016/B978-0-12-821366-7.00002-0, 2022.

Galand, M. and Chakrabarti, S.: Proton aurora observed from the ground, Journal of Atmospheric and Solar-Terrestrial Physics, 68, 1488–1501, https://doi.org/10.1016/j.jastp.2005.04.013, passive Optics Aeronomy, 2006.

Galand, M., Fuller-Rowell, T. J., and Codrescu, M. V.: Response of the upper atmosphere to auroral protons, Journal of Geophysical Research: Space Physics, 106, 127–139, https://doi.org/10.1029/2000JA002009, 2001.

Gallardo-Lacourt, B., Nishimura, Y., Donovan, E., Gillies, D. M., Perry, G. W., Archer, W. E., Nava, O. A., and Spanswick, E. L.: A Statistical Analysis of STEVE, Journal of Geophysical Research: Space Physics, 123, 9893–9905, https://doi.org/10.1029/2018JA025368, 2018a.

Gallardo-Lacourt, B., Liang, J., Nishimura, Y., and Donovan, E.: On the Origin of STEVE: Particle Precipitation or Ionospheric Skyglow?, Geophysical Research Letters, 45, 7968–7973, https://doi.org/10.1029/2018GL078509, 2018b.

Gallardo-Lacourt, B., Frey, H. U., and Martinis, C.: Proton Aurora and Optical Emissions in the Subauroral Region, Space Science Reviews, 217, 1–36, https://doi.org/10.1007/S11214-020-00776-6, 2021.

Gallardo-Lacourt, B., Nishimura, Y., Kepko, L., Spanswick, E. L., Gillies, D. M., Knudsen, D. J., Burchill, J. K., Skone, S. H., Pinto, V. A., Chaddock, D., Kuzub, J., and Donovan, E. F.: Unexpected STEVE Observations at High Latitude During Quiet Geomagnetic Conditions, Geophysical Research Letters, 51, e2024GL110 568, https://doi.org/10.1029/2024GL110568, e2024GL110568 2024GL110568, 2024.

Galperin, Y. I.: Proton bombardment in aurora, Planet. Space Sci, 10, 187–193, https://doi.org/10.1016/0032-0633(63)90016-3, 1963.

Gillies, D. M., Donovan, E., Hampton, D., Liang, J., Connors, M., Nishimura, Y., Gallardo-Lacourt, B., and Spanswick, E.: First Observations From the TREx Spectrograph: The Optical Spectrum of STEVE and the Picket Fence Phenomena, Geophysical Research Letters, 46, 7207–7213, https://doi.org/10.1029/2019GL083272, 2019.

Gillies, D. M., Liang, J., Gallardo-Lacourt, B., and Donovan, E.: New Insight Into the Transition From a SAR Arc to STEVE, Geophysical Research Letters, 50, e2022GL101 205, https://doi.org/10.1029/2022GL101205, e2022GL101205 2022GL101205, 2023.

Gilmore, F. R., Laher, R. R., and Espy, P. J.: Franck–Condon factors, r-centroids, electronic transition moments, and Einstein coefficients for many nitrogen and oxygen band systems, Journal of physical and chemical reference data, 21, 1005–1107, 1992.

Gingell, I., Schwartz, S. J., Eastwood, J. P., Stawarz, J. E., Burch, J. L., Ergun, R. E., Fuselier, S. A., Gershman, D. J., Giles, B. L., Khotyaintsev, Y. V., Lavraud, B., Lindqvist, P. A., Paterson, W. R., Phan, T. D., Russell, C. T., Strangeway, R. J., Torbert, R. B., and Wilder, F.: Statistics of Reconnecting Current Sheets in the Transition Region of Earth's Bow Shock, Journal of Geophysical Research: Space Physics, 125, e2019JA027 119, https://doi.org/10.1029/2019JA027119, 2020.

Glaßmeier, K.: Geomagnetic pulsations, pp. 333–334, Springer Netherlands, Dordrecht, https://doi.org/10.1007/978-1-4020-4423-6_122, 2007.

Go Stargazing: Light pollution map - Go Stargazing — gostargazing.co.uk, https://gostargazing.co.uk/light-pollution-map/, [Accessed 14-07-2025], 2025.

Goertz, C. K., Nielsen, E., Korth, A., Glassmeier, K. H., Haldoupis, C., Hoeg, P., and Hayward, D.: Observations of a possible ground signature of flux transfer events, Journal of Geophysical Research: Space Physics, 90, 4069–4078, https://doi.org/10.1029/JA090iA05p04069, 1985.

Golumbic, Y. N., Orr, D., Baram-Tsabari, A., and Fishbain, B.: Between Vision and Reality: A Study of Scientists' Views on Citizen Science, Citizen Science: Theory and Practice, 2, 6, https://doi.org/10.5334/cstp.53, 2017.

Gosling, J. T., Skoug, R. M., McComas, D. J., and Smith, C. W.: Direct evidence for magnetic reconnection in the solar wind near 1 AU, Journal of Geophysical Research: Space Physics, 110, 1107, https://doi.org/10.1029/2004JA010809, 2005.

Grandin, M., Palmroth, M., Whipps, G., Kalliokoski, M., Ferrier, M., Paxton, L. J., Mlynczak, M. G., Hilska, J., Holmseth, K., Vinorum, K., and Whenman, B.: Large-Scale Dune Aurora Event Investigation Combining Citizen Scientists' Photographs and Spacecraft Observations, AGU Advances, 2, e2020AV000 338, https://doi.org/10.1029/2020AV000338, 2021.

Grandin, M., Bruus, E., Ledvina, V. E., Partamies, N., Barthelemy, M., Martinis, C., Dayton-Oxland, R., Gallardo-Lacourt, B., Nishimura, Y., Herlingshaw, K., Thomas, N., Karvinen, E., Lach, D., Spijkers, M., and Bergstrand, C.: The Gannon Storm: citizen science observations during the geomagnetic superstorm of 10 May 2024, Geoscience Communication, 7, 297–316, https://doi.org/10.5194/gc-7-297-2024, 2024.

Grandin, M., Ledvina, V. E., Musset, S., Partamies, N., Frissell, N. A., Bruus, E., Nicoll, K. A., Mkrtchyan, H., Gallardo-Lacourt, B., Alfonsi, L., Jonassen, M. O., Whiter, D., Herlingshaw, K., Enengl, F., Doornbos, E., Jia, J., Kosar, B., Evans, L. P., Haberle, V., Laundal, K. M., and Barthelemy, M.: Citizen Science in Space and Atmospheric Sciences: Opportunities and Challenges, Surveys in Geophysics, https://doi.org/10.1007/s10712-025-09888-6, 2025.

Greenwald, R. A., Baker, K. B., Dudeney, J. R., Pinnock, M., Jones, T. B., Thomas, E. C., Villain, J. P., Cerisier, J. C., Senior, C., Hanuise, C., Hunsucker, R. D., Sofko, G., Koehler, J., Nielsen, E., Pellinen, R., Walker, A. D., Sato, N., and Yamagishi, H.: DARN/SuperDARN - A global view of the dynamics of high-latitude convection, Space Science Reviews, 71, 761–796, https://doi.org/10.1007/BF00751350, 1995.

Häkkilä, T., Grandin, M., Battarbee, M., Szeląg, M. E., Alho, M., Kotipalo, L., Kalakoski, N., Verronen, P. T., and Palmroth, M.: Atmospheric odd nitrogen response to electron forcing from a 6D magnetospheric hybrid-kinetic simulation, Annales Geophysicae, 43, 217–240, https://doi.org/10.5194/ANGEO-43-217-2025, 2025.

Han, D., Xiong, Y., Shi, R., Qiu, H., Feng, H., Han, D., Xiong, Y., Shi, R., Qiu, H., and Feng, H.: A unified model of cusp spot, High Latitude Dayside aurora (HiLDA)/(Space Hurricane), and 15MLT-PCA, Earth and Planetary Physics, 2023, Vol. 7, Issue 4, Pages: 513-519, 7, 513–519, https://doi.org/10.26464/EPP2023046, 2023.

Harding, B. J., Mende, S. B., Triplett, C. C., and Wu, Y. J. J.: A Mechanism for the STEVE Continuum Emission, Geophysical Research Letters, 47, https://doi.org/10.1029/2020GL087102, 2020.

Herlingshaw, K.: SolarMaX — solarmaxmission.com, https://www.solarmaxmission.com/, [Accessed 10-07-2025], 2025.

Herlingshaw, K., Lach, D., Dayton-Oxland, R., Bruus, E., Karvinen, E., Ledvina, V., Partamies, N., Grandin, M., Spijkers, M., and Nishimura, Y.: ARCTICS Aurora Field Guide and Handbook for Citizen Science, ARCTICS Working Group, https://doi.org/10.5281/zenodo.13932081, 2024a.

Herlingshaw, K., Partamies, N., van Hazendonk, C. M., Syrjäsuo, M., Baddeley, L., Johnsen, M., Eriksen, N. K., McWhirter, I., Aruliah, A. L., Engebretson, M. J., Oksavik, K., Sigernes, F., Lorentzen, D. A., Nishiyama, T., Cooper, M. B., Meriwether, J. W., Haaland, S., and Whiter, D. K.: Science Highlights from the Kjell Henriksen Observatory on Svalbard, Arctic Science, https://doi.org/10.1139/as-2024-0009, 2024b.

Herzberg, G.: Molecular Spectra and molecular structure-Vol I, vol. 1, Read Books Ltd, 2013.

Holmen, S. E.: Trends and variability of polar mesopause region temperatures attributed to atmospheric dynamics and solar activity, Ph.D. thesis, The Arctic University of Norway, Tromsø, URL https://kho.unis.no/doc/phd_thesis_holmen_final.pdf, 2016.

Huber, K. P. and Herzberg, G. H.: "Constants of Diatomic Molecules" (data prepared by Jean W. Gallagher and Russell D. Johnson, III), in: NIST Chemistry WebBook, NIST Standard Reference Database Number 69, Eds. P.J. Linstrom and W.G. Mallard, National Institute of Standards and Technology, Gaithersburg MD, 20899, https://doi.org/https://doi.org/10.18434/T4D303, 2025.

Hundhausen, A. J.: Composition and dynamics of the solar wind plasma, Reviews of Geophysics, 8, 729–811, https://doi.org/10.1029/RG008i004p00729, 1970.

Hunten, D. M.: Sunlit aurora and the N2+ ion: a personal perspective, Planetary and Space Science, 51, 887–890, https://doi.org/10.1016/S0032-0633(03)00079-5, 2003.

Immel, T. J., Mende, S. B., Frey, H. U., Patel, J., Bonnell, J. W., Engebretson, M. J., and Fuselier, S. A.: ULF Waves Associated with Enhanced Subauroral Proton Precipitation, Geophysical Monograph Series, 159, 71–84, https://doi.org/10.1029/159GM05, 2005.

Innis, J., Dyson, P., and Greet, P.: Further observations of the thermospheric vertical wind at the auroral oval/polar cap boundary, Journal of Atmospheric and Solar-Terrestrial Physics, 59, 2009–2022, https://doi.org/10.1016/S1364-6826(97)00034-5, 1997.

Jackman, C. H., McPeters, R. D., Labow, G. J., Fleming, E. L., Praderas, C. J., and Russell, J. M.: Northern hemisphere atmospheric effects due to the July 2000 Solar Proton Event, Geophysical Research Letters, 28, 2883–2886, https://doi.org/10.1029/2001GL013221, 2001.

Johnson, D. R., Ecklund, E. H., and Lincoln, A. E.: Narratives of Science Outreach in Elite Contexts of Academic Science, Science Communication, 36, 81–105, https://doi.org/10.1177/1075547013499142, 2014.

Jokiaho, O.-P.: Spectral modelling of molecular nitrogen in Aurora, Ph.D. thesis, University of Southampton, Southampton, URL http://eprints.soton.ac.uk/id/eprint/161195, 2009.

Jones, A. V.: Aurora, Geophysics and Astrophysics Monographs, 9, 1974.

Jones, S.: Space- and ground-based observations of pulsating aurora, Ph.D. thesis, 2010.

Kalakoski, N., Verronen, P. T., Szeląg, M. E., and Jackman, C. H.: Global ozone loss following extreme solar proton storms based on the July 2012 coronal mass ejection, Scientific Reports 2023 13:1, 13, 1–10, https://doi.org/10.1038/s41598-023-40129-1, 2023.

Kaplan, J.: New band system in nitrogen, Physical Review, 45, 675, 1934.

Kataoka, R., Miyoshi, Y., Shiokawa, K., Nishitani, N., Keika, K., Amano, T., and Seki, K.: Magnetic Storm-Time Red Aurora as Seen From Hokkaido, Japan on 1 December 2023 Associated With High-Density Solar Wind, Geophysical Research Letters, 51, e2024GL108 778, https://doi.org/10.1029/2024GL108778, 2024.

Khazanov, G. V., Sibeck, D. G., Tel'Nikhin, A. A., and Kronberg, T. K.: Stochastic acceleration of ions driven by Pc1 wave packets, Physics of Plasmas, 22, 72 901, https://doi.org/10.1063/1.4926823, 2015.

Kim, H., Clauer, C. R., Gerrard, A. J., Engebretson, M. J., Hartinger, M. D., Lessard, M. R., Matzka, J., Sibeck, D. G., Singer, H. J., Stolle, C., Weimer, D. R., and Xu, Z.: Conjugate observations of electromagnetic ion cyclotron waves associated with traveling convection vortex events, Journal of Geophysical Research: Space Physics, 122, 7336–7352, https://doi.org/10.1002/2017JA024108, 2017.

Kim, H., Shiokawa, K., Park, J., Miyoshi, Y., Miyashita, Y., Stolle, C., Connor, H. K., Hwang, J., Buchert, S., Kwon, H. J., Nakamura, S., Nakamura, K., Oyama, S. I., Otsuka, Y., Nagatsuma, T., and Sakaguchi, K.: Isolated Proton Aurora Driven by EMIC Pc1 Wave: PWING, Swarm, and NOAA POES Multi-Instrument Observations, Geophysical Research Letters, 48, e2021GL095 090, https://doi.org/10.1029/2021GL095090, 2021.

King, J. H. and Papitashvili, N. E.: Solar wind spatial scales in and comparisons of hourly Wind and ACE plasma and magnetic field data, Journal of Geophysical Research: Space Physics, 110, https://doi.org/10.1029/2004JA010649, 2005.

Kirkpatrick, S., Gelatt, C. D., and Vecchi, M. P.: Optimization by Simulated Annealing, Science, 220, 671–680, https://doi.org/10.1126/SCIENCE.220.4598.671, 1983.

Kivelson and Russel: Introduction to Space Physics, Cambridge University Press, https://doi.org/10.1017/9781139878296, 1995.

Kontar, E.: Plasma Theory & Diagnostics 2, University of Glasgow, Lecture Series, 2019.

Krcelic, P., Fear, R. C., Whiter, D., Lanchester, B., Aruliah, A. L., Lester, M., and Paxton, L.: Fine-Scale Electric Fields and Joule Heating From Observations of the Aurora, Journal of Geophysical Research: Space Physics, 128, https://doi.org/10.1029/2022JA030628, 2023.

Kurihara, J., Abe, T., Oyama, K. I., Griffin, E., Kosch, M., Aruliah, A., Kauristie, K., Ogawa, Y., Komada, S., and Iwagami, N.: Observations of the lower thermospheric neutral temperature and density in the DELTA campaign, Earth, Planets and Space, 58, 1123–1130, https://doi.org/10.1186/BF03352001/METRICS, 2006.

Laher, R. R. and Gilmore, F. R.: Improved fits for the vibrational and rotational constants of many states of nitrogen and oxygen, Journal of physical and chemical reference data, 20, 685–712, 1991.

Land-Zandstra, A., Agnello, G., and Gültekin, Y. S.: Participants in citizen science, in: The Science of Citizen Science, pp. 243–259, Springer International Publishing, https://doi.org/10.1007/978-3-030-58278-4{_}13, 2021.

Lehtinen, M. S. and Huuskonen, A.: General incoherent scatter analysis and GUISDAP, Journal of Atmospheric and Terrestrial Physics, 58, 435–452, https://doi.org/10.1016/0021-9169(95)00047-X, 1996.

Lewandowski, E., Caldwell, W., Elmquist, D., and Oberhauser, K.: Public Perceptions of Citizen Science, Citizen Science: Theory and Practice, 2, 3, https://doi.org/10.5334/cstp.77, 2017.

Lewenstein, B.: The need for feminist approaches to science communication, Journal of Science Communication, 18, https://doi.org/10.22323/2.18040301, 2019.

Liang, J. and Donovan, E.: Quantum Calculation of the Vibrational Excitation of Nitrogen Molecules by Fast Ions: Can It Contribute to STEVE Formation?, Geophysical Research Letters, 51, https://doi.org/10.1029/2024GL110986, 2024.

Liang, J., Donovan, E., Connors, M., Gillies, D., St-Maurice, J. P., Jackel, B., Gallardo-Lacourt, B., Spanswick, E., and Chu, X.: Optical Spectra and Emission Altitudes of Double-Layer STEVE: A Case Study, Geophysical Research Letters, 46, 13 630–13 639, https://doi.org/10.1029/2019GL085639, 2019.

Liang, J., Gillies, D., Donovan, E., Parry, H., Mann, I., Connors, M., and Spanswick, E.: On the green isolated proton auroras during Canada thanksgiving geomagnetic storm, Frontiers in Astronomy and Space Sciences, 9, 1040 092, https://doi.org/10.3389/fspas.2022.1040092, 2022.

Lockwood, M., Sandholt, P., Cowley, S., and Oguti, T.: Interplanetary magnetic field control of dayside auroral activity and the transfer of momentum across the dayside magnetopause, Planetary and Space Science, 37, 1347–1365, https://doi.org/10.1016/0032-0633(89)90106-2, 1989.

Lozinskaia, T. A. and Sitnik, T. G.: Optical studies of the kinematics of NGC 7822 (W1), 1977.

Lühr, H., Rother, M., Köhler, W., Ritter, P., and Grunwaldt, L.: Thermospheric up-welling in the cusp region: Evidence from CHAMP observations, Geophysical Research Letters, 31, https://doi.org/10.1029/2003gl019314, 2004.

Lummerzheim, D. and Galand, M.: The profile of the hydrogen H β emission line in proton aurora, Journal of Geophysical Research: Space Physics, 106, 23–31, https://doi.org/10.1029/2000JA002014, 2001.

Ma, L., Yu, Y., Tian, X., and Cao, J.: An Empirical Model of the Proton Isotropic Boundary (IB), Journal of Geophysical Research: Space Physics, 127, https://doi.org/10.1029/2022JA030843, 2022.

MacDonald, E. A., Donovan, E., Nishimura, Y., Case, N. A., Megan Gillies, D., Gallardo-Lacourt, B., Archer, W. E., Spanswick, E. L., Bourassa, N., Connors, M., Heavner, M., Jackel, B., Kosar, B., Knudsen, D. J., Ratzlaff, C., and Schofield, I.: New science in plain sight: Citizen scientists lead to the discovery of optical structure in the upper atmosphere, Science Advances, 4, https://doi.org/10.1126/sciadv.aaq0030, 2018.

Macho, E. P., Bristow, W., Gallardo-Lacourt, B., Shepherd, S. G., Ruohoniemi, J. M., and Correia, E.: Exploring the relationship between STEVE and SAID during three events observed by SuperDARN, Frontiers in Astronomy and Space Sciences, 11, 1422 164, https://doi.org/10.3389/FSPAS.2024.1422164/BIBTEX, 2024.

Martinez, N.: The Meridian Imaging Svalbard Spectrograph 2: Enhancing Auroral Tracking Capacities, Ph.D. thesis, Luleå Tekniska Universitet, URL https://aurora.unis.no/doc/Nicolas_MISS2.pdf, 2024.

Martinis, C., Griffin, I., Gallardo-Lacourt, B., Wroten, J., Nishimura, Y., Baumgardner, J., and Knudsen, D. J.: Rainbow of the Night: First Direct Observation of a SAR Arc Evolving Into STEVE, Geophysical Research Letters, 49, e2022GL098 511, https://doi.org/10.1029/2022GL098511, 2022.

Matsuda, S., Kasahara, Y., Miyoshi, Y., Nomura, R., Shoji, M., Matsuoka, A., Kasaba, Y., Kurita, S., Teramoto, M., and Ishisaka, K.: Spatial Distribution of Fine-Structured and Unstructured EMIC Waves Observed by the Arase Satellite, Geophysical Research Letters, 45, 11,530–11,538, https://doi.org/10.1029/2018GL080109, 2018.

Meinel, A.: A New Band System of N^{+} 2 in the Infrared Auroral Spectrum., Astrophysical Journal, vol. 112, p. 562, 112, 562, 1950.

Meinel, A. B.: Origin of the Continuum in the Night-Sky Spectrum., The Astrophysical Journal, 118, 200, https://doi.org/10.1086/145742, 1953.

Mende, S. B. and Turner, C.: Color Ratios of Subauroral (STEVE) Arcs, Journal of Geophysical Research, 124, 5945–5955, https://doi.org/10.1029/2019JA026851, 2019.

Mende, S. B., Harding, B. J., and Turner, C.: Subauroral Green STEVE Arcs: Evidence for Low-Energy Excitation, Geophysical Research Letters, 46, 14 256–14 262, https://doi.org/10.1029/2019GL086145, 2019.

Menk, F. W., Fraser, B. J., Hansen, H. J., Newell, P. T., Meng, C.-I., and Morris, R. J.: Multistation Observations of Pc1-2 ULF Pulsations in the Vicinity of the Polar Cusp, Journal of geomagnetism and geoelectricity, 45, 1159–1173, https://doi.org/10.5636/JGG.45.1159, 1993.

Mishin, E. and Streltsov, A.: STEVE and the Picket Fence: Evidence of Feedback-Unstable Magnetosphere-Ionosphere Interaction, Geophysical Research Letters, 46, 14 247–14 255, https://doi.org/10.1029/2019GL085446, 2019.

Mishin, E. and Streltsov, A.: On the Kinetic Theory of Subauroral Arcs, Journal of Geophysical Research: Space Physics, 127, e2022JA030 667, https://doi.org/10.1029/2022JA030667, 2022.

Moen, J., Lorentzen, D. A., and Sigernes, F.: Dayside moving auroral forms and bursty proton auroral events in relation to particle boundaries observed by NOAA 12, Journal of Geophysical Research: Space Physics, 103, 14 855–14 863, https://doi.org/10.1029/97ja02877, 1998.

Mursula, K., Blomberg, L. G., Lindqvist, P. A., Marklund, G. T., Bräysy, T., Rasinkangas, R., and Tanskanen, P.: Dispersive Pc1 bursts observed by Freja, Geophysical Research Letters, 21, 1851–1854, https://doi.org/10.1029/94GL01584, 1994.

Nakamura, K., Shiokawa, K., Otsuka, Y., Shinbori, A., Miyoshi, Y., Connors, M., Spence, H., Reeves, G., Funsten, H. O., MacDowall, R., Smith, C., Wygant, J., and Bonnell, J.: Simultaneous Observation of Two Isolated Proton Auroras at Subauroral Latitudes by a Highly Sensitive All-Sky Camera and Van Allen Probes, Journal of Geophysical Research: Space Physics, 126, e2020JA029 078, https://doi.org/10.1029/2020JA029078, 2021.

Nakamura, K., Shiokawa, K., Nosé, M., Nagatsuma, T., Sakaguchi, K., Spence, H., Reeves, G., Funsten, H. O., MacDowall, R., Smith, C., Wygant, J., Bonnell, J., and Mann, I. R.: Multi-Event Study of Simultaneous Observations of Isolated Proton Auroras at Subauroral Latitudes Using Ground All-Sky Imagers and the Van Allen Probes, Journal of Geophysical Research: Space Physics, 127, e2022JA030 455, https://doi.org/10.1029/2022JA030455, 2022.

Nanjo, S., Hofstra, G. A., Shiokawa, K., Shinbori, A., Nozawa, S., and Hosokawa, K.: Post-midnight purple arc and patches appeared on the high latitude part of the auroral oval: Dawnside counterpart of STEVE?, Earth, Planets and Space, 76, https://doi.org/10.1186/s40623-024-01995-9, 2024.

Naudé, S. M.: The Rotational Analysis of the First Positive Nitrogen (N 2) Bands, Physical Review, 38, 372, 1931.

Next Spaceflight: Falcon 9 Block 5 | Fram2 — nextspaceflight.com, https://nextspaceflight.com/launches/details/7615, [Accessed 10-07-2025], 2025.

Nicholls, R. and Stewart, A.: Atomic and molecular processes, Academic Press Inc., New York, N. Y, 1962.

Nilsen, K., Kero, A., Verronen, P. T., Szeląg, M. E., Kalakoski, N., and Jia, J.: Sensitivity of Middle Atmospheric Ozone to Solar Proton Events: A Comparison Between a Climate Model and Satellites, Journal of Geophysical Research: Atmospheres, 126, e2021JD034 549, https://doi.org/10.1029/2021JD034549, 2021.

Nishimura, Y., Gallardo-Lacourt, B., Zou, Y., Mishin, E., Knudsen, D. J., Donovan, E. F., Angelopoulos, V., and Raybell, R.: Magnetospheric Signatures of STEVE: Implications for the Magnetospheric Energy Source and Interhemispheric Conjugacy, Geophysical Research Letters, 46, 5637–5644, https://doi.org/10.1029/2019GL082460, 2019.

Nishimura, Y., Bruus, E., Karvinen, E., Martinis, C. R., Dyer, A., Kangas, L., Rikala, H. K., Donovan, E. F., Nishitani, N., and Ruohoniemi, J. M.: Interaction Between Proton Aurora and Stable Auroral Red Arcs Unveiled by Citizen Scientist Photographs, Journal of Geophysical Research: Space Physics, 127, e2022JA030 570, https://doi.org/10.1029/2022JA030570, 2022.

Nishimura, Y., Gallardo-Lacourt, B., Donovan, E. F., Angelopoulos, V., and Nishitani, N.: Auroral and Magnetotail Dynamics During Quiet-Time STEVE and SAID, submitted to Journal of Geophysical Research, 2024.

Nishiyama, T., Kagitani, M., Furutachi, S., and et al.: The first simultaneous spectroscopic and monochromatic imaging observations of short-wavelength infrared aurora of Meinel (0,0) band at 1.1 m with incoherent scatter radar, Earth Planets Space, 76, https://doi.org/10.1186/s40623-024-01969-x, 2024.

Noll, S., Plane, J. M. C., Feng, W., Kalogerakis, K. S., Kausch, W., Schmidt, C., Bittner, M., and Kimeswenger, S.: Structure, variability, and origin of the low-latitude nightglow continuum between 300 and 1800 nm: evidence for HO_2 emission in the near-infrared, Atmospheric Chemistry and Physics, 24, 1143–1176, https://doi.org/10.5194/acp-24-1143-2024, 2024a.

Noll, S., Plane, J. M. C., Feng, W., Kalogerakis, K. S., Kausch, W., Schmidt, C., Bittner, M., and Kimeswenger, S.: Structure, variability, and origin of the low-latitude nightglow continuum between 300 and 1800 nm: evidence for HO_2 emission in the near-infrared, Atmospheric Chemistry and Physics, 24, 1143–1176, https://doi.org/10.5194/acp-24-1143-2024, 2024b.

Nomura, R., Shiokawa, K., Omura, Y., Ebihara, Y., Miyoshi, Y., Sakaguchi, K., Otsuka, Y., and Connors, M.: Pulsating proton aurora caused by rising tone Pc1 waves, Journal of Geophysical Research: Space Physics, 121, 1608–1618, https://doi.org/10.1002/2015JA021681, 2016.

Ozaki, M., Shiokawa, K., Miyoshi, Y., Kataoka, R., Connors, M., Inoue, T., Yagitani, S., Ebihara, Y., Jun, C. W., Nomura, R., Sakaguchi, K., Otsuka, Y., Uchida, H. A., Schofield, I., and Danskin, D. W.: Discovery of 1 Hz Range Modulation of Isolated Proton Aurora at Subauroral Latitudes, Geophysical Research Letters, 45, 1209–1217, https://doi.org/10.1002/2017GL076486, 2018.

Ozaki, M., Shiokawa, K., Horne, R. B., Engebretson, M. J., Lessard, M., Ogawa, Y., Hosokawa, K., Nosé, M., Ebihara, Y., Kadokura, A., Yagitani, S., Miyoshi, Y., Hashimoto, S., Sinha, S., Sinha, A. K., Seemala, G. K., and Jun, C. W.: Magnetic Conjugacy of Pc1 Waves and Isolated Proton Precipitation at Subauroral Latitudes: Importance of Ionosphere as Intensity Modulation Region, Geophysical Research Letters, 48, e2020GL091 384, https://doi.org/10.1029/2020GL091384, 2021.

Ozaki, M., Shiokawa, K., Kataoka, R., Mlynczak, M., Paxton, L., Connors, M., Yagitani, S., Hashimoto, S., Otsuka, Y., Nakahira, S., and Mann, I.: Localized mesospheric ozone destruction corresponding to isolated proton aurora coming from Earth's radiation belt, Scientific Reports 2022 12:1, 12, 1–11, https://doi.org/10.1038/s41598-022-20548-2, 2022.

Palmroth, M., Grandin, M., Helin, M., Koski, P., Oksanen, A., Glad, M. A., Valonen, R., Saari, K., Bruus, E., Norberg, J., Viljanen, A., Kauristie, K., and Verronen, P. T.: Citizen Scientists Discover a New Auroral Form: Dunes Provide Insight Into the Upper Atmosphere, AGU Advances, 1, e2019AV000 133, https://doi.org/10.1029/2019AV000133, 2020.

Papitashvili, N. E. and King, J. H.: OMNI 5-min Data Set [Data set], NASA Space Physics Data Facility, https://doi.org/10.48322/gbpg-5r77, 2020.

Partamies, N., Dayton-Oxland, R., Herlingshaw, K., Virtanen, I., Gallardo-Lacourt, B., Syrjäsuo, M., Sigernes, F., Nishiyama, T., Nishimura, T., Barthelemy, M., Aruliah, A., Whiter, D., Mielke, L., Grandin, M., Karvinen, E., Spijkers, M., and Ledvina, V. E.: First observations of continuum emission

in dayside aurora, Annales Geophysicae, 43, 349–367, https://doi.org/10.5194/angeo-43-349-2025, 2025.

Pateman, R., Dyke, A., and West, S.: The diversity of participants in environmental citizen science, Citizen Science: Theory and Practice, 6, https://doi.org/10.5334/CSTP.369, 2021.

Paulson, K. W., Smith, C. W., Lessard, M. R., Torbert, R. B., Kletzing, C. A., and Wygant, J. R.: In situ statistical observations of Pc1 pearl pulsations and unstructured EMIC waves by the Van Allen Probes, Journal of Geophysical Research: Space Physics, 122, 105–119, https://doi.org/10.1002/2016JA023160, 2017.

Phan, T. D., Kistler, L. M., Klecker, B., Haerendel, G., Paschmann, G., Sonnerup, B. U., Baumjohann, W., Bavassano-Cattaneo, M. B., Carlson, C. W., DiLellis, A. M., Fornacon, K. H., Frank, L. A., Fujimoto, M., Georgescu, E., Kokubun, S., Moebius, E., Mukai, T., Øieroset, M., Paterson, W. R., and Reme, H.: Extended magnetic reconnection at the Earth's magnetopause from detection of bi-directional jets, Nature 2000 404:6780, 404, 848–850, https://doi.org/10.1038/35009050, 2000.

Plank, J.: On the evolution of turbulent fluctuations at collisionless shock waves, Ph.D. thesis, University of Southampton, URL https://eprints.soton.ac.uk/494742/1/PhD_Thesis_Final_3b.pdf, 2024.

Plank, J. and Gingell, I. L.: Intermittency at Earth's bow shock: Measures of turbulence in quasi-parallel and quasi-perpendicular shocks, Physics of Plasmas, 30, 82 906, https://doi.org/10.1063/5.0160439/2908491, 2023.

Price, D. J.: Observations of thermospheric heating signatures associated with sub-kilometer scale auroral electrodynamics, Ph.D. thesis, University of Southampton, Southampton, URL https://eprints.soton.ac.uk/455066/1/Thesis_Final_w_corrections_David_Price.pdf, 2021.

Rees, M. H. and Roble, R. G.: Observations and theory of the formation of stable auroral red arcs, Reviews of Geophysics, 13, 201–242, https://doi.org/10.1029/RG013I001P00201, 1975.

Regi, M., Marzocchetti, M., Francia, P., and Lauretis, M. D.: A statistical analysis of Pc1-2 waves at a near-cusp station in Antarctica 3. Space science, Earth, Planets and Space, 69, 1–16, https://doi.org/10.1186/S40623-017-0738-8/, 2017.

Roos, P. A. and Reskin, B. F.: Occupational Desegregation in the 1970s: Integration and Economic Equity?, Sociological Perspectives, 35, 69–91, https://doi.org/10.2307/1389369, 1992.

Safargaleev, V., Serebryanskaya, A., Koustov, A., Lester, M., Pchelkina, E., and Vasilyev, A.: A possible origin of dayside Pc1 magnetic pulsations observed at high latitudes, Annales Geophysicae, 22, 2997–3008, https://doi.org/10.5194/angeo-22-2997-2004, 2004.

Sakaguchi, K., Shiokawa, K., Leda, A., Miyoshi, Y., Otsuka, Y., Ogawa, T., Connors, M., Donovan, E. F., and Rich, F. J.: Simultaneous ground and satellite observations of an isolated proton arc at subauroral latitudes, Journal of Geophysical Research: Space Physics, 112, 4202, https://doi.org/10.1029/2006JA012135, 2007.

Sakaguchi, K., Shiokawa, K., Miyoshi, Y., and Connors, M.: Isolated Proton Auroras and Pc1/EMIC Waves at Subauroral Latitudes, Auroral Dynamics and Space Weather, pp. 59–70, https://doi.org/10.1002/9781118978719.ch5, 2015.

Schadee, A.: The formation of molecular lines in the solar spectrum (errata: 17 537), Bulletin of the Astronomical Institutes of the Netherlands, Vol. 17, p. 311, 17, 311, 1964.

Shinagawa, H., Oyama, S., Nozawa, S., Buchert, S., Fujii, R., and Ishii, M.: Thermospheric and ionospheric dynamics in the auroral region, Advances in Space Research, 31, 951–956, https://doi.org/10.1016/S0273-1177(02)00792-5, 2003.

Shiokawa, K., Otsuka, Y., and Connors, M.: Statistical Study of Auroral/Resonant-Scattering 427.8-nm Emission Observed at Subauroral Latitudes Over 14 years, Journal of Geophysical Research: Space Physics, 124, 9293–9301, https://doi.org/10.1029/2019JA026704, 2019.

Shirk, J. L., Ballard, H. L., Wilderman, C. C., Phillips, T., Wiggins, A., Jordan, R., McCallie, E., Minarchek, M., Lewenstein, B. V., Krasny, M. E., and Bonney, R.: Public participation in scientific research: A framework for deliberate design, Ecology and Society, 17, https://doi.org/10.5751/ES-04705-170229, 2012.

Sigernes, F., Lloyd, N., Lorentzen, D. A., Neuber, R., Hoppe, U.-P., Degenstein, D., Shumilov, N., Moen, J., Gjessing, Y., Havnes, O., Skartveit, A., Raustein, E., Ørbæk, J. B., and Deehr, C. S.: The red-sky enigma over Svalbard in December 2002, Annales Geophysicae, 23, 1593–1602, https://doi.org/10.5194/angeo-23-1593-2005, 2005.

Skjæveland, S., Carlson, H. C., and Moen, J. I.: A statistical survey of heat input parameters into the cusp thermosphere, Journal of Geophysical Research: Space Physics, 122, 9622–9651, https://doi.org/10.1002/2016JA023594, 2017.

Smalley, R. E., Wharton, L., and Levy, D. H.: The fluorescence excitation spectrum of rotationally cooled NO2, The Journal of Chemical Physics, 63, 4977–4989, https://doi.org/10.1063/1.431244, 1975.

Solomon, S., Rusch, D. W., Gitrard, J.-C., Red, G. C., and Crutzenk, P. J.: The effect of particle precipitation events on the neutral and ion chemistry of the middle atmosphere: II. odd hydrogen, Planet. Space SC, 29, 885–892, 1981.

Spanswick, E., Liang, J., Houghton, J., Chaddock, D., Donovan, E., Gallardo-Lacourt, B., Keenan, C., Rosehart, J., Nishimura, Y., Hampton, D., and Gillies, M.: Association of structured continuum emission with dynamic aurora, Nature Communications, 15, https://doi.org/10.1038/s41467-024-55081-5, 2024a.

Spanswick, E., Liang, J., Houghton, J., Donovan, E., Gallardo-Lacourt, B., Nishimura, Y., Chaddock, D., Keenan, C., Rosehart, J., and Gillies, D.: Through a New Lense: Structured Coupling Between the Aurora and Neutral Atmosphere, revised to Nature Communications, 2024b.

Spasojević, M., Thomsen, M. R., Chi, P. J., and Sandel, B. R.: Afternoon subauroral proton precipitation resulting from ring current—plasmasphere interaction, Inner Magnetosphere Interactions: New Perspectives from Imaging, 159, 85–99, https://doi.org/10.1029/159GM06, 2013.

States, R. J. and Gardner, C. S.: Thermal Structure of the Mesopause Region (80–105 km) at 40°N Latitude. Part I: Seasonal Variations, Journal of the Atmospheric Sciences, 57, 66–77, https://doi.org/10.1175/1520-0469(2000)057<0066:TSOTMR>2.0.CO;2, 2000.

Statistics.gov.scot: Scottish Government Statistics, Council area, Argyll and Bute, https://statistics.gov.scot/atlas/resource?uri=http%3A%2F%2Fstatistics.gov.scot%2Fid%2Fstatistical-geography%2FS12000035, [Accessed 10-07-2025], 2023.

Sternberg, J. R. and Ingham, M. F.: Observations of the Airglow Continuum, Monthly Notices of the Royal Astronomical Society, 159, 1–20, https://doi.org/10.1093/mnras/159.1.1, 1972.

Strasser, B. J., Tancoigne, É., Baudry, J., Piguet, S., Spiers, H., Marquez, J. L.-F., Kasparian, J., Grey, F., Anderson, D., and Lintott, C.: Quantifying online citizen science: Dynamics and demographics of public participation in science, Plos One, 18, https://doi.org/https://doi.org/10.1371/journal.pone.0293289, 2023.

Svalbard Aurora Chasers: New Team more Strange Aurora: Svalbard Aurora Chasers, https://svalbardaurorachasers.wordpress.com/2024/02/26/new-team-more-strange-aurora/, [Accessed 18-09-2025], 2025.

Swanson, D. G.: Plasma waves, p. 456, URL https://www.ark.no/produkt/boker/fagboker/plasma-waves-9780750309271, 2003.

Szeląg, M. E., Marsh, D. R., Verronen, P. T., Seppälä, A., and Kalakoski, N.: Ozone impact from solar energetic particles cools the polar stratosphere, Nature Communications 2022 13:1, 13, 1–8, https://doi.org/10.1038/s41467-022-34666-y, 2022.

Tian, X., Yu, Y., Gong, F., Ma, L., Cao, J., Solomon, S. C., Shreedevi, P. R., Shiokawa, K., Otsuka, Y., ichiro Oyama, S., and Miyoshi, Y.: Ionospheric Modulation by EMIC Wave-Driven Proton Precipitation: Observations and Simulations, Journal of Geophysical Research: Space Physics, 128, e2022JA030 983, https://doi.org/10.1029/2022JA030983, 2023.

Tyssøy, H. N., Stadsnes, J., Sørbø, M., Mertens, C. J., and Evans, D. S.: Changes in upper mesospheric and lower thermospheric temperatures caused by energetic particle precipitation, Journal of Geophysical Research: Space Physics, 115, 10 323, https://doi.org/10.1029/2010JA015427, 2010.

Unterfrauner, E., Fabian, C. M., Hemming, G., and Garcia, B.: What's in it for citizen scientists? An analysis of participant's gains from a democratisation perspective, Open Research Europe, 4, 124, https://doi.org/10.12688/openreseurope.17436.1, 2024.

Varlamov, I., Parnikov, S., Ievenko, I., Baishev, D., and Shiokawa, K.: Registration of synchronous geomagnetic pulsations and proton aurora during the substorm on March 1, 2017, EPJ Web Conf., 254, 2012, https://doi.org/10.1051/epjconf/202125402012, 2021.

Vegard, L.: New types of emission spectra, Nature, 125, 14–14, 1930.

Vegard, L.: Hydrogen Showers in the Auroral Region, Nature, 144, 1089–1090, https://doi.org/10.1038/1441089b0, 1939.

Virtanen, I. I., Tesfaw, H. W., Roininen, L., Lasanen, S., and Aikio, A.: Bayesian Filtering in Incoherent Scatter Plasma Parameter Fits, Journal of Geophysical Research: Space Physics, 126, e2020JA028 700, https://doi.org/10.1029/2020JA028700, 2021.

Virtanen, I. I., Tesfaw, H. W., Aikio, A. T., Varney, R., Kero, A., and Thomas, N.: F1 Region Ion Composition in Svalbard During the International Polar Year 2007–2008, Journal of Geophysical Research: Space Physics, 129, e2023JA032 202, https://doi.org/10.1029/2023JA032202, e2023JA032202 2023JA032202, 2024.

Wall, M.: SpaceX to launch 4 people on historic Fram2 mission over Earth's poles in late 2024 — space.com, https://www.space.com/spacex-fram2-first-human-spaceflight-earth-poles, [Accessed 10-07-2025], 2025.

Wang, N., Qian, L., Yue, J., Wang, W., Mlynczak, M. G., and Russell, J. M.: Climatology of Mesosphere and Lower Thermosphere Residual Circulations and Mesopause Height Derived From SABER Observations, Journal of Geophysical Research: Atmospheres, 127, e2021JD035 666, https://doi.org/10.1029/2021JD035666, 2022.

Wannberg, G., Wolf, I., Vanhainen, L. G., Koskenniemi, K., Röttger, J., Postila, M., Markkanen, J., Jacobsen, R., Stenberg, A., Larsen, R., Eliassen, S., Heck, S., and Huuskonen, A.: The EISCAT Svalbard radar: A case study in modern incoherent scatter radar system design, Radio Science, 32, 2283–2307, https://doi.org/10.1029/97RS01803, 1997a.

Wannberg, G., Wolf, I., Vanhainen, L.-G., Koskenniemi, K., Röttger, J., Postila, M., Markkanen, J., Jacobsen, R., Stenberg, A., Larsen, R., Eliassen, S., Heck, S., and Huuskonen, A.: The EISCAT Svalbard radar: A case study in modern incoherent scatter radar system design, Radio Science, 32, 2283–2307, https://doi.org/10.1029/97RS01803, 1997b.

Warren, H.: SpaceX launches Fram2 crewed mission to historic polar orbit - NASASpaceFlight.com — nasaspaceflight.com, https://www.nasaspaceflight.com/2025/03/fram2-launch/, [Accessed 10-07-2025], 2025.

Whiter, D. K., Lanchester, B. S., Gustavsson, B., Ivchenko, N., and Dahlgren, H.: Using multispectral optical observations to identify the acceleration mechanism responsible for flickering aurora, Journal of Geophysical Research: Space Physics, 115, https://doi.org/10.1029/2010JA015805, 2010.

Whiter, D. K., Sundberg, H., Lanchester, B. S., Dreyer, J., Partamies, N., Ivchenko, N., Di Fraia, M. Z., Oliver, R., Serpell-Stevens, A., Shaw-Diaz, T., and Braunersreuther, T.: Fine-scale dynamics of fragmented aurora-like emissions, Annales Geophysicae, 39, 975–989, https://doi.org/10.5194/angeo-39-975-2021, 2021.

Wüst, S., Bittner, M., Espy, P. J., French, W. J. R., and Mulligan, F. J.: Hydroxyl airglow observations for investigating atmospheric dynamics: Results and challenges, Atmospheric Chemistry and Physics, 23, 1599–1618, https://doi.org/10.5194/ACP-23-1599-2023, 2023.

Xiao, F., Zong, Q., Su, Z., Yang, C., He, Z., Wang, Y., and Gao, Z.: Determining the mechanism of cusp proton aurora, Scientific Reports, 3, https://doi.org/10.1038/SREP01654, 2013.

Yahnin, A. G. and Yahnina, T. A.: Energetic proton precipitation related to ion cyclotron waves, Journal of Atmospheric and Solar-Terrestrial Physics, 69, 1690–1706, https://doi.org/10.1016/J.JASTP.2007.02.010, 2007.

Yahnina, T. A., Yahnin, A. G., Kangas, J., and Manninen, J.: Proton precipitation related to Pcl pulsations, Geophysical Research Letters, 27, 3575–3578, https://doi.org/10.1029/2000GL003763, 2000.

Yonker, J.: Spectroscopy of the N_2 Vegard-Kaplan bands in the dayglow, Ph.D. thesis, University of Alaska Fairbanks, URL http://hdl.handle.net/11122/6189, 2005.

Yuan, Z., Xiong, Y., Li, H., Huang, S., Qiao, Z., Wang, Z., Zhou, M., Wang, D., Deng, X., Raita, T., and Wang, J.: Influence of precipitating energetic ions caused by EMIC waves on the subauroral ionospheric e region during a geomagnetic storm, Journal of Geophysical Research: Space Physics, 119, 8462–8471, https://doi.org/10.1002/2014JA020303, 2014.

Zhang, Y.-p., Deng, L.-h., Zhang, J., and Chen, Y.-q.: Rotational Analysis of A 2 Π u- X 2 Σ g+ System of 14 N 2+, Chinese Journal of Chemical Physics, 28, 134–142, 2015.

"Well, I am going back into the open air, to see what the wind and sky are doing".

J.R.R. Tolkien/Legolas in *The Two Towers*